Cosmological and astrophysical implications of the internal structure of dark matter halos

Tamara Richardson

PSL
UNIVERSITÉ PARIS

THÈSE DE DOCTORAT
DE L'UNIVERSITÉ PSL

Préparée à l'Observatoire de Paris

Implications cosmologiques et astrophysiques de la structure interne des halos de matière noire

Soutenue par

Tamara Rose Grace Richardson

Le December 11, 2023

École doctorale n°127

Astronomie et Astrophysique d'île de France

Spécialité

Cosmologie

Composition du jury :

Benoit Semelin Prof, LERMA - Observatoire de Paris	*Président*
Benoit Famaey DR, Observatoire de Strasbourg	*Rapporteur*
Marco De Petris Prof, La Sapienza University of Rome	*Rapporteur*
Jean-Baptiste Melin DR, CEA	*Examinateur*
Sandrine Codis CR, CEA	*Examinateur*
Sandrine Pires CR, CEA	*Examinateur*
Emmanuel Nezri CR, LAM - Université Aix-Marseille	*Examinateur*
Pier-Stefano Corasaniti DR, LUTH - Observatoire de Paris	*Directeur de thèse*

l'Observatoire de Paris | PSL

To Sasha

But the helm of her secrecy had fallen from her, and her bright hair, released from its bonds, gleamed with pale gold upon her shoulders. Her eyes grey as the sea were hard and fell, and yet tears were on her cheek. A sword was in her hand, and she raised her shield against the horror of her enemy's eyes.

- J.R.R. Tolkien, *The Return of the King*

Acknowledgements

Well here we are, three years of work summarised in 150 pages. It is crazy to think how fast these last few years have gone by. Looking back, it almost feels mad to know that, at the end of the day, one thing lead to another and I've ended up here. Not that it was easy, far from it, but that all of this work emerged simply from a continuous string of ideas, events and accidentally being in the right place at the right time. Some say that the point of the journey is not the destination but the friends you make along the way, and I feel it would be arrogant not the recognise all the help I have gotten throughout the years. Not only when it comes to the work presented here but also making me who I am today. As such, I would like to immortalise in a few words a part of them that will, I hope, forever be a part of me.

Starting with the elephant in the room and possibly the person that has had the largest influence these past three years, at least on the work presented here, Pier-Stefano. I feel like we got off to a slow start, between a global pandemic and not being able to interact as much as I would have liked to. It was only really after the second year rolled around that things started moving. While you were my advisor I felt that you really valued my opinion on things and gave me the space to go my own way. I really appreciated our discussions, both those about science and all the random ones about completely unrelated topics. You choosing to work with me all those years ago started this amazing adventure and I'm really grateful that you gave me this opportunity.

I'd like to also mention the other members of the COS group, Yann, Amandine and Iñigo. Yann, I loved every time you would just pop round my office and unleashed a torrent of ideas. Just ideas, nothing we could work on right then right now, but it was always super interesting. Amandine for the hour long discussions we would have on the zoom once everybody left the meeting. And my friend Iñigo, with whom I've enjoyed working with immensely and hope to be able to continue doing so in the years to come.

Beyond our small group the LUTH as a whole has been an amazing adoptive family. A special thanks to the other research groups for taking me in for lunch when my team couldn't make it. Marie and Livia for taking care of so many things in the background. Stephane and Fabrice for taking care of any IT related issues and somehow keeping advil and bingo alive, actual wizards. With an honourable mention to the coffee machine, you don't realise what you had until it is gone.

A special thanks also goes out to all the friends I've made along the way. To Julia, just for being awesome and amazing and all the support you've given since we met in MAUCA. To Julien, for pushing the shy little girl you met in the bachelor into the world of cosmology. To Andrew, for your bright shinning kindness and determination. To Axel, who I wish I could have told to look in the mirror and see how good he is instead of looking up to me. To Ziad, for introducing me to the amazing world of Dungeons and Dragons. To Gaëtan, in the words of ABBA, thank you for the music, the songs I'm singing. To Anna, for your strength, radiating so much kindness even when you were fighting your hardest battles. To Eve, for the endless discussions we had

over a cup of tea. To Corentin, for showing me that kindness can be well hidden. Lami, for giving me the contact for that flat right at the start of the thesis. And of course Jordan and Gaël, for the jokes, they still aren't funny but I'm going to miss them. To Selee, for being the friend I never knew I needed. To the people at DIPC, Jens, Marcos, Matteo, Giovanni, Lurdes, who while meeting me at a time of great turmoil, provided a kind and friendly environment in which I could rebuild myself. And of course thank you to Oliver and Raúl for making that trip to Spain possible.

To all the people I met at the Euclid schools for all the fun nights, to the Raphael Wicker, for being a badass. To Raphael Kou, for trying to teach me how to dance in the sand. To Emilie, for reminding me how small the world is. To Elizabeth, for being there when I broke down in tears, even when you had only known me for little over a week. To the people from Grenoble, Correntin, Alice, Marina, Mannon and Damien, who made my two weeks surrounded by transphobes in Ronces-les-Bains a great time I'll never forget. To Enya, for the chaos. To Emma, for counteracting that chaos. And to, Miren, Constantin, Romain, Adrien, Hubert for the laughs, the pints and the good nights.

To my fellow PhD representatives at the doctoral school, Eduardo, Tania, Mathilde, Ariane, Christian and in particular Camille who was not only a brilliant colleague but also helped me grow throughout my PhD. To Thierry for giving me so many opportunities and placing so much trust in me. To the people at the CEV, for giving me a chance to fight some of the darkness of this world.

Finally let us not forget the people that have been with me for the longest time and that I wouldn't give up for anything. To Sasha, my beloved partner, for staying by my side throughout all the good times and the bad, for being there when I needed you most and for all of the help you have given me to become who I am today. To Edward, who kept me sane and down to earth with simple things like memes and Pokémon. To Charles, who despite being a bit of a knob from time to time is one of the people with the biggest hearts I know. To Amelia, Ebony and now little Theodore, for all the fun we've had online. To my late farther, Roland Richardson, who I miss deeply and without whom I may have not followed the dreams and ambitions that brought me here. To my mother, for your love and support throughout the years. To Sasha's family, Céline, David, Michel, Mirielle, for taking me in as one of their own children for the last eight years. To my extended family, Deborah and Johnathan, Andrew and Dawn, Paul and Vicky, Charlotte and Sam, for all the love and support. And a special thanks to my high-school biology teacher Sophie, for seeing my potential and pushing me onward and upward all those years ago. Finally I would like to thank my cat, Pilk, who just walked in from the street one day and decided that he was going to live with us, I love you my baby.

Simulations, databases and codes

This work was granted access to HPC resources of TGCC through allocations made by GENCI (Grand Équipement National de Cal- cul Intensif) under the allocations 2020-A0090402287 and 2021- A0110402287.

The CosmoSim database used in this work is a service by the Leibniz-Institute for Astrophysics Potsdam (AIP). The MultiDark database was developed in cooperation with the Spanish MultiDark Consolider Project CSD2009-00064.

The author gratefully acknowledges the Gauss Centre for Supercomputing e.V. (www.gauss-centre.eu) and the Partnership for Advanced Supercomputing in Europe (PRACE, www.prace-ri.eu) for funding the MultiDark simulation project by providing

computing time on the GCS Supercomputer SuperMUC at Leibniz Supercomputing Centre (LRZ, www.lrz.de). The Bolshoi simulations have been performed within the Bolshoi project of the University of California High-Performance AstroComputing Center (UC-HiPACC) and were run at the NASA Ames Research Center.

The author thanks Instituto de Astrofisica de Andalucia (IAA-CSIC), Centro de Supercomputacion de Galicia (CESGA) and the Spanish academic and research network (RedIRIS) in Spain for hosting Uchuu DR1, DR2 and DR3 in the Skies & Universes site for cosmological simulations. The Uchuu simulations were carried out on Aterui II supercomputer at Center for Computational Astrophysics, CfCA, of National Astronomical Observatory of Japan, and the K computer at the RIKEN Advanced Institute for Computational Science. The Uchuu Data Releases efforts have made use of the skun@IAA_RedIRIS and skun6@IAA computer facilities managed by the IAA-CSIC in Spain (MICINN EU-Feder grant EQC2018-004366-P).

The author thanks the developers and maintainers of the COLOSSUS package (Diemer, 2018) that was used in this work. The plots presented in this work were produced with the MATPLOTLIB (Hunter, 2007) package. A significant amount of the numerical computations were carried out using the NUMPY (Harris et al., 2020), SCIPY (Virtanen et al., 2020), and SCIKIT-LEARN (Pedregosa et al., 2011) packages.

Contents

List of Figures

List of Tables

Acronyms & Abbreviations

- AMICO: Adaptive Matched Identifier of Clustered Objects
- AMR: Adaptive Mesh Refinement
- AUC: Area Under the (ROC) Curve
- BAO: Baryonic Acoustic Oscillations
- CIC: Cloud-In-Cell
- $c - M$ (relation): concentration-Mass relation
- CMB: Cosmic Microwave Background
- DE: Dark Energy
- DM: Dark Matter
  - CDM: Cold Dark Matter
  - FDM: Fuzzy Dark Matter
  - WDM: Warm Dark Matter
  - SIDM: Self-interacting Dark Matter
- EdS: Einstein de Sitter Cosmology
- FFT: Fast Fourier Transform
- FLRW: Friedmann-Lemaître-Robertson-Walker
- FoF: Friends of Friends
- GR: General Relativity
- HMF: Halo Mass Function
- ICM: Intra-Cluster Medium
- KiDS: Kilo Degree Survey
- MAH: Mass Accretion History
- MCMC: Markov Chain Monte-Carlo
- MMP: Most Massive Progenitor
- NFW: Navarro, Frenk & White (profile)

- PDF: Probability Distribution Function
- PM: Particle Mesh
- ROC: Receiver Operating Characteristic (curve)
- SO: Spherical Overdensity
- SVM: Support Vector Machine

1 | Introduction

Observations of the Universe have led to the scientific consensus that the latter is mainly composed of invisible components. Many cosmological probes such as, the Cosmic Microwave Background (CMB) (Hinshaw et al., 2013; Planck Collaboration et al., 2020), the clustering of galaxies and weak lensing shear (DESI Collaboration et al., 2016; Abbott et al., 2022; Sugiyama et al., 2023), type Ia supernovae (Riess et al., 2022), all point to an accelerated expansion of the universe powered by an invisible form of exotic matter dubbed dark energy as well as strongly favouring the existence of an undetected matter component, which only interacts through gravitation dubbed Cold Dark Matter (CDM).

In recent years, these probes have become in tension with one another, inferring values of some of the cosmological parameters which are at odds with one another. In particular, the $5-\sigma$ tension between the low value of $H_0 = 67.36 \pm 0.55$ kms^{-1}Mpc^{-1}, inferred from observations of the CMB (Planck Collaboration et al., 2020) and the high value, $H_0 = 73.04 \pm 1.04$ kms^{-1}Mpc^{-1}, inferred from the SH0ES analysis (Riess et al., 2022) has garnered much attention due to the potential physical implications it may have (see e.g. Di Valentino et al., 2021; Abdalla et al., 2022; Schöneberg et al., 2022, for reviews). In this landscape, new cosmological probes have emerged allowing new measurements of this parameter with different systematics, such as replacing the Cepheid anchored distance ladder by one anchored using the tip of the red giant branch (e.g. Freedman et al., 2020), lensed quasar time delays (e.g. Shajib et al., 2023) and gravitational waves (Abbott et al., 2021).

A second, and sometimes omitted, tension also exists on the combined parameter, $S_8 = \sigma_8 \sqrt{\Omega_\mathrm{m}/0.3}$, where σ_8 is the amplitude of the linear matter density fluctuations on the scale of $8h^{-1}$Mpc and Ω_m is the matter density parameter. This $2-\sigma$ tension between the CMB (Planck Collaboration et al., 2020) and local measurements of galaxy clustering and weak lensing shear (DESI Collaboration et al., 2016; Abbott et al., 2022; Sugiyama et al., 2023), has also sourced numerous physical interpretations (e.g. Abdalla et al., 2022, for a review), which attempt to alleviate the tension. This calls for the identification of novel cosmological probes capable of providing complementary independent constraints on the cosmological parameters. This is the spirit of the work presented throughout this thesis where we present a novel approach based on the internal structure of galaxy clusters.

As the most massive gravitationally bound structures in the Universe, galaxy clusters provide unique opportunities to study both astrophysics and cosmology. The mass budget of these structures is for the most part dominated by a massive dark matter halo, $f_\mathrm{DM} \sim 80$ percent of the total mass, within which has accumulated a large quantity of hot ionoized gas, $f_\mathrm{gas} \sim 15$ percent, with only the remaining 5 percent being the stars we are able to see in visible light. Over the past decades, these objects have been subject to countless studies to link the physical properties of galaxy clusters, most notably mass, to visible quantities such as the richness of the cluster or the properties of the X-ray

emitting gas (e.g Bellagamba et al., 2019; Mulroy et al., 2019; Bahar et al., 2022).

Recently, it has become possible to extract information about the internal structure of these objects (Umetsu et al., 2020; Eckert et al., 2022a). With the recent advent of dedicated high quality cluster observing campaigns (e.g Romualdez et al., 2016; Adam et al., 2018; CHEX-MATE Collaboration et al., 2021), as well as the arrival of wide surveys such as, *Euclid* (Laureijs et al., 2011) and the Rubin observatory's Legacy Survey of Space and Time (LSST) (Ivezić et al., 2019) in the visible and *eROSITA* (Merloni et al., 2012) in X-rays, we expect that in upcoming years a considerable amount of large homogeneous data-sets, ranging in size from at least a few hundred objects to a few thousands, will be available. In this work, we show that these data can be used to constrain cosmology through the introduction of a novel statistical proxy for the shape of the mass profile of clusters. Moreover, these constraints that can be completely independent of both sides of the S_8 tension debate. For instance potentially providing constraints solely from X-ray observations. As such, this thesis aims to both define this probe and begin to outline the systematics that affect it and how these can be controlled.

As such, this thesis is structured as follows. In Chapter 2 we overview the physical processes that lead to the formation of galaxy clusters. Taking a dynamical approach, we first describe the evolution of the cosmological background and how small density perturbations evolve in the early universe. We then describe the gravitational collapse of density field and the formation of cosmic structures such as haloes, filaments, walls, and voids. After providing a brief overview of cosmological simulations, we end this chapter by discussing past and current models of the halo mass function and internal structure of haloes.

In Chapter 3, we introduce the notion of halo sparsity. Defined as a simple mass ratio, this quantity can be measured for any object without needing to assume a parametric mass profile. We show that this non-parametric nature allows us to relate the internal structure of haloes to the halo mass function and in turn unify descriptions of the profile through a stochastic mathematical formalism. This description allows us to anchor our formalism as a generalisation of previously independent results. Most notably, this formalism allows us to predict the Navarro-Frenk-White concentration mass relation directly from a model of the halo mass function.

Chapter 4, is devoted to the study of how halo sparsity reacts to halo mergers, the main process through which dark matter haloes acquire their mass. In particular, we focus on major mergers, which we defines as mergers where the secondary halo is at least one third of the mass of the primary halo. We find, in agreement with Wang et al. (2020a), that sparsity reacts in a systematic fashion, displaying a strong pulse like feature in the sparsity history. We use this feature to design a statistical methodology to detect clusters that have recently undergone a major merger, and even provide a first estimate of when the event took place. While not very accurate at predicting the time of the merger, this approach provides a simple and fast method of sifting through large catalogues and flagging clusters for further investigation.

In Chapter 5, we present the cosmological applications of sparsity. After a brief overview of the methods previously used by Corasaniti et al. (2018) we design a novel approach to constrain cosmology using the internal structure of galaxy clusters. This method treats each object in a sample as an individual data point rather than condensing them into a summary statistic. We show that this approach has the potential to strongly increase the constraining power of sparsity based methods without needing any additional data. Nevertheless, this increase in constraining power comes at the cost

of new systematic effects, which we begin to characterise in order to apply this novel approach to observational data in the near future.

On a different topic, in Chapter 6 we present work devoted to constraining non-standard scenarios of dark matter through the lensing effect produced by cosmic structures. In particular, we focus on the contribution of structures other than haloes such as filaments and walls which are more abundant in certain dark matter scenarios. To do so, we model observations of quadruply lensed quasars, which we then perturb using different types of structures. We find that non-halo structures in warm dark matter cosmologies can indeed cause sizeable perturbations to flux ratio observations due to the production of step like features in the surface density field.

Finally in Chapter 7 we present our conclusions on this work and perspectives on how it can, much like the Universe, expand in the future.

This work led to the publication of three peer-reviewed articles (Richardson et al., 2022; Richardson & Corasaniti, 2022, 2023) as well as contributions to a fourth article (Corasaniti et al., 2022), which have been distributed throughout the thesis. In particular, Chapter 3 and Chapter 5 contain sections adapted from Richardson & Corasaniti (2023), while Chapter 4 and Chapter 6 are respectively adapted from Richardson & Corasaniti (2022) and Richardson et al. (2022).

2 | The standard cosmological scenario

As stated in the previous chapter, the ΛCDM model is currently the leading scenario which is able to account for the bulk of current cosmological observations. This expanding universe model is based on two primary pillars: General Relativity and the cosmological principle. The latter states that the universe must be homogeneous and isotropic at least at some scale. This predicts a hot and dense beginning where the Universe is dominated by radiation before rapidly cooling under the effects of the expansion. This first epoch is then followed by a period dominated by matter, where we see structures form under the influence of gravity before finally giving way to an epoch dominated by a dark energy component, which accelerates the expansion. In this chapter, we will go over in detail how these structures form and how we can describe them.

To do so we will first have to describe how the Universe evolves at large scales as this will provide the background within which we can paint the scene of structure formation. Following the chronology of events, we will then present how to model perturbations in the early Universe and discuss their evolution at early times. Moving forward in time, we will see how these perturbations collapse to form structures. Through the theoretical description of the gravitational collapse of matter we will infer the properties of the final population of collapsed objects. Finally, we will present the inner workings of cosmological simulation codes and how these can be used to solve the full dynamics of matter inside the Universes. We will then use results from these codes to understand the limitations of the theoretical models, while also providing a brief presentation of past work describing the trends seen in these simulations.

2.1 The expanding homogeneous background

Before studying the formation of structures, let us first review the evolution of both the background cosmological model and background density field. The foundational assumption of the ΛCDM scenario, known as the cosmological principle, is that the distribution of matter in the Universe is homogeneous and isotropic on large scales. Within the framework of general relativity, this translates into the homogeneous and isotropic Friedmann-Lemaître-Robertson-Walker (FLRW) metric,

$$\mathrm{d}s^2 = -c^2\mathrm{d}t^2 + a(t)^2\left(\frac{\mathrm{d}r^2}{1-kr^2} + r^2\left\{\mathrm{d}\theta^2 + \sin^2\theta\mathrm{d}\varphi^2\right\}\right), \tag{2.1}$$

where ds is the infinitesimal space-time distance element, c is the metric's Minkowski velocity also commonly referred to as the speed of light, t is a time-like coordinate, a is the scale factor, a dimensionless factor which defines the scale of the universe with respect to today, r, θ and φ, define a comoving reference frame such that distances

in this reference frame do not change with time, finally k defines the curvature of the universe such that,

$$\begin{cases} k < 0 & \text{the Universe is spatially open,} \\ k = 0 & \text{the Universe is spatially flat,} \\ k > 0 & \text{the Universe is spatially closed.} \end{cases} \tag{2.2}$$

This geometrical parameter not only influences how distances are measured on this metric, but also the evolution of the Universe itself. Given this metric, the dynamics of the homogeneous Universe is completely determined by the evolution of the scale factor which can be obtained from Einstein's field equations,

$$R_{\mu\nu} - \frac{1}{2}Rg_{\mu\nu} + \Lambda g_{\mu\nu} = \frac{8\pi G}{c^4}T_{\mu\nu}, \tag{2.3}$$

where $g_{\mu\nu}$ is the metric tensor, Λ is the cosmological constant, $R_{\mu\nu}$ and R are respectively the Ricci tensor and Ricci scalar which define how the metric is deformed under the influence of matter described by the stress-energy tensor, $T_{\mu\nu}$, which for a homogeneous and isotropic perfect fluid can be written as,

$$T_{\mu\nu} = (\rho + p/c^2)u_\mu u_\nu + pg_{\mu\nu} \tag{2.4}$$

with ρ and p, the density and pressure of the fluid and u_μ its 4-velocity. Explicitly writing these equations for the FLRW metric, we obtain the Friedmann equations for the evolution of the scale factor,

$$\left(\frac{\dot{a}}{a}\right)^2 = \frac{8\pi G}{3}\rho - \frac{c^2 k}{3a^2} + \frac{\Lambda c^2}{3}, \tag{2.5}$$

$$\frac{\ddot{a}}{a} = -\frac{4\pi G}{3}\left(\rho + \frac{3p}{c^2}\right) + \frac{\Lambda c^2}{3}. \tag{2.6}$$

Introducing the Hubble parameter, $H = \dot{a}/a$, and its value at the current epoch, H_0, these equations can be rewritten to express the evolution of the background as well as the density of the fluid,

$$H^2 = H_0^2\left(\frac{8\pi G}{3H_0^2}\rho - \frac{c^2 k}{3H_0^2 a^2} + \frac{\Lambda c^2}{3H_0^2}\right), \tag{2.7}$$

$$\dot{\rho} = -3H\left(\rho + \frac{p}{c^2}\right). \tag{2.8}$$

Finally, by solving this second equation as a function of a for a generic perfect fluid with equation of state, $p = w\rho c^2$, and introducing the critical density of the universe at the current epoch, $\rho_{\rm c} = \frac{3H_0^2}{8\pi G}$, we can rewrite the three terms on the right hand side of this equation as dimensionless density parameters Ω_i,

$$H^2(a) = H_0^2\left(\sum_i \Omega_i a^{-3(w_i+1)} + \Omega_{\rm k}a^{-2} + \Omega_\Lambda\right), \tag{2.9}$$

where the sum is made over the different species of fluid we want to consider. Typically we consider the Universe to be filled with three fluids, radiation which has non-vanishing pressure $w_{\rm r} = 1/3$, ordinary matter known as baryons, and dark matter, which are, for

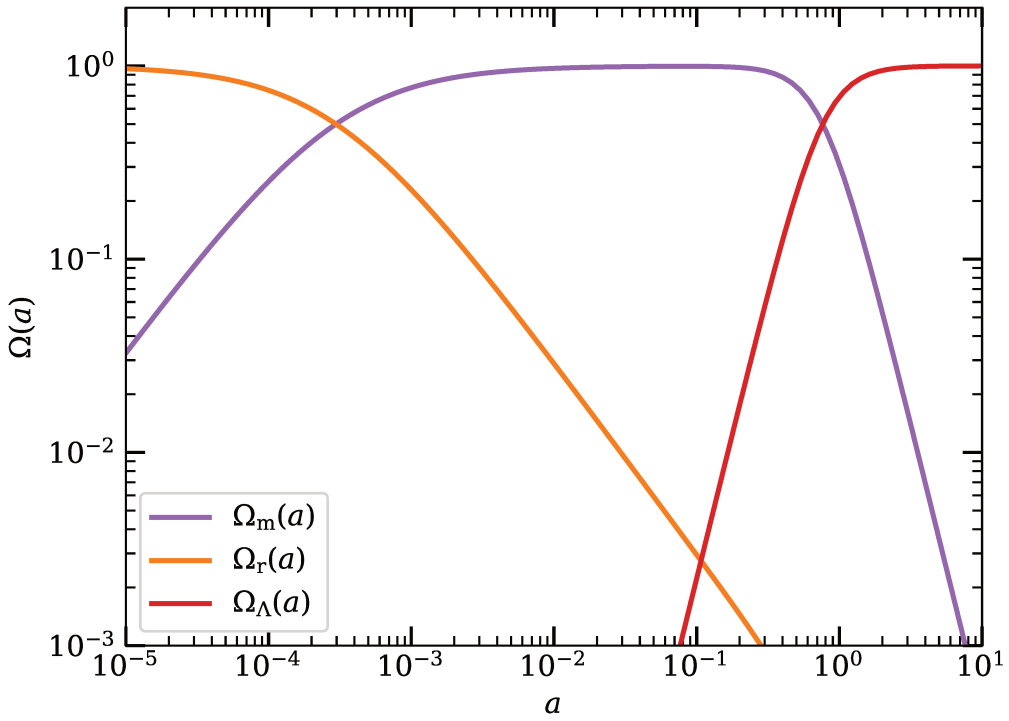

Figure 2.1: Evolution of the density parameters with respect to the scale factor a. Here we can clearly identify three regions were each parameter dominates, the early universe dominated by radiation, Followed by matter domination and dark energy domination at late times.

simplicity, both considered pressureless, $w_\mathrm{b} = w_\mathrm{c} = 0$, and thus regrouped into a single matter term. The Friedmann equation then takes the form,

$$H^2(a) = H_0^2 \left(\Omega_\mathrm{r} a^{-4} + \Omega_\mathrm{m} a^{-3} + \Omega_\mathrm{k} a^{-2} + \Omega_\Lambda \right), \tag{2.10}$$

where Ω_k and Ω_Λ are the density parameters respectively associated to curvature and the cosmological constant. With this definition, it is easy to understand why Ω_Λ is often considered as a contribution from an undetected dark energy component, as we can relate it to an effective fluid with equation of state parameter $w_\Lambda = -1$. Finally by recasting the curvature parameter as, $\Omega_\mathrm{k} = 1 - \Omega_\mathrm{r} - \Omega_\mathrm{m} - \Omega_\Lambda$, we can interpret the curvature as a surplus or deficit of density with respect the to critical density, ρ_c.

In Eq. (2.10) the density parameters are evaluated at the current epoch, with the time evolution made explicit. When considered alone, these parameters must also account for the time evolution of the critical density $\rho_c \propto H^2(a)$. Thus, the time evolution of the density parameters,

$$\Omega_i(a) = \Omega_i \frac{H_0^2}{H^2(a)} a^{-3(w_i+1)}, \tag{2.11}$$

also inherits the time evolution of the Hubble parameter.

In Fig. 2.1, we show the evolution of the density parameters assuming their values correspond to the best fit parameters of the Planck collaboration's 2015 analysis (Planck

Collaboration et al., 2016), see Tab. 2.1. We can clearly see that over the course of cosmic time each individual parameter dominates over the others. Indeed, in the early Universe the medium is dominated by radiation, while at later times it is subsequently dominated by matter and then the cosmological constant. These subsequent periods of domination by the various species translates into difference in the evolution of the Universe at these epochs, most notably in the rate at which the universe expands.

Often, the scale factor is used interchangeably with the observed redshift, z, as the latter is an observable quantity. The relation between the two can be derived simply by considering that between the emission of a bundle of light at wavelength λ_e at time t_e and its observation at wavelength λ_o at time t_o the universe would have grown by a factor $a(t_\mathrm{o})/a(t_\mathrm{e})$. If we consider that the light bundle is observed today we have,

$$\frac{\lambda_\mathrm{o}}{\lambda_\mathrm{e}} = \frac{1}{a} = 1 + z. \tag{2.12}$$

This interchangeability not only cements the cosmological origin of the redshifting of distant galaxies, but also directly links how distances are measured and an observable property of distant objects. Indeed, accounting for the expansion of the universe the comoving distance, $d_\mathrm{C}(z)$, between us and an object with redshift, z, is given by (see e.g. Dodelson, 2003; Weinberg, 2008),

$$d_\mathrm{C}(z) = d_\mathrm{H} \int_0^z \frac{\mathrm{d}z'}{E(z)}, \tag{2.13}$$

where for convenience we introduced the Hubble distance, $d_\mathrm{H} = c/H_0$, and the dimensionless Hubble parameter, $E(z) = H(z)/H_0$. Again, for the sake of convenience three other distance measure are typically introduced:

- The transverse comoving distance,

$$d_\mathrm{T}(z) = \begin{cases} \frac{d_\mathrm{H}}{\sqrt{\Omega_\mathrm{k}}} \sinh\left(\sqrt{\Omega_k}\frac{d_\mathrm{C}(z)}{d_\mathrm{H}}\right) & \text{if } \Omega_k > 0, \\ d_\mathrm{C}(z) & \text{if } \Omega_k = 0, \\ \frac{d_\mathrm{H}}{\sqrt{|\Omega_\mathrm{k}|}} \sin\left(\sqrt{|\Omega_k|}\frac{d_\mathrm{C}(z)}{d_\mathrm{H}}\right) & \text{if } \Omega_k < 0, \end{cases} \tag{2.14}$$

  which is defined such that the comoving distance between two objects at the same redshift separated on the sky by an angle $\delta\theta$ is simply $d_\mathrm{T}\delta\theta$, with this particular definition emphasising the role of the curvature parameter. This distance measure is then used to define the two others.

- The angular diameter distance,

$$d_\mathrm{A}(z) = \frac{d_\mathrm{T}(z)}{(1+z)}, \tag{2.15}$$

  which is defined in such a way that angular size, $\delta\theta$, of an object of physical size, δl, will simply be $\delta\theta = \delta l/d_\mathrm{A}(z)$.

- The luminosity distance,

$$d_\mathrm{L}(z) = (1+z)d_\mathrm{T}(z), \tag{2.16}$$

  which is defined in such a way that the flux F from a point source of intrinsic luminosity, L, at redshift, z, is $F = \frac{L}{4\pi d_\mathrm{L}^2}$.

2.2 The seeds of inhomogeneity

With the definitions presented above, we are now able to describe the evolution of the background and measure distances in the case of a universe filled with homogeneous and isotropic fluids. This description while accurate at large scales is unable to describe the formation of cosmic structures which are, by definition, inhomogenous.

Let us now assume that the matter component of our universe is all contained within a single self-gravitating, non-relativistic fluid which is dynamically evolving within the expanding background. In addition, let us assume that the fluid is homogeneous and isotropic on large scales, and that local inhomogeneities only represent a small perturbation with respect to the background such that we can define the local density of the fluid, $\rho = \rho_{\rm m}(1+\delta)$, in terms of a dimensionless perturbation, δ, where we also define, $\rho_{\rm m} \equiv \rho_{\rm c}\Omega_m$, the mean density of the fluid.

In the standard cosmological scenario, these density perturbations are generated by quantum fluctuations in the early universe. As such, they are inherently stochastic by nature and so their spatial variation can only be studied statistically. Assuming that the particles created by these quantum fluctuations are at thermal equilibrium or thermalise rapidly, the density perturbation field can be described as a Gaussian random field. In this case the perturbations can be fully described by two quantities, the field's ensemble mean $\langle\delta(\mathbf{x})\rangle$ which is vanishing by definition, because of homogeneity and isotropy, and its two-point correlation function, $\xi(\mathbf{x}_1,\mathbf{x}_2) = \langle\delta(\mathbf{x}_1)\delta(\mathbf{x}_2)\rangle$. The assumption that the field is statistically homogeneous on large scales, allows us to express the latter solely as a function of the separation vector, $\mathbf{x} = \mathbf{x}_1 - \mathbf{x}_2$, between both points. By further assuming the field is ergodic, the averaging operation over all possible states of the field can be replaced by an average over a sufficiently large volume. This allows us to express the two-point correlation function,

$$\xi(\mathbf{x}) = \langle\delta(\mathbf{x}')\delta(\mathbf{x}'+\mathbf{x})\rangle = \frac{1}{V}\int_V \mathrm{d}^3\mathbf{x}'\delta(\mathbf{x}')\delta(\mathbf{x}'+\mathbf{x}), \tag{2.17}$$

as a convolution of the field with itself over a sufficiently large volume V.

Convolutions being complicated to evaluate, both analytically and numerically, it is often more convenient to study their Fourier transform where this operation is replaced by a product. To do so, we define

$$\delta(\mathbf{k}) = \int \mathrm{d}^3\mathbf{x}\; e^{-i\mathbf{k}\cdot\mathbf{x}}\delta(\mathbf{x}) \text{ and } \delta(\mathbf{x}) = \frac{1}{(2\pi)^3}\int \mathrm{d}^3\mathbf{k}\; e^{i\mathbf{k}\cdot\mathbf{x}}\delta(\mathbf{k}), \tag{2.18}$$

respectively the Fourier transform and its inverse.

Considering that the Fourier transform of a Gaussian random field is also a Gaussian random field. If we now write the two-point correlation function in Fourier space between the field and its complex conjugate,

$$\langle\delta(\mathbf{k})\delta^*(\mathbf{k}')\rangle = \int \mathrm{d}^3\mathbf{x}_1 \int \mathrm{d}^3\mathbf{x}_2\; e^{-i\mathbf{k}\cdot\mathbf{x}_1}e^{i\mathbf{k}'\cdot\mathbf{x}_2}\langle\delta(\mathbf{x}_1)\delta(\mathbf{x}_2)\rangle, \tag{2.19}$$

and again introduce the separation vector $\mathbf{x} = \mathbf{x}_1 - \mathbf{x}_2$,

$$\langle\delta(\mathbf{k})\delta^*(\mathbf{k}')\rangle = \int \mathrm{d}^3\mathbf{x}_1\; e^{-i(\mathbf{k}-\mathbf{k}')\cdot\mathbf{x}_1}\int \mathrm{d}^3\mathbf{x}\; e^{i\mathbf{k}'\cdot\mathbf{x}}\langle\delta(\mathbf{x}_1)\delta(\mathbf{x}_1+\mathbf{x})\rangle, \tag{2.20}$$

$$= \delta_D(\mathbf{k}-\mathbf{k}')\int \mathrm{d}^3\mathbf{x}\; e^{i\mathbf{k}'\cdot\mathbf{x}}\xi(\mathbf{x}), \tag{2.21}$$

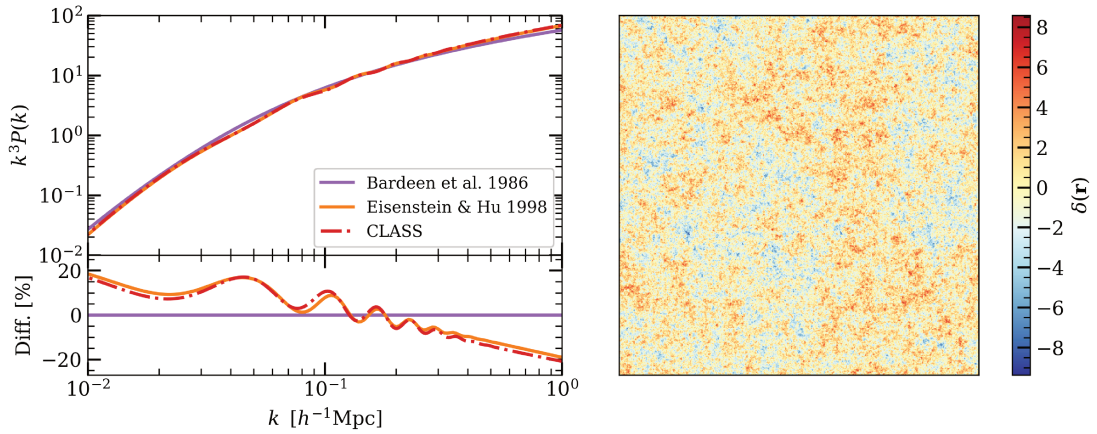

Figure 2.2: *Upper left panel:* power spectrum of matter density fluctuations for two approximate models (Bardeen et al., 1986; Eisenstein & Hu, 1998), and a numerical solution produced with CLASS (Lesgourgues, 2011). *Lower left panel:* the relative difference between the model of Bardeen et al. (1986) and the other two models. The *wiggle* feature seen in the models accounting for baryonic effects are known as the baryonic acoustic oscillations (BAO). *Right panel:* 100 h^{-1}kpc slice of a simulated density perturbation field linearly extrapolated to $z = 0$, assuming the Eisenstein & Hu (1998) transfer function, within a 50 h^{-1}Mpc periodic box with 512 cells per dimension.

a Dirac delta distribution, $\delta_D(\mathbf{k} - \mathbf{k}')$, appears. This indicates that the left hand side of this expression is only ever non-zero when $\mathbf{k} = \mathbf{k}'$ allowing us to equate the Fourier transform of the real-space two-point correlation function to the power spectrum, $P(\mathbf{k})$, of the field such that,

$$\langle \delta(\mathbf{k}) \delta^*(\mathbf{k}') \rangle = (2\pi)^3 \delta_{\mathrm{D}}(\mathbf{k} - \mathbf{k}') P(\mathbf{k}). \tag{2.22}$$

A final simplification can be made by invoking the assumption of isotropy at large scales, which removes the dependence on direction of both the two point correlation function and power spectrum. In which case they only depend on the norms, r and k, of their respective vector parameters.

The power spectrum is usually written in the form of,

$$P(k) = A_{\mathrm{s}} k^{n_{\mathrm{s}}} T(k), \tag{2.23}$$

splitting it into two parts. The first factor, known as the primordial scalar curvature perturbation spectrum, introduces two additional cosmological parameters, A_{s} and n_{s}, the amplitude and spectral index of scalar curvature perturbations. The second, known as the transfer function, $T(k)$, encodes the dynamics of the fluid we are studying.

While A_s may seem the more natural definition for the amplitude of fluctuations, historically the latter has been quantified by,

$$\sigma_R^2 = \frac{1}{2\pi} \int_0^\infty \mathrm{d}k k^2 \hat{W}^2(kR) P(k), \tag{2.24}$$

the variance of the density field smoothed over a sphere of radius R, which by convention is chosen to be 8 h^{-1}Mpc thus defining a new cosmological parameter, σ_8. Here,

$$\hat{W}(kR) = 3 \frac{\sin(kR) - kR\cos(kR)}{(kR)^3} \tag{2.25}$$

Parameter	Planck 2013	Planck 2015	Planck 2018
h	0.674 ± 0.14	0.6774 ± 0.0046	0.6736 ± 0.0055
Ω_m	0.314 ± 0.020	0.6911 ± 0.0062	0.3153 ± 0.0073
Ω_Λ	0.686 ± 0.020	0.3089 ± 0.0062	0.6847 ± 0.0073
Ω_b	0.0486 ± 0.0021	0.0486 ± 0.016	0.04930 ± 0.00087
$10^5\Omega_r$	9.32 ± 0.62	9.16 ± 0.19	9.27 ± 0.23
σ_8	0.814 ± 0.027	0.8159 ± 0.0086	0.8111 ± 0.0060
n_s	0.9616 ± 0.0094	0.9667 ± 0.0040	0.9649 ± 0.0042

Table 2.1: Cosmological parameters resulting from the Planck analysis (Planck Collaboration et al., 2014a, 2016, 2020). Unless specified otherwise we will use the parameters from the 2015 analysis throughout the rest of this work.

is a window function defining a real space top hat filter or radius R.

The shape of the transfer function has been studied in detail with models of increasing complexity. In the left panel of Fig. 2.2 we've reproduced some of the most used shapes of the power spectrum. Bardeen et al. (1986) produced the first widely used approximation, which gave the overall shape of the power spectrum. This approximation was subsequently improved by Sugiyama (1995); Eisenstein & Hu (1998) and Eisenstein & Hu (1999) to include the effect of the gravo-thermal collapse of baryons on the shape of the matter power spectrum. Indeed in Fig. 2.2, we notice the presence of an oscillatory pattern, known as Baryonic Acoustic Oscilations (BAO), which is caused by this pressure support. With the advent of high performance computing these models based on approximate analytical calculations have been replaced by numerical codes such as CMBFAST (Seljak & Zaldarriaga, 1996), CAMB (Lewis et al., 2000), and CLASS (Lesgourgues, 2011), known as Boltzmann solvers, which are able to account for more complex physical effects. In the right panel of Fig. 2.2, for illustration we also produce a Gaussian random field with the Eisenstein & Hu (1998) power spectrum using the best-fit parameters of the Planck 2015 analysis (Planck Collaboration et al., 2016) for which we summarise the relevant parameters in Tab. 2.1.

2.3 Time evolution of perturbations

Having introduced the statistical quantities that allow us to compare theory with observations, let us now look in more details to the time evolution of the primordial density perturbation field. Recalling that the field is associated to a fluid of matter, we place ourselves in the Newtonian limit and describe the dynamics of this fluid of density, ρ, and velocity field, $\mathbf{u}$ using the fluid equations in Eulerian form in comoving coordinate space.

$$\dot{\rho} + a^{-1}\boldsymbol{\nabla} \cdot (\rho \mathbf{u}) = 0, \tag{2.26}$$

$$\dot{\mathbf{u}} + a^{-1}(\mathbf{u} \cdot \boldsymbol{\nabla})\mathbf{u} + H\mathbf{u} = -a^{-1}\frac{\boldsymbol{\nabla} P}{\rho} - a^{-1}\boldsymbol{\nabla}\phi, \tag{2.27}$$

$$a^{-2}\boldsymbol{\nabla}^2\phi = 4\pi G(\rho - \rho_\mathrm{m}), \tag{2.28}$$

where P is the pressure inside the fluid, ϕ is the gravitational potential sourced by the fluid and $\rho_\mathrm{m}(a) = \Omega_m(a)\rho_\mathrm{c}(a)$ is the mean matter density in the Universe. We see that these equations differ from the standard fluid equations only through the presence of the scale factor and a drag term proportional to the Hubble parameter. Note that, in

the case of collisionless dark matter, even if one may be tempted to neglect the pressure term, the initial velocity dispersion of particles in the fluid may act as an effective pressure.

Let us consider that the inhomogeneities only represent a small perturbation with respect to the homogeneous and isotropic background, $\rho = \rho_{\rm m}(1+\delta)$, allowing us to linearise these equations by rewriting them in terms of δ and the divergence of the velocity field $\theta = \boldsymbol{\nabla}\cdot\mathbf{u}$,

$$\dot{\delta} + a^{-1}\theta = 0, \tag{2.29}$$

$$\dot{\theta} + H\theta = -\frac{c_{\rm s}^2}{a}\boldsymbol{\nabla}^2\delta - a^{-1}\boldsymbol{\nabla}^2\phi, \tag{2.30}$$

$$a^{-2}\boldsymbol{\nabla}^2\phi = 4\pi G\rho_m\delta. \tag{2.31}$$

where we have introduced the sound speed, $c_{\rm s}^2 = \frac{\partial P}{\partial\rho}$. These equations can further be reduced into a single second order differential equation by eliminating θ and ϕ,

$$\ddot{\delta} + 2H\dot{\delta} - \left(\frac{3H_0^2}{2a^3}\Omega_{m,0} + \frac{c_{\rm s}^2}{a^2}\boldsymbol{\nabla}^2\right)\delta = 0, \tag{2.32}$$

which in Fourier space reads,

$$\ddot{\delta} + 2H\dot{\delta} + \left(\frac{c_{\rm s}^2}{a^2}k^2 - \frac{3H_0^2}{2a^3}\Omega_{m,0}\right)\delta = 0. \tag{2.33}$$

We see that in the small perturbation limit $\delta \ll 1$ individual scales are decoupled from one another. This equation exhibits two types of solution, one monotonically growing and a second oscillating solution. We see that the type of solution which is produced depends only on the sound speed and scale of study. For baryons, the oscillating mode corresponds to the propagation of sound waves within the fluid, while for collisionless dark matter this corresponds to free streaming. The growing solution, on the other hand, corresponds to the gravitational collapse of the perturbation. What can also be seen is that, as the Universe expands, the sign of the third term can switch meaning that an initially oscillating mode can eventually freeze out and collapse. For baryons in the standard picture of a ΛCDM universe, this occurs at the time of recombination when radiation pressure drops rapidly due to drop in the density of free electrons. For collisionless dark matter, the time where this occurs depends on the initial *warmth* of the fluid. In both cases, after gravity surpasses pressure the dynamics of the fluid simplifies even further,

$$\ddot{D} + 2H\dot{D} - \frac{3H_0^2}{2a^3}\Omega_{m,0}D = 0. \tag{2.34}$$

Since the equation only depends on time, we introduce the linear growth factor D to separate the temporal evolution and spatial distribution of $\delta(\mathbf{x},t) = D(t)\delta(\mathbf{x},t_0)$. This equation exhibits an analytical solution,

$$\frac{D(a)}{D_0} = \frac{H(a)}{H_0}\int_0^a {\rm d}a'\left[\Omega_{\rm r}a'^{-2} + \Omega_{\rm m}a'^{-1} + \Omega_\Lambda a'^2 + \Omega_{\rm k}\right]^{-3/2}, \tag{2.35}$$

where D_0 is chosen such that $D(a=1) = 1$. The behaviour of this integral can be evaluated analytically when we consider that one density parameter dominates over the others. As such we can show that during:

- Radiation domination, $D(a) \propto a^2$,

- Matter domination, $D(a) \propto a$ and
- Dark Energy domination, $D(a)$ becomes constant.

An interpretation of this result is that for most of the history of the Universe the perturbations grow, and eventually freeze out. But what does this mean for the properties of the field? As we have separated out the temporal evolution of the perturbations and neglected the spatial evolution of the field, the perturbations remain Gaussian and so we can continue to fully describe them through their mean and power spectrum. By definition the mean of the density perturbation field does not change, $\langle\delta(t)\rangle = 0$. The power spectrum however,

$$\begin{aligned} P(\mathbf{k},t) &= \frac{1}{(2\pi)^3}\delta_{\mathrm{D}}(\mathbf{k}-\mathbf{k}')\langle\delta(\mathbf{k},t)\delta(\mathbf{k}',t)\rangle, \\ &= \frac{1}{(2\pi)^3}\int \mathrm{d}^3\mathbf{x} e^{i\mathbf{k}\cdot\mathbf{x}}\langle\delta(\mathbf{x}',t)\delta(\mathbf{x}'+\mathbf{x},t)\rangle, \\ &= \frac{1}{(2\pi)^3}\int \mathrm{d}^3\mathbf{x} e^{i\mathbf{k}\cdot\mathbf{x}} D(t)^2\langle\delta(\mathbf{x}',t_0)\delta(\mathbf{x}'+\mathbf{x},t_0)\rangle, \\ P(\mathbf{k},t) &= D(t)^2 P(\mathbf{k},t_0), \end{aligned} \tag{2.36}$$

is proportional to $D(t)^2$, simply implying that the amplitude of fluctuations is indeed increasing with time.

This steady increase in the amplitude however implies that the hypothesis of small perturbations is only valid for a time, commonly referred to as the linear regime, and eventually breaks down. Once the perturbations become large, we can no longer treat them using this formalism. However, before having to resort to cosmological simulations, the evolution of these perturbations can be studied further.

2.4 Following the Flow

As said previously, the main issue encountered by perturbation theory is that eventually the assumption that δ is small breaks down. It is however possible to drop this assumption completely, simply by changing point of view. This is achieved simply by switching to the Lagrangian formulation of the fluid equations, in essence instead of studying the dynamics of a fluid within a fixed frame of reference, we follow the flow of a fluid element and study how it evolves. In this formalism any quantity X which is transported by the flow remains within the fluid element. As such, where in a Eulerian framework the transport derivative,

$$\frac{\mathrm{D}X}{\mathrm{D}t} = \dot{X} + (\mathbf{u}\cdot\boldsymbol{\nabla})X, \tag{2.37}$$

exhibits a highly non trivial term on the right hand side, making it notoriously difficult to solve. In a Lagrangian framework it simply becomes $\dot{X}$, making the resolution significantly easier. In the case at hand for example, the Euler equation, e.g. Eq (2.27), becomes,

$$\dot{\mathbf{u}} + H\mathbf{u} = -a^{-1}\boldsymbol{\nabla}\phi, \tag{2.38}$$

which is significantly simpler than its Eulerian counterpart. Note we have dropped the pressure term because as we have mentioned it vanishes rapidly for collisionless dark matter soon after production and similarly for baryons after recombination.

This simplification is however not sufficient to solve the dynamics of the system. Indeed, the main obstacle preventing us from achieving this is the complex time evolution of the potential. Lagrangian perturbation theory circumvents this issue by introducing additional assumptions on the trajectory of the fluid element, which in turn becomes an indirect assumption on the evolution of the potential. The first order of approximation, introduced by Zel'dovich (1970) and named the Zel'dovich Approximation, assumes that the fluid elements move along straight lines, implicitly this requires that the spatial distribution of the potential remains fixed while the amplitude simply grows. This is, surprisingly, the result from linear theory,

$$\phi(\mathbf{x}, t) = \frac{D(t)}{a(t)}\phi(\mathbf{x}, t_0) = \frac{D(t)}{a(t)}\phi_\mathrm{i}, \tag{2.39}$$

that we have derived above and seems counter intuitive as we have previously said that linear theory breaks down quite rapidly. However, the Laplacian operator in the Poisson equation significantly smooths out the small scale structure in δ, making this assumption far more reasonable at later times. This approximation remains valid until the trajectories of the fluid elements start intersecting, a moment known as shell crossing. Indeed in this approximation, as the fluid elements move along straight lines, they simply continue on their way, while in the full non-linear system the local gravitational potential would significantly change and possibly bind them together.

Using Eq. (2.39), we can solve the motion of the fluid elements analytically,

$$\begin{aligned}
\dot{\mathbf{u}} + H\mathbf{u} &= -\frac{D}{a^2}\boldsymbol{\nabla}\phi_\mathrm{i}, \\
\frac{1}{a}\partial_t(a\mathbf{u}) &= -\frac{D}{a^2}\boldsymbol{\nabla}\phi_\mathrm{i}, \\
\mathbf{u} &= -\frac{1}{a}\boldsymbol{\nabla}\phi_\mathrm{i}\int \mathrm{d}t\frac{D}{a}.
\end{aligned} \tag{2.40}$$

The integral on the right hand side can be solved by rearranging the differential equation for the linear growth factor by introducing,

$$a^2\ddot{D} + 2a^2H\dot{D} = \partial_t(a^2\dot{D}). \tag{2.41}$$

After only some minor modifications, Eq. (2.34) then becomes,

$$\int \mathrm{d}t\frac{D}{a} = \frac{a^2\dot{D}}{\frac{3}{2}H_0^2\Omega_\mathrm{m}}, \tag{2.42}$$

from which we get the velocity,

$$\mathbf{u} = -\frac{a\dot{D}}{\frac{3}{2}H_0^2\Omega_\mathrm{m}}\boldsymbol{\nabla}\phi_\mathrm{i}, \tag{2.43}$$

and comoving position, knowing that $\mathbf{u} = a\dot{\mathbf{x}}$,

$$\mathbf{x} = \mathbf{q} - \frac{D}{\frac{3}{2}H_0^2\Omega_\mathrm{m}}\boldsymbol{\nabla}\phi_\mathrm{i}, \tag{2.44}$$

where we have introduced the Lagrangian coordinate, $\mathbf{q}$. By introducing,

$$\psi = -(\frac{3}{2}H_0^2\Omega_\mathrm{m})^{-1}\phi_\mathrm{i}, \tag{2.45}$$

the equations take a very simple form,

$$\mathbf{x} = \mathbf{q} + D\boldsymbol{\nabla}\psi, \tag{2.46}$$

$$\mathbf{u} = a\dot{D}\boldsymbol{\nabla}\psi, \tag{2.47}$$

$$\boldsymbol{\nabla}^2\psi = -\delta_{\mathrm{i}}, \tag{2.48}$$

where we can clearly see that the growth factor plays the role of a time coordinate and the Lagrangian coordinate the initial position of the fluid element.

Now that we are able to describe the motion of individual fluid elements, we want to investigate how this motion alters the overall density of the fluid. To do so let us consider a mass,

$$M = \int_V \mathrm{d}^3\mathbf{q}\,\rho_{\mathrm{m}}(t_{\mathrm{i}}), \tag{2.49}$$

contained within an initial volume, V, considering that initially the density inside the volume is close to the mean density of the Universe. If we consider that the boundaries of the volume are attached to fluid elements, at later times this volume is distorted by the motion of these fluid elements. The mass inside the volume however, remains constant allowing us to compare the density at both epochs,

$$\int_V \mathrm{d}^3\mathbf{q}\,\rho_{\mathrm{m}}(t_{\mathrm{i}}) = \int_V \mathrm{d}^3\mathbf{x}\,\rho_{\mathrm{m}}(t)[1+\delta(\mathbf{x},t)] = \int_V \mathrm{d}^3\mathbf{q}\,\rho_{\mathrm{m}}(t)[1+\delta(\mathbf{q},t)]\left|\frac{\partial\mathbf{x}}{\partial\mathbf{q}}\right|, \tag{2.50}$$

where we transform the integration variables using the determinant of the Jacobian and reintroduce the overdensity δ. We note that in this case we have not made the assumption that δ remains small. Since we have not specified V both integrands must be identical allowing us to infer,

$$1+\delta(\mathbf{q},t) = \left|\frac{\partial\mathbf{x}}{\partial\mathbf{q}}\right|^{-1} = \left|\delta_{ij} + D(t)\frac{\partial^2\psi}{\partial q_i \partial q_j}\right|^{-1}, \tag{2.51}$$

where δ_{ij} is the Kronecker delta symbol. The determinant on the right hand side is that of a symmetric real valued matrix, as such it necessarily has three real eigenvalues allowing to express the overdensity contrast,

$$1+\delta(\mathbf{q},t) = \frac{1}{|(1+D(t)\lambda_1)(1+D(t)\lambda_2)(1+D(t)\lambda_3)|}, \tag{2.52}$$

as a function of these eigenvalues, where λ_i are the eigenvalues of the second derivative. These eigenvalues depend only on the Lagrangian position of the fluid element, informing us on the behaviour of the fluid. Indeed, we see that when we have $\lambda_i < 0$, the monotonous growth of $D(t)$ makes $1 + D\lambda_i$ a decreasing function of time, which eventually reaches a point when $1 + D\lambda_i = 0$ and the overdensity diverges, we can therefore consider that the volume has collapsed along this dimension. On the other hand, if $\lambda_i > 0$, then $1 + D\lambda_i$ is an increasing function of time and therefore the volume expands along this dimension.

This result leads to the introduction of a simple classification of structures that form in the Universe based on the signs of these eigenvalues.

- *Voids*, all eigenvalues are positives and the region expands along all dimensions.
- *Pancakes* or *walls*, only one eigenvalue is negative and the volume collapses along one dimension forming a two dimensional structure.

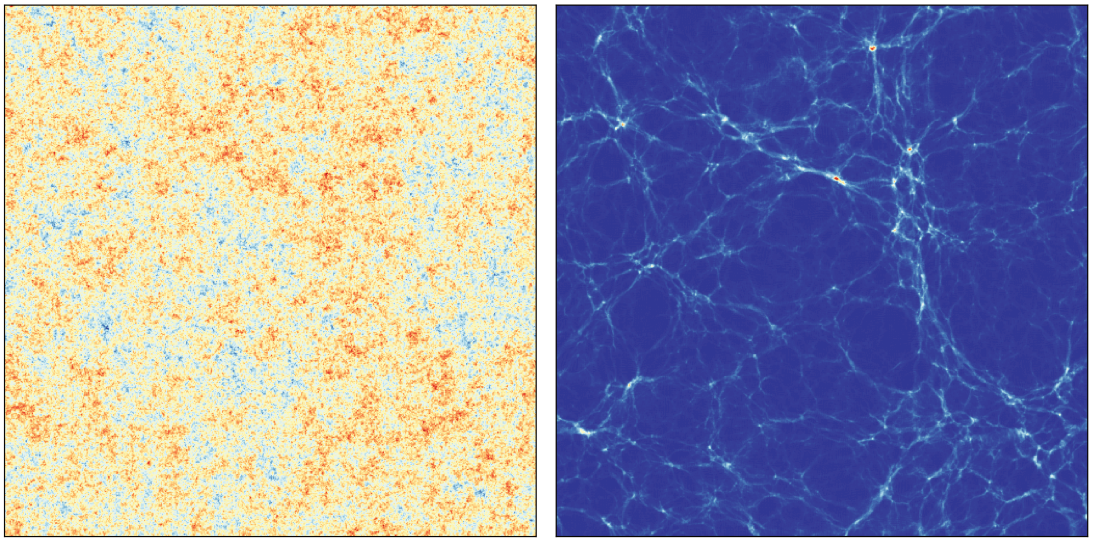

Figure 2.3: *Left panel:* slice of a simulated density perturbation field, assuming the Eisenstein & Hu (1998) transfer function, within a 50 h^{-1}Mpc periodic box with 512 cells per dimension. This is the same slice as the right panel of Fig. 2.2. *Right panel:* Same region of the simulated volume but evolved to redshift, $z = 0$, under the Zel'dovich approximation. Here we can clearly see various types of structure, most notably large empty regions, *voids*, elongated *filaments* and a few dense *haloes* which appear in red.

- *Filaments*, two eigenvalues are negative, the volume collapses along two dimensions resulting in an elongated one dimensional object.

- *Haloes*, all eigenvalues are negative, the volumes collapses into a compact structure.

It is inside the dense environment of haloes that most astrophysical processes take place as they form deep potential wells inside which baryonic matter accumulates to form stars and galaxies. In the left panel of Fig. 2.3, we show a Gaussian random density field generated using the Eisenstein & Hu (1998) transfer function within a comoving periodic box of side length $50h^{-1}$Mpc on a grid of 512^3 cells. To evolve this density field we replace each cell with a particle, representing a fluid element, carrying the cell's mass. We then displace the particles according to the Zel'dovich approximation and finally reassign their mass to the grid using the Cloud-In-Cell (CIC) algorithm. Here, we can easily see at least three of the four types of structure listed above. Indeed, we see large empty voids, elongated filaments forming the cosmic web at the nodes of which we find a few haloes. We should however remember that here we have extrapolated the Zel'dovich approximation beyond its realm of validity since, the objects seen here have experienced shell crossing. This process would bind the fluid elements into a new structure. In contrast, in the Zel'dovich Approximation they continue to follow straight trajectories, thus disrupting any large scale structure into smaller fragments. As such we cannot study the haloes produce here in detail.

To do so, in the following we will focus on an overdensity collapsing into a halo and study in detail the properties of the density during and after collapse. This will allow us to grasp a picture of what a halo actually is.

2.5 Spherical Collapse

Let us first simplify the scope by focusing on a spherical shell of physical radius r_i at some initial time t_i. This shell is contained within a local overdensity $\delta_\mathrm{i} = \delta(t_\mathrm{i})$ with respect to the background mean density, $\rho_\mathrm{m}(t_\mathrm{i})$. Let us also focus on a universe dominated by matter, $(\Omega_\mathrm{m} = 1, \Omega_\Lambda = 0)$, known as an Einstein de Sitter (EdS) model, As this makes the analytical computation simpler. Moreover, let us assume that this matter is entirely composed of dark matter. In this cosmological model the mean density becomes,

$$\rho_\mathrm{m} = \frac{1}{6\pi G t^2}, \tag{2.53}$$

and the linear growth factor is equal to the scale factor, $D(a) = a \propto t^{2/3}$.

The spherical shell we are interested in initially encloses a mass,

$$M = \frac{4\pi}{3} r_\mathrm{i}^3 \rho_\mathrm{m}(t_\mathrm{i})[1 + \delta_\mathrm{i}] = \frac{4\pi}{3} r(t)^3 \rho_\mathrm{m}(t)[1 + \delta(t)], \tag{2.54}$$

where we are able to write the second equality due to the fact that the mass inside of the shell is conserved. Again this is only valid up to shell-crossing, when the shell crosses itself on an outward trajectory.

In this geometry the equation of motion of the shell can be established through Newton's first law,

$$\ddot{r} = -\frac{GM}{r^2}. \tag{2.55}$$

The integrated form of this equation reads as,

$$\frac{1}{2}\dot{r}^2 - \frac{GM}{r} = E, \tag{2.56}$$

being akin to the standard energy conservation equation in Newtonian mechanics, where E is an integration constant which plays the roll of the total mechanical energy of the system. By analogy with the two body problem, this equation exhibits two types of solution depending on the sign of E. For $E \geq 0$, the expansion of the Universe overcomes gravity and the shell expands, for $E < 0$, the shell is gravitationally bound to the perturbation and collapses in on itself. In the second case the equation of motion admits a parametric solution,

$$r = A(1 - \cos\theta) \quad \text{with } A = \frac{GM}{2|E|}, \tag{2.57}$$

$$t = B(\theta - \sin\theta) \quad \text{with } B = \frac{GM}{(2|E|)^{2/3}}, \tag{2.58}$$

where $\theta \in [0, 2\pi]$. This parameteric solution tells us that after an initial phase of expansion from $r = 0$, $\theta = 0$ and $t = 0$ the shell reaches a maximal radius, r_max at $\theta = \pi$ and $t_\mathrm{max} = \pi B$. The shell then turns around and collapses returning to $r = 0$ at $\theta = 2\pi$ and $t_\mathrm{coll} = 2t_\mathrm{max} = 2\pi B$. This implies that any perturbation that has negative mechanical energy will eventually collapse. The mechanical energy of a spherical shell inside perturbation is however not a quantity that we can easily access and evaluate. Let us therefore transform this condition for collapse into a condition on the density perturbation.

To do so let us assume that the peculiar velocity of the shell is negligible with respect to the Hubble flow. As such, the initial velocity is simply,

$$v_\mathrm{i} = \dot{r}_\mathrm{i} = \frac{\mathrm{d}a x_\mathrm{i}}{\mathrm{d}t} = \dot{a} x_\mathrm{i} + a\dot{x}_\mathrm{i} \simeq \dot{a} x_\mathrm{i} = H_\mathrm{i} r_\mathrm{i}, \tag{2.59}$$

where x_i is the initial comoving radius of shell. Under this assumption, we are able to write the initial mechanical energy of the shell,

$$E_\mathrm{i} = \frac{1}{2}H_\mathrm{i}^2 r_\mathrm{i}^2 - \frac{GM}{r_\mathrm{i}}. \tag{2.60}$$

We can go a step further by replacing the mass,

$$M = \frac{4\pi}{3} r_\mathrm{i}^3 \rho_\mathrm{m}(t_\mathrm{i})[1+\delta_\mathrm{i}] = \frac{H_\mathrm{i}^2 r_\mathrm{i}^2}{2G}[1+\delta_\mathrm{i}], \tag{2.61}$$

in the Eq. (2.60), which significantly simplifies the latter,

$$E_\mathrm{i} = \frac{1}{2}H_\mathrm{i}^2 r_\mathrm{i}^2 - \frac{1}{2}H_\mathrm{i}^2 r_\mathrm{i}^2[1+\delta_\mathrm{i}] = -\frac{1}{2}H_\mathrm{i}^2 r_\mathrm{i}^2 \delta_\mathrm{i}. \tag{2.62}$$

As H_i and r_i are both always positive, we see that in the EdS model, the sufficient condition for the shell to be bound and eventually collapse is that it is within an overdense region, $\delta_\mathrm{i} > 0$ implying that in an EdS universe all overdensities eventually collapse. More generally, for non-EdS cosmologies, this is not the case and it can be shown that, for the specific case of ΛCDM, this condition becomes $\delta_i > \Omega_\mathrm{m}(t_\mathrm{i})^{-1} - 1$ (Mo et al., 2010).

Now that we know which overdensities will collapse, the natural question that follows is: *when will they collapse?* The obvious answer to this question, i.e. when $\theta = 2\pi$,

$$t_\mathrm{coll} = 2\pi B = 2\pi \frac{GM}{H_\mathrm{i}^3 r_\mathrm{i}^3 \delta_\mathrm{i}^{3/2}}, \tag{2.63}$$

is not very helpful as it again depends on a number of parameters that we do not *a priori* know. The way around this issue is to compare the evolution of the perturbation with an equivalent linear theory extrapolation. In essence, this would allow one to compare the extrapolated density field to some collapse threshold δ_c and know which regions have collapsed. This is illustrated in Fig. 2.4, where the desired threshold is marked by a circle. To find this threshold let us first match the initial condition on the density perturbation to linear theory.

To this effect we begin by studying how the overdensity evolves at the start of the spherical collapse model. Recalling that the overdensity is defined as the ratio of the mean density within the shell and background density,

$$1 + \delta = \frac{\rho}{\rho_\mathrm{m}}, \tag{2.64}$$

we can recover its dependency on θ by explicitly writing both densities as functions of this variable,

$$\rho = \frac{3M}{4\pi r^3} = \frac{3M}{4\pi A^3}\left(1-\cos\theta\right)^{-3}, \tag{2.65}$$

$$\rho_\mathrm{m} = \frac{1}{6\pi G t^2} = \frac{1}{6\pi G B^2}\left(\theta-\sin\theta\right)^{-2}, \tag{2.66}$$

which, when put together, yields:

$$1 + \delta = \frac{9}{2}\frac{(\theta-\sin\theta)^2}{(1-\cos\theta)^3}. \tag{2.67}$$

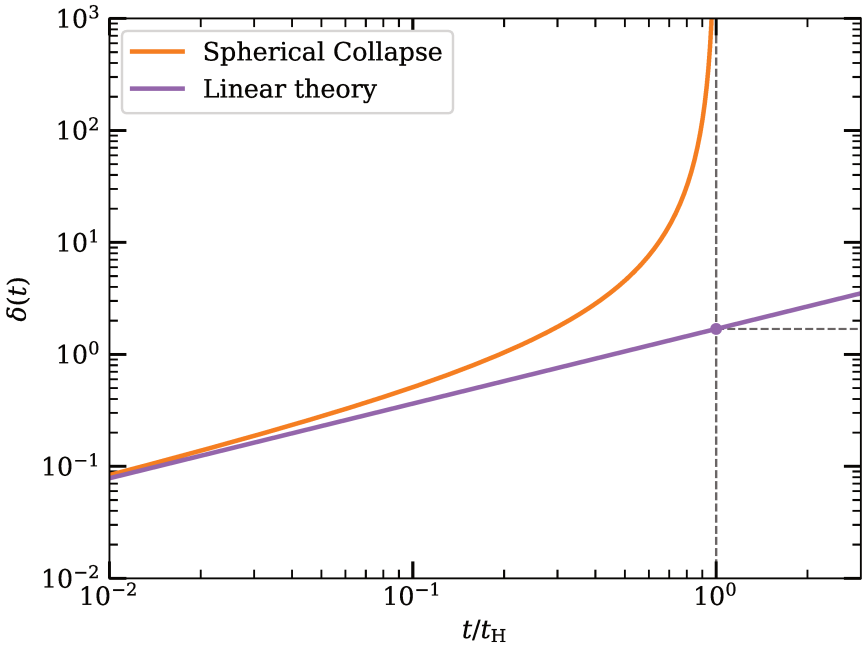

Figure 2.4: Evolution of the overdensity as a function of time in both the spherical collapse model and linear theory, where we have chosen that the collapse takes place after one Hubble time, marked by a vertical dashed line, in and EdS cosmology. We can see that when the shell collapses the overdensity diverges in the spherical collapse model while in linear theory it is precisely $\delta = \frac{3}{5}\left(\frac{3\pi}{2}\right)^{2/3}$, marked by a horizontal dashed line.

Being as we are interested in what is happening at the very start of the evolution, we expand this solution for $\theta \ll 1$ and find that the overdensity evolves quadratically with the θ parameter,

$$\delta_{\rm i} \simeq \frac{3}{20}\theta^2. \tag{2.68}$$

In the same fashion we can expand the parametric solution for the time parameter,

$$\frac{t}{t_{\rm max}} = \frac{\theta - \sin\theta}{\pi} \simeq \frac{\theta^3}{6\pi}, \tag{2.69}$$

and thus obtain the time evolution of the overdensity at the start of the collapse,

$$\delta_{\rm i} \simeq \frac{3}{20}\left(6\pi\frac{t}{t_{\rm max}}\right)^{2/3}. \tag{2.70}$$

Previously, we have shown that in linear theory the overdensity grows like $D(t) \propto t^{2/3}$,

$$\delta_{\rm lin} = \delta_{\rm i}\left(\frac{t}{t_{\rm i}}\right)^{2/3} = \frac{3}{20}\left(6\pi\frac{t}{t_{\rm max}}\right)^{2/3}, \tag{2.71}$$

which, being consistent with the early time limit of the spherical collapse model, allows us to write the second equality by simply identifying the values of the various terms. From all of this we now have the expression of the overdensity at the time of collapse extrapolated from linear theory,

$$\delta_{\rm c} = \frac{3}{20}(12\pi)^{2/3} = \frac{3}{5}\left(\frac{3\pi}{2}\right)^{2/3} \simeq 1.686, \tag{2.72}$$

which can be used to identify where and when collapse will occur simply by extrapolating the initial condition using linear theory. This is the main philosophy of excursion set theory that we will explore later to predict the properties and population of haloes. It is worth noting that in the more general case of ΛCDM this collapse density only varies slowly with the matter density parameter (see e.g. Mo et al., 2010),

$$\delta_{\rm c} = \frac{3}{5}\left(\frac{3\pi}{2}\right)^{2/3} \Omega_{\rm m}(t_{\rm coll})^{0.0055}. \tag{2.73}$$

Once the shell has collapsed this model can no longer accurately follow its evolution as it inevitably mixes with other shells. However, keeping in spirit with this model by looking at the energy of the shell, we can get some insight on the final object that is formed. Indeed, if we consider that once the shells mix the object virialises, we can consider that the shells obey the virial theorem,

$$2K_{\rm f} + U_{\rm f} = 0, \tag{2.74}$$

where $K_{\rm f}$ and $U_{\rm f}$ are respectively the kinetic and potential energy, such that we can write the final energy of the system,

$$E_{\rm f} = \frac{U_{\rm f}}{2} = -\frac{GM}{2r_{\rm vir}}, \tag{2.75}$$

in such a way that it only depends on the mass, M, and $r_{\rm vir}$, the virial radius of the halo. Considering that the mechanical energy of the system is conserved, this energy can then be equated to the energy at turn around,

$$E_{\rm ta} = -\frac{GM}{r_{\rm max}}, \tag{2.76}$$

which takes a very similar form. This, in turn, tells us that the radius of the collapsed object is half of what it was at turn around, $r_{\rm vir} = r_{\rm max}/2$, which also implies, assuming that mass is conserved, that inside the halo the density is 8 times larger. Recalling the definition of the overdensity, i.e. Eq. (2.64), we also need to know how the background density has changed between the time of virialisation and turn around. For simplicity we consider that the structure virialises rapidly after collapse, $t_{\rm vir} \simeq t_{\rm coll}$. Within the framework of an EdS cosmology the evolution of the background is sufficiently simple for us to write,

$$\rho_{\rm m}(t_{\rm coll}) = \rho_{\rm m}(t_{\rm ta})\left(\frac{t_{\rm coll}}{t_{\rm ta}}\right)^{-2} = \frac{\rho_{\rm m}(t_{\rm ta})}{4}. \tag{2.77}$$

This allows us to fully express the virial overdensity contrast,

$$1 + \Delta_{\rm vir} = \frac{\rho(t_{\rm coll})}{\rho_{\rm m}(t_{\rm coll})} = 32(1 + \delta_{\rm max}) = 18\pi^2 \simeq 178, \tag{2.78}$$

as a function of the overdensity at turn around, $\delta_{\rm max}$, which we know thanks to Eq. (2.67). We find that the resulting overdensity does not depend on the mass of the object or the time at which it formed, a direct consequence of having assumed spherical symmetry,

making it a universal characteristic of haloes in an expanding Universe. This result is however dependent on the cosmological model (Bryan & Norman, 1998),

$$\Delta_{\rm vir}(t) \simeq \frac{1}{\Omega_{\rm m}(t)}\left(18\pi^2 + 82(\Omega_{\rm m}(t)-1) - 39(\Omega_{\rm m}(t)-1)^2\right), \tag{2.79}$$

which also introduces a time dependence.

Combining all that we have explored over the last sections, we now have a broad view of what is going to happen to overdensities inside the universe. These primordial fluctuations first go through a phase of initial growth proportional to the growth factor, $D(t)$. After this initial phase these overdenisities collapse to form virialised haloes.

2.6 Counting haloes

Now that we have a vague understanding of how, when and where, dark matter haloes will form, we want to answer the question: *how many haloes will form?* More specifically: *how many haloes of a given mass will form?* Formally to answer this question we want to derive what is known as the Halo Mass function (HMF), $\frac{{\rm d}n}{{\rm d}M}$, which quantifies how many haloes we expect to find with a mass contained between M and $M + {\rm d}M$ inside a infinitesimal volume ${\rm d}V$. Assuming that the number density ${\rm d}n$ is equal to the infinitesimal volume fraction ${\rm d}F/V$, with $V = M/\rho_{\rm m}$, we relate this number of objects,

$$\frac{{\rm d}n}{{\rm d}M} = \frac{\rho_{\rm m}}{M}\frac{{\rm d}F}{{\rm d}M}, \tag{2.80}$$

to the fraction ${\rm d}F$ of the total mass inside contained in haloes with masses between M and $M + {\rm d}M$. In this section we will present two analytical approaches which allow us to express F, and therefore ${\rm d}F$.

2.6.1 Press & Schechter approach

Following the derivation of Press & Schechter (1974), let us begin by considering what we have seen in the previous sections. We have seen that under the spherical collapse model a halo forms when the linearly extrapolated density field reaches the threshold density, $D(t)\delta(\mathbf{x}) > \delta_{\rm c}$. This condition can be recast in order to keep the density field constant in time, $\delta > \delta_{\rm c}/D(t) = \delta_{\rm c}(t)$, and have the threshold, which we will also refer to as collapse barrier, evolve instead. Press & Schechter (1974) postulate that this condition also applies to the density field smoothed over a radius R,

$$\delta_R(\mathbf{x}) = \int {\rm d}^3\mathbf{x}'\, \delta(\mathbf{x}')W_R(\mathbf{x}-\mathbf{x}'), \tag{2.81}$$

allowing us to assign a mass, $M = \gamma\rho_{\rm m}R^3$, to the field, where γ is a constant that depends on the type of window function $W_R(\mathbf{x})$ used. As R and M are in this case simply a label for the window function we can use them interchangeably, $\delta_R = \delta_M$. The authors further postulate that $F(>M,t) = P_{\rm r}(\delta_M > \delta_{\rm c})$ meaning 'the probability that, $\delta_M > \delta_{\rm c}(t)$, is equal to the mass fraction that at time t is contained in haloes with mass greater than M'.

To this effect we need to first understand the nature of the new random field δ_M. As we have simply smoothed a Gaussian random field, this field will also be Gaussian. Thus, the field can be fully described in terms of its mean and variance. The mean will remain unchanged, $\langle\delta_M\rangle = \langle\delta\rangle = 0$. The variance, on the other hand, will change.

We do however, already know what the variance of such a field is as we used a similar definition in Eq. (2.24) when introducing the σ_8 cosmological parameter, which we recall here to avoid page flipping:

$$\sigma_R^2 = \frac{1}{2\pi}\int_0^\infty \mathrm{d}k k^2 \hat{W}^2(kR)P(k). \tag{2.82}$$

For CDM models σ_R^2 will be a monotonically decreasing function of R and M, as these are interchangeable in this case. We then define the Probability Distribution Function (PDF),

$$\rho(\delta_M)\mathrm{d}\delta_M = \frac{1}{\sqrt{2\pi}\sigma_M}\exp\left[-\frac{\delta_M^2}{2\sigma_M^2}\right]\mathrm{d}\delta_M \tag{2.83}$$

of the height of a peak of the random field. From which we can therefore express,

$$\begin{aligned} F(>M,t) = P_\mathrm{r}(\delta_M > \delta_\mathrm{c}) &= \frac{1}{\sqrt{2\pi}\sigma_M}\int_{\delta_c}^\infty \mathrm{d}\delta_M \exp\left[-\frac{\delta_M^2}{2\sigma_M^2}\right] \\ &= \frac{1}{2}\left[1-\mathrm{erf}\left(\frac{\delta_c(t)}{2\sigma_M}\right)\right], \end{aligned} \tag{2.84}$$

the fraction of mass contained in haloes with mass greater than M. Note that, in the limit where $R \to 0$, equivalently $\sigma_M \to \infty$, we find that only half of the matter ends up inside haloes where one would expect that all the matter eventually collapses into haloes. Under this observation, the authors of the original derivation correct by manually introducing a factor two with poor justification.

Next, we want to obtain the HMF from $F(>M)$. To do so we simply need to insert our result into the definition of the HMF discussed above,

$$\begin{aligned} \frac{\mathrm{d}n}{\mathrm{d}M}\mathrm{d}M &= 2\frac{\rho_\mathrm{m}}{M}\frac{\partial F(>M)}{\partial M}\mathrm{d}M, \\ &= \sqrt{\frac{2}{\pi}}\frac{\rho_\mathrm{m}}{M^2}\left|\frac{\mathrm{d}\ln\sigma_M}{\mathrm{d}\ln M}\right|\frac{\delta_\mathrm{c}}{\sigma_M}\exp\left(-\frac{\delta_\mathrm{c}^2}{2\sigma_M^2}\right)\mathrm{d}M. \end{aligned} \tag{2.85}$$

This result, stemming from a relatively simple approach, gives us significant insight into the behaviour of the population of haloes as a whole. Indeed assuming a CDM model, the HMF approximately resembles a power law which slowly converges to M^{-2} for small masses and is exponentially suppressed on the high mass end.

2.6.2 Excursion set theory

This result, while insightful, however has a number of issues. Not only regarding the assumptions that are made to obtain it, for instance that all structures collapse spherically which we have seen while discussing the Zel'dovich approximation (see Sec. 2.4) is generally not the case, but also the justification of the fudge factor which is generally regarded as unsatisfactory.

In the early 1990's a new, more rigorous, approach was developed (Bond et al., 1991). Instead of studying the density field itself the authors decided to treat individual positions on this field as random variables. By filtering the density field at different scales, as in Eq. (2.81), and successively evaluating it at the same position, one observes that the measurements perform a random walk. Following the notation of Corasaniti & Achitouv (2011), this random walk is described in terms of a Langevin equation

$$\frac{\partial\delta_R}{\partial R} = \zeta(R) \tag{2.86}$$

with a stochastic noise term,

$$\zeta(R) = \frac{1}{(2\pi)^3} \int \mathrm{d}^3\mathbf{k}\delta(\mathbf{k}) \frac{\partial W(\mathbf{k}, R)}{\partial R} e^{-i\mathbf{k}\cdot\mathbf{x}}, \tag{2.87}$$

of which the properties depend both on the density field and the filter. We have already seen that the initial density field is Gaussian with $\langle\delta(\mathbf{k})\rangle = 0$ and $\langle\delta(\mathbf{k})\delta^*(\mathbf{k}')\rangle = (2\pi)^3\delta_\mathrm{D}(\mathbf{k}-\mathbf{k}')P(k)$. By taking ensemble averages of the noise term, we can show that $\langle\zeta(R)\rangle = 0$ and

$$\langle\zeta(R)\zeta(R')\rangle = \frac{1}{2\pi^2} \int \mathrm{d}k\ k^2 P(k) \frac{\partial W}{\partial R} \frac{\partial W}{\partial R'}, \tag{2.88}$$

which implies that for a general filter $W(\mathbf{k}, R)$ the random walk will be correlated between R and R'. This is for instance the case of the real space top hat filter we have used previously. While this filter is easy to comprehend and physically assign a mass to, it becomes detrimental in this context as it introduces correlations between individual steps of the random walk making these trajectories difficult to study analytically.

An exception to this rule is the sharp-k filter,

$$\delta_R(\mathbf{x}) = \int \mathrm{d}^3\mathbf{k}\ \hat{W}_\mathrm{sk}(kR)\delta(\mathbf{k})e^{-i\mathbf{k}\cdot\mathbf{x}} = \int_{k<1/R} \mathrm{d}^3\mathbf{k}\ \delta(\mathbf{k})e^{-i\mathbf{k}\cdot\mathbf{x}}, \tag{2.89}$$

also known as a Fourier space top hat filter, for which the correlation between the noise term at different scales is only non-zero for $R = R'$. This implies that for each new scale one only introduces new and independent modes to the random walk. This property makes the walk Markovian allowing us to study its properties analytically. The main issue of this filter is that it has infinite support in real-space,

$$W_\mathrm{sk}(r, R) = \frac{1}{2\pi^2 R^3} \left[\sin(r/R) - \frac{r}{R}\cos(r/R)\right] \tag{2.90}$$

and integrating over this infinite support leads to a diverging volume integral. Mo et al. (2010) propose that this issue can be circumvented if one considers that the effective volume normalises the filter such that, $W_\mathrm{sk}(0, R)V(R) = 1$. Under this assumption, this leads to the sharp-k filter representing a volume, $V(R) = 6\pi^2R^3$. While this particular workaround is not rigorous to the definition of a physical volume it however permits us, in a similar fashion to the real space top-hat, to relate the scale R of the filter to a mass $M = 6\pi^2R^3\rho_\mathrm{m}$.

Regardless of the filter used, a sole boundary condition can be assigned to these random walks. Considering the cosmological principle implies that for a large enough scale, or mass, the density is homogeneous and isotropic, $\lim_{R\to\infty} \delta_R(\mathbf{x}) = 0$. Since a boundary condition at $R \to \infty$ is not practical, it is customary to recast the random walks in terms of $S = \sigma_R^2$, given that in the CDM paradigm the variable is positively defined and monotonically decreasing as a function of the scale of the filter, such that $\lim_{R\to\infty} S = 0$, thus corresponding to a single starting point for all trajectories ($S = 0,\ \delta_S = 0$).

Letting each trajectory evolve up to a certain mass, the Press & Schechter approach would then be equivalent to counting the number of trajectories that at a given mass are above the threshold density. In this context, however, another flaw in this approach becomes apparent. Let us consider a trajectory that first crosses the boundary at some mass M_1, but then crosses it again at some lower mass $M_2 < M_1$. This would mean that for a mass $M < M_2$, where the trajectory is below $\delta_\mathrm{c}(t)$, the fluid element associated to

the trajectory is considered as no being inside of a halo with mass above M. If we now consider the trajectory at a second mass M' such that, $M_2 < M' < M_1$, the trajectory being above the threshold is now considered as being part of a halo with mass above M'. These two statements are in contradiction, indeed how can a fluid not be part of a halo more massive than M, when it has to also be part of a halo with mass above $M' > M$, This is known as the cloud-in-cloud problem.

In excursion set theory the cloud-in-cloud problem is solved through the introduction of an ordering system, i.e the scale of the filter or the mass. Instead of looking at the proportion trajectories that, at some scale M, are above or below the threshold, we now consider that all trajectories that have crossed the barrier for the first time at a scale $M_1 > M$ are bound to haloes with masses lower than M_1, even if they cross the boundary again.

Given these considerations, for the sharp-k filter we can summarise the trajectory as a Markovian random walk,

$$\frac{\partial \delta}{\partial S} = \eta_\delta(S), \tag{2.91}$$

where $\eta_\delta(S)$ is a white noise term such that, $\langle \eta_\delta(S) \rangle = 0$ and $\langle \eta_\delta(S)\eta_\delta(S') \rangle = \delta_{\rm D}(S - S')$. To this random walk we associate the probability Π of finding the trajectory at a given over-density δ at a given scale S. As the random walk is Markovian, this probability is described by the Fokker-Planck equation,

$$\frac{\partial \Pi}{\partial S} = \frac{1}{2}\frac{\partial^2 \Pi}{\partial S^2}, \tag{2.92}$$

which can be solved given the initial condition, $\delta(0) = 0$ and absorbing boundary at $\delta = \delta_{\rm c}$, such that:

$$\Pi(\delta_{\rm c}, \delta, S) = \frac{1}{\sqrt{2\pi S}}\left[\exp\left\{-\frac{\delta^2}{2S}\right\} - \exp\left\{-\frac{(2\delta_{\rm c} - \delta)^2}{2S}\right\}\right]. \tag{2.93}$$

From this, the fraction of trajectories, $F_{\rm FU}$, which have still to cross the barrier for the first time at a given scale S is simply,

$$\begin{aligned} F_{\rm FU}(S) &= 1 - \int_{-\infty}^{\delta_{\rm c}} \Pi {\rm d}\delta \qquad (2.94)\\ &= 1 - \frac{1}{\sqrt{2\pi S}}\left[\int_{-\infty}^{\delta_{\rm c}} \exp\left\{-\frac{\delta^2}{2S}\right\}{\rm d}\delta - \int_{-\infty}^{\delta_{\rm c}} \exp\left\{-\frac{(2\delta_{\rm c} - \delta)^2}{2S}\right\}{\rm d}\delta\right],\\ &= 1 - \frac{1}{\sqrt{2\pi}}\left[\int_{-\infty}^{\delta_{\rm c}/\sqrt{S}} \exp\left\{-\frac{x^2}{2}\right\}{\rm d}x - \int_{\delta_{\rm c}/\sqrt{S}}^{+\infty} \exp\left\{-\frac{x^2}{2}\right\}{\rm d}x\right],\\ &= 1 - \frac{1}{\sqrt{2\pi}}\left[\int_{-\infty}^{\delta_{\rm c}/\sqrt{S}} \exp\left\{-\frac{x^2}{2}\right\}{\rm d}x - \int_{\delta_{\rm c}/\sqrt{S}}^{+\infty} \exp\left\{-\frac{x^2}{2}\right\}{\rm d}x\right],\\ &= 2 - \frac{2}{\sqrt{2\pi}}\int_{-\infty}^{\delta_{\rm c}/\sqrt{S}} \exp\left\{-\frac{x^2}{2}\right\}{\rm d}x,\\ F_{\rm FU}(S) &= 2\left[1 - \frac{1}{\sqrt{2\pi}}\phi\left(\frac{\delta_{\rm c}}{\sqrt{S}}\right)\right], \qquad (2.95) \end{aligned}$$

where we have introduced $\phi(x) = \int_{-\infty}^{x} \exp\left\{-\frac{x'^2}{2}\right\}{\rm d}x'$.

We see that this shift in perspective is surprisingly equivalent to double counting trajectories that have crossed the boundary after mirroring them with respect to the

boundary, introducing a factor 2. In essence, this not only solves the issue of inconsistency, but also naturally explains the fudge factor. For CDM, if we go to arbitrarily large S, all trajectory will eventually be above the threshold implying that all matter eventually ends up inside haloes.

From this, we can simply write the fraction of mass contained within haloes larger than M,

$$F(> M) = 1 - F(< M), \tag{2.96}$$

as a function of our result from Excursion set theory. We can then start from an intermediate point to derive the HMF,

$$\begin{aligned}\frac{\mathrm{d}n}{\mathrm{d}M}\mathrm{d}M &= \frac{\rho_\mathrm{m}}{M}\frac{\partial F(> M)}{\partial M}\mathrm{d}M,\\ &= -\frac{\rho_\mathrm{m}}{M}\frac{\partial F(< M)}{\partial M}\mathrm{d}M,\\ &= -\frac{\rho_\mathrm{m}}{M}\frac{\mathrm{d}S}{\mathrm{d}M}\frac{\partial F(> S)}{\partial S}\mathrm{d}M,\\ &= \frac{\rho_\mathrm{m}}{M}\left|\frac{\mathrm{d}S}{\mathrm{d}M}\right| f_\mathrm{FU}(S)\mathrm{d}M,\end{aligned} \tag{2.97}$$

where,

$$f_\mathrm{FU}(S) = \frac{\mathrm{d}F_\mathrm{FU}}{\mathrm{d}S} = \frac{1}{\sqrt{2\pi}}\frac{\delta_\mathrm{c}}{S^{3/2}}\exp\left(-\frac{\delta_\mathrm{c}^2}{2S}\right), \tag{2.98}$$

is the fraction of trajectories that have their first up-crossing between S and $S + \mathrm{d}S$. Finally if we replace, $S = \sigma_M^2$, we find

$$\frac{\mathrm{d}n}{\mathrm{d}M}\mathrm{d}M = \sqrt{\frac{2}{\pi}}\frac{\rho_\mathrm{m}}{M^2}\left|\frac{\mathrm{d}\ln\sigma_M}{\mathrm{d}\ln M}\right|\frac{\delta_\mathrm{c}}{\sigma_M}\exp\left(-\frac{\delta_\mathrm{c}^2}{2\sigma_M^2}\right)\mathrm{d}M, \tag{2.99}$$

recovering the result of Press & Schechter without needing a fudge factor. While this result is now anchored to a much sturdier mathematical foundation, there still remains the issue of the multiple assumptions that needed to be made in order to obtain it. Firstly as we have seen, in full generality gravitational collapse is not spherical and secondly the mass, M considered here is ill defined. Indeed, as we will see in the following defining the mass of dark matter halo is a problem of its own. Multiple advances have been made in order to assess these shortcomings. For example, Sheth & Tormen (2002) derived the HMF using excursion set theory assuming a moving barrier calibrated in order to introduce information on the ellipsoidal nature of gravitational collapse and Maggiore & Riotto (2010a) showed that it is in fact possible to derive an analytical results for filters producing correlated random walks using a path integral formalism. This second result was expanded by Maggiore & Riotto (2010b) to solve the excursion set problem with a diffusing barrier and was later used by Corasaniti & Achitouv (2011) to obtain the HMF for a diffusing barrier accounting for ellipsoidal collapse. These analytical formulations were however quickly overshadowed by N-body simulations due to the rapid increase in computation power and arrival of new efficient algorithms.

2.7 Cosmological Simulations

In previous sections we have explored multiple analytical descriptions of the formation of cosmological structures. While these results are already extremely valuable, they are

limited by their underlying assumptions. For instance, Linear and Lagrangian perturbation theory are only valid for a short time after which their results stray far from reality, and the spherical collapse model elegantly derives a threshold for when gravitational collapse may occur, but becomes increasingly difficult once the assumption of sphericity is dropped.

An alternative approach still remains to be explored, that of discretising the fluid equations and solving the full system, or in other words numerical simulations. In this section, we will discuss a number of aspects relating to cosmological simulations from how one initialises a simulation to the algorithms that allow them to move forward in time and finally presenting how we can recover haloes from within these volumes and comparing some basic analyses of the resulting data. The aim here is to provide a brief overview of the methods we will be using in the rest of this work as well as some alternatives. On the other hand we will not provide any comparison among the various methods and will not discuss how baryonic physics enter into this picture.

2.7.1 Simulating the Universe

Let us consider a ΛCDM universe filled only with a single self gravitating matter fluid. This fluid is fully described by its phase space distribution function, $f(\mathbf{x}, \mathbf{v}, t)$, and its dynamics are described by the Boltzmann equation,

$$\frac{\partial f}{\partial t} + \frac{\tilde{\mathbf{v}}}{a^2} \cdot \boldsymbol{\nabla}_{\mathbf{x}} f - \boldsymbol{\nabla}_{\mathbf{x}} \phi \cdot \boldsymbol{\nabla}_{\tilde{\mathbf{v}}} f = \left.\frac{\mathrm{d}f}{\mathrm{d}t}\right|_{\mathrm{coll}}, \tag{2.100}$$

where $\mathbf{x}$ is the comoving position and where we have introduced $\tilde{\mathbf{v}} = a\mathbf{v}$, the super-comoving velocity vector. $\boldsymbol{\nabla}_{\mathbf{x}}$ and $\boldsymbol{\nabla}_{\tilde{\mathbf{v}}}$ are gradient operations in configuration and velocity space, ϕ is the fluids gravitational potential source by the density,

$$\nabla^2_{\mathbf{x}} \phi = 4\pi G \rho_{\mathrm{m}} \delta = \frac{3}{2} H_0^2 \Omega_{\mathrm{m},0} \frac{\delta}{a} \tag{2.101}$$

and finally, $\left.\frac{\mathrm{d}f}{\mathrm{d}t}\right|_{\mathrm{coll}}$, represents a generic collision term. In the case of a collisionless fluid this term is considered vanishing, Thus reducing the system of equations to the Vlasov-Poisson system of equation.

The Vlasov-Poisson system simply describes the conservation of the phase space distribution, notably it implies the phase space density is advected in configuration space by the velocity field and advected in velocity space by the gravitational force. This results in the phase space density being conserved along phase-space trajectories,

$$\dot{\mathbf{x}} = a^{-2} \tilde{\mathbf{v}}, \tag{2.102}$$

$$\dot{\tilde{\mathbf{v}}} = -\boldsymbol{\nabla}_{\mathbf{x}} \phi, \tag{2.103}$$

also known as 'characteristics'. We see that these trajectories are the same as those that would be followed by a point mass evolving within the potential ϕ, indicating that one can simulate the evolution of the phase space density simply by sampling the distribution with point masses and evolving the $N-$body system. We note however that if we source the potential from the point masses this only remains an accurate description as long as we can neglect two body interaction between point masses.

To this effect, these point masses, commonly referred to as particles, represent individual fluid elements, as such their masses, initial positions and initial velocities, are representative of this function. Let us take the example used in Fig. 2.3, where

we ran the Zel'dovich approximation beyond its realm of validity. Here, the particles were initialised on a grid of $N = 512$ particles per dimension, and represent an approximately homogeneous fluid, with density ρ_m, inside a periodic volume of with side length $L_{\rm box} = 50h^{-1}$Mpc. The mass of each individual particle is then,

$$m_{\rm p} = \rho_{\rm m} \left(\frac{L_{\rm box}}{N} \right)^3 \simeq 8 \cdot 10^7 h^{-1} M_\odot. \tag{2.104}$$

While placing the particles on a regular grid is probably the most straight forward choice for initialising the position, other options include placing the particles randomly (e.g. Carlberg & Couchman, 1989) and more advanced methods such as 'glass' initial conditions (see e.g. Crocce et al., 2006), or capacity constrained Voronoi tessellations (Liao, 2018), each having their strengths an weaknesses.

The initial velocities of the particles are then assigned using Lagragian Perturbation Theory, of which the Zel'dovich approximation discussed above is the first order. This first order is however not accurate enough to initialise large simulations which use the second or third order expansion. Typically the generation of initial conditions are handled independently from the cosmological simulation itself, and is done with external codes such as MPGRAPHIC (Prunet et al., 2008) or MUSIC (Hahn & Abel, 2011).

The distribution function of the fluid is now represented by a discrete set of particles with positions, $\mathbf{x}$, velocities, $\mathbf{v}$, and masses, $m_{\rm p}$. In order to evolve the system we simply have to solve the equations of motion for the $N-$body system, i.e. Eq. (2.102) and Eq. (2.103). To do so cosmological simulation codes require two main components, an efficient algorithm to calculate the forces applied to the individual particles and an efficient time-stepping algorithm.

Focusing on the force calculation, the simplest approach is to calculate the force

$$\mathbf{F}_i = -G m_{\rm p}^2 \sum_{j \neq i} \frac{\mathbf{x_i} - \mathbf{x_j}}{|\mathbf{x_i} - \mathbf{x_j}|^3} \tag{2.105}$$

applied to each particle explicitly, usually introducing a softening length to avoid numerical instabilities when two particles are too close to one another. This algorithm is however computationally prohibitive when running simulations with a large number of particles, making it incompatible with the type of simulation needed for cosmological studies.

When the particle distribution is sufficiently smooth a more efficient approach is to assign the mass of the particles to a grid and solve the Poisson equation directly using either a finite difference scheme or discrete Fourier transforms, which can be greatly accelerated using the Fast Fourier Transform (FFT) algorithm. While the Particle-Mesh (PM) algorithm greatly increases the efficiency of the force calculation it introduces a preferential scale, that of grid, significantly affecting dynamics below this scale. This makes it ill suited for clustered problems like the case at hand where we want to resolve the internal dynamics of haloes at kpc scale but also large scale dynamics at Gpc scales.

Having here one algorithm that is well suited to small scale problems and another that performs efficiently for large scale problems, a natural design choice is to combine both. This is the philosophy of the TreePM algortihm which combines Tree and PM algorithms. The Tree algorithm groups particles together in 'leaves' within which the force calculation is done through direct summation. The gravitational potential generated by the entire leaf is then decomposed into multipoles to account for the particle distribution within the group. The leaf then acts as a meta-particle producing this corrected potential. The TreePM algorithm separates the short range and long range

contribution to the gravitational potential using the Tree for the short range contribution and the PM algorithm to compute the long range contribution by assigning the mass of particles to a grid to efficiently compute the large scale potential using FFT. This is, for example, the approach adopted in GADGET (Springel, 2005; Springel et al., 2021) and GREEM (Ishiyama et al., 2009).

A second approach consists in using the PM algorithm with a set of nested meshes with increasingly higher resolution. These higher resolution grids are dynamically defined in areas where they are needed, typically where there is a high concentration of particles. This approach, known as Adaptive Mesh Refinement (AMR), is for example used in RAMSES (Teyssier, 2002).

Once the force applied to each particle has been computed the time stepping is done using a symplectic integration algorithm. This class of algorithm is specifically designed to solve Hamiltonian systems such as the motion of point particles inside a gravitational potential. The "leap-frog" algorithm,

$$\begin{aligned}
\mathbf{x}_i(t + \Delta t/2) &= \mathbf{x}_i(t) + \frac{\Delta t}{2}\, a(t)^{-2}\, \mathbf{v}_i(t), \\
\mathbf{v}_i(t + \Delta t) &= \mathbf{v}_i(t) + \Delta t\, \mathbf{F}(\mathbf{x}_i(t + \Delta t/2)), \\
\mathbf{x}_i(t + \Delta t) &= \mathbf{x}_i(t + \Delta t/2) + \frac{\Delta t}{2}\, a(t + \Delta t)^{-2}\, \mathbf{v}_i(t + \Delta t),
\end{aligned} \tag{2.106}$$

here adapted for an expanding universe, is commonly used inside cosmological codes as it provides a good balance between simplicity, requiring only one force evaluation per time step, and accuracy, this simplectic algorithm being designed to conserve mechanical energy and be accurate to second order in Δt. All simulations presented here use this algorithm.

At the end of a simulation we observed that the particles have clustered. This can be seen directly upon visual inspection of a density field coming from such a simulation, such as Fig. 2.5 where we reproduce a slice from a RAMSES simulation with side length $L_{\rm box} = 328.125 h^{-1}$Mpc and $N_{\rm part} = 512^3$ particles[1], this slice is projected over 10 h^{-1}Mpc. In the same figure we also add a square cutout showing a 50 h^{-1}Mpc wide region around several large haloes.

If we compare a region of Fig. 2.5 with an equivalent size to Fig. 2.3, i.e. 50 h^{-1}Mpc wide, we see that while the Zel'dovich approximation yields structures which resemble the large scale structure of the Universe, a considerable amount of structure on small scales is missing. Indeed, we see that gravity binds a large amount of matter inside small haloes which are disrupted by the Zel'dovich approximation.

When running the simulation forward in time we observe that small haloes form first. These small haloes then attract each other and go through a series of mergers to form larger and larger structures. If we naively link the mass of a halo to the type of luminous structure we may observe in the real Universe, this tells us that galaxies start out their existence as dwarfs and then gradually merge with their neighbours to form larger and larger galaxies such as the Milky-Way or Andromeda. The haloes within which these galaxies are located are often much larger than the galaxy itself and start to dominate their surroundings. At larger masses we then find groups of a few galaxies which orbit within a single halo. Finally, at the top of the hierarchy, we find galaxy clusters which sometimes host over a thousand galaxies.

[1] This particular simulation is taken from a suite of simulations run by Iñigo Saèz Casarez.

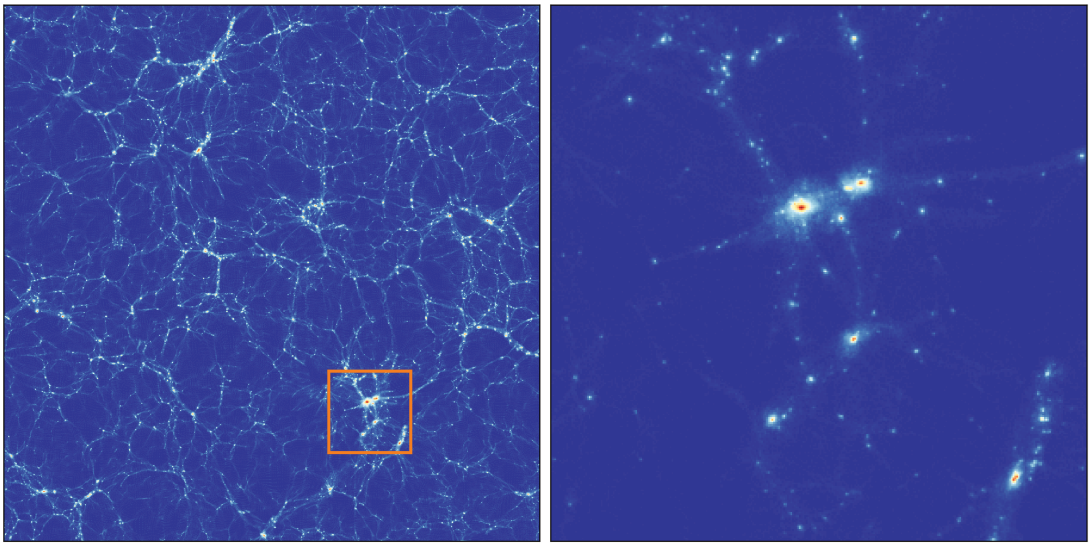

Figure 2.5: In the left panel we can see a slice of the denisty field from a simulation with side length $L_{\rm box} = 328.125\ h^{-1}$Mpc and $N_{\rm part} = 512^3$ particles. This slice is projected over a depth of 10 h^{-1}Mpc showing the entire simulation box. The orange square represents a $(50\ h^{-1}\text{Mpc})^2$ cutout shown in the right panel. We can see that the density field appears much more structured than in Fig 2.3 with many small haloes surrounding larger ones.

2.7.2 Halo Finders

Throughout this work we are going to be particularly interested in the properties of haloes. In order to extract these properties from the distribution of particles inside simulations, we employ a third class of algorithms known as halo finders. These algorithms employ two main approaches upon which a large variety of codes are built, the Friends-of-Friends (FoF) algorithm which groups nearby particles on the basis of a percolation criterion, and the spherical overdensity (SO), which selects particles that reside within a sphere within which the mean density is higher than a given threshold of collapse.

Friends-of-Friends links particles together that are closer than a linking length $d = b\bar{r}$, where $\bar{r}$ is the mean inter-particle distance inside the simulation and b is a free parameter usually taken to be $b = 0.2$ as the resulting mass $M_{\rm FoF}$ is approximately equal to $M_{\rm vir}$. This approach effectively defines a halo by an iso-density surface of unconstrained geometry, this allows it to accurately capture the ellipsoidal shape of haloes. Nevertheless, such a flexibility also represents the algorithm's limit as it will sometimes link particles that are in dense regions but not necessarily inside a halo, for example forming bridges between two haloes that are colliding or detecting structures that are not gravitationally bounds, as in the case of caustics that form during shell crossing. This technique, originally introduced by Press & Davis (1982), has given rise to a variety of codes used by the community including: a parallelised version, PFOF (Roy et al., 2014), a 6-dimensional version using additional information in velocity space, ROCKSTAR (Behroozi et al., 2013a) and a version using additional binding criteria, SUBFIND (Springel et al., 2001).

The Spherical Overdensity algorithm takes a different approach by first making a ranked list of particles according to there local density, the algorithm then places itself on the position of the most highly ranked particle and iteratively grows a sphere out-

ward until the mean density within the sphere reaches a desired threshold, for instance the virial overdensity threshold $\Delta_{\rm vir}$ which we defined previously. Once the algorithm reaches the desired threshold it assigns all the particles within the sphere to a halo and removes them from the ranked list, it then continues from the next highest ranked particle and grows a new sphere. This process is repeated until all the particles have been visited. The main advantage of this algorithm is that it is closer to the theorical definition of a halo allowing for a simpler understanding of the parameters at play. It is also agnostic of particles masses and as such performs fairly well with minimal changes when using simulations with varying particles masses, such as hydrodynamical simulations or zooms. Moreover it pairs well with mesh based simulation codes, as the information from a density or potential grid can easily be incorporated and used as a starting point for the algorithm. It does however come with the downside of being rigid when it comes to the shape of a halo, wherein it forces a spherical shape. This can lead to some issues for haloes presenting ellipsoidal shapes, this down side does however protect it from the spurious bridging that may occur when using FoF.

While the SO approach explicitly defines a threshold for detection, it is worth noting that for both FoF and SO one can readily define masses according to any desired criterion, allowing the halo finders to accommodate for the diverse mass definitions currently in use. Indeed, different communities use different contrasts with for instance, observational studies more focused on the hot gas trapped within galaxy clusters, i.e. X-ray and Sunyaev-Zel'dovich observation, will favour higher density contrasts, such as $\Delta = 500$c or $\Delta = 2500$c, while weak lensing and dynamical studies will favour mass definitions at lower over density contrasts, such as $\Delta = 200$c and $\Delta = \Delta_{\rm vir}$. This choice being driven by some mass definitions better corresponding to the signal that is being observed. This freedom in the definition of halo mass, while confusing for newcomers, can however be advantageous when it comes to studying how matter is distributed inside of haloes.

2.8 Simulation data

Throughout this work we will use data coming from multiple simulations. Thus, before analysing these data, let us first present these simulations, their parameters and their specificities which we also summarise in Tab. 2.2. Note that all the simulations presented below only account for gravitational dynamics and as such do not include baryonic feedback effects.

MultiDark PLanck 2 The MultiDark PLanck 2 (MDPL2) simulation is a gravity only, $(1\ h^{-1}\mathrm{Gpc})^3$, cosmological volume run using GADGET-2 with a *Planck* (Planck Collaboration et al., 2014a) cosmology and sampled by 3840^3 particles, resulting in a particle mass $m_{\rm p} = 1.51 \cdot 10^9\ h^{-1}\mathrm{M}_\odot$. This publicly available[2] simulation data-set, part of the MultiDark series (Klypin et al., 2016), was analysed using ROCKSTAR (Behroozi et al., 2013a,b) to produce both the halo catalogues and merger trees that we use in Chapter 4.

Uchuu The Uchuu simulation (Ishiyama et al., 2021) is very similar to MDPL2 in several key aspects, notably it is also a publicly available[3] gravity only simulation run with a *Planck* cosmology (Planck Collaboration et al., 2016) and analysed using ROCKSTAR. Although it differs in volume, $(2\ h^{-1}\mathrm{Gpc})^3$, and number of particles, 12800^3,

[2] https://www.cosmosim.org/
[3] https://skiesanduniverses.iaa.es/

Table 2.2: Simulation data-set properties used in this work. References: [1] Klypin et al. (2016); [2] Ishiyama et al. (2021); [3] Sáez-Casares et al. (2023, in prep.) ; [4] Stücker et al. (2020, 2022).

Name	Cosmology	$L_{\rm box}[h^{-1}{\rm Mpc}]$	$N_{\rm part}$	Code	Halo Finder
MDPL2 [1]	*Planck13*	1000	3840^3	GADGET-2	ROCKSTAR
Uchuu [2]	*Planck15*	2000	12800^3	GREEM	ROCKSTAR
e-MANTIS [3]	wCDM	328.125	512^3	RAMSES	PFOF
S+R sims [4]	ΛWDM	20	512^3	GADGET-3	SUBFIND

resulting in a mass resolution, $m_{\rm p} = 3.27 \cdot 10^8\ h^{-1}{\rm M}_\odot$, that is smaller by almost an order of magnitude. This simulation was also run using GREEM. The large volume and small particle mass makes this data-set very versatile with it being used profusely throughout this work.

e-MANTIS The e-MANTIS simulations, run by Iñigo Sáez Casares, is a set of many, smaller $(328.125\ h^{-1}{\rm Mpc})^3$, and lower resolution 512^3, simulations spanning a wide range of wCDM cosmologies and $f(R)$ cosmologies (Sáez-Casares et al., 2023, in prep.). These simulations are designed to train an emulation algorithm to predict multiple cosmological observables, some of which are developed in this work, in particular in Chapter 5. Here we use this data-set primarily for visualisation and to study the cosmology dependence of these observables.

Sheet + Release simulations In Chapter 6, we use a specific type of sheet+release simulation designed and run by Jens Stücker (Stücker et al., 2020, 2022). The force calculation implemented in GADGET-3 is designed to accurately follow the evolution of the dark matter phase space distribution function to avoid smooth density structures in WDM cosmologies being fragmented by numerical discreteness effects. These simulations are much more computationally expensive than standard N-body, limiting them to a small size, $(20\ h^{-1}{\rm Mpc})^3$. Nonetheless, as we discuss in detail in Chapter 6, these alterations allow to sample the density field to arbitrarily small mass resolutions in sufficiently smooth regions.

2.9 Basic properties of haloes

Now that we are able to run a simulation up to the current cosmological epoch and extract information from it we can now study its content. In the following, we will focus on haloes and their main properties. We will start by studying the statistical distribution of haloes as measured by the halo mass function before studying the properties of individual haloes and particularly their density profiles.

2.9.1 The Halo Mass Function

Measuring the HMF from a catalogue of haloes is relatively simple as it amounts to counting the number of haloes one finds per unit mass and normalising by the volume of the simulation. From what we have seen in Sec. 2.6 the HMF is a decreasing function of halo mass, in a CDM scenario, and so we expect to see more small haloes than large haloes. As we are counting a discrete number of objects, we expect that the error on this measurement is Poissonian and thus larger for a smaller number of objects, this

means that if we want to investigate what happens at the high mass end we require large volume simulations to increase our odds of producing enough large objects. This is exacerbated further at the very high mass end due to the exponential cutoff in the HMF, indeed if we want to accurately probe this regime the size of the simulations we would need also increases dramatically.

To measure the HMF in the following we will use the Uchuu simulation (Ishiyama et al., 2021). This simulation was produced with GREEM using the cosmological parameters inferred from the Planck collaboration's 2015 analysis, see Tab. 2.1, and represents a periodic box of side length $L_{\rm box} = 2h^{-1}{\rm Gpc}$ with a total of 12800^3 particles giving this simulation one of the smallest particle masses, $m_{\rm part} = 3.27 \times 10^8 h^{-1}{\rm M}_\odot$, relative to its size. The haloes that formed within this simulation were extracted using ROCKSTAR, in the following it is these catalogues that we will be using for our measurements.

Let us start by comparing the HMF from the simulation to the Press & Schechter model derived above. Nevertheless, we must first ask ourselves the question: *what mass do we want to look at?* In the theoretical models presented above, the specific mass definition is not made explicit. Nevertheless, we can infer that because these theoretical models are based on the spherical collapse model, whose mass definition corresponds to the mass that will collapse onto and virialise within the halo, then, it is more appropriate to compare these theoretical results to a HMF measured for $M_{\rm vir}$.

In Fig. 2.6, we compare the measured HMF with the model proposed by Press & Schechter. It is clear that there is a significant offset in between the prediction and the measurement. Indeed, we see that the Press & Schechter model predicts too many small haloes and not enough large haloes. This is primarily due to the assumption that haloes are spherical which we already knew, from the Zel'dovich approximation, was not the case. This apparent mismatch between the theoretical prediction and what was seen in simulations spearheaded a number of studies which attempted to find better parameterisations of the HMF in order to match what was seen in simulation.

The general philosophy behind these parameterisations was to keep the Press & Schechter formula,

$$\frac{{\rm d}n}{{\rm d}M_\Delta} = 2\frac{\rho_{\rm m}}{M_\Delta^2}\left|\frac{{\rm d}\ln\sigma}{{\rm d}\ln M_\Delta}\right| f(\sigma) \tag{2.107}$$

which factorises the HMF into two terms, depending respectively on the background cosmology, statistics of the linear density field, and a third term encoding the details of the non-linear collapse of matter known as the multiplicity function, $f(\sigma)$, where we have dropped the index $\sigma \equiv \sigma_M$ which we used in the previous sections. According to Press & Schechter (1974) the multiplicity function,

$$f(\sigma) = \frac{1}{\sqrt{2\pi}}\frac{\delta_{\rm c}}{\sigma}\exp\left(-\frac{\delta_{\rm c}^2}{2\sigma^2}\right), \tag{2.108}$$

does not have an explicit dependence on cosmology or redshift, which are implicitly hidden within σ. This particular property dubbed universality of the mass function is key to the design of many models of the HMF but also the source of much debate as to whether this holds up in practice given the increasing resolution of simulations. One of the first widespread models is that of Sheth & Tormen (1999) which provided a generalisation of the Press & Schechter multiplicity function,

$$f(\sigma) = A\sqrt{\frac{a}{2\pi}}\frac{\delta_{\rm c}}{\sigma}\left[1+\left(a\frac{\delta_{\rm c}^2}{\sigma^2}\right)^{-p}\right]\exp\left[-a\frac{\delta_{\rm c}^2}{2\sigma^2}\right], \tag{2.109}$$

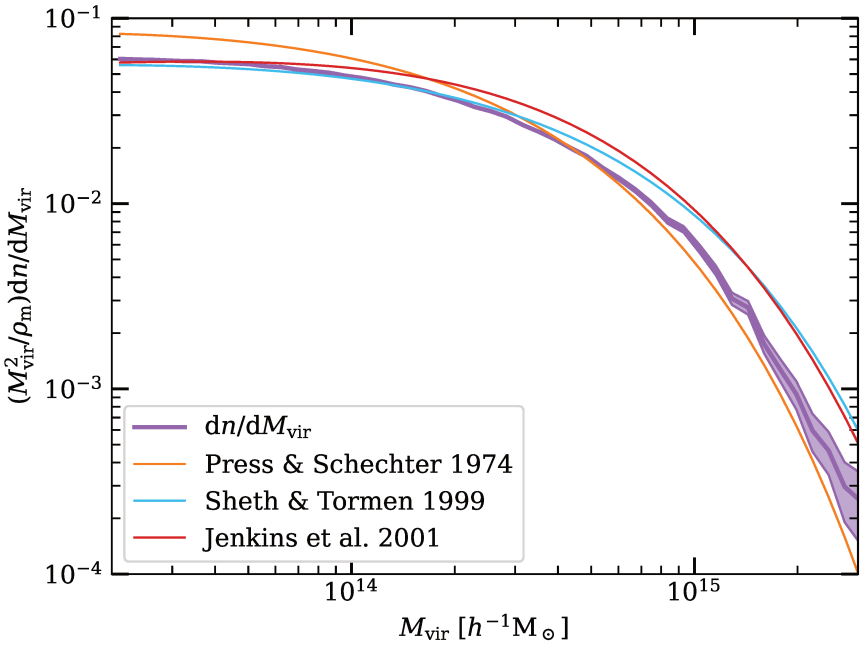

Figure 2.6: Halo Mass function at the virial density contrast and estimated in the Uchuu simulation at redshift $z = 0$ (purple shaded area), the shaded area represents the 1-σ statistical error interval around the measurement estimated over 1000 bootstrap iterations. This measurement is plotted against the theoretical model of Press & Schechter (orange line) and the fitting function of Sheth & Tormen (blue line) and Jenkins et al. (red line). We see that these early models have significant difficulty accurately reproducing the HMF, with the Press & Schchter framework overestimating the population of small haloes and the later models, introduced to correct this issue, overestimating the abundance of massive haloes.

including three new parameters, $A \simeq 0.322,\ a = 0.707$ and $p = 0.3$, which do not depend on cosmology or redshift. This formulation was particularly well received as not only it would reduce to that of Press & Schechter in the specific case $A = 1/2,\ a = 1, p = 0$, but also provided parameters related to an "ellipsoidal" collapse barrier that could be used in excursion set theory.

Another model to gain significant popularity at the time was that of Jenkins et al. (2001), which provided another three parameter fitting function,

$$f(\sigma) = \frac{A}{2} \exp\left(-\left|\ln \sigma^{-1} + a\right|^p\right), \tag{2.110}$$

where each parameter depends on the mass definition. For FoF masses close to the virial mass for instance, these parameters are: $A = 0.315,\ a = 0.61$ and $p = 3.8$. Here again the authors of the study consider the HMF to be universal in cosmology and redshift. This particular model gained significant popularity due to the simplicity of the fitting formula, making it much easier to use than the model of Sheth & Tormen without having to sacrifice accuracy.

In Fig. 2.6 we have plotted the virial HMF, measured from the simulated halo catalogues, against the three models discussed so far. We can see that the fitted HMFs generaly perform better than the original analytical formulation. These fits are however not perfect and where they do correct the issue of overestimating the number of smaller

haloes, they nonetheless have difficulty accurately capturing the exponential cut off at high masses.

The first full investigation of the dependence of the parameters on the mass definition was proposed by Tinker et al. (2008). The authors of this study use a multiplicity function that somewhat resembles that of Sheth & Tormen,

$$f(\sigma) = \frac{A}{2}\left[\left(\frac{\sigma}{b}\right)^{-a} + 1\right]\exp\left(-\frac{c}{\sigma^2}\right), \tag{2.111}$$

but freeing up an additional parameter. These parameters are then fitted for nine mass definitions ranging from $\Delta = 200$ to $\Delta = 3200$. One then has to interpolate between these points to obtain the set of parameters, $\{A_0, a_0, b_0, c_0\}$, at redshift, $z = 0$, at the density contrast of interest. The final parameters finally have to be rescaled to account for the redshift dependence of the parameters,

$$\begin{aligned} A(z) &= A_0(1+z)^{-0.14}, \\ a(z) &= a_0(1+z)^{-0.06}, \\ b(z) &= b_0(1+z)^{-\alpha(\Delta)}, \\ c &= c_0, \\ \log_{10}\alpha(\Delta) &= -\left[\frac{0.75}{\log_{10}(\Delta/75)}\right]^{1.2}, \end{aligned} \tag{2.112}$$

with the inclusion of an explicit dependence on redshift marking a step away from universality. Accounting for all of this procedure, this model relies on a set of 40 numbers measured from simulations. This model has come to dominate the literature as it allowed for the first time the possibility to provide accurate predictions for the HMF at density contrasts differing from the virial contrast.

This approach was revisited by Watson et al. (2013), using the same multiplicity function but recomputing the parameters,

$$\begin{aligned} A(z) &= \Omega_{\rm m}(z)\left[0.990(1+z)^{-3.216} + 0.074\right], \\ a(z) &= \Omega_{\rm m}(z)\left[5.907(1+z)^{-3.058} + 2.349\right], \\ b(z) &= \Omega_{\rm m}(z)\left[3.136(1+z)^{-3.599} + 2.344\right], \\ c &= 1.318, \end{aligned} \tag{2.113}$$

to include an explicit dependency on the Ω_m cosmological parameter. In contrast to the previous model, the authors however separate the contribution from the mass definition into a second function, $\Gamma(\Delta, \sigma, z)$, such that the multiplicity function at the desired density contrast,

$$f_\Delta(\sigma, z) = \Gamma(\Delta, \sigma, z)\, f_{\rm vir}(\sigma, z), \tag{2.114}$$

is simply the product of the latter with the multiplicity function at the virial density contrast. This function,

$$\Gamma(\Delta, \sigma, z) = C(\Delta)\left(\frac{\Delta}{178}\right)^{d(z)}\exp\left[-\frac{p}{\sigma^q}\left(1 - \frac{\Delta}{178}\right),\right], \tag{2.115}$$

adds another set of parameters that however also need to be fitted to simulations,

$$\begin{aligned} C(\Delta) &= \exp\left[0.023\left(\frac{\Delta}{178}-1\right)\right], \\ d(z) &= -0.456\,\Omega_{\rm m}(z) - 0.139, \\ p &= 0.072, \\ q &= 2.130, \end{aligned} \tag{2.116}$$

considerably reducing the total amount of fitted numbers down to 15. In this particular model, it is clear that the universality of the HMF is completely abandoned at the cost of a much more complex model, which can feel somewhat artificial.

While the previous example shows a model that completely abandons the idea of a universal mass function, this was not the case of other models. For instance Despali et al. (2016), presents a model which assumes that the mass function is only universal for the virial density contrast, and that non-universality at other definitions comes from the profile of haloes. This widely used model assumes the same shape for the multiplicity function as Sheth & Tormen, i.e. Eq. (2.109), and recalculates the fitting parameters for a wide range of mass definitions, redshifts and cosmologies. The authors find that when expressed as functions of, $x \equiv \log_{10}(\Delta(z)/\Delta_{\rm vir}(z))$, the fitted parameters can be very well approximated by quadratic functions,

$$\begin{aligned} a &= 0.4332x^2 + 0.2263x + 0.7665, \\ p &= -0.1151x^2 + 0.2553x + 0.2488, \\ A &= -0.1362x + 0.3292, \end{aligned} \tag{2.117}$$

greatly reducing the number of parameters. We can also see that with this parameterisation the HMF is indeed universal for $\Delta_{\rm vir}$ for all cosmologies and at all redshifts. The authors also investigate the properties of the HMF at different density contrasts when considering matched haloes, i.e. haloes that are detected at two seperate thresholds and then matched according to their positions. They find that in this case two HMFs at two density contrasts can be related by marginalising the HMF,

$$\frac{{\rm d}n}{{\rm d}M_\Delta} = \int {\rm d}M_{\rm vir} \frac{{\rm d}n}{{\rm d}M_{\rm vir}} p(M_\Delta|M_{\rm vir}) \tag{2.118}$$

over the probability, $p(M_\Delta|M_{\rm vir})$, of a halo having a mass M_Δ knowing it's virial mass. If the distribution of masses is sufficiently peaked around some value $g_\Delta(M_{\rm vir})$ then this relation simplifies such that,

$$f_\Delta(\sigma) = g_\Delta(M_{\rm vir}) f_{\rm vir}(\sigma), \tag{2.119}$$

leading to a result similar to the formalism used by Watson et al. (2013) in the previous model. In this context however, the function, $g_\Delta(M_{\rm vir})$, only depends on the properties of the profiles of haloes letting transpire an intrinsic link between the HMF and the profile haloes.

So far all of these models have been calibrated using simulations that only account for the gravitational force between particles. This is primarily due to the high computational cost of hydrodynamical simulations of equivalent volume. However, thanks to the increasing power of computers and design of efficient algorithms in recent years, the realisation of several large hydrodynamical simulation has allowed accurate estimates of the HMF including baryonic effects. Bocquet et al. (2016) for instance, recalibrate

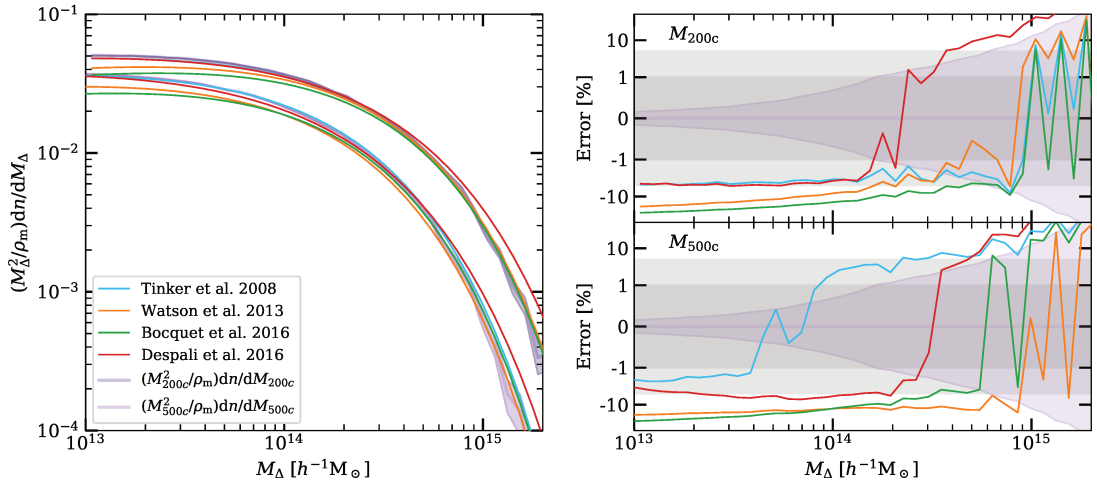

Figure 2.7: *Left panel:* Halo mass function measured from the Uchuu simulation at two density contrasts $\Delta = 200$ and $\Delta = 500$, respectively the dark and light purple shaded areas, the size of which marks the 1-σ statistical error interval around the measurement estimated over 1000 bootstrap iterations. The coloured lines correspond to the various models discussed in detail in the text. *Right panel:* relative error of the model with respect to the measurement. The grey shaded areas represent 1% and 5% error on the measurement.

the HMF on the MAGNETICUM simulations assuming the same multiplicity function as the Tinker model, e.g Eq. (2.111), and assuming a similar redshift evolution of the parameters,

$$\begin{aligned} A(z) &= A_0(1+z)^{A_z}, \\ a(z) &= a_0(1+z)^{a_z}, \\ b(z) &= b_0(1+z)^{b_z}, \\ c(z) &= c_0(1+z)^{c_z}, \end{aligned} \tag{2.120}$$

which are calibrated for three mass definitions, $\Delta = 200\mathrm{m}$, $\Delta = 200\mathrm{c}$ and $\Delta = 500\mathrm{c}$ and both using the full hydrodynamical simulation or using its gravity only counterpart. In this particular study the authors also emphasise the need of an accurate HMF model for cosmological constraints as even the small differences between the models can result in significant systematic biases on the resulting cosmological parameters.

In Fig. 2.7 we compare the four models presented above to measurements of the HMF at $\Delta = 200\mathrm{c}$ and $\Delta = 500\mathrm{c}$. We can see that compared to the models presented in Fig. 2.6 these models are much more efficient at capturing the shape of the HMF, this is especially true for models, such as Tinker et al. (2008) which free the scale at which the exponential cutoff appears. In the right panels of Fig. 2.7 we plot the relative error between the models discussed above and estimates of the HMF for two mass definitions, M_{200c} *top panel* and M_{500c} *bottom panel*. We see that while there is an improve these parametrisations present a relative difference ranging from a few percent to more than ten percent.

In the current era of large scale deep surveys and high resolution simulations, the interest of the community has shifted towards understanding how the HMF is affected by systematics, such as dynamical effects (Seppi et al., 2021), baryons (Castro et al., 2021), or departures from universality (Ondaro-Mallea et al., 2022), and how this would affect

cosmological analyses. Note that for the sake of conciseness, we have skipped many models which have marked the literature (e.g. Warren et al., 2006; Reed et al., 2007; Crocce et al., 2010) or that investigate the behaviour of the HMF in beyond ΛCDM cosmologies (e.g. Bhattacharya et al., 2011; Courtin et al., 2011; Gupta et al., 2022), non-standard simulation configurations (e.g. Angulo et al., 2012; Gavas et al., 2023) or using exotic mass definitions (e.g. Diemer, 2020; García et al., 2023).

2.9.2 The internal structure of haloes

Let us now focus our interest on the internal structure of haloes, and more specifically the density profiles of haloes. Ultimately, we want to study how the internal structure behaves statistically, i.e. over a population of haloes. Before doing so we first need a metric allowing us to quantify and compare this property between haloes and models. As such, lets us first review different profile shapes that have been suggested in the literature.

In a similar fashion to the previous section, let us start with models that date to before the time of large scale cosmological simulations. From analytical computations theorists initially suggested that the initial density fluctuation have power-law profiles Bardeen et al. (1986) and that the profile of haloes resulting from the collapse of these perturbations would also resemble power laws (Gunn & Gott, 1972),

$$\rho(r) = \left(\frac{r}{r_0}\right)^{-\gamma}, \tag{2.121}$$

also known as self-similar profiles. In this case the final power law index, γ, is fully determined by the power law index, ϵ of the initial profile of the density perturbation. Under the assumption of purely radial orbits and spherical symmetry this result leads to profiles having $\gamma \gtrsim 2$. The specific case where $\gamma = 2$ is also known as the isothermal sphere/ellipsoid model as it is also the result one obtains when solving for the profile of an isothermal self-gravitating collisional fluid. If one considers the alternate hypothesis that fluid elements have isotropic orbits within the potential, then one obtains $\gamma \gtrsim 1$. While there is room to argue that power law profiles are unrealistic, nonetheless they are widely used in observational studies, e.g. modelling strong gravitational lenses, due to their simplicity.

Numerical studies have shown that the profile of haloes cannot be accurately modelled by a single power law and that the logarithmic slope of the profile, $\gamma = -\mathrm{d}\ln\rho/\mathrm{d}\ln r$, varies slowly with radius. As such many alternate profiles have been proposed to describe this average shape.

By far the most popular model is the Navarro, Frenk & White (NFW) profile (Navarro et al., 1997). A broken power law profile,

$$\rho(r) = \frac{\rho_0}{r/r_\mathrm{s}(1 + r/r_\mathrm{s})^2}, \tag{2.122}$$

characterised by two parameters, a density normalisation ρ_0, and a scale radius, r_s. We see that the inner logarithmic slope converges toward $\gamma = 1$ and increases to $\gamma = 3$ at outer radii. The popularity of this particular profile is bolstered by the fact that it not only provides a good fit to the mass distribution of haloes but also allows for analytical expressions of the mass within a given radius, or the gravitational potential. This profile does have the drawback that it has infinite extension, meaning that if one integrates out to infinite radii the mass diverges. This issue can be bypassed by stopping the

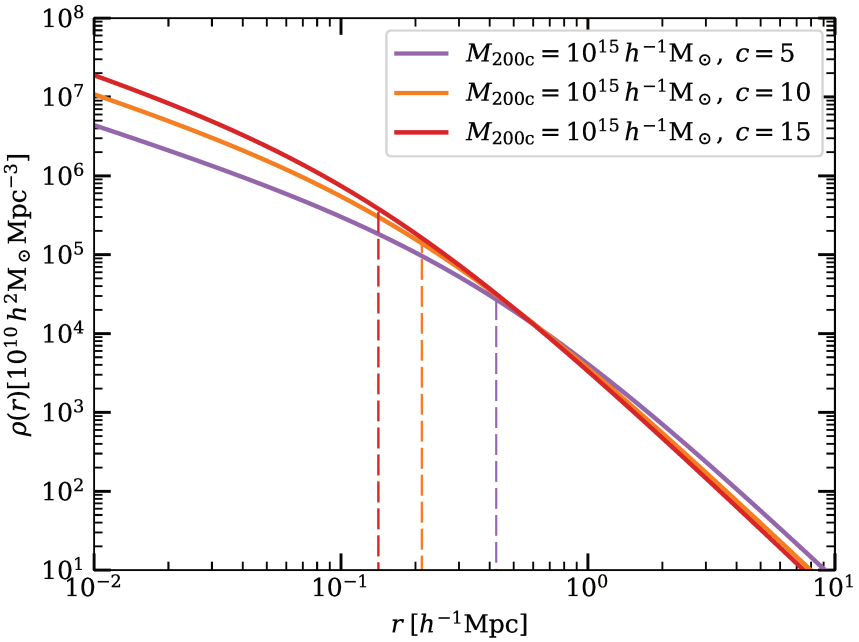

Figure 2.8: The Navarro, Frenk and White profile for three haloes with the same mass, $M_{200c} = 10^{15}h^{-1}\mathrm{M}_\odot$ and increasing concentration c. In addition, the vertical lines show the corresponding scale radius, r_s, of each profile

integration at some radius r_Δ, containing the mass M_Δ, such that,

$$M_\Delta = 4\pi\rho_0 r_\mathrm{s}^3\left[\ln\left(1+\frac{r_\Delta}{r_\mathrm{s}}\right)+\frac{r_\Delta}{r_\mathrm{s}}\frac{1}{1+r_\Delta/r_\mathrm{s}}\right] = \frac{4\pi}{3}\Delta\rho_c r_\Delta^3, \tag{2.123}$$

where, in the right hand side, we simply recall the definition of M_Δ. This particular equality is used to recast the two parameters of the profile in terms of a mass, M_Δ, and a *concentration* parameter, $c_\Delta \equiv r_\Delta/r_\mathrm{s}$. The name of the latter echoes the idea that, a higher concentration indicates that the density is higher in the central part of halo, we can clearly see this in Fig. 2.8 where we plot three NFW profiles at fixed mass and vary the concentration. Note that, the density contrast, Δ is usually chosen to be 200 times the critical density, but this definition can vary from one author to another, unless explicitly specified we will be using this definition for the rest of this work.

This profile and in particular this parameterisation has sparked a myriad of studies which focus on how these two parameters are linked through a correlated distribution known as the concentration mass $(c-M)$ relation, which is either modelled in terms of the formation of haloes or empirically estimated from simulations. The $c-M$ relation, usually describes the mean behaviour of the population and is widely accepted to be dependent on both cosmology and redshift, the scatter around the mean is usually described as following a log-normal distribution with a logarithmic scatter parameter between 0.2 and 0.25 dex. In Fig. 2.9, we plot several models of the $c-M$ relation, which assume the NFW profile, over the conditional distribution of concentrations observed in the Uchuu simulation. We see that there are two outliers, which are mainly due to model assumptions. Indeed, the model of Zhao et al. (2009) is based upon the evolution of the concentration parameter given the average mass accretion history of haloes of a given mass, and the model of Prada et al. (2012) which implements a prescription between the maximal circular velocity inside the halo and concentration. The remaining

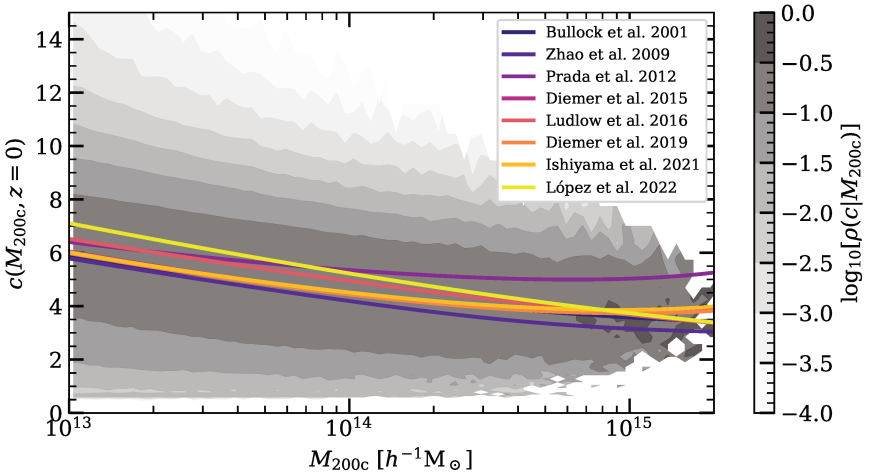

Figure 2.9: Models of the concentration mass relation over the conditional distribution of concentrations in the Uchuu simulation. We see that several models are clustered around the peak of the distribution but there are however some outliers, the latter are models which make different assumptions regarding how one defines concentration, Ludlow et al. (2016) & López-Cano et al. (2022) for instance assume that haloes are described by the Einasto profile rather than the NFW profile, and Prada et al. (2012) defines the concentration of haloes through their maxmimal circular velocity rather than fitting their mass profiles.

models (Bullock et al., 2001; Diemer & Kravtsov, 2015; Diemer & Joyce, 2019; Ishiyama et al., 2021) are simply fitted to N-body simulations.

The fit to profiles from simulations is however far from perfect which has resulted in the introduction of many generalisations of the NFW formula. Most notably freeing up the inner and outer slopes, such as the Dekel-Zhao (Zhao, 1996; Dekel et al., 2017) profile,

$$\rho(r) = \frac{\rho_0}{x^\alpha (1 + x^{1/\beta})^{\beta(\gamma-\alpha)}}, \tag{2.124}$$

where $x \equiv r/r_\mathrm{s}$, and the scale radius is defined to conserve the definition of the concentration. The addition of free independent slopes in the inner and outer profile greatly increases the goodness-of-fit to numerical simulation data, while keeping the analytical nature of the profile intact, though at the cost of a higher complexity resulting from a profile with 5 parameters, namely ρ_0, r_s, α, β and, γ.

While the previous profile helps increase the goodness-of-fit, it does not however solve the issue of the divergent masses at infinite radii, which can be more problematic when for instance modelling weak lensing effects. In the case of the standard NFW profile this is usually achieved through the introduction of a truncation radius, r_t, above which the density sharply decreases. One possible choice is to add a truncation term (Baltz et al., 2009),

$$\rho(r) = \frac{\rho_0}{r/r_\mathrm{s}(1 + r/r_\mathrm{s})^2} \left(\frac{1}{1 + (r/r_\mathrm{t})^2} \right)^2, \tag{2.125}$$

in order to have the mass converge to a finite value. This is for instance the profile used within the AMICO analysis (e.g. Bellagamba et al., 2019) to model weak lensing observations of galaxy clusters. Note that this relatively simple alteration does make the profile loose its analytical properties.

There are alternatives to the NFW profile. One such alternative, that has recently gained a significant backing, is the Einasto profile (Einasto, 1965),

$$\rho(r) = \rho_{-2} \exp\left\{-\frac{2}{\alpha}\left[\left(\frac{r}{r_{-2}}\right)^{-\alpha} - 1\right]\right\}. \tag{2.126}$$

This three parameter profile provides a much better fit to observed haloes than the NFW profile (Wang et al., 2020b), although it does not provide the same "analytical friendlyness" as the latter, making it generally more complex to implement into data analysis pipelines. The main advantage of this profile is its more flexible shape and finite support. Similarly to the other profiles, one can also define a concentration equivalent to the NFW concentration, such that $c \equiv r_{-2}/r_{\Delta}$, and thus measure a $c - M$ relation.

In Fig. 2.9 we plot two models (Ludlow et al., 2016; López-Cano et al., 2022) of the $c - M$ relation which assume the Einasto profile, while these models are also fitted to simulations, they appear as outliers among the other models. This is simply due to the fact that Einasto concentrations are distinct from NFW concentrations (Klypin et al., 2016). And it is this ambiguity between concentrations that often leads to the recurrent question: *what type of concentration are you using?* when comparing two models.

3 | Dark matter halo sparsity

In the previous chapter, we have seen that there is significant freedom in how one can quantify the shape of dark matter halo profiles. In particular we have seen that this quantification is done using a *concentration* statistic, denoted c. This statistic, initially tailored for the NFW profile, has received significant interest in the literature, leading to as many ambiguous definitions as there are proposed profiles shapes. In principle, concentration is a dimensionless measurement denoting a change in slope within the profile, for instance if one uses the NFW profile this corresponds to the scale radius r_s and if one uses the Einasto profile this correspond to the radius at which the logarithmic slope is equal to -2, r_{-2}. This ambiguous nature of concentration along with its definition from profile parameters makes it difficult to use in practice beyond fitting profiles.

As such, in this work we propose to use an alternative metric that is agnostic to the choice of profile,

$$s_{\Delta_1,\Delta_2} = \frac{M_{\Delta_1}}{M_{\Delta_2}} = \frac{\int_0^{r_{\Delta_1}} \mathrm{d}r\ r^2\rho(r)}{\int_0^{r_{\Delta_2}} \mathrm{d}r\ r^2\rho(r)}, \tag{3.1}$$

dubbed halo sparsity, and which was first introduced by Balmès et al. (2014). By convention, we will always assume $\Delta_2 > \Delta_1$, which implies that $s_{\Delta_1,\Delta_2} > 1$. This metric has several advantages over concentration: firstly, it can be defined unambiguously for any profile or simply using measured quantities; secondly, it relies on integrated quantities rather than fitted parameters making it more robust to small scale density fluctuations; finally, as both mass definitions are freely defined, we can also define multiple sparsities allowing us to effectively define as many sparsities as there would be parameters describing the profile.

In the following we will first describe in Section 3.1, the general properties of sparsity. We will then discuss in Section 3.2, how we can link sparsity to parametric descriptions of the halo profile. We expand these initial observations to a statistical description, in Section 3.3 and link this statistical description of sparsities to that of the HMF in Section 3.4. Finally, we discuss how to express the relation between profile parameters and sparsities within this statistical framework in Section 3.5.

Part of this chapter, in particular Section 3.4 and Section 3.5, are based upon work that led to the publication of Richardson & Corasaniti (2023).

3.1 An overview of s_{Δ_1,Δ_2}

To begin, let us investigate what sparsities tell us about the profile of haloes as they can be interpreted in two ways. Firstly, sparsity can be seen as the fraction of mass contained between r_{Δ_1} and r_{Δ_2}, relative to the mass contain within r_{Δ_2}. This can be

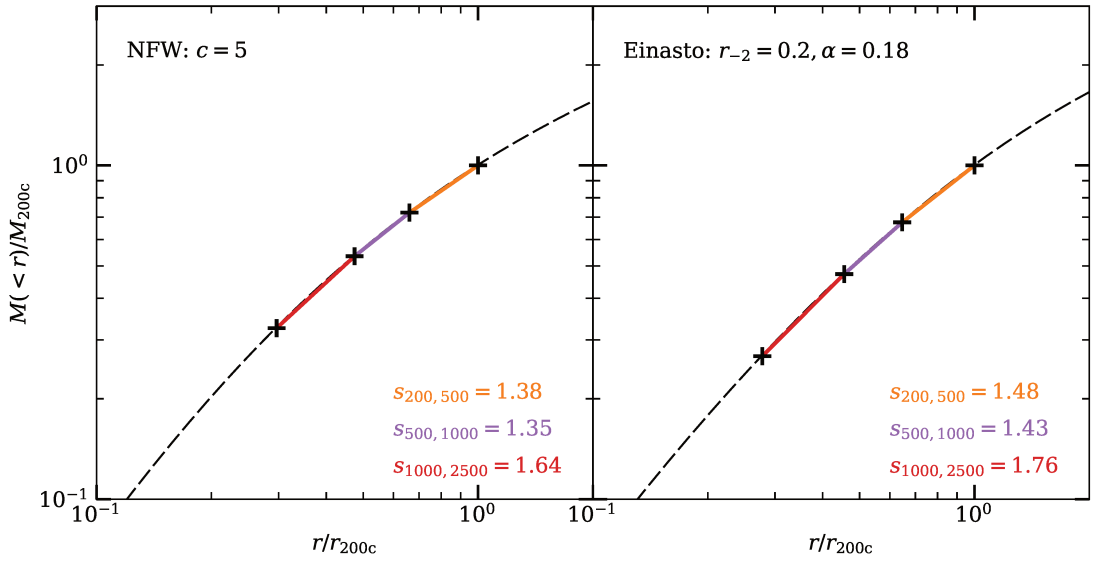

Figure 3.1: Dark matter halo profiles locally approximated using power law profiles calculated from their sparsity. Both halo profiles are computed for a mass $M_{200c} = 10^{14}h^{-1}\mathrm{M}_\odot$. From left to right in each subplot, the black crosses mark the position of M_{2500c}, M_{1000c}, M_{500c}, and M_{200c}.

shown simply by rearranging the definition of sparsity,

$$s_{\Delta_1,\Delta_2} = \frac{M_{\Delta_1}}{M_{\Delta_2}} = \frac{M_{\Delta_1} - M_{\Delta_2}}{M_{\Delta_2}} + 1 = \frac{\Delta M}{M_{\Delta_2}} + 1, \tag{3.2}$$

which can be used to give qualitative insight as to how mass is distributed within a halo.

This view can be further refined into a second interpretation by relating sparsity to the local logarithmic slope of the mass profile between M_{Δ_1} and M_{Δ_2},

$$\gamma = \frac{\ln M_{\Delta_1} - \ln M_{\Delta_2}}{\ln r_{\Delta_1} - \ln r_{\Delta_2}}. \tag{3.3}$$

We can easily show that this quantity,

$$\gamma = \frac{3\log_{10}(s_{\Delta_1,\Delta_2})}{\log_{10}(\Delta_2/\Delta_1) + \log_{10}(s_{\Delta_1,\Delta_2})}, \tag{3.4}$$

can be expressed solely as a function of the sparsity. Focusing on the physical range $s_{\Delta_1,\Delta_2} > 1$, we see that the slope is contained withing the range $0 < \gamma < 3$. The upper bound implies that the spherically averaged density should be monotonously decreasing, with $M(r) \propto r^3$ implying constant density. The lower bound implies that the mass within a radius r is monotonously growing, note that this is not incompatible with profiles with a convergent mass. Generally, these conditions are always fulfilled by dark matter haloes. In Fig. 3.1 we use Eq. (3.2) and Eq. (3.4) to locally approximate both an NFW profile and an Einasto profile. We see that four mass measurements, in this case M_{2500c}, M_{1000c}, M_{500c}, and M_{200c} are already able to obtain a reasonable approximation for the shape of both the NFW and the Einasto profile.

As sparsities are defined as ratios, these statistics are not all independent being linked through a chain rule,

$$s_{\Delta_1,\Delta_2} = \frac{M_{\Delta_1}}{M_{\Delta_2}} = \frac{M_{\Delta_1}}{M_{\Delta_3}}\frac{M_{\Delta_3}}{M_{\Delta_2}} = \frac{s_{\Delta_1,\Delta_3}}{s_{\Delta_2,\Delta_3}}. \tag{3.5}$$

Moreover, while by convention we choose $\Delta_1 < \Delta_2$, even if this is not the case we can always manipulate the sparsity, $s_{\Delta_1,\Delta_2} = 1/s_{\Delta_2,\Delta_1}$, to make ensure this convention is respected. It is worth noting that due to these two properties, given a set of n masses, we can only obtain $n-1$ independent sparsities in total. Although, formally with n masses one can compute $N_s = \binom{n}{2} = \frac{n!}{2(n-2)!}$ sparsities, one can express most of these as a function of a restricted set of $n-1$, which can, by convention, be chosen to be $\mathbf{s} = \{s_{\Delta_1,\Delta_2}, s_{\Delta_2,\Delta_3}, \dots, s_{\Delta_i,\Delta_j}, \dots, s_{\Delta_{n-1},\Delta_n}\}$, where we successively increment the values of the overdensity contrast $\Delta_1 < \Delta_2 < \cdots < \Delta_n$. This can in fact be seen in Fig. 3.1 where given the four masses, we only employ three sparsities to reproduce the mass profiles, when we could in theory use up to six.

3.2 Density profile - halo sparsity relations

Despite the simple definition of sparsity, we see that this statistics already holds a substantial amount of information about the profile of dark matter haloes and that this information can be refined by using multiple sparsities in tandem. We now turn our interest towards the ability of sparsity to unify prior quantifications of the internal structure of haloes. As its definition does not require any prior assumption on a given profile shape, we can define this statistic for any physical profile. In the following, we will be particularly interested in relating a given set of sparsities to the parameters of fitted profiles, in particular the NFW and Einasto profiles.

3.2.1 Sparsity of the NFW profile

To relate the NFW concentration parameter, which we define here as $c = c_{200c} := r_s/r_{200c}$, to sparsity we simply need to inject the analytical form of the mass M_Δ, as given by Eq. (2.123), into the definition of sparsity,

$$s_{\Delta_1,\Delta_2} = \frac{\ln\left(1+\frac{r_{\Delta_1}}{r_s}\right) - \frac{r_{\Delta_1}}{r_s}\frac{1}{1+r_{\Delta_1}/r_s}}{\ln\left(1+\frac{r_{\Delta_2}}{r_s}\right) - \frac{r_{\Delta_2}}{r_s}\frac{1}{1+r_{\Delta_2}/r_s}}. \tag{3.6}$$

This equation can be significantly simplified by removing the explicit dependence on the radii, which is acheived by fixing $\Delta_1 = 200$, $\Delta_2 = \Delta$, and introducing $y_\Delta = r_\Delta/r_{200c}$, such that $s_{200,\Delta} = \frac{200}{\Delta} y_\Delta^{-3}$, and

$$y_\Delta^3 \frac{\Delta}{200} = \frac{\ln(1+cy_\Delta) - \frac{cy_\Delta}{1+cy_\Delta}}{\ln(1+c) - \frac{c}{1+c}}, \tag{3.7}$$

which can then be solved numerically given a value of c (Balmès et al., 2014). Note that, although this equation can only be solved to obtain $s_{200,\Delta}$, using the chain rule we can in practice use this equation to calculate any sparsity, even for $\Delta < 200$ if we temporarily forgo the indexing convention, by simply solving this equation twice.

In Fig. 3.2 we solve Eq. (3.7) for three overdensity contrasts, $\Delta = \{500, 1000, 2500\}$. We see that generally sparsity is a decreasing function of concentration. The latter

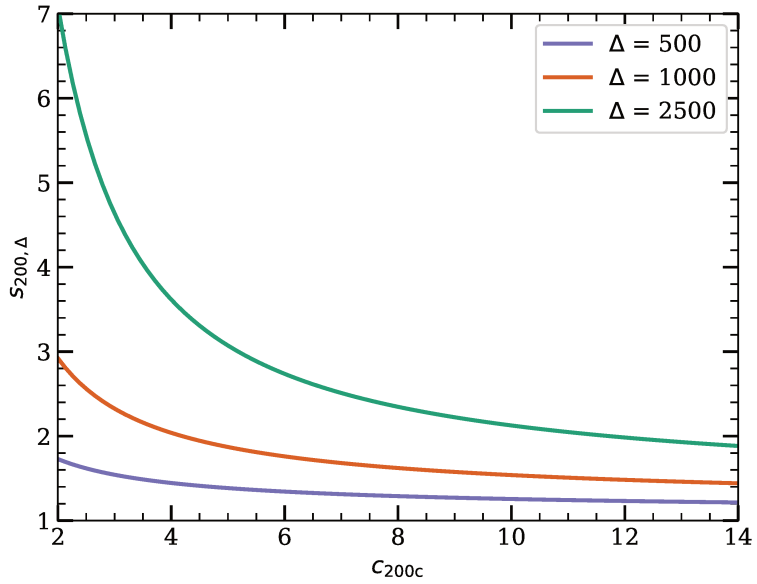

Figure 3.2: Three sparsities, $s_{200,500}$, $s_{200,1000}$, and $s_{200,2500}$, respectively the blue, orange and green lines, as a function of the NFW concentration parameter as obtain by solving Eq. (3.7).

decreases rapidly for small concentrations but slows significantly for larger concentrations. This behaviour justifies the name *sparsity*, indeed if a halo is less concentrated then it is more sparse. We also find that the sparsity is a monotonous function of the concentration meaning that formally we can define,

$$s_{\Delta_1,\Delta_2} = f_{\rm s}(c) \qquad \text{and} \qquad c = f_{\rm c}(s_{\Delta_1,\Delta_2}), \tag{3.8}$$

as respective inverse functions, although these are only defined for strictly positive concentrations, $c > 0$.

3.2.2 Sparsity of the Einasto profile

While in the case of the NFW profile the relation between concentration and sparsity is decoupled from mass, i.e only depending on the concentration, this is not a general feature when converting from profile parameters to sparsities. Indeed, repeating the same exercise with the Einasto profile one finds that the transformation to sparsity now depends on all three parameters of the profile,

$$s_{\Delta_1,\Delta_2} = f_{\rm s}(r_{-2}, \alpha, M_{200c}), \tag{3.9}$$

where we use M_{200c} to denote halo mass and calibrate $\rho_{-2}(r_{-2}, \alpha, M_{200c})$. This makes the transformation much more complex to use in practice, in addition to the non-analytical nature of the Einasto mass profile. In this configuration, several sets of parameters can yield the same sparsity, indicating that in principle this function is not invertible. To obtain a one to one mapping between sparsity and Einasto parameters we thus have to introduce additional sparsity measurements. Indeed, as long as the mass profile is not degenerate, meaning two different sets of parameters do not produce the exact same profile, then we can also expect the sparsities we measure to also not be degenerate.

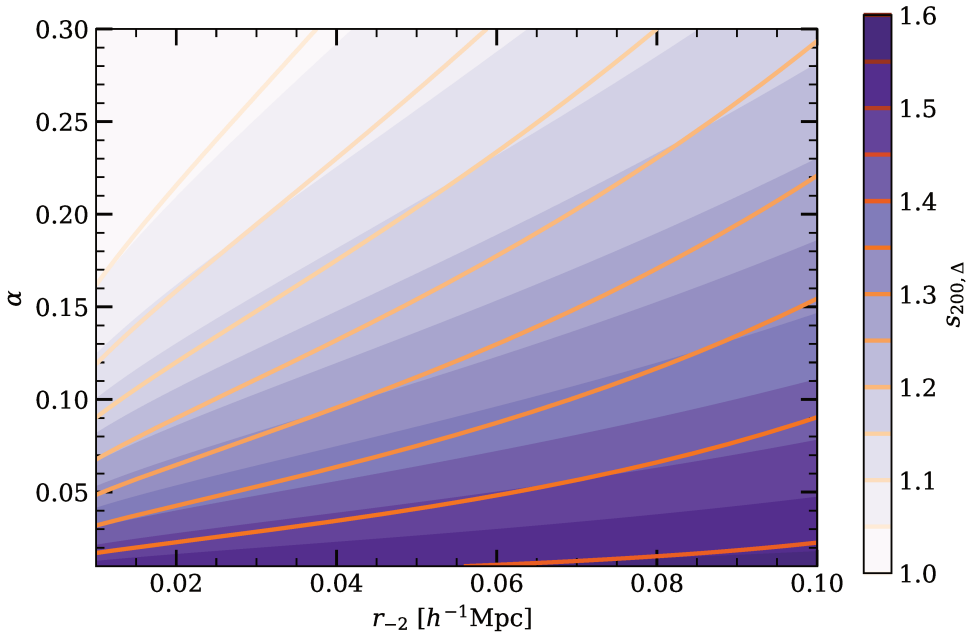

Figure 3.3: Sparsities, $s_{200,500}$ (purple filled contours) and $s_{500,1000}$ (orange contours), calculated assuming the Einasto profile with a mass $M_{200c} = 10^{14}h^{-1}\mathrm{M}_{\odot}$. The figures shows that the contours intersect and do not change at exactly the same rate. This small difference indicates that for every pair of parameters $(r_{-2},\ \alpha)$ corresponds a unique pair $(s_{200,500},\ s_{500,1000})$.

In Fig. 3.3 we calculate the sparsities $s_{200,500}$ and $s_{500,1000}$ for a range of Einasto shape parameters $(r_{-2},\ \alpha)$ fixing $M_{200c} = 10^{14}h^{-1}\mathrm{M}_{\odot}$, which we show respectively as purple and orange contours. While the effect is small, we can see that these contours intersect and as such do not have the exact same dependence on the parameters. This indicates that each unique pair $(r_{-2},\ \alpha)$ defines a unique pair $(s_{200,500},\ s_{500,1000})$, which in turn means we can indeed describe this profile simply using sparsities with an invertible mapping,

$$[s_{200,500},\ s_{500,1000}]^{\top} = \mathbf{f}_{\mathrm{s}}(r_{-2},\ \alpha;\ M_{200c}). \tag{3.10}$$

As such we can conclude that despite the simple definition of halo sparsity it is sufficient to accurately capture the range of profiles used to describe dark matter haloes. As such in the following we will now investigate some of the main properties of this statistic in more detail.

3.3 Statistical properties of s_{Δ_1,Δ_2}

We now move away from parametric profiles to investigate the statistical behaviour of sparsity in more detail. To do so we analyse the halo catalogues produced from the Uchuu simulation to get a detailed view of this behaviour before analysing the cosmology dependence with the e-MANTIS simulations spanning a wide range of cosmological models.

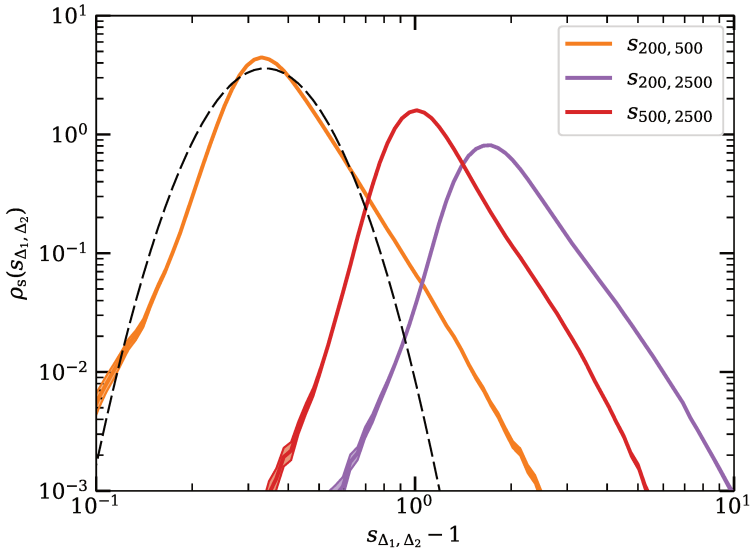

Figure 3.4: Marginal probability distribution functions for three sparsities, $s_{200,500}$, $s_{500,2500}$, and $s_{200,2500}$, respectively in orange, red and purple, estimated at $z = 0$. We see that these distributions are skewed towards large sparsities. The shaded area corresponds to the 95 per cent confidence region as estimate using 10^3 bootstrap iterations, while the dashed lines correspond to a log-normal distribution with the same scale and width as the distribution of $s_{200,500}$.

3.3.1 The distribution of sparsities

To start we turn our interest towards the marginal sparsity distribution, $\rho_s(s_{\Delta_1,\Delta_2})$. We estimate this distribution function for three sparsities, $s_{200,500}$, $s_{200,2500}$, and $s_{500,2500}$ using haloes with $M_{200c} > 10^{13}h^{-1}M_\odot$ in the Uchuu simulation. The resulting distributions, shown in Fig. 3.4, all present a similar shape, characterised by a single peak and strong tail towards large values. Indeed, we find this skewness towards large values of sparsity is a common feature for most sparsity. It is therefore worth noting that any statistic we measure using sparsity will be influenced by this skewness. For example: the mode, median and sample mean will be biased with respect to one another.

Overall we find that the distribution of sparsities is best described in terms of $\ln(s-1)$. To first approximation the peak can be described by a Gaussian distribution in this space as can be seen in Fig. 3.4 where we plot a Gaussian distribution with the same median and scale, as measured by the biweight midvariance, in terms of $\ln(s_{200,500}-1)$. Although, this does not properly account for the tails of the distribution, which are better described in terms of power-laws, this Gaussian model provides an acceptable first approximation to the measured distribution while respecting the physical boundary, $s_{\Delta_1,\Delta_2} > 1$.

3.3.2 Mass dependence

Let us now consider that the distribution may vary depending on the mass of the objects we are studying, as such we estimate the conditional sparsity distribution, $\rho_s(s_{\Delta_1,\Delta_2}|M_{200c})$, using the Uchuu catalogues. In Fig. 3.5, we see that the conditional sparsity distribution is also skewed towards large values and note that the mode of this distribution is increasing with mass. This increasing trend, of the order of 10 per cent

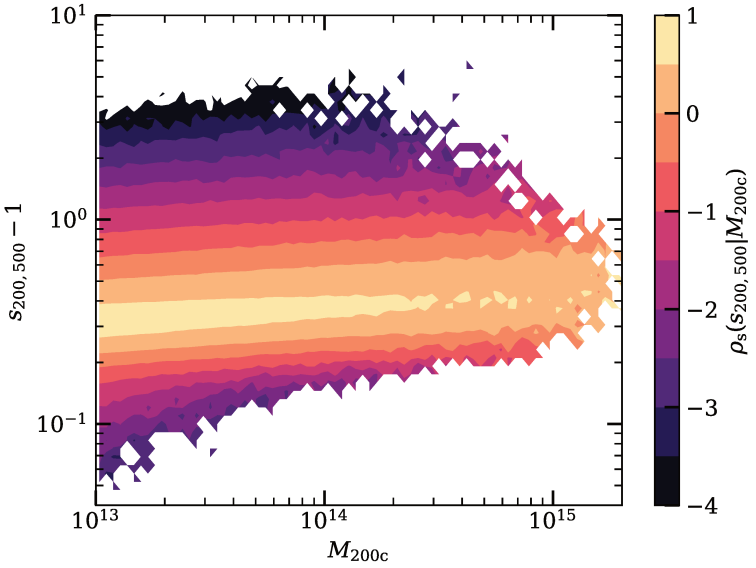

Figure 3.5: Conditional probability distribution functions $\rho_s(s_{200,500}|M_{200c})$. We see that there is a small mass dependence of the distribution with the peak shifting by approximately 10 per cent over 2 orders of magnitude.

over two orders of magnitude in mass, is consistent with models of the $c - M$ relation which predict that concentrations decrease, thus sparsities increase, with mass, although we do see that the variation in sparsity is both much smaller and simpler than the $c - M$ relation.

Considering that to first approximation, the sparsity distribution can be modelled as a Gaussian distribution of $\ln(s_{\Delta_1,\Delta_2} - 1)$. In Fig. 3.6 we measure the median and biweight midvariance, which we hereafter refer to as *the moments*, of the distribution after binning the haloes by mass. We choose to use these estimators due to their robustness to outliers as compared to the mean and standard deviation. We find that both the location and scale of the distribution increase with mass at $z = 0$. The behaviour of both statistics in logarithmic units is well approximated by a second order polynomial in $x = \log_{10}\left(\frac{M_{200c}}{10^{14}h^{-1}M_\odot}\right)$,

$$\log_{10}\{\lambda(\ln[s_{200,500} - 1]|M_{200c})\} = \alpha_\lambda x^2 + \beta_\lambda x + \gamma_\lambda, \tag{3.11}$$

where λ is a placeholder symbol for the moments and where the parameters of these power laws depending on redshift and cosmology. Naively measuring the median and biweight midvariance as a function of redshift we find that for the Uchuu simulation these moments are well approximated by,

$$\begin{cases} \alpha_{\rm med}(z) & = -0.0162z^4 + 0.0639z^3 - 0.0333z^2 - 0.0761z - 0.0186, \\ \beta_{\rm med}(z) & = -0.0334z^4 + 0.186z^3 - 0.267z^2 - 0.139z + 0.175, \\ \gamma_{\rm med}(z) & = 0.0044z^4 + 0.0322z^3 - 0.217z^2 + 0.251z - 0.866, \end{cases} \tag{3.12}$$

for the median and,

$$\begin{cases} \alpha_{\rm bw}(z) & -0.000567z^4 - 0.0111z^3 + 0.038z^2 - 0.0297z + 0.00327, \\ \beta_{\rm bw}(z) & -0.0158z^4 + 0.045z^3 - 0.0161z^2 - 0.0207z + 0.012, \\ \gamma_{\rm bw}(z) & -0.0116z^4 + 0.051z^3 - 0.0731z^2 + 0.0669z + 0.102, \end{cases} \tag{3.13}$$

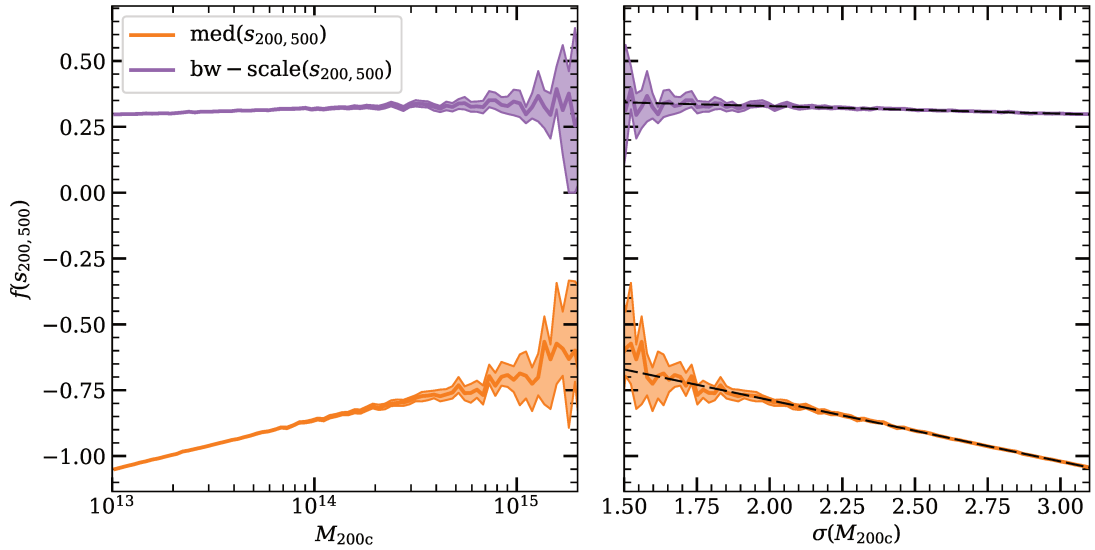

Figure 3.6: *Left panel:* Moments of the sparsity probability distribution function conditional to mass, $\rho_s(s_{200,500}|M_{200c})$. *Right panel:* Moments of the sparsity probability distribution function conditional to the linear variance of the density field smoothed over a length scale corresponding to a spherical top hat of mass M_{200c}, $\rho_s(s_{200,500}|\sigma\{M_{200c}\})$. Here we measure the location and scale of the distribution using the median and biweight mid-variance, as these are more robust than the sample mean and variance. The dashed lines in the right panel correspond to linear regressions.

for the biweight midvariance. We find that at intermediate reshift, $z \simeq 0.5$, the median sparsity exhibits a peak around $M_{200c} = 10^{14}h^{-1}\mathrm{M}_\odot$ and at higher, $z \gtrsim 1$ redshifts the slope inverts, making the median sparsity a decreasing function of mass. This is consistent with description of the $c-M$ relation in Uchuu (Ishiyama et al., 2021), which was also found to exhibit a turn over at higher redshifts.

As a first test, analogously to parameterisations of the HMF, we can describe the behaviour of the distribution in terms of $\sigma(M_{200c})$, the variance of the linear density field at the mass scale M_{200c}. Doing so we find that the moments can be, to very good approximation as shown in Fig. 3.6, expressed as second order polynomials,

$$\log_{10}\{\lambda(\ln[s_{200,500}-1]|M_{200c})\} = \alpha_\lambda\sigma^2 + \beta_\lambda\sigma + \gamma_\lambda. \tag{3.14}$$

in such a form, constant parameters, with respect to redshift and cosmology, would indicate that there is an underlying universal description of the internal structure of haloes. However, we find that this is not the case and that the parameters of these linear regression do depend strongly on redshift and cosmology.

3.3.3 Cosmology dependence

Briefly returning to the marginal sparsity distribution, we find that the cosmology dependence manifests as a shifting of the mode. Indeed, in Fig. 3.7 we see that changing the cosmological parameters causes the distribution to shift to higher or lower values of s_{Δ_1,Δ_2}. We see that the distribution is particularly correlated with Ω_m and σ_8, specifically it is correlated with the amplitude of matter fluctuations parameter, $S_8 = \sigma_8\sqrt{\Omega_\mathrm{m}/0.3}$. Lower values of S_8 will produce higher sparsities on average in op-

position to high values of S_8 will produce lower sparsities. In addition, we find that sparsity is also correlated to the n_s parameter and only weakly dependent on H_0.

Regarding the conditional distribution, we observe similar trends with for example S_8 producing on average lower or higher sparsities. However, we also see that these shifts do not affect all masses in the same way resulting in a change in the slope, $\alpha_{\rm med}$, of the median. A possible interpretation, is that the sparsity correlates with the formation time of haloes, similarly to the description of the concentration by Zhao et al. (2009). This would, in theory, indicate that any cosmological parameter which affects the formation time of haloes will leave a trace in the sparsities. This interpretation also has implications for beyond ΛCDM cosmologies, meaning that any alteration that impacts the formation time of haloes could be constrained using sparsity. As such, sparsity could be used to constrain the dark energy equation of state parameter, w, or possibly modified gravity scenarios (Corasaniti et al., 2020), in addition to extension that alter the profile directly such as dark matter self interactions or interference scale of dark matter condensates.

3.4 Relating s_{Δ_1,Δ_2} to the halo mass function

In the previous section we have seen that sparsity is best described in a statistical setting, i.e. in terms of a distribution rather than a restricted set of moments. Here we will present how this statistical point of view allows us to relate the distribution of sparsities and the halo mass function.

3.4.1 Algebra with random variates

In the following we are going to treat halo properties, masses and sparsities, as random variates. In this context, the properties of an individual halo will simply be a realisation of these variates which are drawn from their respective probability distribution functions (PDF). In particular, we are going to be applying algebraic operations on these random variates. However, before doing so, let us first recall how algebraic operations on random variates also sets relations between their respective PDFs.

Let X and Y be two random variates drawn respectively from $\rho_x(x)$ and $\rho_y(y)$, and related through a deterministic function, $Y = f(X)$. Due to the conservation of probability, $\rho_y(y)\mathrm{d}y = \rho_x(x)\mathrm{d}x$, we can relate the two PDFs:

$$\rho_y(y) = \rho_x(f^{-1}(y)) \left| \frac{\mathrm{d}f^{-1}}{\mathrm{d}y} \right|, \tag{3.15}$$

assuming the transformation is invertible.

Here, we are interested in transformations involving two random variates: $Z = f(X,Y)$. However, relating the PDF of Z to the joint distribution, $\rho_{xy}(x,y)$ of X and Y, requires additional thought compared to the one-dimensional case. In most cases the function $f(X,Y)$ will not be invertible. Nonetheless, this can be circumvented through the introduction of a fourth variable W. We define two column vectors,

$$\begin{bmatrix} Z \\ W \end{bmatrix} = \mathbf{f}(X,Y) = \begin{bmatrix} f_Z(X,Y) \\ f_W(X,Y) \end{bmatrix} \tag{3.16}$$

and

$$\begin{bmatrix} X \\ Y \end{bmatrix} = \mathbf{g}(Z,W) = \begin{bmatrix} g_X(Z,W) \\ g_Y(Z,W) \end{bmatrix}, \tag{3.17}$$

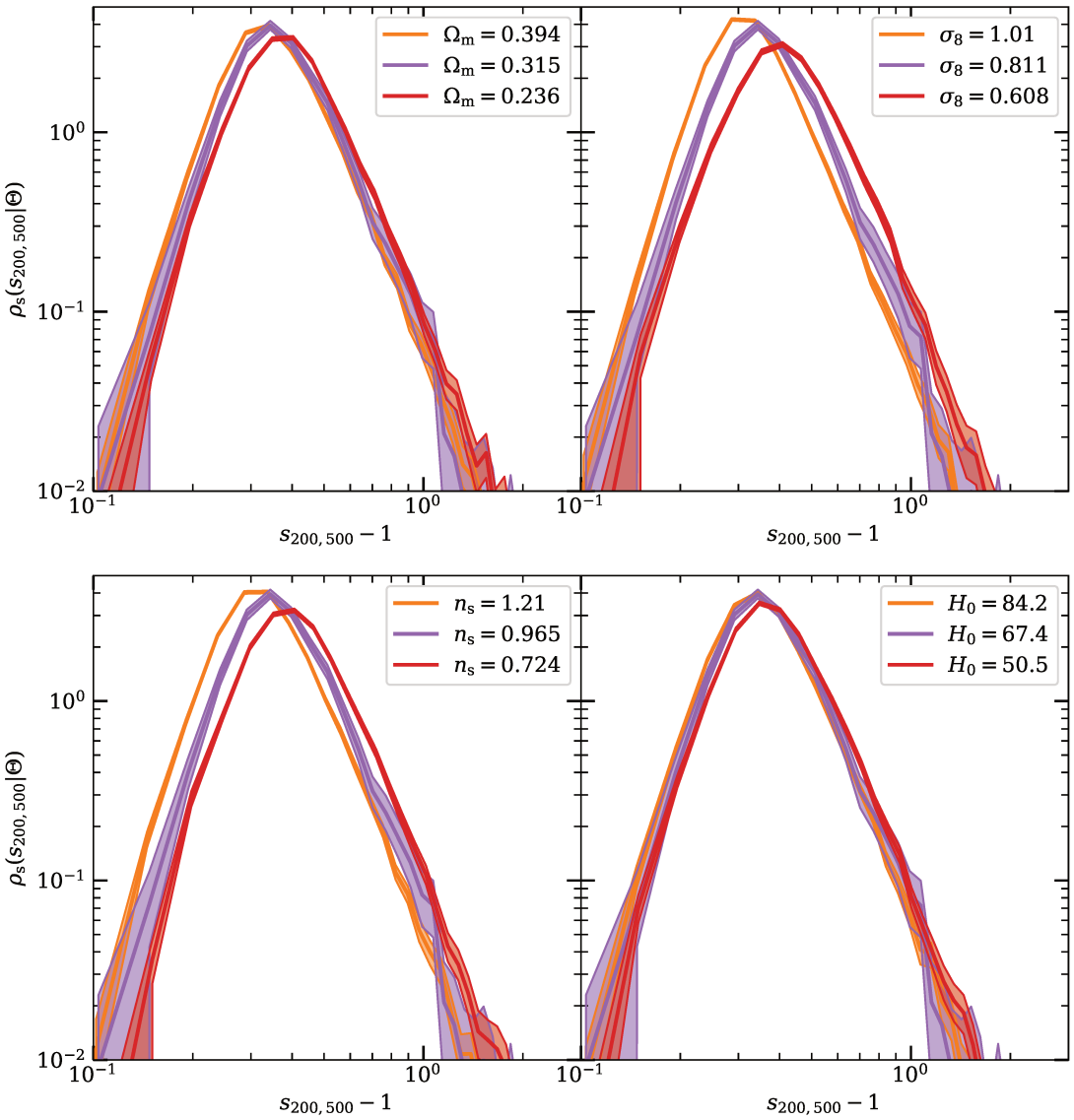

Figure 3.7: Variation of the marginal sparsity distribution as a function of four cosmological parameters, Ω_m, σ_8, n_s, and H_0. We see that the primary effect each parameter has is shifting the mode of the distribution to larger or smaller sparsities.

as the transformations between these variables. Through the conservation of probability, the joint distribution, $\rho_{zw}(Z, W)$, can be written as

$$\rho_{zw}(z, w) = \rho_{xy}[g_X(z, w), g_Y(z, w)] \begin{vmatrix} \partial_z g_X & \partial_w g_X \\ \partial_z g_Y & \partial_w g_Y \end{vmatrix}. \tag{3.18}$$

The distribution for Z can then be obtained by marginalising over W:

$$\rho_z(z) = \int \rho_{zw}(z, w) \mathrm{d}w. \tag{3.19}$$

In this work we are particularly interested in the PDF of the product, $Z = XY$, and ratio, $Z = X/Y$, of two random variables. In the case of the product, we define

$$\begin{bmatrix} Z \\ W \end{bmatrix} = \begin{bmatrix} XY \\ Y \end{bmatrix} \text{ and } \begin{bmatrix} X \\ Y \end{bmatrix} = \begin{bmatrix} Z/W \\ W \end{bmatrix} \tag{3.20}$$

as the transformation between the four random variables. We can then write

$$\rho_z(z) = \int \frac{1}{|w|} \rho_{xy}(z/w, w) \mathrm{d}w, \tag{3.21}$$

the PDF of Z. The ratio $Z = X/Y$ similarly leads to

$$\begin{bmatrix} Z \\ W \end{bmatrix} = \begin{bmatrix} X/Y \\ Y \end{bmatrix} \text{ and } \begin{bmatrix} X \\ Y \end{bmatrix} = \begin{bmatrix} ZW \\ W \end{bmatrix}, \tag{3.22}$$

resulting in the ratio distribution

$$\rho_z(z) = \int |w| \rho_{xy}(zw, w) \mathrm{d}w. \tag{3.23}$$

3.4.2 Changing halo mass definition

We have seen in Section 2.6 that the mass of a halo can be seen as a random variate, specifically we saw that this interpretation could be used to predict the overall shape of the HMF, making the HMF the distribution function of halo masses. Thus, let us consider that we have two halo masses, M_{Δ_1} and M_{Δ_2}, each drawn from their respective HMF, $\mathrm{d}n/\mathrm{d}M_{\Delta_1}$ and $\mathrm{d}n/\mathrm{d}M_{\Delta_2}$, which we want to relate.

Introducing the sparsity, s where for simplicity we drop the indices, drawn from the distribution $\rho_\mathrm{s}(s|M_{\Delta_1})$ which we have briefly described in Section 3.3.2. Then, considering the algebraic relation, $M_{\Delta_2} = M_{\Delta_1}/s$, we can simply use Eq. (3.23) to express the relation between both HMF as a ratio distribution,

$$\frac{\mathrm{d}n}{\mathrm{d}M_{\Delta_2}}(M_{\Delta_2}) = \int_1^\infty s\, \rho_\mathrm{s}(s|sM_{\Delta_2}) \frac{\mathrm{d}n}{\mathrm{d}M_{\Delta_1}}(sM_{\Delta_2})\, \mathrm{d}s, \tag{3.24}$$

which we will refer to as the inwards transformation. If instead we want to express the HMF of the outer mass as a function of that of the inner mass, then again using sparsity we can define the algebraic relation, $M_{\Delta_1} = sM_{\Delta_2}$, between the random variates and therefore express the relation between the three PDFs as a product distribution,

$$\frac{\mathrm{d}n}{\mathrm{d}M_{\Delta_1}}(M_{\Delta_1}) = \int_1^\infty \frac{1}{s} \rho_\mathrm{s}(s|M_{\Delta_1}/s) \frac{\mathrm{d}n}{\mathrm{d}M_{\Delta_2}}(M_{\Delta_1}/s) \mathrm{d}s, \tag{3.25}$$

which we refer to as the outward transformation, where s is here drawn from $\rho_\mathrm{s}(s|M_{\Delta_2})$. Therefore, given both Eq. (3.24) and Eq. (3.25) we can transform the HMF to any overdensity contrast as long as we know the HMF for at least one mass definition and have a description for the distribution of halo sparsities.

3.4.3 Validation with N-body halo mass functions

Given these relations, we now test their accuracy using the halo catalogues from the Uchuu simulation. In Fig. 3.8 we plot the HMF for three mass definitions with the shaded areas marking the 68 per cent confidence interval around the HMF as measured using 10^3 bootstrap iterations. We use Eq. (3.24) and Eq. (3.25) to convert each HMF from one mass definition to the others using the distributions of sparsities measured directly from the haloes.

First, not making any approximations on $\rho_{\rm s}$, that is using the full conditional sparsity distribution, we find that the relations are exact and we indeed see that the reconstructed HMF, marked by solid lines, recover the measured HMF within the statistical uncertainty. Nonetheless, we notice that the outward reconstructions are severely dampened at the low mass end. This effect results from Eq. (3.25) where we should, in theory, integrate the HMF down to arbitrarily small masses. This is not possible in practice where the HMF is truncated at the low mass end due to selection effects. We see that this does not affect the inward reconstruction as in this case we are integrating out to arbitrarily large masses and are therefore shielded by the exponential cutoff of the HMF at the high mass end.

If we now repeat this test but replace the full sparsity distribution $\rho_{\rm s}(s|M_\Delta)$ by the marginalised distribution $\rho_{\rm s}(s)$, we obtain the dashed lines shown in Fig. 3.8. We see that overall this proves to be a poor approximation, exceeding the 10 per cent error level, with the reconstructed HMFs being considerably offset from the measured HMF, this is particularly the case for the innermost mass, $M_{2500{\rm c}}$. We see that when using a sparsity distribution that is independent of mass, the HMFs we recover more closely resemble the shape of the HMF we are using to perform the reconstruction. A consequence of this is that inward reconstructions are underestimated at low masses and overestimated at high masses, while the opposite is seen for outward reconstructions which are overestimated at low masses and underestimated at high masses.

3.4.4 Approximate expressions

The formalism introduced here provides a general framework to understand the relation between the HMF and internal structure of haloes. We can in fact show that these relations are the generalisation of mass definition conversions previously suggested in the literature.

For example, Bocquet et al. (2016) and Ragagnin et al. (2021) convert the mass definition using:

$$\frac{{\rm d}n}{{\rm d}M_{\Delta_2}} \equiv \frac{{\rm d}n}{{\rm d}M_{\Delta_1}}\frac{{\rm d}M_{\Delta_1}}{{\rm d}M_{\Delta_2}} = \left[\frac{\rho_m}{M_{\Delta_2}^2}\frac{{\rm d}\ln\sigma^{-1}}{{\rm d}\ln M_{\Delta_2}} f_{\Delta_1}(\sigma)\right]\frac{M_{\Delta_2}}{M_{\Delta_1}}. \tag{3.26}$$

If we consider our formalism, specifically the inwards reconstruction of Eq. 3.24, assuming that the sparsity distribution is highly peaked around the mean value,

$$\rho_{\rm s}(s|M_{\Delta_1}) \simeq \delta_{\rm D}\left[s - \langle s_{\Delta_1,\Delta_2}\rangle(M_{\Delta_1})\right]. \tag{3.27}$$

We obtain a simplified transformation,

$$\frac{{\rm d}n}{{\rm d}M_{\Delta_2}} = s_0\frac{{\rm d}n}{{\rm d}M_{\Delta_1}}(s_0 M_{\Delta_2}), \tag{3.28}$$

where s_0 is the root of the argument of the Dirac distribution, $s_0 - \langle s_{\Delta_1,\Delta_2}\rangle = 0$. If the mean sparsity does not vary significantly as function of the halo mass (i.e.

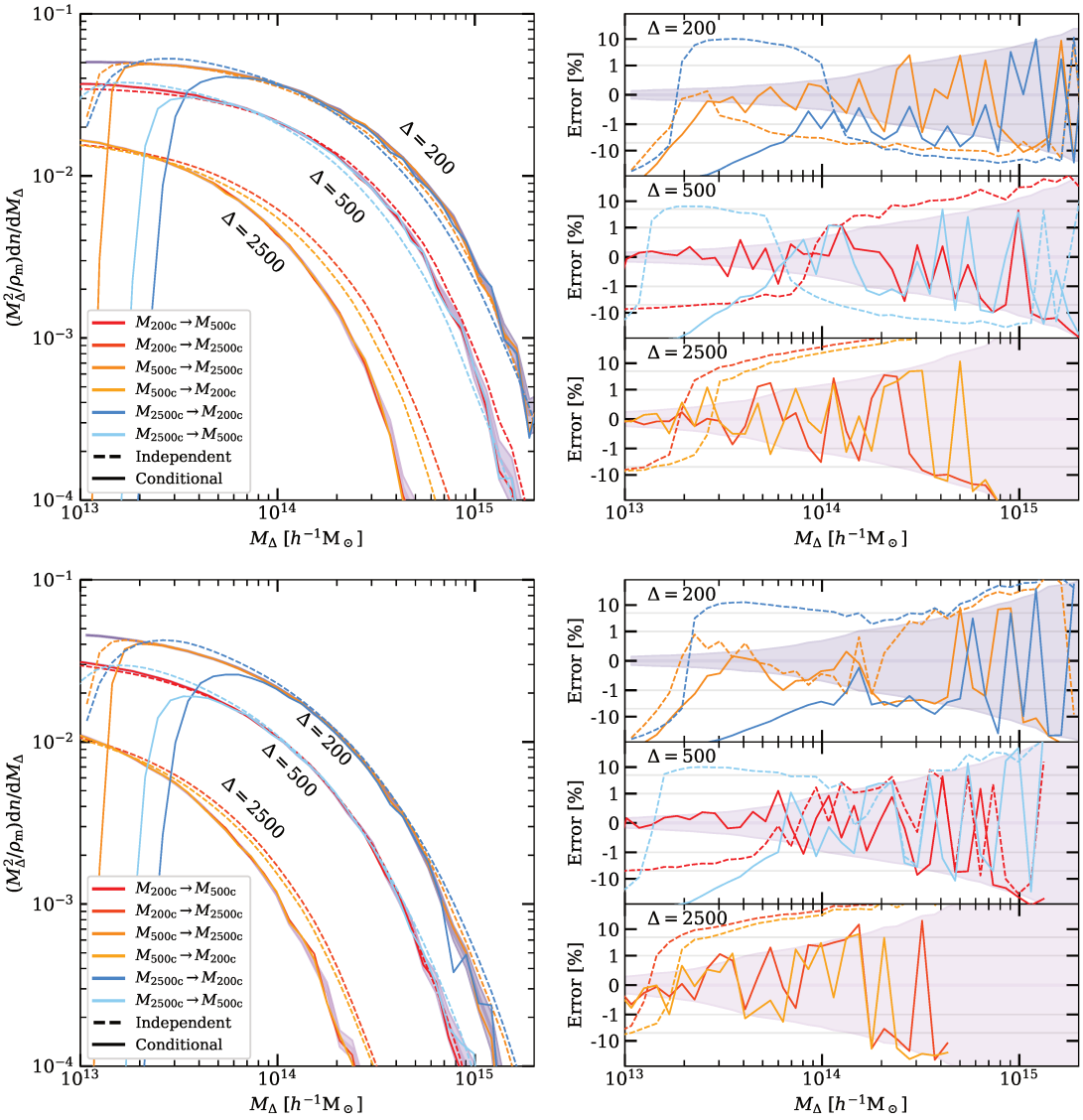

Figure 3.8: Comparison of the accuracy of the mass dependent HMF transfer formalism with the marginalised formalism. The latter provides poor reconstructions while accounting for the mass dependence results with predictions that are exact to the level of statistical uncertainty. Left panel: Estimated HMFs (purple shaded area) at $z = 0$ (top panels) and $z = 0.5$ (bottom panels) from the Uchuu halo catalogues for overdensities $\Delta = 200$, 500, and 2500 (in units of the critical density) plotted against the inward ($200 \to 500$, $200 \to 2500$, and $500 \to 2500$) and outward ($2500 \to 500$, $2500 \to 200$, and $500 \to 200$) reconstructed HMFs from Eq. (3.24) and Eq. (3.25), respectively, assuming the marginal sparsity distribution (dashed lines) and conditional distribution (solid lines). Right panels: Relative error between the reconstructions and the measured HMF at $\Delta = 200$ (top panel), $\Delta = 500$ (mid panel), and $\Delta = 2500$ (bottom panel). The shaded areas around the measured HMFs represents the statistical error on the measurement estimated as the standard deviation over 10^3 bootstrap iterations.

$\mathrm{d}\langle s_{\Delta_1,\Delta_2}\rangle/\mathrm{d}M_{\Delta_1} \simeq 0$), then $s_0 \simeq \langle s_{\Delta_1,\Delta_2}\rangle$. Thus we can show,

$$\begin{aligned}\frac{\mathrm{d}n}{\mathrm{d}M_{\Delta_2}} &= \langle s_{\Delta_1,\Delta_2}\rangle \frac{\mathrm{d}n}{\mathrm{d}M_{\Delta_1}}(\langle s_{\Delta_1,\Delta_2}\rangle M_{\Delta_2}) \\ &= \langle s_{\Delta_1,\Delta_2}\rangle \frac{\rho_\mathrm{m}}{\langle s_{\Delta_1,\Delta_2}\rangle^2 M_{\Delta_2}} \frac{\mathrm{d}\ln\sigma^{-1}}{\mathrm{d}\ln\langle s_{\Delta_1,\Delta_2}\rangle M_{\Delta_2}^2} f_{\Delta_1}\left[\sigma\left(\langle s_{\Delta_1,\Delta_2}\rangle M_{\Delta_2}\right)\right] \\ &= \frac{1}{\langle s_{\Delta_1,\Delta_2}\rangle}\frac{\rho_\mathrm{m}}{M_{\Delta_2}^2}\frac{\mathrm{d}\ln\sigma^{-1}}{\mathrm{d}\ln M_{\Delta_2}} f_{\Delta_1}\left[\sigma\left(\langle s_{\Delta_1,\Delta_2}\rangle M_{\Delta_2}\right)\right] \\ &= \left\langle\frac{M_{\Delta_2}}{M_{\Delta_1}}\right\rangle \frac{\rho_\mathrm{m}}{M_{\Delta_2}^2}\frac{\mathrm{d}\ln\sigma^{-1}}{\mathrm{d}\ln M_{\Delta_2}} f_{\Delta_1}\left[\sigma\left(\left\langle\frac{M_{\Delta_1}}{M_{\Delta_2}}\right\rangle M_{\Delta_2}\right)\right].\end{aligned} \tag{3.29}$$

This result is similar to the conversion shown in Eq. 3.26, with the only major difference being the presence of the expectation value. In fact, we can show that a similar solution holds when performing an outwards reconstruction. Indeed, under the same assumptions Eq. (3.25) becomes,

$$\frac{\mathrm{d}n}{\mathrm{d}M_{\Delta_1}} = \frac{1}{s_0}\frac{\mathrm{d}n}{\mathrm{d}M_{\Delta_2}}\left(\frac{M_{\Delta_1}}{s_0}\right) \simeq \frac{1}{\langle s_{\Delta_1,\Delta_2}\rangle}\frac{\mathrm{d}n}{\mathrm{d}M_{\Delta_2}}\left(\frac{M_{\Delta_1}}{\langle s_{\Delta_1,\Delta_2}\rangle}\right), \tag{3.30}$$

which can again be expanded into,

$$\begin{aligned}\frac{\mathrm{d}n}{\mathrm{d}M_{\Delta_1}} &= \langle s_{\Delta_1,\Delta_2}\rangle \frac{\rho_\mathrm{m}}{M_{\Delta_1}^2}\frac{\mathrm{d}\ln\sigma^{-1}}{\mathrm{d}\ln M_{\Delta_1}} f_{\Delta_2}\left[\sigma\left(\frac{M_{\Delta_1}}{\langle s_{\Delta_1,\Delta_2}\rangle}\right)\right] \\ &= \left\langle\frac{M_{\Delta_1}}{M_{\Delta_2}}\right\rangle \frac{\rho_\mathrm{m}}{M_{\Delta_1}^2}\frac{\mathrm{d}\ln\sigma^{-1}}{\mathrm{d}\ln M_{\Delta_1}} f_{\Delta_2}\left[\sigma\left(\left\langle\frac{M_{\Delta_2}}{M_{\Delta_1}}\right\rangle M_{\Delta_1}\right)\right],\end{aligned} \tag{3.31}$$

to recover a formula closely resembling Eq. (3.26).

Another interesting consequence of the formalism presented here is that it allows to unify seemingly distant results. For instance, Eq. (3.24) can also serve as a starting point from which we can derive the seminal equation,

$$\int_{\ln M_\mathrm{i}}^{\ln M_\mathrm{f}} \frac{\mathrm{d}n}{\mathrm{d}M_{\Delta_2}}\mathrm{d}\ln M_{\Delta_2} = \langle s\rangle \int_{\ln\langle s\rangle M_\mathrm{i}}^{\ln\langle s\rangle M_\mathrm{f}} \frac{\mathrm{d}n}{\mathrm{d}M_{\Delta_1}}\mathrm{d}\ln M_{\Delta_1}, \tag{3.32}$$

first introduced by Balmès et al. (2014) to predict the mean sparsity of a sample of clusters and perform cosmological inferences (see Corasaniti et al., 2018, 2021, 2022), where the masses, M_i and M_f, in the integration bounds are free parameters that are adapted to the cluster sample.

Assuming that the sparsity distribution does not vary significantly with mass between M_i and M_f, we can write Eq. (3.24),

$$\frac{\mathrm{d}n}{\mathrm{d}M_{\Delta_2}} = \int_1^\infty s\rho_\mathrm{s}(s)\frac{\mathrm{d}n}{\mathrm{d}M_{\Delta_1}}(sM_{\Delta_2})\mathrm{d}s \tag{3.33}$$

in terms of the marginal sparsity distribution $\rho_\mathrm{s}(s)$, where we have dropped the indices on the sparsity variable for ease of reading. Integrating both sides this equation,

$$\int_{\ln M_\mathrm{i}}^{\ln M_\mathrm{f}} \frac{\mathrm{d}n}{\mathrm{d}M_{\Delta_2}}\mathrm{d}\ln M_{\Delta_2} = \int_1^\infty s\rho_\mathrm{s}(s)\int_{\ln M_\mathrm{i}}^{\ln M_\mathrm{f}} \frac{\mathrm{d}n}{\mathrm{d}M_{\Delta_1}}(sM_{\Delta_2})\mathrm{d}\ln M_{\Delta_2}\mathrm{d}s, \tag{3.34}$$

redefining $M_{\Delta_1} = sM_{\Delta_2}$,

$$\int_{\ln M_\mathrm{i}}^{\ln M_\mathrm{f}} \frac{\mathrm{d}n}{\mathrm{d}M_{\Delta_2}} \mathrm{d}\ln M_{\Delta_2} = \int_1^\infty s\rho_\mathrm{s}(s) \int_{\ln sM_\mathrm{i}}^{\ln sM_\mathrm{f}} \frac{\mathrm{d}n}{\mathrm{d}M_{\Delta_1}}(M_{\Delta_1})\mathrm{d}\ln M_{\Delta_1}\mathrm{d}s, \tag{3.35}$$

and assuming the sparsity distribution to be sharply peaked around the mean, $\rho_\mathrm{s} = \delta_\mathrm{D}(s - \langle s\rangle)$, we recover,

$$\int_{\ln M_\mathrm{i}}^{\ln M_\mathrm{f}} \frac{\mathrm{d}n}{\mathrm{d}M_{\Delta_2}} \mathrm{d}\ln M_{\Delta_2} = \langle s\rangle \int_{\ln\langle s\rangle M_\mathrm{i}}^{\ln\langle s\rangle M_\mathrm{f}} \frac{\mathrm{d}n}{\mathrm{d}M_{\Delta_1}} \mathrm{d}\ln M_{\Delta_1}. \tag{3.36}$$

the desired expression.

Here, we have seen that through the use of sparsity we have been able to unify several previously distant results under two more general equations. We have also shown that this unified sparsity formalism allows us to derive new results, such as Eq. (3.28) and Eq. (3.30), which can be seen as mass dependent alternatives to Eq. (3.32). More importantly, we have shown that it is information about the internal stucture of haloes, through sparsity, which governs this generalised transformation.

3.5 Sparsity statistics and profile parameters

In Section 3.2 we have seen that sparsity can be used as a non-parametric quantification of the density profiles of dark matter haloes. Moreover, we have shown that it is possible to map a given set of halo sparsities into a set of parameters if we assume a shape for the profile. In Section 3.4, we have also shown that the distribution of sparsities can be used to relate two HMF a different overdensities. In this section we will merge both these results. First, by extending the relation between sparsities and profile parameters to distributions of sparsities and distribution of profile parameters. Secondly, we will examine how Eq. (3.24) and Eq. (3.25) can be used to relate the HMF to models of the $c - M$ relation and even predict the latter.

3.5.1 Sparsity distributions from parametric models

Lets us begin by considering the $c - M$ relation for the NFW density profile. Usually referring to a single value, $c(M_{\Delta_1}, z, \boldsymbol{\Theta})$[1], it is commonly accepted that concentrations are scattered around this relation. This distribution of concentrations is typically modelled with a log-normal density function, $\rho_\mathrm{c}(c|M_{\Delta_1})$, of which the mean is given by the c-M relation and a width parameter $\sigma \simeq 0.25$ corresponding to a logarithmic standard deviation of 0.24 dex (see e.g. Bullock et al., 2001; Dolag et al., 2004; Macciò et al., 2007).

We have shown that for the NFW profile we can define, at least numerically, a one-to-one relation

$$s_{\Delta_1,\Delta_2} = f_\mathrm{s}(c) \qquad \text{and its inverse} \qquad c = f_\mathrm{c}(s_{\Delta_1,\Delta_2}), \tag{3.37}$$

between a single sparsity and concentration, as can be seen in Fig. 3.2. Injecting these into Eq. (3.15) we obtain,

$$\rho_\mathrm{s}(s_{\Delta_1,\Delta_2}|M_{\Delta_1}) = \rho_\mathrm{c}(f_\mathrm{c}(s_{\Delta_1,\Delta_2})|M_{\Delta_1}) \left|\frac{\mathrm{d}f_\mathrm{c}}{\mathrm{d}s}(s_{\Delta_1,\Delta_2})\right| \tag{3.38}$$

[1] $\boldsymbol{\Theta}$ designates additional parameters such as cosmology and astrophysics

the sparsity distribution corresponding to a concentration distribution. In Fig. 3.9 we plot as iso-contours the conditional sparsity distribution as function of M_{200c} obtained from the estimated sparsities of the Uchuu halo catalogue at $z = 0$ (top panel), the NFW sparsities obtained from the concentrations of the same haloes (middle panel), and the NFW sparsities predicted assuming a log-normal concentration distribution for which the mean is given by the concentration-mass relation measured from the analysis of Uchuu haloes (Ishiyama et al., 2021) and width parameter $\sigma = 0.25$ (bottom panel). The solid lines correspond to the mean values of the distributions, estimated from sparsities in red, from concentrations in orange, and in yellow from the log-normal distribution. We see that in all cases the distributions have very similar means, while there are some clear differences in the scatter. Indeed, we see that scatter in the low sparsity tail of the distribution estimated from measured concentration is considerably underestimated. Moreover, introducing the log-normal description of the $c-M$ relation results in the high sparsity tail also being suppressed, resulting in a distribution with much smaller scatter than what is seen in the simulation data.

If we now consider profiles with more than one shape parameter, such as the Einasto profile, the complexity of the transformation increases rapidly. We have seen in Section 3.2 each unique pair of Einasto parameters defines a unique pair of sparsities. As such, similarly to the NFW profile we can define an invertible mapping between sparsities and profile parameters. If we wish to translate the joint distribution of Einasto parameters, $\rho_{r_{-2},\alpha}$, into a joint sparsity distribution then we simply have to inject this mapping into Eq. (3.18).

If we only want to obtain the marginal distribution of a single sparsity, we can simplify this expression. Let us consider, in the formalism of Eq. (3.18) that $Z = s_{\Delta_1,\Delta_2}$, $X = r_{-2}$ and $W = Y = \alpha$. This choice considerably simplifies the Jacobian,

$$\rho_{\mathrm{s},\alpha} = \rho_{r_{-2},\alpha}[g_{r_{-2}}(s,\alpha),\alpha]\left|\partial_{\mathrm{s}} g_{r_{-2}}\right|, \tag{3.39}$$

while keeping the mapping invertible, although $g_{r_{-2}}(s,\alpha)$ still has to be estimated numerically. From this, the sparsity distribution can be obtained by marginalising over the second profile parameter,

$$\rho_{\mathrm{s}} = \int \rho_{r_{-2},\alpha}[g_{r_{-2}}(s,\alpha),\alpha]\left|\partial_{\mathrm{s}} g_{r_{-2}}\right| \mathrm{d}\alpha. \tag{3.40}$$

In principle, this methodology can be extended to any number of profile parameters, as long as one is able to find an invertible mapping between the parameters and sparsity and at the cost of computing an $n-1$ dimensional integral for a profile with n parameters.

3.5.2 $c-M$ relation and halo mass function conversions

Considering the HMF reconstruction equations presented in Section 3.4 and the transformation of the distribution of concentrations presented in Section 3.5.1, it is natural to assume that we can combine these expressions to obtain reconstruction formulae assuming a $c-M$ relation. As such, combining Eq, (3.38) with Eq. (3.24) and Eq. (3.25) leads to the inward,

$$\frac{\mathrm{d}n}{\mathrm{d}M_{\Delta_2}}(M_{\Delta_2}) = \int_1^\infty s\rho_{\mathrm{c}}(f_{\mathrm{c}}(s)|sM_{\Delta_2})\left|\frac{\mathrm{d}f_{\mathrm{c}}}{\mathrm{d}s}\right|\frac{\mathrm{d}n}{\mathrm{d}M_{\Delta_1}}(sM_{\Delta_2})\mathrm{d}s, \tag{3.41}$$

and outward,

$$\frac{\mathrm{d}n}{\mathrm{d}M_{\Delta_1}}(M_{\Delta_1}) = \int_1^\infty \frac{1}{s}\rho_{\mathrm{c}}(f_{\mathrm{c}}(s)|M_{\Delta_1}/s)\left|\frac{\mathrm{d}f_{\mathrm{c}}}{\mathrm{d}s}\right|\frac{\mathrm{d}n}{\mathrm{d}M_{\Delta_2}}(M_{\Delta_1}/s)\mathrm{d}s, \tag{3.42}$$

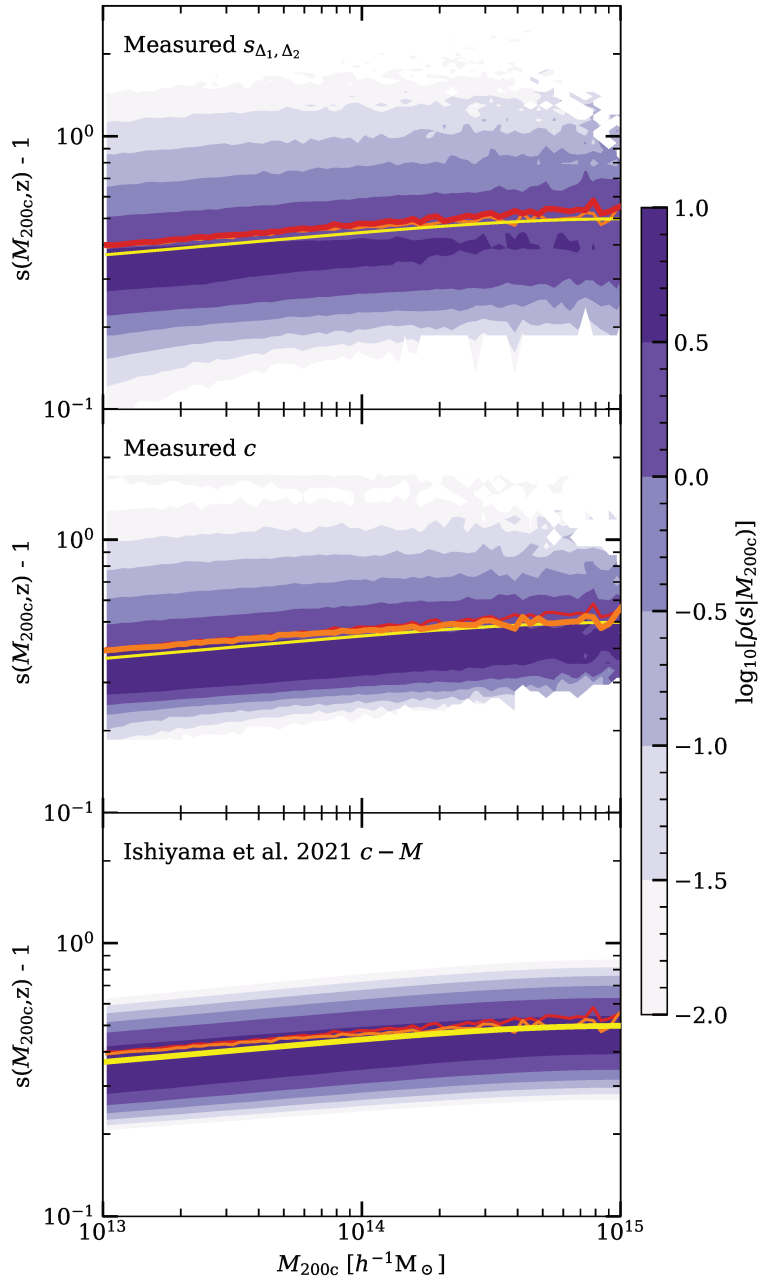

Figure 3.9: Iso-contours of the conditional density distribution of the halo sparsity, $\rho(s_{200,500}|M_{200c})$. Measurements are from the Uchuu halo catalogue at $z = 0$, (top panel), estimated from the distribution of measured concentrations (central panel), and predicted assuming a log-normal distribution of the concentration parameter for which the mean is given by the $c-M$ relation of Ishiyama et al. (2021) calibrated on the Uchuu catalogues and width parameter $\sigma = 0.25$ (bottom panel). The coloured lines correspond to the mean of the distribution of measured sparsities (red), and that inferred from the measured concentrations (orange) and from the log-normal distribution (yellow).

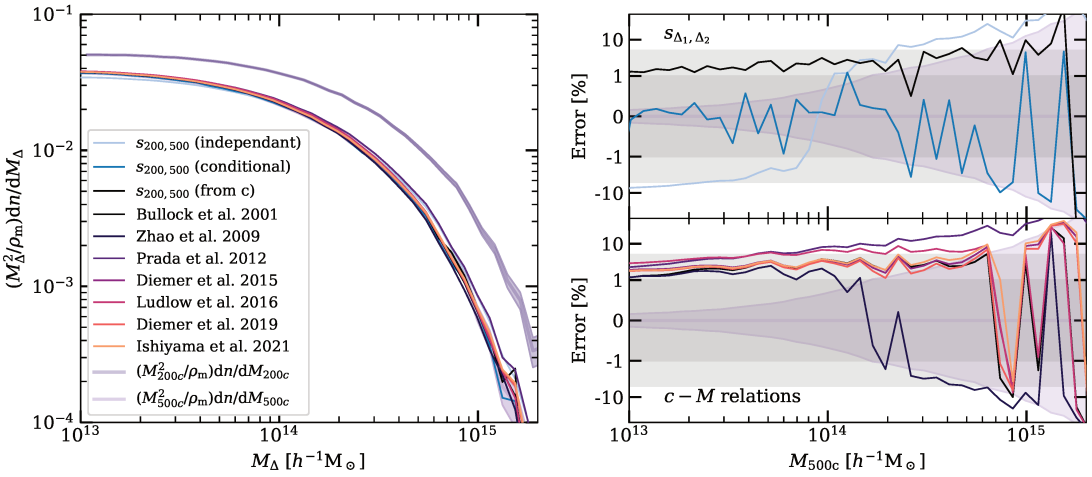

Figure 3.10: Measuring the effectiveness of transforming the halo mass function from one density contrast to another assuming a $c-M$ relation. Left panel: HMF at $\Delta_1 = 200$ (dark magenta line) and $\Delta_2 = 500$ (light magenta line) from the Uchuu halo catalogue at $z = 0$ against the reconstructed HMF at $\Delta_2 = 500$ obtained for the different $c - M$ relation models shown in the legend (see text for further information). Right panel: Relative error on these reconstructions. As in Fig. 3.8, the shaded areas around the measured HMFs represent the statistical error on the measurement estimated as the standard deviation over 10^3 bootstrap iterations.

reconstructions of the HMF assuming the NFW profile and a $c-M$ relation. In a similar fashion to how we derived Eq. (3.28) and Eq. (3.30), if we assume the distribution of concentrations to be highly peaked about its mean, i.e. $\rho_c \simeq \delta_D[c - \langle c\rangle]$, then we can see that this formulation is consistent with that of Hu & Kravtsov (2003).

In Fig. 3.10 we perform an inward reconstruction of the HMF at $\Delta_2 = 500$ starting from the HMF estimated from the Uchuu catalogue at $\Delta_1 = 200$ assuming:

1. the marginal sparsity distribution;
2. the conditional sparsity distribution;
3. the conditional sparsity distribution computed from measured concentrations;
4. the sparsity distribution predicted assuming a log-normal distribution of the concentration with $\sigma = 0.25$ and the mean specified by different $c - M$ relations from Bullock et al. (2001); Zhao et al. (2009); Prada et al. (2012); Diemer & Kravtsov (2015); Ludlow et al. (2016); Diemer & Joyce (2019); Ishiyama et al. (2021)

In addition, we plot the mass functions estimated from the Uchuu halo catalogues against the reconstructed ones at M_{500c} in the left panel, and the relative differences between the two HMF in the right panel. As in Fig. 3.8, the shaded areas correspond to the 68 per cent confidence interval on the N-body mass function estimated as the standard deviation of 10^3 bootstrap iterations. As seen previously, using the conditional sparsity distribution provides a reconstruction that is within the statistical error on the HMF while using the marginal sparsity distribution provides a relatively poor agreement with errors on the reconstruction exceeding the 10 per cent level. If we now consider the $c - M$ based reconstructions, we see that all models deviate from the measured HMF within 1 to 10 per cent. Nonetheless most of these models are in general agreement on

Table 3.1: χ^2 statistics of the reconstructed HMFs at $\Delta_2 = 500$ and $z = 0.00$, 0.25, 0.50, 1.00, and 2.00 for different reconstruction model assumptions.

Model	$z = 0$	$z = 0.25$	$z = 0.5$	$z = 1$	$z = 2$
$s_{200,500}$ (independent)	329.6	289.5	363.6	243.9	8.0
$s_{200,500}$ (conditional)	13.5	21.1	7.4	12.2	7.0
$s_{200,500}$ (from c)	205.1	180.6	916.0	1902.4	382.2
Bullock et al. 2001	310.0	237.4	158.8	896.5	664.1
Zhao et al. 2009	135.1	66.1	70.8	184.9	1710.3
Prada et al. 2012	1857.6	1984.6	1728.8	553.0	32.0
Diemer et al. 2015	321.4	152.0	55.2	196.4	76.2
Ludlow et al. 2016	1131.1	1282.1	953.8	121.5	188.7
Diemer et al. 2019	258.9	181.5	79.5	111.5	71.6
Ishiyama et al. 2021	334.0	217.4	81.8	105.9	69.2

their respective reconstructions. In particular if we compare these models to the HMF reconstructed using the distribution of sparsities estimated from measurements of the NFW concentration, we find that they follow a very similar trend. This indicates, that the observed bias in the reconstruction may originate from the assumption of the NFW profile.

To quantify how well each model reconstructs the HMF we introduce,

$$\chi^2 = \sum_{i=0}^{N} \frac{1}{\sigma_i^2} \left[\frac{\mathrm{d}n_{\mathrm{rec}}}{\mathrm{d}M_{500\mathrm{c}}}(M^i_{500\mathrm{c}}) - \frac{\mathrm{d}n_{\mathrm{N-body}}}{\mathrm{d}M_{500\mathrm{c}}}(M^i_{500\mathrm{c}}) \right]^2 , \tag{3.43}$$

where the index i runs over the N mass bins at which the HMF is estimated from the Uchuu halo catalogues and σ_i is the corresponding statistical error. We do note that the number of mass bins effectively varies with redshift due to the exponential decrease in the HMF. Indeed while at $z = 0$ we define $N = 27$ bins between $M_{500\mathrm{c}} = 4.5{\cdot}10^{13} h^{-1}\mathrm{M}_\odot$ and $M_{500\mathrm{c}} = 2 \cdot 10^{15} h^{-1}\mathrm{M}_\odot$ this effectively decreases to $N = 11$ bins between $M_{500\mathrm{c}} = 4.5{\cdot}10^{13} h^{-1}\mathrm{M}_\odot$ and $M_{500\mathrm{c}} = 2{\cdot}10^{14} h^{-1}\mathrm{M}_\odot$ at $z = 2$ simply because the higher mass bins are empty. In Tab. 3.1, we record these *goodness-of-fit* measurements for all the models used in Fig. 3.10 at $z = 0.00,\ 0.25,\ 0.50,\ 1.00$ and 2.00. We again find similar trends with the conditional sparsity distribution outperforming other models at all redshifts. Although, there is some improvement at higher redshift for most $c - M$ based models these still remain significantly biased.

3.5.3 $c - M$ relation from halo mass function

An interesting byproduct of the considerations we have presented here is that we can effectively invert these relations to predict the $c - M$ relation from a model of the HMF. To do so, we perform the inverse transformation to that of Eq. (3.38),

$$\rho_{\mathrm{c}}(c|M_{\Delta_1}) = \rho_{\mathrm{s}}(f_{\mathrm{s}}(c)|M_{\Delta_1}) \left| \frac{\mathrm{d}f_s}{\mathrm{d}c}(c) \right| \tag{3.44}$$

and assume that the sparsity distribution is, again, highly peaked around the mean $\rho_{\mathrm{s}}(s|M_{\Delta_1}) \simeq \delta_{\mathrm{D}}[s - \langle s_{\Delta_1,\Delta_2} \rangle]$. This results in a concentration distribution that is also described by a Dirac distribution,

$$\rho_{\mathrm{c}}(c|M_{\Delta_1}) = \delta_{\mathrm{D}}[c - f_{\mathrm{c}}(\langle s_{\Delta_1,\Delta_2} \rangle)], \tag{3.45}$$

peaked around $\tilde{c} = f_c(\langle s_{\Delta_1,\Delta_2}\rangle)$. Given that we can predict $\langle s_{\Delta_1,\Delta_2}\rangle(M_{\Delta_1})$ without any additional assumptions, simply by numerically solving Eq. (3.30). We can therefore use $\tilde{c}$, to provide a prediction for the $c - M$ relation.

In Fig. 3.11, we show the mean concentration $\langle c_{200c}\rangle$ as a function of M_{200c} from the Uchuu halo catalogue at $z = 0$ (solid orange line) with iso-contours of the conditional concentration distribution against the mean $c_{200c} - M_{200c}$ relation obtained from the mean sparsity mass relation $\langle s_{200,500}\rangle(M_{200c})$ measured from the same halo catalogue (solid blue), and that predicted using the HMFs at $\Delta = 200\rho_c$ and $\Delta = 500\rho_c$ from Tinker et al. (2008), Watson et al. (2013), Bocquet et al. (2016), and Despali et al. (2016) and measured HMFs respectively the green, red, pink, yellow and grey lines.

We find that the predicted mean $c - M$ relations deviate by 10 to 40 per cent with respect to the mean relations measured directly from the simulation. In addition, we see considerable scatter between the different HMF models, resulting from the compounding effect of model choices, at low masses, and statistical uncertainty on model calibration at high masses. Indeed, we see that at high masses all models agree within their respective 1-σ error regions marked by the shaded areas in the two lower panels, which we obtain from 10^3 bootstrap iterations assuming the error on the HMF model is the same as the statistical error on the measured HMFs. Nonetheless, this is not the case at the low mass end where the statistical uncertainty is much smaller.

Finally, if we measure the mean sparsity relation directly we find that the resulting $c-M$ relation is significantly offset, 20 per cent, from the prediction of the mean sparsity estimated using the HMF as well as the mean $c - M$ relation measured directly on the simulation. This is primarily due to our assumption that the sparsity distribution is highly peaked around the mean. Indeed, we have seen in Section 3.3.2 that the distribution of sparsities is both broad and skewed. It is in fact this skewness which significantly offsets the mean from the mode of the distribution. This can clearly be seen by replacing the mean sparsity by the median, which is closer to the mode. Indeed, the measured median sparsity is much closer to the prediction from the measured HMF.

3.6 Summary

We see that sparsity, which may at first glance appear to be just a simple mass ratio, has a number of interesting properties. Firstly, we have seen that it is sufficient to fully describe the mass profile and due to it's non parametric nature can be related to the parameters of any mass profile. This, gives sparsity flexibility while also removes ambiguity as the measurement is clearly defined. Secondly, we showed that sparsity exhibits a mass dependence which is both much smaller, only increasing around 10 per cent over 2 orders of magnitude in mass, and simpler, can very accurately be modelled by a straight line, than $c-M$ relations. Finally, sparsity has a cosmological dependence. Its distribution being shifted by changes in the cosmological parameters in particular the amplitude of matter fluctuations parameter S_8.

Furthermore, by describing sparsity as a stochastic quantity, we have derived exact relations between the distribution of sparsities and the HMF, which allow one to recast the HMF from one mass definition to another. These relations can be slightly altered in order to use them with parametric profile parameters. Nevertheless, we note that the assumption of a parametric profile shape introduces a small error, between 1 to 10 per cent, error on the reconstruction. Finally, we have shown that these relations can be inverted allowing the prediction of the mean sparsity from the HMF. While these predictions are consistent with the distribution of sparsities measured inside the

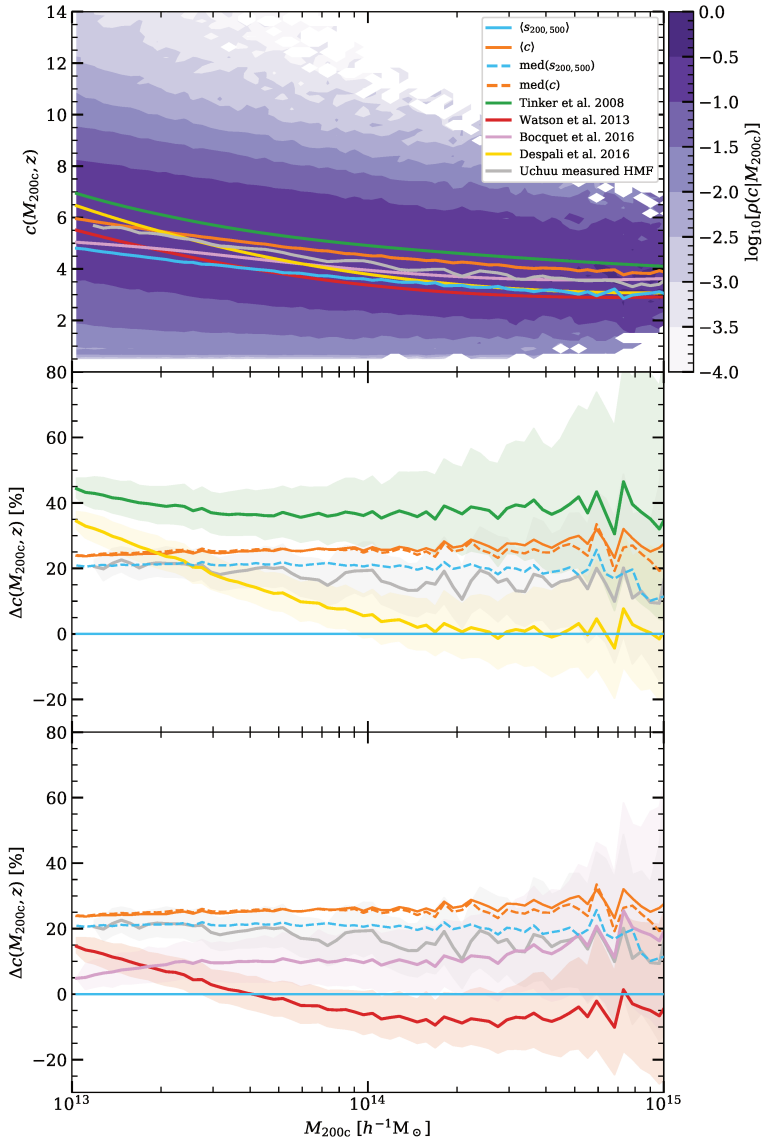

Figure 3.11: Comparison of the concentration distribution inside the Uchuu simulation, measured $c - M$ relation, and model predictions. Top panel: Iso-contours of the conditional concentration c_{200c} from the Uchuu halo catalogues at $z = 0$ as a function of M_{200c}. The solid lines correspond to the mean $c - M$ relation measured from the concentration (orange line) and mean sparsity $s_{200,500}$ (blue line) of the N-body haloes, and predicted from the measure HMF (grey lines) and HMFs models by Tinker et al. (2008) (green line), Watson et al. (2013) (red line), Bocquet et al. (2016) (pink line), and Despali et al. (2016) (yellow line). Middle and Bottom panels: Relative difference between the concentration mass relation predicted from the measured mean sparsity and that measured or predicted using other methods. The shaded area around each model represents one standard deviation around the latter assuming the statistical uncertainty of the HMF measured in the Uchuu simulation. Dashed lines represent the concentration-mass relation predicted from the median sparsity and concentration.

simulations, we find a strong dependence on the details of the chosen HMF model.

4 | Major Mergers & Sparsity

Now that we have investigated the general behaviour of sparsity we turn our interest towards how specific physical processes may cause some haloes to deviate significantly from this distribution. If we again put baryonic effects to one side, the most common astrophysical event encountered by haloes are mergers, the main process through which they acquire mass. In this chapter, we will investigate how the distribution of sparsities is affected and how we can use these results as a method of detecting merging galaxy clusters.

To do so we will analyse the sparsities of haloes from two gravity only simulations. This will allow us to understand how mergers affect sparsities and we will characterise this effect in order to build a novel method for detecting merging clusters using statistical detection methods. Finally, we test the resulting method in order to assess its applicability to observational datasets.

4.1 A brief overview of merging clusters

Galaxy clusters are the most massive gravitationally bound structures in the Universe. Being hosted by the most massive dark matter haloes, this places them a the top of the hierarchy of structure formation, with the size and mass of these objects making them perfect candidates for the study of astrophysics and cosmology. These structures are typically split into three components, stars and galaxies representing only 5% of the total mass of these objects, a massive host dark matter halo and many sub-haloes, which in total represent roughly 80% of the total mass of the cluster, and hot diffuse gas, known as the Intra-Cluster Medium (ICM) trapped within the gravitational potential and representing about 15% of the total mass. This specific structure makes galaxy clusters inherently multi wavelength objects, permitting observations to extensively probe the properties of object. Indeed the hot ICM not only emits X-ray radiation through bremsstrahlung (see e.g. Vikhlinin et al., 2005; Ebeling et al., 2010; Pierre et al., 2016; CHEX-MATE Collaboration et al., 2021) but also scatters CMB photons due to the Sunyaev-Zel'dovich effect (see e.g. Sunyaev & Zeldovich, 1970; Staniszewski et al., 2009; Menanteau et al., 2013; Reichardt et al., 2013; Planck Collaboration et al., 2014b; Bleem et al., 2015) making clusters visible at millimetre wavelengths. In optical bands, while clusters are associated to over densities in the distribution of galaxies which can be studied directly, their gravitational potential produced by the dark matter halo also deflects light coming from background sources (see e.g. Umetsu et al., 2011; Postman et al., 2012; Rykoff et al., 2016; Maturi et al., 2019) giving observers direct access to information about the dark matter distribution inside these objects. Here, we will be particularly interested in the dark matter component with the two other components assumed to be biased tracers of the dark matter.

Observations of relaxed galaxy clusters have revealed that their matter density at

large radii is consistent with the NFW profile (Navarro et al., 1997) seen in simulations, but that there can be significant deviations from the latter at small radii (see e.g. Newman et al., 2013; Annunziatella et al., 2017; Collett et al., 2017; Sartoris et al., 2020) where baryonic effects become non-negligible. In these systems the gas rests inside the potential and thermalises through the propagation of shock waves. This sets the ICM into a state of hydrostatic equilibrium resulting in a self-similar density profile (Ettori et al., 2019; Ghirardini et al., 2019, 2021).

Nonetheless, many non-thermal processes take place within the ICM (Biffi et al., 2016) that cause the gas to strongly depart from this state of equilibrium, for instance contributions from active galactic nuclei or major merger events. In such systems, these processes can significantly alter the density profile resulting in a significant bias on any measurement that relies on the assumption of self similarity (see e.g. Planelles & Quilis, 2009; Rasia et al., 2011; Chen et al., 2019; Pratt et al., 2019). This is especially true for mass estimate which assume hydrostatic equilibrium, or scaling relations which are derived under this same assumption. Ultimately this would result in systematic effects being carried over into any cosmological analysis which relies on the measurement of cluster masses.

While major merger may seem like a nuisance for cosmological analyses based on mass estimates they do however provide the ideal environment to study both the properties of the ICM (Markevitch & Vikhlinin, 2007; Zuhone & Roediger, 2016) and underlying dark matter, this for instance was attempted in observations of the Bullet Cluster (Markevitch et al., 2004; Clowe et al., 2004). As such we see that identifying such systems is both crucial for cosmology while also providing significant insight for the astrophysics of these systems.

A variety of methods has been proposed to identify unrelaxed clusters, each relying on different cluster observables (see Molnar, 2016; De Luca et al., 2021; Vallés-Pérez et al., 2023, for reviews). These include, but are not limited to, the detection of radio relics and haloes which can be associated to the propagation of shock fronts after a merging event has taken place. Alternatively one can measure the offset between the peak X-ray emission or centroid of S-Z signal, which both trace the collisional gas, with respect to the position of the brightest cluster galaxy or the centre of the weak lensing signal, which trace the gravitational potential mainly sourced by dark matter. Indeed as both components do not react in the same way to a merger, one component being collisional and the other collisionless, this creates an offset which can be measured.

As mentioned in previous chapters, merger events are the main growth mechanism through which structures acquire their mass. This has been studied extensively in the past using N-body simulations, for instance it has been shown that dark matter haloes initially go through a phase of fast accretion which is then followed by a 'slow accretion state' (Zhao et al., 2003). During this first phase of rapid growth haloes acquire most of their mass through major mergers (Li et al., 2007), which we define as mergers between haloes of a similar mass, i.e. with a mass ratio no lower than 1 to 3. This is in opposition with the quiescent phase where the primary source of mass is through minor merger events. These works have also shown that the greater the mass of a halo the later the rapid growth phase ends.

Here, we are going to investigate how major mergers impact the internal structure of haloes. This has already been investigated through the scope of the NFW concentration parameter, with the particular interest of linking the mass accretion history of haloes to their concentrations (see e.g. Neto et al., 2007; Zhao et al., 2009; Ludlow et al., 2012; Lee et al., 2017; Rey et al., 2019). Recently, Wang et al. (2020a) have shown that

major mergers have a universal impact on the evolution of the median concentration. In particular, after a large initial response, in which the concentration undergoes a large excursion, the halo recovers a more quiescent dynamical state within a few dynamical times. Surprisingly, the authors have also found that even minor mergers can have a non-negligible impact on the mass distribution of haloes, contributing to the scatter of the concentration parameter.

The use of concentration in this context can however be problematic as this entails that one assumes the profile is well described by the NFW profile. This is generally not the case with merging galaxy clusters often displaying complex profiles with significant deviations from the NFW profile. These effects are compounded with deviations from typical measurements in N-body simulations sourced by astrophysical processes (see e.g. Mead et al., 2010; King & Mead, 2011), which may also be aggravated by merger activity.

It is within this context that the use of sparsity,

$$s_{\Delta_1,\Delta_2} = \frac{M_{\Delta_1}}{M_{\Delta_2}}, \tag{4.1}$$

proves beneficial. Indeed the standard definition of sparsity naturally avoids many of the difficulties faced by concentration. Firstly, it can be defined directly from mass estimations of observed clusters, which are far easier to access than an estimate of the profile. Secondly, the weak mass dependence of sparsity for certain choices of density contrast pairs and the reduced scatter with respect to concentration (Balmès et al., 2014; Corasaniti et al., 2018; Corasaniti & Rasera, 2019) allows for clearer identification of outliers. Finally, sparsity being intrinsically linked to the cosmological background, as we will discuss in Chapter 5, allows for the theoretical prediction for the distribution of sparsities from a model of the HMF (Corasaniti et al., 2018, 2021; Richardson & Corasaniti, 2023), providing a theoretical base line to which we can compare outliers.

This chapter is devoted to studying how halo sparsity correlates to the mass accretion history of haloes through the analysis of large volume N-body simulations. In particular we will fully characterise the distribution of sparsities for a given time since the last major merger occurred. Allowing us to build a statistical tool to rapidly detect mergers in catalogues of sparsities and even provide a first estimate of when the last major merger took place.

For the purpose of this work, we have made use of two publicly available cosmological simulation datasets, one coming from the MultiDark Planck 2 (MDPL2) (Klypin et al., 2016) simulation and the second coming form the Uchuu simulation (Ishiyama et al., 2021). Both datasets take the form of ROCKSTAR halo catalogues and merger trees (Behroozi et al., 2013a,b). Here, the halo finder was used in its default setup entailing that only particles gravitationally bound to a halo are considered as belonging to the latter. Limiting our study to the most massive objects found inside the simulations, $M_{200c} > 10^{13} h^{-1} \mathrm{M}_\odot$, and relatively low redshifts, $z < 2$, these catalogues give us access to four mass measurements, the virial mass and three additional density contrast, $\Delta =$ 200c, 500c and 2500c, from which we compute three sparsities, $s_{200,500}, s_{500,2500}, s_{200,2500}$. In addition to these we have access to the NFW scale radius r_s from which we can compute the concentration parameter, $c = r_{200c}/r_\mathrm{s}$, along with the offset of the peak of the potential with respect to the centre of mass x_off, from which we derive the relative displacement of the centre of mass, $\Delta_r = x_\mathrm{off}/r_\mathrm{vir}$. Finally, the halo finder also provides the scale factor, a_LMM at which the last major merger took place. In this context the halo finder considers a major merger event to be the moment when the mass of a halo

suddenly increases by 30%. It is important to note that due to the design of the halo finder this corresponds to the moment when all particles fall within one iso-density contour in phase space and does not correspond to the time of first core passage usually estimated for Bullet-like cluster.

In the following, we will present the methodology and results that lead to the publication of Richardson & Corasaniti (2022). In section 4.2 we will analyse the simulation data in order to understand the link between halo sparsity and major merger. In section 4.3 we devise statistical tools to detect the imprint of major merger in galaxy clusters and discuss the possibility of estimating the time at which these events took place. In section 4.4 we discuss the limits of this approach when applying it to observational samples, notably we assess how robust it is to observational biases, before finally concluding this chapter in section 4.5 .

4.2 Halo Sparsity & major mergers

4.2.1 A first look at merging haloes

In order to get a first look at how sparsity reacts to major mergers we split the population of haloes into two categories. To do so we normalise the time coordinate with respect to the dynamical times of dark matter haloes (Jiang & van den Bosch, 2016; Wang et al., 2020a),

$$T(z|z_{\rm LMM}) = \frac{\sqrt{2}}{\pi}\int_{z_{\rm LMM}}^{z}\frac{\sqrt{\Delta_{\rm vir}(z)}}{z+1}dz, \tag{4.2}$$

where $\Delta_{\rm vir}$, introduced in Chapter 2, is the virial overdensity contrast (Bryan & Norman, 1998). It is interesting to note that this definition does not depend on any properties of the haloes such as their mass or concentration and depends solely on the background cosmology. This definitions differs from that of Jiang & van den Bosch (2016) and Wang et al. (2020a) by a minus sign. This is due to the fact that in this case we place ourselves at a fixed point in time, specifically at a fixed redshift z, and look backwards to the time, equivalently to a larger redshift $z_{\rm LMM}$, when the last major merger took place. This entails that haloes with $T = 0$, are currently merging while haloes with $T < 0$ have undergone there last major merger at some time in the past. Under this new time coordinate haloes return to a stable configuration after $T \sim 2$ dynamical times.

In order to maximise the difference between the two categories we do not seperate them exactly at $T = -2$, and prefer to define:

- *Merging haloes*: a sample of haloes that have had less than half of a dynamical time since their last major merger ($T > -1/2$), and are therefore still in the process of rearranging their mass distribution,

- *Quiescent haloes*: a sample of haloes for which their last major merger occurred far in the past ($T \leq -4$), thus they have had sufficient time to rearrange their mass distribution recover a state of equilibrium,

Looking specifically at the haloes from the $z = 0$ catalogue. Merging haloes, with $T > -1/2$, correspond to all haloes for which the last major merger, as tagged by the algorithm, occurred later than $a_{\rm LMM} > 0.897$ ($z_{\rm LMM} < 0.115$), while the samples of quiescent haloes, with $T \leq -4$, in the same catalogue are characterised by a last major merger prior to $a_{\rm LMM} < 0.464$ ($z_{\rm LMM} > 1.155$). We repeat this selection for the

Table 4.1: Characteristics of the selected halo samples at $z = 0, 0.2, 0.4$ and 0.6 (columns from left to right). Quoted in the rows are the number of haloes in the samples and the redshift of the last major merger $z_{\rm LMM}$ used to select the haloes for each sample.

	Merging Halo Sample ($T > -1/2$)			
	$z = 0.0$	$z = 0.2$	$z = 0.4$	$z = 0.6$
#-haloes	23164	28506	31903	32769
$z_{\rm LMM}$	< 0.113	< 0.326	< 0.540	< 0.754
	Quiescent Halo Sample ($T < -4$)			
	$z = 0.0$	$z = 0.2$	$z = 0.4$	$z = 0.6$
#-haloes	199853	169490	140464	113829
$z_{\rm LMM}$	> 1.15	> 1.50	> 1.86	> 2.22

catalogues at $z = 0.2, 0.4$ and 0.6 respectively, in order to study any redshift dependence. The characteristics of the different samples can be found in Tab. 4.1.

As a first test we wish to measure how the sparsity, estimated using the SO masses provided in the catalogues, deviates from that deduced by solving Eq. (3.1), which in the specific case of the NFW profile reduces to solving (Balmès et al., 2014),

$$x_\Delta^3 \frac{\Delta}{200} = \frac{\ln\left(1 + c_{\rm 200c} x_\Delta\right) - \frac{c_{\rm 200c} x_\Delta}{1 + c_{\rm 200c} x_\Delta}}{\ln\left(1 + c_{\rm 200c}\right) - \frac{c_{\rm 200c}}{1 + c_{\rm 200c}}}, \tag{4.3}$$

where $x_\Delta = r_\Delta / r_{\rm 200c}$ and using as input the concentration measured by the halo finder. From the solution of this equation we can then derive the NFW sparsity of haloes,

$$s^{\rm NFW}_{200,\Delta} = \frac{200}{\Delta} x_\Delta^{-3}. \tag{4.4}$$

It is important to note that while from Eq. (4.3) we can only compute $s_{200,\Delta}$ for any $\Delta > 200$, this is however sufficient to estimate the sparsity at any other pair of overdensities $\Delta_1 \neq \Delta_2 > 200$ as given by $s_{\Delta_1,\Delta_2} = s_{200,\Delta_1} / s_{200,\Delta_2}$.

It has been previously shown (Balmès et al., 2014) that deviations from the NFW profile, contribute to a considerable amount of scatter in the distribution of concentrations, not only due to the physical changes in the profile but also due to numerical artefacts originating from poor fit quality. This effect is visible in Fig. 4.1 where we plot the distribution of relative deviations with respect to the expected NFW value for $\delta_{200,500} = 1 - s^{\rm NFW}_{200,500} / s_{200,500}$ (dashed lines) and $\delta_{200,2500} = 1 - s^{\rm NFW}_{200,2500} / s_{200,2500}$ (solid lines) in the case of the merging (blue lines) and quiescent (orange lines) haloes at $z = 0.0, 0.2, 0.4$ and 0.6 respectively. For quiescent haloes we can see that this produces an unimodal and almost Gaussian distribution. More specifically, in the case $\delta_{200,500}$ we can see that the distribution has a narrow scatter with a peak that is centred at the origin at $z = 0.6$, and slightly shifts toward positive values at smaller redshifts with a maximal displacement at $z = 0$. This corresponds to an average bias of the NFW-estimated sparsity $s^{\rm NFW}_{200,500}$ of order ~ 4 per cent at $z = 0$. A similar trend occurs for the distribution of $\delta_{200,2500}$, though with a larger scatter and a larger shift in the location of the peak of the distribution at $z = 0$, which corresponds to an average bias of $s^{\rm NFW}_{200,2500}$ of order ~ 14 per cent at $z = 0$. Such systematic differences are indicative of the limits of the NFW-profile in reproducing the halo mass profile of haloes both in the outskirt regions and the inner ones. This is consistent with the findings of Child et al. (2018), which describe how the NFW profile is in fact best suited for haloes at higher redshift.

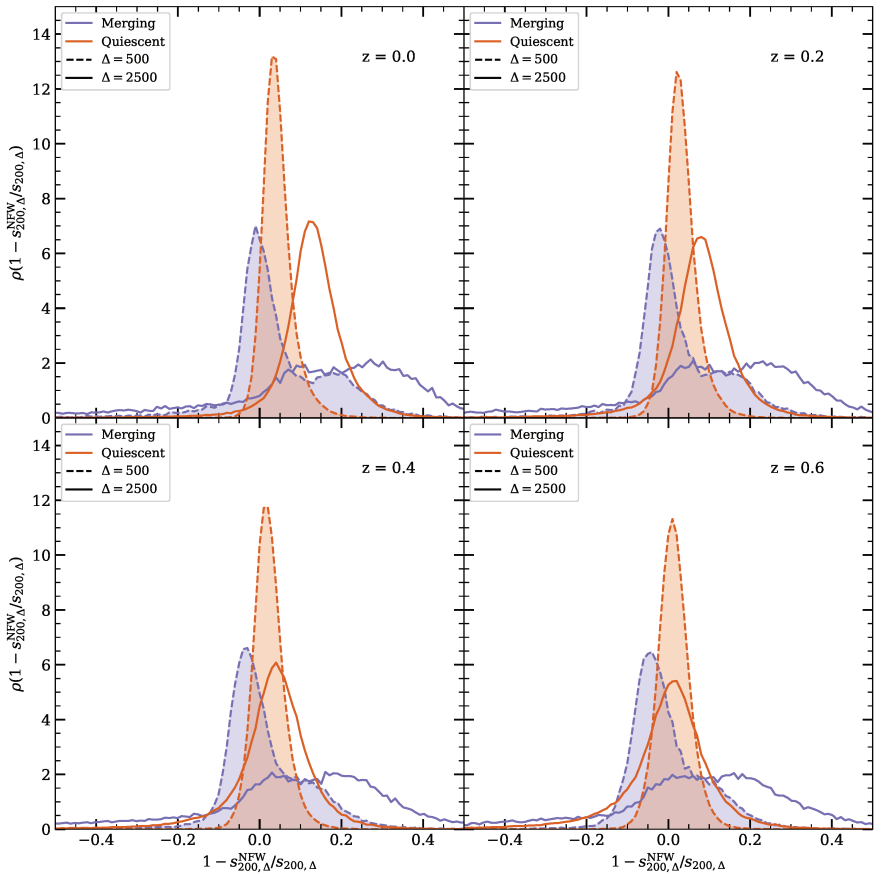

Figure 4.1: Distribution of the relative deviations of individual halo sparsities with respect to the expected NFW value for $\delta_{200,500} = 1 - s^{\rm NFW}_{200,500}/s_{200,500}$ (dashed lines) and $\delta_{200,2500} = 1 - s^{\rm NFW}_{200,2500}/s_{200,2500}$ (solid lines) in the case of the merging (blue lines) and quiescent (orange lines) haloes at $z = 0.0$ (top left panel), 0.2 (top right panel), 0.4 (bottom left panel) and 0.6 (bottom right panel) respectively

When looking at the perturbed sample however we see that the distribution is highly irregular, with the latter being both displaced and strongly non-gaussian. Moreover we see that the two sparsities respond differently to the perturbation, with $\delta_{200,500}$ presenting a main peak and a smaller secondary peak while $\delta_{200,2500}$ presents two peaks of roughly equal height. We also see that both distributions are displaced by respectively 20 per cent and 40 per cent. From this simple test we can already see that in this regime the concentration becomes unreliable, and sparsity becomes a more accurate representation of the profile.

4.2.2 Evolution of Halo sparsity

Let us now investigate how sparsity evolves over time. To do so we reconstruct the sparsity histories of all the haloes in our sample from the mass accretion histories generated by the halo finder. In Fig. 4.2, we plot the median sparsity evolution of $s_{200,500}$ (top panel), $s_{500,2500}$ (middle panel) and $s_{200,2500}$ (bottom panel) as function of the scale factor. In the left panels we show the case of a sample of 10^4 randomly selected haloes, thus behaving as quiescent haloes in the redshift range considered, while in the right panels we plot the evolution of the sparsity of all haloes in the $z = 0$ catalogue undergoing a major merger at $a_{\rm LMM} = 0.67$. The shaded area corresponds to the 68% sparsity excursion around the median, while the vertical dashed line marks the value of the scale factor of the last major merger.

We note that, as we briefly discussed in the previous chapter, sparsity can be seen as a estimation of the mass fraction contained between the two radii, r_{Δ_1} and r_{Δ_2}. As such, sparsities calculated using masses estimated at outer radii will probe the outer regions of haloes while sparsities estimated using inner masses while probe inner regions of the halo. Looking at the left side panels of Fig. 4.2 we see that all sparsities follow a generally decreasing trend with time. We also observe that the decrease is stronger for inner regions. This is consistent with the picture that haloes form through the successive layering of dark matter shells deposited by merger events (Wang et al., 2011). In this picture the core forms first and then subsequent shells are deposited around the latter. This entails that the core becomes more concentrated, or less sparse, overtime while the outer regions remain roughly constant due to the arrival of new material.

In the right hand panels of Fig. 4.2, we repeat the same procedure but this time only selecting haloes which have a major merger at $a = 0.67$. We see that before this epoch the evolution of the sparsity is similar to the full population seen in the left hand panels, but once the merger takes place the sparsity is strongly perturbed by a pulse like feature. This is consistent with the findings of Wang et al. (2020a) for the median concentration and scale radius. The use of sparsity here however ensures that we are indeed observing a physical effect, free from artefacts which may arise from fitting the halo density profile with the NFW formula.

Here, this can clearly be seen in the diversity in the pulse shape. We see the perturbation strongly perturbs $s_{200,500}$, which probes the outer halo, at the very start of the merger exhibits a high peak sparsity and later exhibits a smaller secondary peak. The opposite is seen for $s_{500,2500}$, which probes the inner halo, where the first peak is low and the second peak is high. This tells us the accreated halo first passes through the outskirts of the host halo before turning around and being confined to the inner halo, where it finally settles as the resulting halo recovers a quiescent state.

In Fig. 4.3 we plot the median sparsity histories of haloes identified in the MDPL2 catalogue at $z = 0$ as having major mergers at five different redshifts $z_{\rm LMM}$ as a function of the backward interval of time T (in units of the dynamical time) since the last major

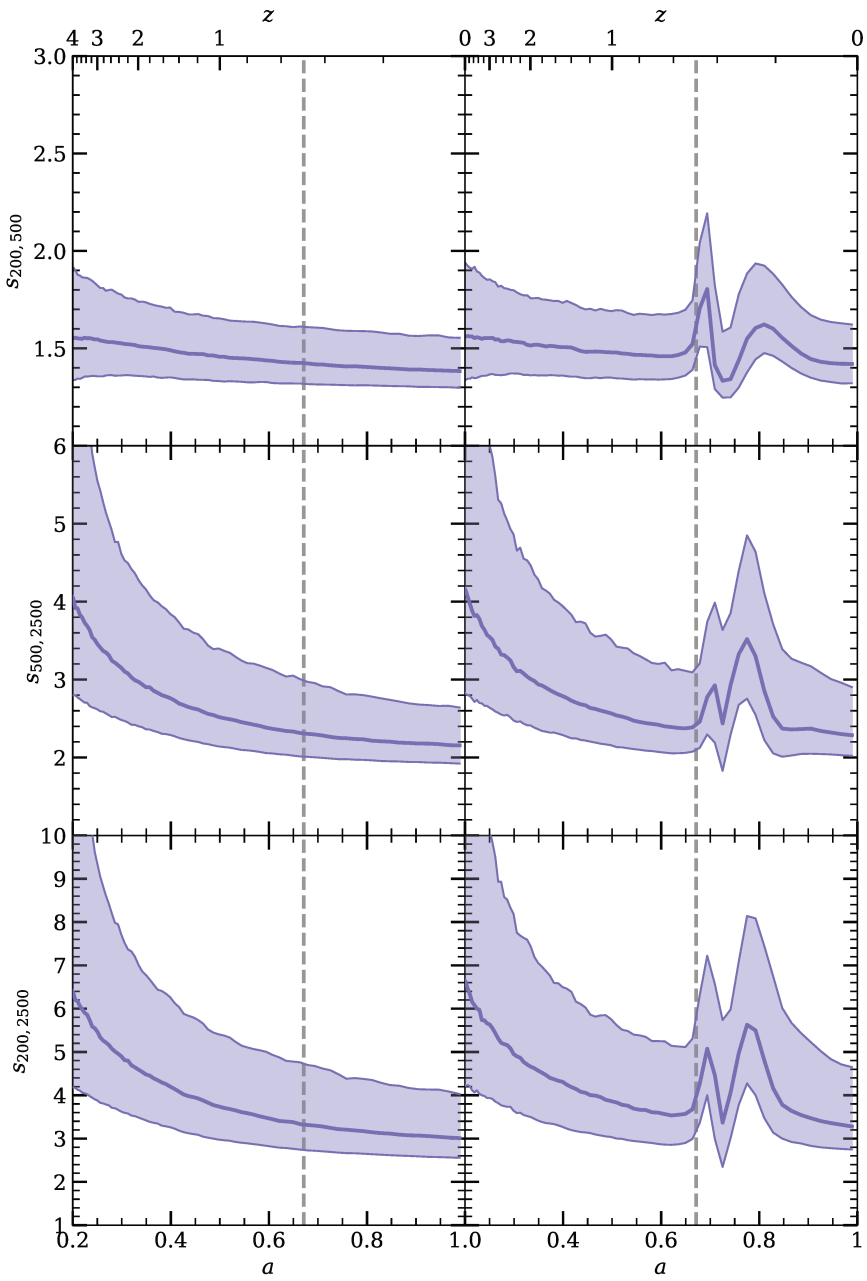

Figure 4.2: Evolution with scale factor a (redshift z) of the median sparsity $s_{200,500}$ (top panels), $s_{500,2500}$ (middle panels) and $s_{200,2500}$ (bottom panels) for a sample of 10^4 randomly selected haloes from the MDPL2 halo catalogue at $z = 0$ (left panels) and the sample of all haloes with a last major merger event at $a_{\mathrm{LMM}} = 0.67$ (right panels). The solid lines correspond to the median sparsity computed from the mass accretion histories of the individual haloes, while the shaded area corresponds to the 68% region around the median.

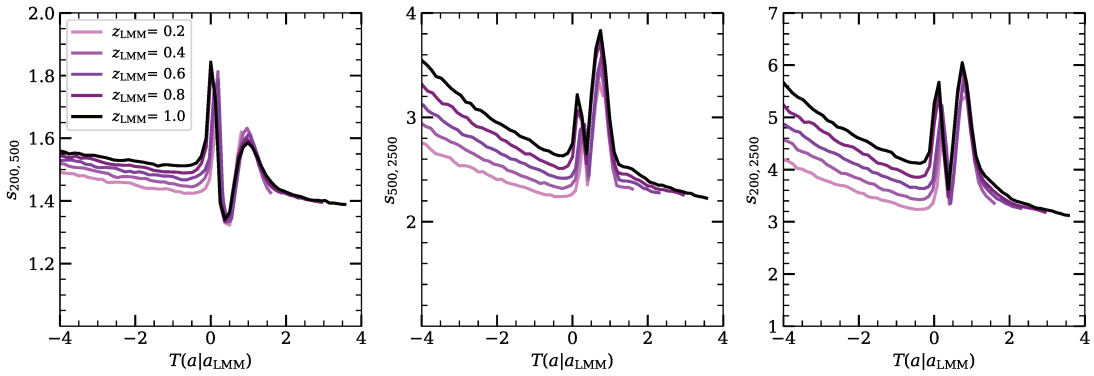

Figure 4.3: Median sparsity histories as function of the backward time interval since the major merger events T (in units of dynamical time) for halo samples from the MDPL2 catalogue at $z = 0$ with different last major merger redshifts $z_{\rm LMM} = 0.2, 0.4, 0.6, 0.8, 0.8$ and 1 (curves from bottom to top). Notice that the backward time interval used here differ by a minus sign from that given by Eq. (4.2) to be consistent with the definition by Wang et al. (2020a).

merger. Notice that T used in this plot differs by a minus sign from that given by Eq. (4.2) to conform to the definition by Wang et al. (2020a). We can see that after the merger takes place all the curves line up, indicating that the reaction of haloes to major mergers is somewhat universal, producing the same pulse no matter at what time the merger took place. We see that all sparsities recover a quiescent state after two dynamical times, which is again consistent with the findings of Wang et al. (2020a). It is important to note that the patterns seen here are the result of a purely gravitational process, as such one may expect that these features are sensitives to the underlying theory of gravity and also small scale non-gravitational processes such as baryonic physics or dark matter self-interactions.

4.2.3 Distribution of post-merger sparsities

In the previous section we have seen that halo sparsities are perturbed in a similar fashion after major merger occurs. These events leave a universal imprint on these statistics which only depends on the choice of mass used. This universality is well highlighted when using the backward time interval T normalised by the dynamical time of haloes. In this section we shift our focus towards a wider study of how the general population haloes react to major merger events. Specifically we study the behaviour of the distribution of sparsities rather than just its median. Note that we now revert to the definition of T given by Eq. (4.2). In this context T is thus relative to the time at which we are looking at the population, i.e. the redshift z at which the halo catalogue is produced. Hence, $T = 0$ for haloes currently undergoing a major merger at $z_{\rm LMM} = z$, and $T < 0$ for those where the merger occurred in the past, $z_{\rm LMM} > z$.

For conciseness, we only investigate the joint distribution $p(s_{200,500}, T)$ shown in Fig. 4.4 in the form of iso-probability contours in the $s_{200,500} - T$ plane at $z = 0$ (top left panel), 0.2 (top right panel), 0.4 (bottom left panel) and 0.6 (bottom right panel). In each panel the horizontal solid line marks the characteristic time interval $|T| = 2$. As shown by the analysis of the evolution of the halo sparsity, haloes with $|T| > 2$ have recovered a quiescent state, while those with $|T| < 2$ are still undergoing the merging process. The marginal conditional probability distributions $p(s_{200,500}|T < -2)$

and $p(s_{200,500}|T > -2)$ are shown in the inset plot. If we repeat this plot for other halo sparsities, such as $s_{200,2500}$, and $s_{500,2500}$, we retrieve a similar behaviour with the exception that the shape with the perturbed region, $|T| < 2$, is altered.

In Fig. 4.4, we notice that the joint probability distribution does not exhibits any strong trend with the redshift at which we study the haloes, showing only a slight shift to higher values when looking at higher redshifts with this shift being larger for other sparsities, see Fig. 4.2. The general structure of the distribution generally remains untouched, where at the bottom of each pannel, $T < -2$, we see a population of haloes that are in a quiescent state, having not undergone a recent merger. These haloes all behave in a similar fashion, independently of when their last major merger took place. If we now look at the top of each panel, $-2 < T < 0$, corresponding to the population of merging haloes, we see a strong dependency with the time at which the last major merger occurred with the shape of this dependency being reminiscent of the pulse features seen in Fig. 4.2 and Fig. 4.3.

In the inset plots we marginalise over the two populations, this is equivalent to studying the PDF of the sparsities of all the haloes above or below the horizontal line at $T = -2$, in each plot. We choose to differentiate both populations in such a manner as to provide a conservative estimate of the time after which haloes recover a quiescent state. We see that distribution of merging haloes (in orange) systematically shows a much heavier tail towards high sparsities, contributing to a higher dispersion, than their quiescent counterparts (in blue). Thus, it is merging haloes which are primarily contributing to the scatter of the full distribution of halo sparsities. With this difference in the two distributions in mind, we expect that measurements of cluster sparsities can be used to identify perturbed systems that have recently undergone a major merger.

4.3 Identifying galaxy cluster major mergers

The analyses presented in the previous section allow us to conclude that there is a significant difference between the distribution of sparsities characterising a population of quiescent haloes and that of merging haloes. We have also seen, that the two populations can be delimited by the normalised time coordinate T, which allows us to give a formal definition to the two groups. In this section our goal is to formalise these results into calibrated distributions that we can then use to test whether or not a galaxy cluster has undergone a major merger.

To do so we design a binary test, as defined in the context of detection theory (see e.g. Kay, 1998), to differentiate between both groups. Formally, this translates into defining two hypotheses denoted as $\mathcal{H}_0$, the null hypothesis, and $\mathcal{H}_1$, the alternate hypothesis. In our case this translates to,

- $\mathcal{H}_0$: *The halo has not undergone a recent major merger*,
- $\mathcal{H}_1$: *The halo has undergone a recent major merger*.

Which given our definition of merging or non merging haloes can be rewritten,

$$\begin{cases} \mathcal{H}_0 : \ T(a_{\rm LMM}|a(z)) < -2 \\ \mathcal{H}_1 : \ T(a_{\rm LMM}|a(z)) \geq -2. \end{cases} \tag{4.5}$$

In Fig. 4.4 this correspond to the two regions delimited by black horizontal lines and more specifically the inset plots of each panel.

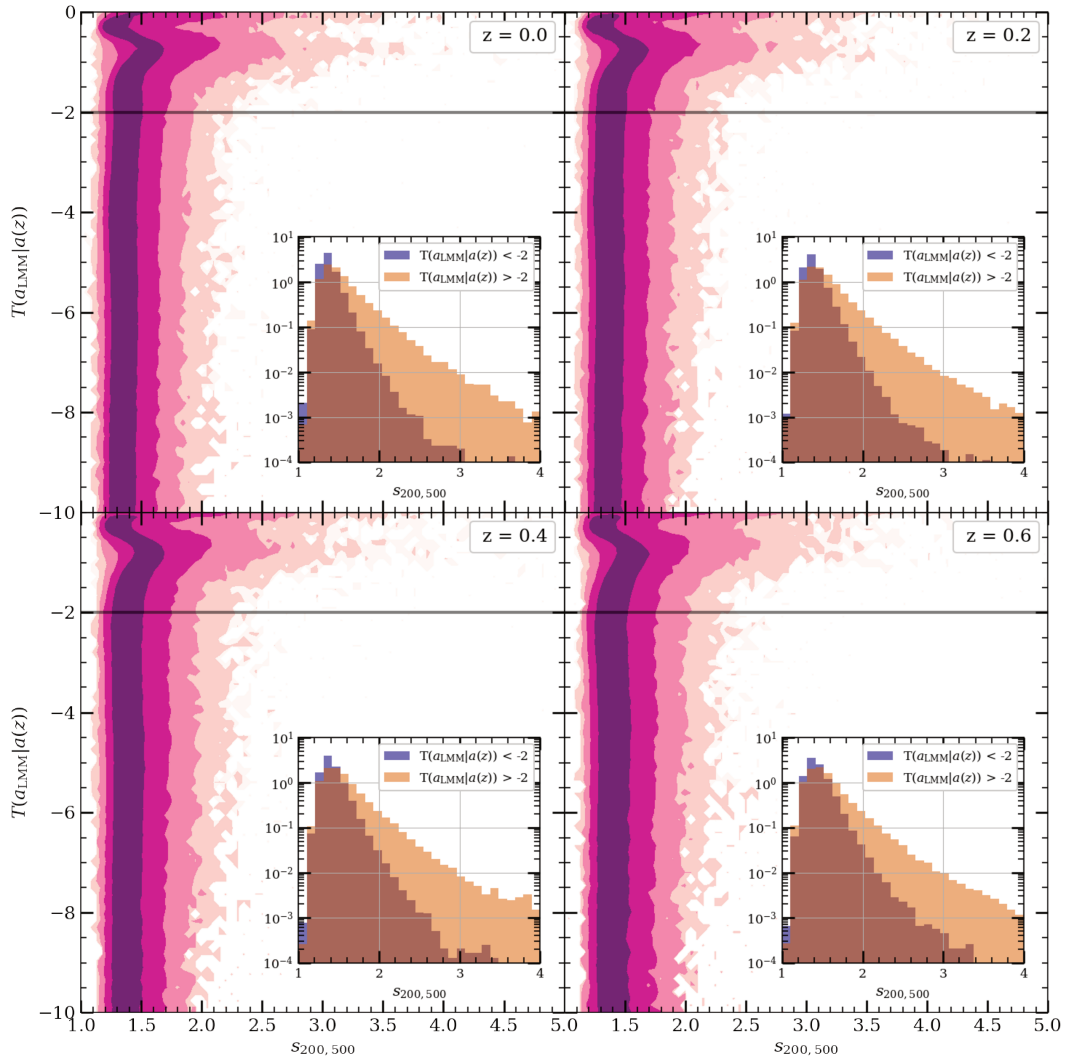

Figure 4.4: Iso-probability contours of the joint probability distribution in the $s_{200,500} - T$ plane for the haloes from the MDPL2 catalogues at $z = 0.0, 0.2, 0.4$ and 0.6 respectively. The solid horizontal line marks the value $T = -2$. The inset plots show that marginal probability distribution for haloes with $T > -2$ (blue histograms) and $T < -2$ (orange histograms) respectively.

Table 4.2: Best fitting parameters for the distribution of sparsities at $z = 0$ under both hypotheses. Here, we quote each parameter with its 95 percent confidence interval estimated over 1000 bootstrap iterations.

Parameter	$\mathcal{H}_0$	$\mathcal{H}_1$
α	$1.4^{+0.1}_{-0.1}$	$1.5^{+0.2}_{-0.2}$
β	$0.61^{+0.03}_{-0.03}$	$0.71^{+0.10}_{-0.08}$
p	$7.7^{+0.3}_{-0.3}$	$4.1^{+0.4}_{-0.3}$
q	$0.304^{+0.002}_{-0.003}$	$0.370^{+0.008}_{-0.008}$

Detection theory, tells us that to differentiate between the cases we must confront some observable test statistic,

$$\Gamma \underset{\mathcal{H}_0}{\overset{\mathcal{H}_1}{\gtrless}} \Gamma_{\rm th}, \tag{4.6}$$

to a threshold, $\Gamma_{\rm th}$, defined from the theory. Following this general philosophy we will now study multiple ways of defining both the test statistic and threshold. Here we will follow formal approaches as to unambiguously define these quantities and to ensure the robustness of each method by checking that everything remains consistent.

4.3.1 Frequentist approach

To begin, the simplest choice of test statistic is to use the sparsity itself, for now let us focus on $s_{200,500}$. As mentioned previously we separate the data according to our two hypotheses. We then model the resulting PDFs as generalised β' distributions,

$$\rho(x, \alpha, \beta, p, q) = \frac{p\left(\frac{x}{q}\right)^{\alpha p - 1}\left(1 + \left(\frac{x}{q}\right)^{p}\right)^{-\alpha-\beta}}{q\, B(\alpha, \beta)}, \tag{4.7}$$

where $B(\alpha, \beta)$ is the Beta function and where $x = s_{200,500} - 1$. Using our two samples we calibrate the parameters of these two distributions with a standard least squares fitting approach. For $z = 0$, we reproduce the resulting parameters in Tab. 4.2 and show the best fitting distribution in Fig. 4.5. In both case we also give the 95 per cent confidence interval estimated using 10^3 bootstrap iterations. Note that at higher redshifts these parameters change and require one to recalibrate them. We can see in Fig. 4.5 that while these fits accurately capture the peaks of the distributions they degrade significantly when looking at the tails of these same distributions.

In this Frequentist approach we want to compare the use of sparsity to the use of a likelihood ratio (LR) test statistic, $\sigma(x) = \rho(x|\mathcal{H}_1)/\rho(x|\mathcal{H}_0)$, which under the Neyman-Pearson lemma (see e.g. Kay, 1998) constitutes the most powerful detector for a given binary test. While the fits may seem of poor quality they are sufficient to provide us with an estimate, $\tilde{\Sigma}$ of this LR statistic. Using the best fitting parameters at $z = 0$ we find:

$$\begin{aligned}\tilde{\Sigma}(x) &\propto x^{\alpha_1 p_1 - \alpha_0 p_0}\frac{(1 + (x/q_1)^{p_1})^{-\alpha_1-\beta_1}}{(1 + (x/q_0)^{p_0})^{-\alpha_0-\beta_0}}, \\ &= x^{-4.6}\frac{(1 + (x/0.370)^{4.1})^{-2.2}}{(1 + (x/0.304)^{7.7})^{-2.0}}.\end{aligned} \tag{4.8}$$

If we focus on the high sparsity regime, $x \gg 0.3$, then this expression reduces to, $\tilde{\Sigma} \propto x^{1.8}$. This indicates that in the large sparsity regime the LR statistic is simply

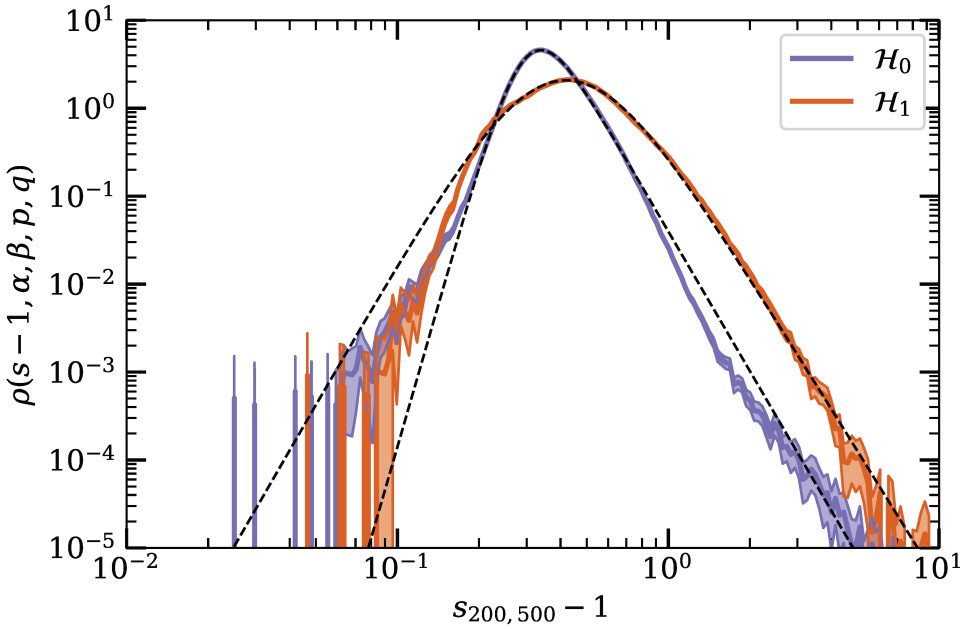

Figure 4.5: Estimated probability distribution functions for $\mathcal{H}_0$ (purple solid line) and $\mathcal{H}_1$ (orange solid line) hypotheses at $z = 0$ along with best fitting generalised beta prime distribution functions (dashed black lines). The shaded area corresponds to the 95 percent confidence interval estimated over 1000 bootstrap iterations.

a monotonously increasing function of $s_{200,500}$, meaning that in this regime sparsity will have a similar constraining power to the true LR statistic. This result can also be shown to hold at higher redshift. This indicates that we can use sparsity to efficiently differentiate between the two populations.

Now that we are assured that $s_{200,500}$ is an efficient statistic in the high sparsity regime, we want to set the thresholds to which we will compare this measurement. To do so we use simple p-values

$$\mathrm{p} = \mathrm{P_r}(s_{200,500} > s^{\mathrm{th}}_{200,500}|\mathcal{H}_0) = 1 - \int_0^{s^{\mathrm{th}}_{200,500}-1} \rho(x|\mathcal{H}_0)dx, \tag{4.9}$$

which define the probability of finding a sparsity higher than a given threshold, $s^{\mathrm{th}}_{200,500}$, assuming the dark matter halo is quiescent. This allows us to root the threshold to a chosen level of the p-value by simply inverting this relation numerically. We estimate these thresholds for three widely used p-values $p = 0.05$, $p = 0.01$, and $p = 0.005$ repeating the operation up to redshift $z = 4$ recalibrating the distribution for each redshift. In Fig. 4.6 we show the resulting thresholds which can be used to quickly estimate the values of sparsity above which a cluster at a given redshift z can be considered as having undergone a recent major merger.

We note however that here we have calibrated these distributions using gravity only simulations. Masses, and therefore sparsities, retrieved from observed cluster being affected by baryonic physics are biased with respect to these masses and therefore may be affected by systematic uncertainties and may differ depending on the type of observations. For example, Corasaniti et al. (2018) show that using halo catalogues coming from hydrodynamical cosmological simulations with an extreme AGN feedback model, results in an offset of up to 4 per cent in $s_{200,500}$ and up to 15 per cent in $s_{200,2500}$ at

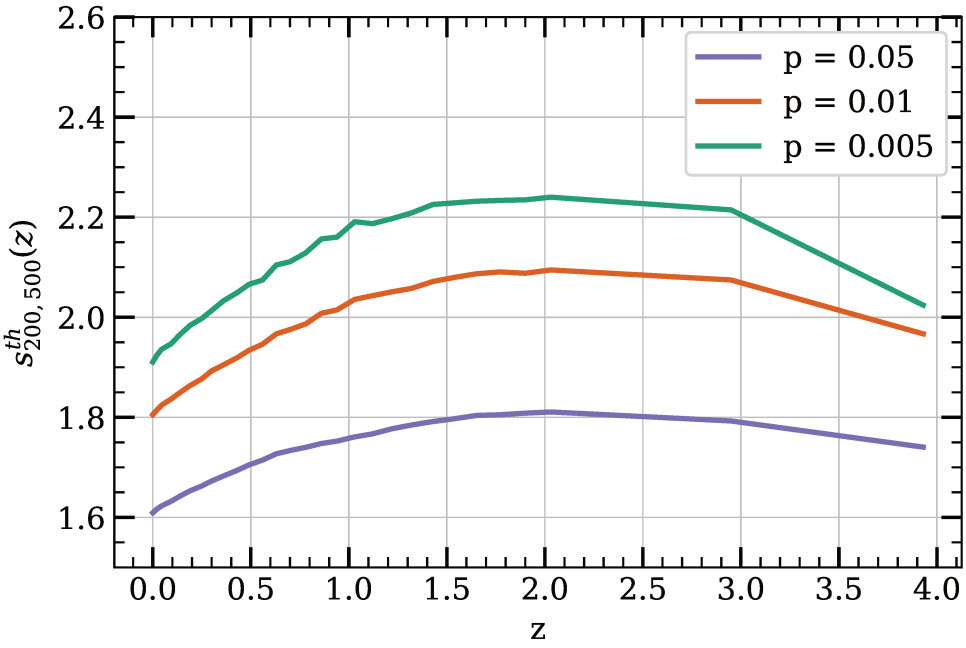

Figure 4.6: Sparsity thresholds $s^{\rm th}_{200,500}$ as function of redshift for p−values= 0.05 (purple solid line), 0.01 (orange solid line) and 0.005 (green solid line) computed using the Frequentist Likelihood-Ratio approach.

the low-mass end. In section 4.4 we will briefly investigate how such effects along with biasses induced by measurements can influence the results of our detector.

4.3.2 Bayesian approach

In the previous section we have used a Frequentist approach to set thresholds on sparsity measurement. The main philosophy of this approach is to study how likely a dataset $\boldsymbol{x}$ is given a model characterised by a set of parameters $\boldsymbol{\theta}$ which is achieved through the definition of a likelihood function $p(\boldsymbol{x}|\boldsymbol{\theta})$. An alternate way of tackling this problem is to now ask ourselves the question, how likely is a model given an observation. In this case we are no longer interested in the likelihood but the posterior distribution $p(\boldsymbol{\theta}|\boldsymbol{x})$. This simple inversion of two variables actually corresponds to a completely different way of handling data. Indeed in the Frequentist paradigm one considers that data is plentiful and experiments can be repeated indefinitely. In contrast, in its Bayesian counterpart one considers that data is scarce and hard to come by. In this light it is clear to see why the latter is usually favoured for cosmological data analysis, and given rise to many cosmology specific codes, such as CosmoMC (Lewis & Bridle, 2002), CosmoHammer (Akeret et al., 2013), and CobayA (Torrado & Lewis, 2019), as this way of thinking corresponds well with observational realities, for example we only have as single sky and can only look at a given object from a single angle.

A Bayesian approach however comes with some significant complications. In most practical cases the posterior distribution is extremely difficult if not impossible to express directly. As such it is customary to express it through the use of Bayes' Theorem,

$$p(\boldsymbol{\theta}|\boldsymbol{x}) = \frac{p(\boldsymbol{x}|\boldsymbol{\theta})\pi(\boldsymbol{\theta})}{\pi(\boldsymbol{x})}, \tag{4.10}$$

where $\pi(\boldsymbol{\theta})$ is the prior distribution for the parameter vector $\boldsymbol{\theta}$ and

$$\pi(x) = \int p(x|\boldsymbol{\theta})\pi(\boldsymbol{\theta})d\boldsymbol{\theta}, \tag{4.11}$$

is a normalisation factor, known as evidence. While these expressions may seem simple they often hide multidimensional integrals with complex boundaries, to avoid having to solve these equations one typically resorts to estimating the posterior distribution using Markov Chain Monte-Carlo (MCMC). We will not go into the details of the many different algorithms (see e.g Dunkley et al., 2005; Akeret et al., 2013, for reviews) and simply use the EMCEE[1] library (Foreman-Mackey et al., 2013), which uses the Goodman & Weare (2010) affine invariant algorithm.

Once we have estimated the posterior distribution we can, within the Bayesian formalism, systematically define the most powerful detection statistic associated to our binary test known as the Bayes factor

$$B_{\rm f} = \frac{\int_{V_1} p(\boldsymbol{x}|\boldsymbol{\theta})\pi(\boldsymbol{\theta})d\boldsymbol{\theta}}{\int_{V_0} p(\boldsymbol{x}|\boldsymbol{\theta})\pi(\boldsymbol{\theta})d\boldsymbol{\theta}}. \tag{4.12}$$

Where V_1 and V_0 denote the volumes of the parameter space respectively attributed to hypothesis $\mathcal{H}_1$ and $\mathcal{H}_0$. This statistic is also usually associated to a standard interpretation of its value (see e.g. Kass & Raftery, 1995; Trotta, 2007) relating it to the strength of the evidence in favour of $\mathcal{H}_1$. For instance, given a value of the Bayes factor the evidence can be seen as,

$$\begin{aligned} 0 < \log_{10} B_{\rm f} \leq 1/2, &\quad \text{marginal,} \\ 1/2 < \log_{10} B_{\rm f} \leq 1, &\quad \text{substantial,} \\ 1 < \log_{10} B_{\rm f} \leq 2, &\quad \text{strong, or} \\ 2 < \log_{10} B_{\rm f}, &\quad \text{decisive.} \end{aligned}$$

Returning to the task at hand, in order to access this information we must first model the likelihood. To do so we use the numerical catalogues from the MDPL2 simulation to calibrate the latter. In this case we increase the complexity of the model by not only separating the distribution of sparsities into two parts, corresponding to our two hypotheses, but into many sub-sets defined by $a_{\rm LMM}$, the scale factor at which the last major merger occurred, in order to capture any dependence on this parameter. We again find that the distributions of each sub-set are well fitted by a generalised β' distribution. From this we obtain a set of parameters $[\alpha, \beta, p, q]^\top$ which depend solely on $a_{\rm LMM}$. It is in fact this parameter that we will sample within our MCMC with the other four parameters being interpolated between our calibration points at each step. For simplicity, we choose to use a uniform prior on $a_{\rm LMM} \sim \mathcal{U}(0; a(z))$, where the upper bound of the prior is set to the epoch at which we observe the cluster.

Before moving onward to more complex models let us first compare the two detectors we have made so far. To do so we choose to plot their respective receiver operating characteristic (ROC) curves (see e.g. Fawcett, 2006), which show the probability of having a true detection, $\mathrm{P_r}(\Gamma > \Gamma_{\rm th}|\mathcal{H}_1)$, plotted against the probability of a false detection, $\mathrm{P_r}(\Gamma > \Gamma_{\rm th}|\mathcal{H}_0)$ for the same threshold. In other words, this means we are simply plotting the probability of finding a value of Γ that is larger than the threshold under the alternate hypothesis against that of finding a value of Γ larger than the

[1] https://emcee.readthedocs.io/en/stable/

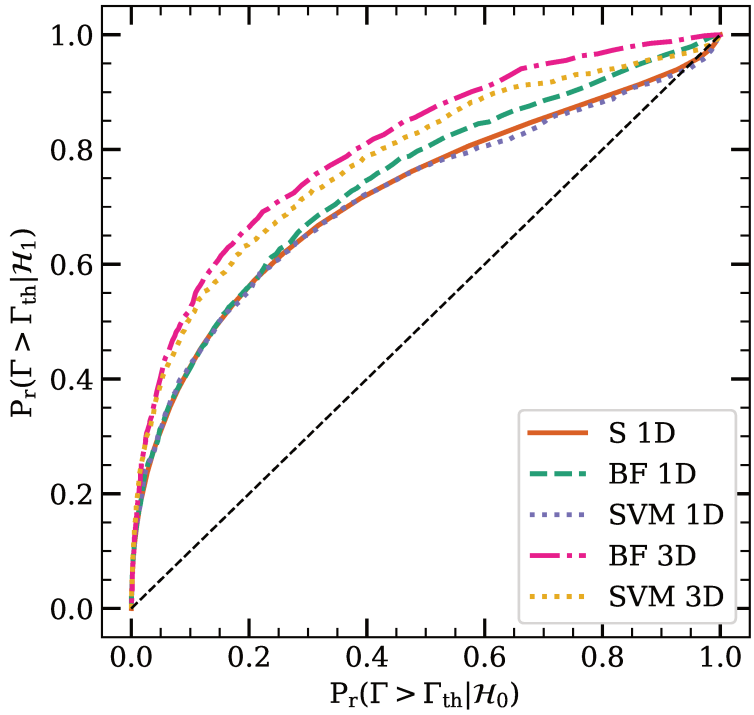

Figure 4.7: ROC curves associated with the binary tests studied in this work: the Frequentist sparsity test (S 1D, solid orange line), the Bayes Factor based on a single sparsity value (BF 1D, dashed green line) and using three values (BF 3D, dash-dotted magenta line), the Support Vector Machines with one sparsity value (SVM 1D, dotted purple line) and three sparsities (SVM 3D, dotted yellow line). What can be observed is that all 1D tests are equivalent at small false alarm rates and the only way to significantly increase the power of the test is to increase the amount of input data, i.e. adding a third mass measurement as in the BF 3D and SVM 3D cases.

same threshold under the null hypothesis. Essentially, we can graphically gauge the effectiveness of a given detector by looking how it behaves at a given false detection rate, if the detector has a higher rate of true detections then it is more effective, on the other hand if it has a lower rate of true detections then it is less effective. This graphically implies that the closer the ROC curve gets to the top left corner of the plot the more powerful the detector is at differentiating between the two hypotheses.

In Fig. 4.7 we plot the ROC curves corresponding to all the tests we have studied in this chapter. These curves have been evaluated using a sub-sample of 10^4 randomly selected haloes from the MDPL2 catalogues at $z = 0$ with masses $M_{200c} > 10^{13}\,h^{-1}\mathrm{M}_\odot$. These haloes are excluded from the calibration set. So far we have only introduced two of these detectors, the Frequentist direct sparsity approach (S 1D) and the single sparsity Bayes Factor (BF 1D). We see that these two methods yield a similar ROC curve at low false detection rates, with the Bayes factor only slightly outperforming the sparsity at false detection rates beyond 0.3 which are usually regarded as unreliable.

While this indicates that we do not gain much from the additional computational work needed to estimate the Bayes factor for a single sparsity, the systematic nature of this method makes it particularly simple to expand in order to include additional data, for instance to add additional sparsity measurements at different overdensities. To this effect we add a third mass measurement, M_{2500c}, to our sample, giving us access to

two additional sparsities, $s_{200,2500}$ and $s_{500,2500}$. With these sparsities we define a three dimensional space with coordinates,

$$\begin{cases} x = s_{200,500} - 1 \\ y = s_{200,2500} - 1 \\ z = s_{500,2500} - 1 \end{cases} \tag{4.13}$$

After estimating the joint distribution of sparsities in this space we find that switching to a spherical-like coordinate systems, $\boldsymbol{r} = [r, \vartheta, \varphi]^\top$, makes the descriptions of the likelihood function much simpler. In this coordinate system we can separate the angular and radial dependency of the likelihood. We model this dependency, marked by the two-vector $\boldsymbol{\alpha} = [\vartheta, \varphi]^\top$, with a multivariate normal distribution with mean $\boldsymbol{\mu}$ and covariance $\mathbf{C}$. As we have separated the radial dependency we can proceed by simply modelling the marginal sparsity radius distribution, $f(r; \boldsymbol{\theta})$. We find that this distribution exhibits strong skewness and so cannot be accurately captured into a normal distribution. However, using a Burr type XII distribution (Burr, 1942),

$$f(x, c, k, \lambda, \sigma) = \frac{ck}{\sigma}\left(\frac{x-\lambda}{\sigma}\right)^{c-1}\left[1 + \left(\frac{x-\lambda}{\sigma}\right)^2\right]^{-k-1}, \tag{4.14}$$

with additional displacement, λ which we fix to 0, and scale parameter, σ, provides a reasonably good fit to the marginal distribution of sparsity radii r. The resulting full likelihood,

$$L(\boldsymbol{r}; \boldsymbol{\theta}, \boldsymbol{\mu}, \mathbf{C}) = \frac{f(r; \boldsymbol{\theta})}{2\pi\sqrt{|\mathbf{C}|}} \exp\left[-\frac{1}{2}(\boldsymbol{\alpha} - \boldsymbol{\mu})^\top \mathbf{C}^{-1}(\boldsymbol{\alpha} - \boldsymbol{\mu})\right], \tag{4.15}$$

is thus described by nine parameters, three which are constrained by fitting the marginal sparsity radius distribution, and five which are computed by estimating the unbiased sample mean and covariance of the sparsity angles, respectively two in $\boldsymbol{\mu}$ and three in $\mathbf{C}$.

In a similar fashion to the one dimensional case all these parameters are fitted on sub-sets of haloes depending on their epoch of the last major merger to retrieve their dependence on $a_{\rm LMM}$. We sample the posterior distributions of this parameter using MCMC, again choosing a flat prior on $a_{\rm LMM}$ for the same test sample as previously. We use the resulting posteriors to calculate the Bayes factor and plot the corresponding ROC curve (BF 3D in Fig. 4.7). We see that the addition of information through the extra mass measurement increases the detection power considerably with the ROC curve being raised up with respect to the 1 sparsity test. At a constant false detection rate of 10 per cent the additional mass raises the true detection rate from 40 to 50 per cent.

4.3.3 Support vector machines

A third, less analytically cumbersome, alternative is to use machine learning techniques designed for classification. Machine learning is often associated to Convolutional Neural Networks (see eg. Lecun et al., 2015, for a review) which are very efficient and have been profusely used to classify large datasets, both in terms of dimensionality and size, with recent examples in extra-galactic astronomy including galaxy morphology classification (e.g. Hocking et al., 2018; Martin et al., 2020; Abul Hayat et al., 2020; Cheng et al., 2021; Spindler et al., 2021) detection of strong gravitational lenses (e.g. Jacobs et al., 2017, 2019; Lanusse et al., 2018; Cañameras et al., 2020; Huang et al., 2020, 2021; He et al.,

2020; Gentile et al., 2021; Stein et al., 2021) galaxy merger detection (Ćiprijanović et al., 2021) and galaxy cluster merger time estimation (Koppula et al., 2021). In the case at hand however, as we have a problem with only a small number of dimensions, instead of using high complexity neural networks it is preferable to use simpler techniques such as random forest classifiers (see e.g. Breiman, 2001) or Support Vector Machines (SVM; see e.g. Cristianini & Shawe-Taylor, 2000) which can be trained as classifiers for the two hypotheses defined in Eq. (4.5) using the halo catalogues from the simulations.

We choose to use SVMs which work on the principle of finding the boundary which best separates the two hypotheses. This boundary can have an arbitrary shape by mapping the data points into a new euclidean space through a non-linear transformation where it defines a planar boundary, in opposition to random forests which are confined to using only horizontal and vertical boundaries in the original space, albeit to arbitrary complexity. Non-linear transformations are usually avoided when using large data-sets as they can be slow to converge, and for this reason we restrict ourselves to linear transformation. This approach does have the significant advantage over its Bayesian and Frequentist counterparts of being implemented in the 'user-friendly' SCIKIT-LEARN[2] (Pedregosa et al., 2011) Python package which allows for fast implementations with both little knowledge of Python and little input, beyond the data, from the user.

For comparison with our previous detectors we set-up two SVMs, using as input either one sparsity, $s_{200,500}$ or three sparsities. In Fig. 4.7 we compare how these SVMs fare against the other methods by plotting their ROC curves estimated from the same test data-set that was excluded from the training of the SVMs. We see that the ROC curve of the one sparsity SVM behaves similarly to both the Bayes factor and direct sparsity test and that the three sparsity SVM is only slightly outperformed by the Bayes factor. This result has two main implications, firstly that a statistical test based on sparsity can be designed in a simple way without loss of differentiation power and secondly this comforts our analysis, showing that these results can be recovered through various independent means, making sparsity an all the more viable proxy to identify cluster undergoing a recent major merger.

4.3.4 Estimating the epoch of the last major merger

In the previous sections we have used halo sparsity simply as a means of detecting if a merger has recently taken place or not. An interesting byproduct of the Bayesian approach however is that it can be expanded to not only detect if a merger has recently taken place but also *estimate* when this event is most likely to have happened. This is done by studying the posterior distribution directly instead of simply using it to calculate the Bayes factor.

We again begin by turning our attention to the one sparsity case. In Fig. 4.8 we plot the posterior distributions, $p(a_{\rm LMM}|s_{200,500})$, for four different values of $s_{200,500} = 1.2,\ 1.7,\ 2,$ and 3 at $z = 0$. We see that for larger sparsities the posterior exhibits two peaks. These are generated from the pulse feature seen in the joint distribution in Fig. 4.4 which is a direct consequence of the universal impact major mergers have on the evolution of sparsity as seen in Fig. 4.3. We notice that the higher the sparsity is, the less likely it is to have had its last major merger in the distant past, this is in fact the behaviour we have previously used to detect mergers.

An unwanted consequence of the major merger pulse however is that a considerable number of haloes which have undergone major mergers between $-1/2 < T(a_{\rm LMM}|a(z)) <$

[2] https://scikit-learn.org/stable/

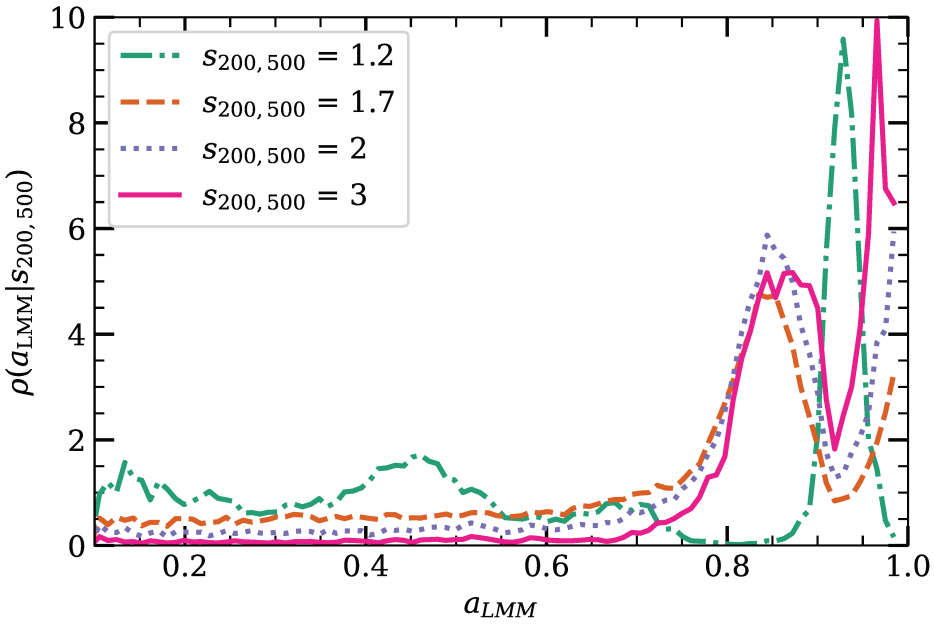

Figure 4.8: Posterior distributions for different values of the sparsity $s_{200,500} = 1.2$ (dash-dotted green line), 1.7 (dashed orange line), 2 (dotted purple line) and 3 (solid magenta line). We can see that for large sparsity values, the distributions are bimodal at recent epoch, while low values produce both a continuous distribution at low scale factor values as well as a single peak at recent epochs corresponding to a confusion region. This induce a degeneracy that needs to be broken if we are to accurately estimate $a_{\rm LMM}$.

$-1/4$, have sparsities in the same range to haloes that have not undergone a recent merger. This overlap in the two regions causes the appearance of a strong peak at recent times when looking at low sparsity values. This peak implies that we may have quiescent haloes be erroneously identified as merging and vice versa, causing a degeneracy.

If we now include the two additional sparsities in our sample we can break this degeneracy due to the sparsity pulses at different overdensities not being exactly in phase. In Fig. 4.9 we show the posteriors for three haloes that fall in this degeneracy. The one sparsity posteriors are shown in orange and the three sparsity posteriors are shown in purple. In addition to the posteriors we show both the median estimated time of the last major merger and the 68 per cent credible interval around this value as a vertical line and coloured region. We compare this recovered value to the true epoch of the last major merger of each halo which is shown as a dashed vertical line. We see that when using only one sparsity each of these haloes is identified as not having a recent merger. This is not the case of the three sparsity estimator which correctly identifies the epoch of the last major merger, within the credible interval, in all three cases. Given what we can see in this figure it is now easy to understand that the increase in differentiation power between a one and three sparsity detectors seen in Fig. 4.7 originates from the same phemenon, i.e. haloes initially misidentified as quiescent now being identified as merging.

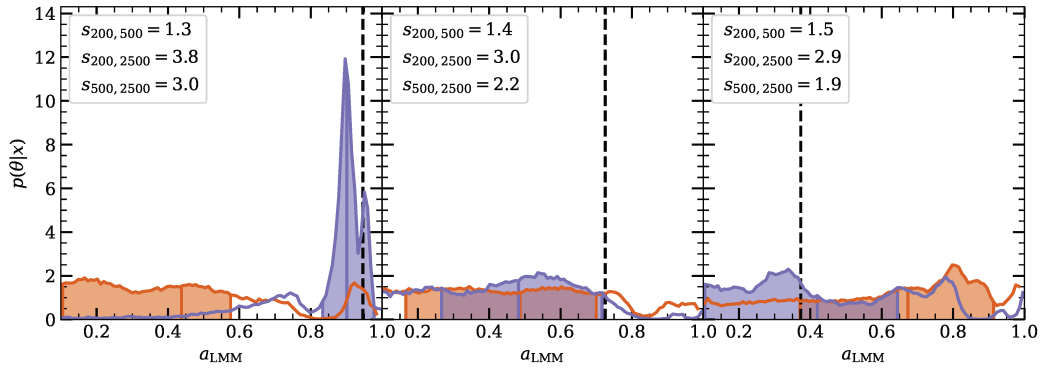

Figure 4.9: Posterior distributions of the last major merger epoch for three selected haloes with different sparsity values from the $z = 0$ halo catalogue. The shaded areas corresponds to the 68% credible interval around the median (coloured vertical line) assuming a single (orange) and three sparsity (purple) measurements. The black vertical dashed lines mark the true fiducial value of $a_{\rm LMM}$ for each of the selected haloes.

4.4 Toward practical applications

Now that we have presented all these statistical tools we wish to apply them to observational data. For this purpose we have specifically developed the numerical code LAMMAS[3] which given the mass measurements M_{200c}, M_{500c} and M_{2500c} of a galaxy cluster computes the sparsity data vector $\boldsymbol{D} = \{s_{200,500}, s_{200,2500}, s_{500,2500}\}$, where the last two values are only computed if the estimate of M_{2500c} is available. The package is designed to calculate the Frequentist statistics discussed in Section 4.3.1 and to perform the Bayesian computation presented in Section 4.3.2. In addition, the code only computes the Frequentist p-value and its associated uncertainty for $s_{200,500}$. Bayesian statistics are measured for both one and three sparsities, these include the posterior distributions $p(a_{\rm LMM}|\boldsymbol{D})$ and their associated marginal statistics, along with the Bayes factor, $B_{\rm f}$, using the available data.

In this section we will first validate and test the efficiency of the code on a sample of haloes that was not used in the calibration, we will then investigate how robust our analysis is to observational biases in particular we will turn our interest towards biases coming from lensing observations, the assumption of hydrostatic equilibrium, or simply how assuming the NFW profile may impact our result. After this we apply our method to perform a preliminary analysis of two galaxy clusters, A383 and A2345.

4.4.1 Validation on simulated haloes

Unlike our previous analysis, LAMMAS is calibrated using data coming from the main Uchuu simulation box (Ishiyama et al., 2021). This choice allows the code to benefit from the larger volume, finer redshift coverage, and higher resolution of the simulation with respect to MDPL2. This choice also comes with the advantage that we do not have to select haloes to form a testing set, i.e. not used for calibration, as we can simply use haloes from MDPL2. This also allows us to test if the code is robust to small changes in the cosmological parameters as the MDPL2 simulation was run using an earlier Planck cosmology, 2013, than the Uchuu simulation, 2015. Finally to ensure that our pipeline

[3] https://gitlab.obspm.fr/trichardson/lammas

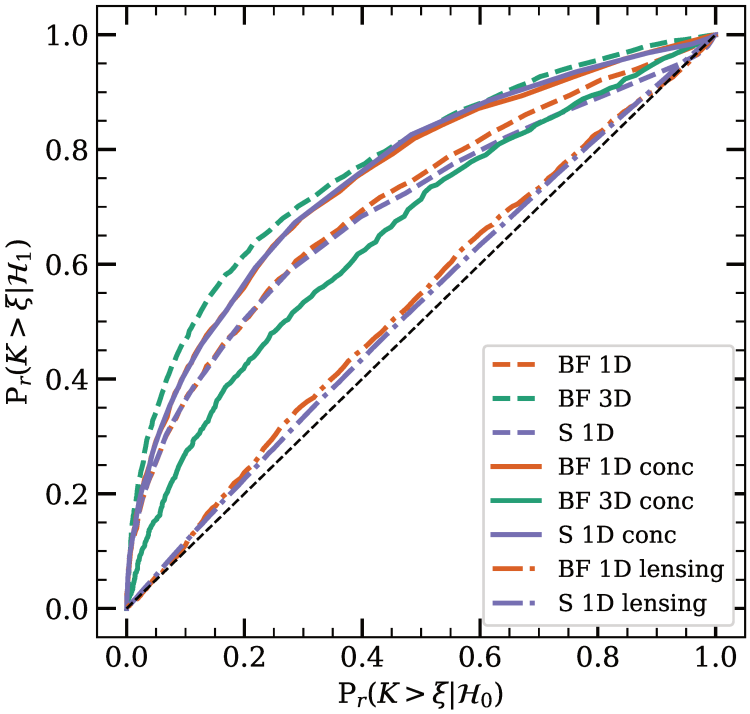

Figure 4.10: ROC curves estimated from the validation dataset for sparsities estimated from the N-body halo masses (dashed lines), from the concentration parameter of the best-fitting NFW-profile (solid lines) and in the case of a conservative model for the mass bias induced by lensing observations (dash-dotted lines) in the case of the single sparsity Bayesian (BF 1D, orange curves) and frequentist (S 1D, blue curves) estimators and the three sparsity Bayesian estimator (BF 3D, green curves). We can see that in all cases, S 1D and BF 1D tests offer a similar detection power. Comparing the BF 3D curves to the S 1D ones, it is clear that while adding an independent sparsity measurement increases the detection power, this is not the case when the sparsities are deduced from the concentration parameter, with the latter having the opposite effect. Finally we can also see that strong mass biases have a strong negative impact on the efficiency of the detection of mergers.

functions in practical settings we choose to perform all validation checks at $z = 0.248$, a typical redshift for lensing observations of clusters (Euclid Collaboration et al., 2019).

Similarly to the analysis in Sections 4.3.1 and 4.3.2, to evaluate the efficiency of each method we estimate their respective ROC curves and plot them in Fig. 4.10. This figure contains many curves which will be commented throughout this section but for now let us focus on the dashed lines which relate to the baseline analysis with no sources of bias. If we compare these lines to those seen in Fig. 4.7 we see that LAMMAS provides a similar detection efficiency to the test statistics shown previously, meaning that our analysis is indeed robust to a change in both resolution and a small change of cosmology.

As the ROC curves presented above are only able to quantify the efficiency of a given detection procedure, in order to quantify how well we are able to estimate when the last major merger took place we introduce three metrics:

1. $\alpha_{\rm cc}$, the accuracy as given by the frequency at which the true value $a_{\rm LMM}$ of a halo is recovered within the $1\,\sigma$ credible interval,

2. $\hat{a}_{\rm LMM}$, the estimated epoch of the last major merger,

3. $\sigma/\hat{a}_{\rm LMM}$, the relative width of the $1\,\sigma$ credible interval.

Fig. 4.11 shows each of these metrics as a function of the scale factor, $a_{\rm LMM}$. We employ the same colour scheme as Fig. 4.9, as such orange curves represent analyses using only $s_{200,500}$ and blue curves using three sparsities, which we hereon refer to as the 1S and 3S estimators, respectively. The two curves in the lower panels of this figure show the median value along with the 68 per cent confidence interval around the latter.

At first glance, one may be tempted to say that the 1S estimator is overall more accurate at finding the correct merger time than the second method. However we must contrast what is seen in the top panel with the two lower panels. Indeed here we see that the main reason for which the accuracy is so high for the 1S estimator is that once two dynamical times have past the estimator simply predicts a central value with very large uncertainty, which in practical cases should only be considered as an upper bound on $a_{\rm LMM}$. In geometric terms the wider the error bars are the more likely the correct answer is to fall within them.

Focusing now on the regime of recent mergers, $0.68 < a_{\rm LMM} < 0.8$, we see that the 3S estimator dominates this regime, not only being more accurate but also providing tight constraints. A strong degeneracy between the two peak endures however, with both estimators favouring the second peak in the 'merger pulse' causing the accuracy to drop for very recent mergers. Finally we see in the central panel that although the degeneracy between the dip of the pulse and the quiescent regime is somewhat weakened by introducing a third mass measurement but is however still somewhat present in the form of a strong dip in $\hat{a}_{\rm LMM}$.

Overall, after this short analysis we are confident that our detection method is robust to small changes in cosmology and data provenance. We have also been able to test the effectiveness of the estimation pipeline and have found that the latter is capable of accurately differentiating between quiescent and merging haloes but still suffers from several degeneracies, most notably between the two peaks and the dip in the pulse feature, which will have to be kept in mind when using this pipeline.

4.4.2 Systematic bias

As previously mentioned the statistical methodology presented here relies on mass estimated coming from N-body simulations. It is a well known fact that these masses are however biased with respect to the masses of objects that can be observed in the sky. These biases can be either deterministic or stochastic in nature and can be sourced by multiple effects, from baryonic processes to observational constraints. As such before we apply our methods to observations we first want to check how robust they are going to be with respect to systematic biases. In practice we will review conservative estimate that we introduce into our data to then quantify the effect they have on the methods. Here we restrict our analysis to the detectors, but note that the estimators will also be influenced by these effects.

Weak lensing mass bias

We first turn our attention towards masses derived from weak lensing observations. These masses are often considered to be closer to the full gravitational mass of the object. They are however affected by multiple biases, stemming from the assumptions made to extract the physical information from the observed tangential shear, quality

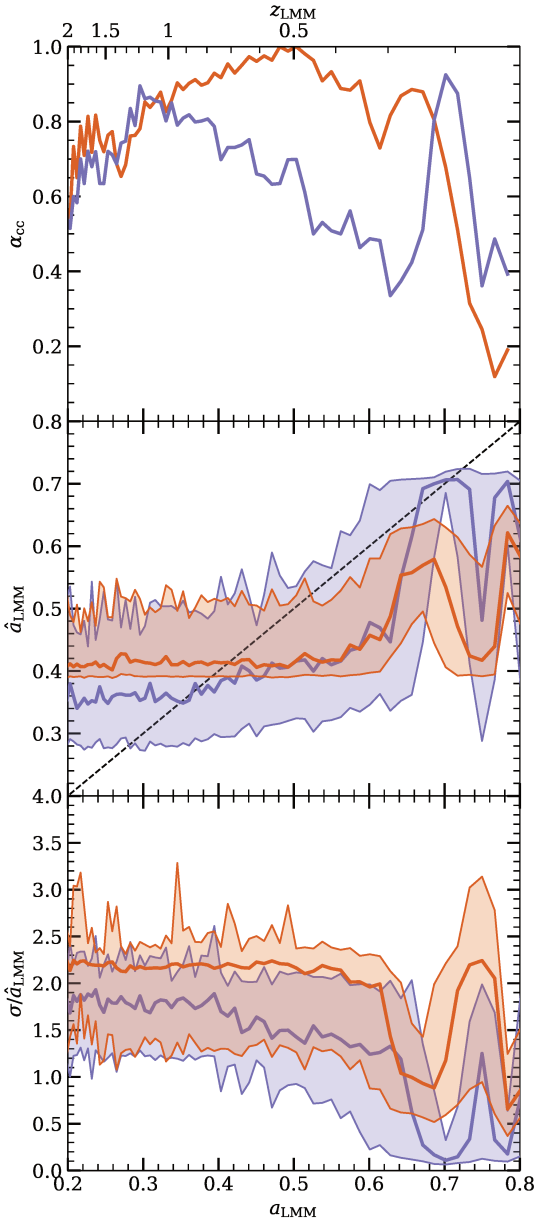

Figure 4.11: *Top:* Accuracy of the estimation of the epoch of the last major merger, $\alpha_{\rm cc}$, as a function of the true value $a_{\rm LMM}$ of the haloes in the validation sample for both the 1S (orange solid line) and 3S (blue solid line) estimators respectively. *Middle:* Median value of the estimated epoch of the last major merger, $\hat{a}_{\rm LMM}$, as function of the true value for the 1S (orange curves) and 3S (blue curves) estimators respectively. The shaded areas correspond to the 68% interval around the median, while the dashed diagonal line gives the ideal value of the estimator $\hat{a}_{\rm LMM} = a_{\rm LMM}$. *Bottom:* relative width of the 68% interval around the median value of $\hat{a}_{\rm LMM}$ as a function of the true value $a_{\rm LMM}$ for the 1S (orange curves) and 3S (blue curves) estimators respectively. We refer the reader to the text for a detailed discussion of the various trends.

Table 4.3: Sparsity bias and scatter obtained from the weak lensing mass bias estimates by Becker & Kravtsov (2011).

	$n_{\rm gal}$	$b^{\rm WL}_{200,500}$	$\sigma^{\rm WL}_{200,500}$
	10	0.04 ± 0.02	0.51 ± 0.03
$z = 0.25$	20	0.01 ± 0.01	0.40 ± 0.02
	40	0.03 ± 0.01	0.35 ± 0.02
	10	0.07 ± 0.07	0.76 ± 0.03
$z = 0.5$	20	0.02 ± 0.02	0.58 ± 0.04
	40	0.03 ± 0.01	0.49 ± 0.03

of the data and systematic effects such as projection effects, intrinsic alignments and redshift calibration.

Becker & Kravtsov (2011) quantify the general systematic error induced on the mass,

$$M^{\rm WL}_{\Delta} = M_{\Delta} \exp(\beta_{\Delta}) \exp(\sigma_{\Delta} X), \tag{4.16}$$

using two bias terms, a deterministic bias β_{Δ} and a stochastic bias σ_{Δ} which quantifies the spread of a log-normal distribution, with $X \sim \mathcal{N}(0,1)$. If we make the pessimistic assumption that the scatter on one mass is independent on the scatter on the other then we can write the resulting biased sparsity as:

$$s^{\rm WL}_{\Delta_1,\Delta_2} = s_{\Delta_1,\Delta_2} \left(b^{\rm WL}_{\Delta_1,\Delta_2} + 1\right) \exp\left(\sigma^{\rm WL}_{\Delta_1,\Delta_2} X\right), \tag{4.17}$$

where $b^{\rm WL}_{\Delta_1,\Delta_2} = \exp(\beta_{\Delta_1} - \beta_{\Delta_2}) - 1$ and $\sigma^{\rm WL}_{\Delta_1,\Delta_2} = \sqrt{\sigma^2_{\Delta_1} + \sigma^2_{\Delta_2}}$. We calculate these biases for the values of Becker & Kravtsov (2011) for $\Delta_1 = 200$ and $\Delta_2 = 500$, and collect the resulting sparsity biases in Tab. 4.3, where errors are propagated from the original errors. These values are computed for two redshifts and at three galaxy number densities, in units of arcmin^{-2} and assuming an intrinsic shape noise of $\sigma_e = 0.3$.

We see that the ratio operation reduces the deterministic bias considerably, with in most cases the resulting sparsity bias being consistent with 0, on the other hand this same operation compounds the scatter making the scatter on the resulting sparsity much larger than the scatter on the two masses. We use these values to generate a sample of biased sparsities $s^{\rm WL}_{200,500}$ by combining the data from the halo catalogues and randomly sampled biases, requiring only that $s^{\rm WL}_{200,500} > 1$. Using the values quoted by Becker & Kravtsov (2011) for a *Euclid*-like survey, i.e. $n_{\rm gal} = 40$ arcmin^{-2} at $z = 0.25$, we run the Frequentist and Bayesian 1S detector in order to produce two ROC curves that we show in Fig. 4.10. We see that these ROC curve are much closer to the diagonal indicating that we have lost considerable detection power. Indeed this is to be expected as the pulse in $s_{200,500}$ on average only increases the sparsity by ~ 0.2, the signal is therefore completely drowned by the noise coming from the observations.

This however raises the question, *when does the sparsity become a viable detector?* To answer this we repeat the Frequentist test, as it is faster than the Bayesian test and yields similar results, whilst varying $\sigma^{\rm WL}_{\Delta_1,\Delta_2}$. As it would be cumbersome to look at each resulting ROC curve individually we compress the information from these curves by evaluating the Area Under the Curve (AUC) to quantify whether the detector is working as intended or not. The general interpretation for this statistic is that a random classifier, i.e. which randomly selects which class to put the data point in, should have AUC $= 0.5$ with its ROC curve on the diagonal and a perfect detector should have

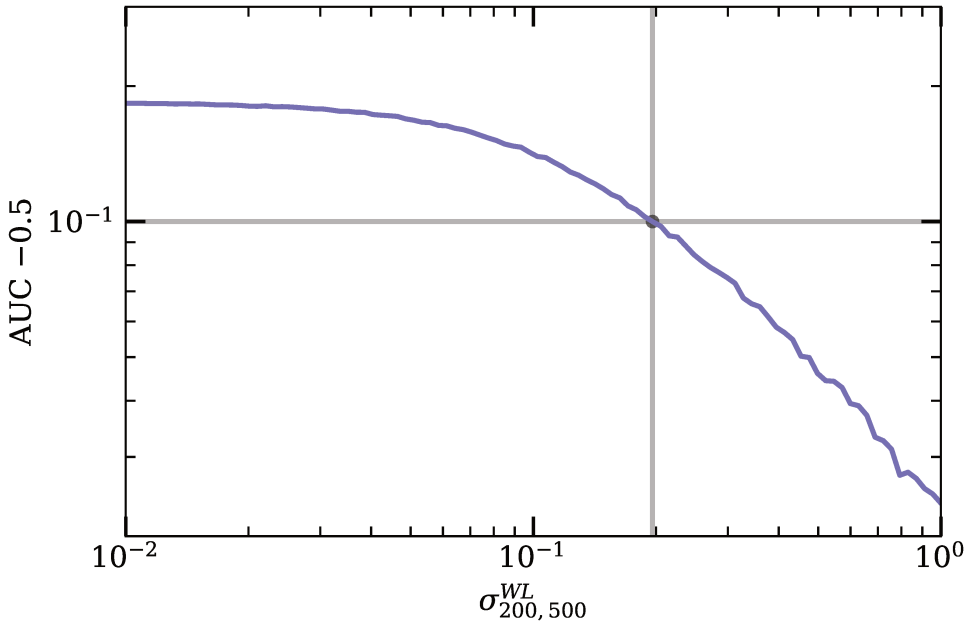

Figure 4.12: Area Under the ROC Curve (AUC) as function of the scatter on the measured sparsity for WL mass estimates. A random classifier has an AUC= 0.5. The vertical and horizontal lines denote AUC = 0.6 and the corresponding scatter $\sigma^{\rm WL}_{200,500} = 0.2$, denoting the point, $\sigma^{\rm WL}_{200,500} > 0.2$, beyond which the detector can be considered ineffective at detecting recent mergers.

AUC = 1. A detector is considered passable if AUC ~ 0.6 and good if AUC > 0.7. In Fig. 4.12 we plot the resulting AUC as a function of the stochastic bias parameter. We see that the AUC remains roughly constant until the scatter reaches the order of magnitude of the signal we are trying to detect, $\sigma^{\rm WL}_{\Delta_1,\Delta_2} \sim 0.1$ and that beyond this value the AUC decreases rapidly. Finally, we mark the point at which $\sigma^{\rm WL}_{\Delta_1,\Delta_2} \simeq 0.2$ at which the noise becomes so large that the detector is no longer considered passable.

Hydrostatic mass bias

Having so far discussed how one can recover the mass and sparsity of a galaxy cluster through weak lensing observations, it is important to recall that one can also recover the masses of cluster using X-ray observations of the ICM. These observations are often more precise as they do not rely on the sparse sampling of background sources. However as we are now studying the baryonic component, which we have neglected throughout this work, these masses are biased with respect to the full mass of the halo. To extract the mass from these observations it is often required to assume the gas is in hydrostatic equilibrium within the cluster's gravitational potential. It has been shown that deviations from this condition tend to introduce a radially dependent bias in the mass reconstruction (see e.g. Biffi et al., 2016; Eckert et al., 2019; Gianfagna et al., 2021; Ettori & Eckert, 2022), which would therefore influence the resulting sparsity. Biffi et al. (2016) studied this bias using a suite of 29 cosmological zoom simulations of clusters modelling both gravitation and baryonic effects. In their analysis they measure the mass bias for three overdensities, $\Delta = 200,\ 500$, and 2500, and seperate their sample into four sub-samples, Cool-Core (CC) or No Cool-Core (NCC) as defined with respect

Table 4.4: Sparsity bias from the hydrostatic mass bias estimated of Biffi et al. (2016) for different categories of simulated clusters.

	$b^{\rm HE}_{200,500}$	$b^{\rm HE}_{500,2500}$	$b^{\rm HE}_{200,2500}$
All	0.003 ± 0.032	-0.037 ± 0.025	-0.033 ± 0.034
CC	-0.009 ± 0.031	-0.151 ± 0.038	-0.162 ± 0.041
NCC	0.019 ± 0.046	0.005 ± 0.027	0.023 ± 0.041
Regular	0.032 ± 0.089	0.025 ± 0.037	0.057 ± 0.082
Disturbed	-0.017 ± 0.077	-0.080 ± 0.086	-0.098 ± 0.052

to the entropy inside the core of the clusters, and regular or perturbed with regards to how the centre of mass is offset with the peak of the potential and the fraction of substructures.

Using these bias estimates and following the procedure of Corasaniti et al. (2018) we estimate the resulting sparsity biases and report them in Tab. 4.4. Again we find that the sparsity strongly reduces the deterministic bias, with biases being only of the order of a few per cent and vanishing in most cases. It is important to note that while these biases are small they do not account for the intrinsic scatter the measurements will have about the true value. As we have seen in the case of Weak lensing it is in fact this stochastic bias which can overshadow the signal and severly hinder the detector from functioning as intended. While the sample analysed by Biffi et al. (2016) is too small to go into the detail of measuring the scatter we can however imagine that the response of the detector will be similar to what is seen in Fig. 4.12, meaning that as long as the intrinsic scatter in the measurements is smaller than the signal we want to detect, i.e. the approximate height of the peak, then the detector will be unaffected by such a bias.

Concentration mass bias

Most methods used to recover the masses from cluster observations resort to assuming a profile for the dark matter component. We have seen at the beginning of this chapter that sparsities that are deduced from the concentration parameter of a best fitted NFW profile are biased with respect to sparsities measured directly using the halo masses.

The question we can now ask ourselves here is, *How does this affect the detection procedure?* To answer this we extract the concentrations from our test sample of haloes and then convert them into sparsities. We run them through our detection algorithms and plot the resulting ROC curves in Fig. 4.7. Surprisingly we find that using the sparsities derived assuming the NFW improves the performance of the 1S detectors. This is likely due to the fact that when haloes are quiescent then the NFW sparsities, as can be seen in Fig. 4.1, are systematically underestimated, while during a merger event the NFW sparsity overestimates its N-body counterpart. This effect, likely due to numerical artefacts in the fitting procedure (Balmès et al., 2014), added to the fact that the scatter generated by the fitting procedure is relatively small, ($\sim 10\%$), compared to the signal we want to detect, results in this increased detection power.

If we now look at the 3S case we see that this is no longer true with the NFW 3S curve being far lower than even the 1S curve using N-body masses. In this case even if the boost in signal-to-noise still occurs for $s_{200,500}$, this is not the case for $s_{200,2500}$, as it can be seen in Fig. 4.1 the merging population also has underestimated sparsities, thus reducing the signal to noise. In addition, the fact that all three sparsities are now correlated through the concentration, changes the shape of the impulses seen at inner

radii. Consequently, they no longer bring any new information, quite the opposite they are detrimental as they no longer break the degeneracy between the dip in the pulse and quiescent state. The end result of this is that many merging haloes are then falsely identified as quiescent.

4.4.3 Preliminary Cluster applications

Keeping all of these effect in mind we will apply our methodology to two well-studied galaxy clusters. One of which is well known to be quiescent and a second one which has all the hallmarks of a perturbed system.

Abell 383

Let us start with Abell 383, a not too distant cluster at $z = 0.187$ which has been the subject of many studies both in X-ray (Böhringer et al., 2004; Vikhlinin et al., 2005) and optical bands (Miyazaki et al., 2002; Postman et al., 2012) and several using gravitational lensing (e.g. Okabe & Smith, 2016; Umetsu et al., 2016; Klein et al., 2019). Overall this cluster is thought to be relaxed, with a roughly spherical X-ray emission profile. The mass of the inner cluster has been constrained to

$$M_{500c} = (3.10 \pm 0.32) \cdot 10^{14}\,\mathrm{M}_\odot \text{ and } M_{2500c} = (1.68 \pm 0.15) \cdot 10^{14}\,\mathrm{M}_\odot$$

using Chandra X-ray observations (Vikhlinin et al., 2005). From these measurements we compute the halo sparsity $s_{500,2500} = 1.84 \pm 0.25$ that is close to the median of the quiescent halo sparsity distribution. While we have not calibrated our pipeline to use this specific sparsity on its own this gives us a good indication that the cluster is indeed relaxed.

As this cluster has also been extensively studied through weak lensing we are able to use the statistical test derived here on the masses provided in the latest version of the Literature catalogues of Lensing Clusters (LC^2 Sereno, 2015). Specifically, we use the mass estimates derived from the analysis of the latest profile data (Klein et al., 2019):

$$\begin{aligned} M_{200c} &= (8.55 \pm 1.7) \cdot 10^{14}\,\mathrm{M}_\odot, \\ M_{500c} &= (5.82 \pm 1.15) \cdot 10^{14}\,\mathrm{M}_\odot, \text{ and} \\ M_{2500c} &= (2.221 \pm 0.439) \cdot 10^{14}\,\mathrm{M}_\odot, \end{aligned}$$

from which we compute the resulting sparsities,

$$\begin{aligned} s_{200,500} &= 1.47 \pm 0.41 \\ s_{200,2500} &= 3.85 \pm 1.08, \text{and} \\ s_{500,2500} &= 2.62 \pm 0.73. \end{aligned}$$

Running these values through the pipeline, we obtain a p-value p = 0.21 and Bayes Factor $B_\mathrm{f} = 0.84$, incorporating errors on the measurement of $s_{200,500}$ yields a higher p-value, p = 0.40, which can be interpreted as an effective sparsity of $s^{\mathrm{eff}}_{200,500} = 1.40$. These results are strongly in favour of A383 not having undergone a recent merger.

Abell 2345

We now move on to study a second cluster, A2345. This cluster is at a similar redshift to the previous one, $z = 0.179$, and has also been thoroughly studied in the literature. In

opposition to the previous cluster this system has been identified as strongly perturbed. Indeed this has been seen through optical observations of its galaxy distribution (Dahle et al., 2002; Boschin et al., 2010), which was initially thought to be peaked around the brightest cluster galaxy (Dahle et al., 2002; Cypriano et al., 2004) but was then shown to have a complex structure, which suggest that the cluster is composed of three large sub-clusters, when looking at large fields of view. Radio and X-ray observations of its ICM (e.g. Giovannini et al., 1999; Bonafede et al., 2009; Lovisari et al., 2017; Golovich et al., 2019; Stuardi et al., 2021) have revealed the presence of large radio relics and disturbed morphology in the X-ray emission usually associated with merger activity.

We again use the weak lensing masses from the LC^2-catalogue (Sereno, 2015),

$$\begin{aligned} M_{200c} &= (28.44 \pm 10.76) \cdot 10^{14}\,\mathrm{M}_\odot, \\ M_{500c} &= (6.52 \pm 2.47) \cdot 10^{14}\,\mathrm{M}_\odot, \text{ and} \\ M_{2500c} &= (0.32 \pm 0.12) \cdot 10^{14}\,\mathrm{M}_\odot, \end{aligned}$$

Which result in the sparsities,

$$\begin{aligned} s_{200,500} &= 4.36 \pm 2.33, \\ s_{200,2500} &= 87.51 \pm 46.83, \text{ and} \\ s_{500,2500} &= 20.06 \pm 10.74. \end{aligned}$$

Using only $s_{200,500}$ results in a very small p-value, p = $4.6 \cdot 10^{-5}$ which remains small even accounting for errors on the measurement , p = $7.5 \cdot 10^{-4}$. The latter can be interpreted as an effective sparsity of $s^{\mathrm{eff}}_{200,500} = 2.76$, while this value is significantly lower than the measured value, both still strongly favour the signature of a major merger event, that is confirmed by the combined analysis of the three sparsity measurements for which we find a divergent Bayes factor.

In Fig. 4.13 we plot the posterior distribution for both the single sparsity $s_{200,500}$ (orange solid line) and for the three sparsity estimates (purple solid line). We indeed see that both cases strongly favour a recent merger with the one sparsity estimator estimating the merger took place at redshift $z_{\mathrm{LMM}} = 0.30^{+0.04}_{-0.07}$, while the 3 sparsity method estimated the event took place earlier at $z_{\mathrm{LMM}} = 0.39 \pm 0.02$. This would suggest that the merger occurred $t_{\mathrm{LMM}} = 2.1 \pm 0.2$ Gyr ago. We note however, in the light of the discussion above, that this event may be in fact more recent as we have seen that both estimators artificially disfavour very recent mergers, typically attributing them to the second peak in the sparsity distribution.

4.5 Summary

In this chapter we have discussed how major mergers affect the mass profiles of massive dark matter haloes in the mass range of galaxy clusters through the scope of halo sparsity. To this end we have studied a sample of dark matter haloes coming from the MDPL2 and Uchuu simulations. We have seen that sparsity is able to provide valuable insight into this period where most fitting formulae, such as the NFW profile, no longer apply.

We found that major mergers leave a characteristic imprint in the sparsity history which manifests as a fast pulse. In addition, the shape of this pulse is independent of when the merger took place but however dependent on the sparsity we are studying. Overall, this pulse manifests as a high value of sparsity which suggest that the merger

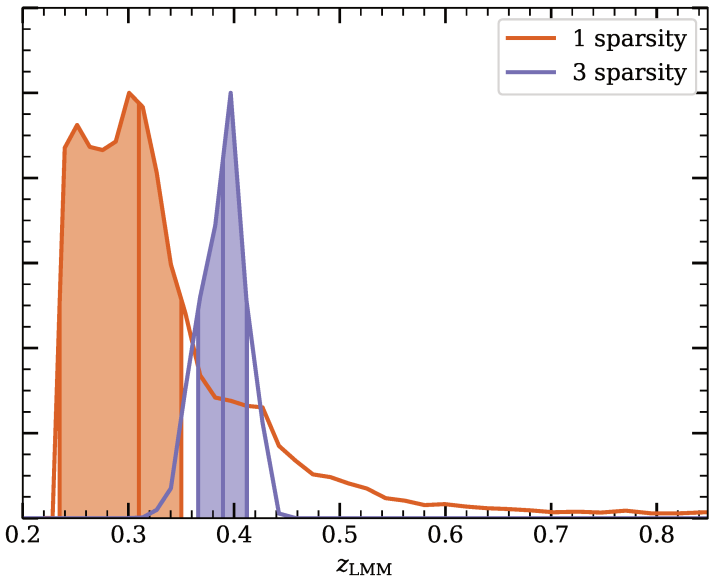

Figure 4.13: Posterior distributions Abell 2345 obtained using three sparsity measurements from the lensing cluster masses in the LC^2 catalogue (Sereno, 2015) using the shear data from (Okabe et al., 2010). The vertical lines indicates the median value of z_{LMM}, while the shaded are corresponds to the 68% credible region around the median.

displace the mass in the inner part of the halo with respect to mass at more distant radii. Similar to the analysis of Wang et al. (2020a) we find that the pulse has a typical duration of ~ 2 dynamical times after which the quiescent regime is recovered.

We find that the universal imprint left by mergers in the sparsity history of haloes is also present in the distribution of sparsities when separating as a function of time since the last major merger. Seperating haloes into two categories, merging and quiescent haloes, shows that the two populations are described by two distinct distributions, with mergers largely contributing to the scatter in the full sparsity distribution.

These differences between the two distributions allow us to statistically distinguish the two populations of haloes, and to test whether or not a galaxy cluster has recently undergone a major merger or not. For this purpose we developed multiple methods based on binary Frequentist test, Bayes factors, and SVMs which yield similar results, which can be improved by introducing additional mass measurements. This has allowed us to develop a numerical code that can be used to investigate if an observed cluster has undergone a recent major merger. As a test case we have presented a preliminary analysis of two clusters, A383 a relatively quiescent cluster, and A2345 a strongly perturbed cluster.

This work can be expanded in several ways, most notably by studying how baryonic physics impact the shape of the merger pulse as this will have a direct impact on the effectiveness of our algorithm. It may also be interesting to investigate if there is a possible cosmology dependence of the pulse signature and if so to what extent, which could be achieved by extending this analysis to large volume simulations in non-standard cosmologies such as the RayGalGroupSims suite (Corasaniti et al., 2018; Rasera et al., 2022).

5 | Cosmology with Sparsity

At the time of writing one of the main topics of discussion in cosmology is tensions between various cosmological probes. In particular, recurrent focus is put on the tension between H_0 measurements from the CMB (e.g. Planck Collaboration et al., 2020) and measurements with Supernovae type Ia (e.g. Riess et al., 2022) and strong lensing time delays (e.g. Treu et al., 2022) and the S_8 tension between measurement on the CMB (e.g. Planck Collaboration et al., 2020) and recent joint analyses of cosmic shear and galaxy clustering (e.g. Abbott et al., 2022; Sugiyama et al., 2023). While the solutions to these tensions remain illusive and have been the source of many works putting foward hypotheses ranging from investigations of possible systematics, all the way to exotic new physics. Another way of lending credibility to either side of the debate is to construct new cosmological probes that are independent from both parties, for instance measuring H_0 using gravitational waves (Abbott et al., 2021). Given that, as we have seen in Chapter 3, the sparsity distribution depends on the underlying cosmology, and in particular on S_8, it is of interest to us to ask ourselves: *how we can retrieve this cosmological information?*.

This chapter is structured as follows: in Section 5.1 we present the generation of synthetic data-sets that will be used throughout the rest of the chapter. The first half of this chapter is devoted to an overview of different approaches to constrain cosmology using the internal structure of galaxy clusters. First, in Section 5.2 we attempt to constrain cosmology using NFW concentration measurements. In Section 5.3.1 and Section 5.3.2 we review two sparsity based methods which use the mean sparsity of a sample to constrain cosmology. In Section 5.4 we present our novel approach designed to use each object as an individual data point rather than the mean of the sample. The second half of the Chapter, is devoted to the prospect of making the methods presented before hand applicable in observational settings. As such, In Section 5.5.2 we investigate how the resulting constraints are influenced by mass measurement errors and biases. In Section 5.6, we present preliminary work studying the sparsity bias induced by observational data pipelines as well as possible combinations of sparsity with other galaxy cluster based cosmological probes, before summarising this chapter in Section 5.7

The work presented in this chapter has been part of several publications. In particular, Section 5.4 and Section 5.5.2 are adapted from results published in Richardson & Corasaniti (2023). Section 5.5.1 relates to work published in Richardson & Corasaniti (2022). Finally Section 5.6 presents two ongoing projects that are yet to be published.

5.1 Bayesian data analysis and synthetic data-sets

As briefly mentioned in Section 4.3.2, many modern cosmological analyses make use of Bayesian statistics in order to infer the values of the cosmological parameters from a

given data-set. This is achieved by recovering the posterior distribution,

$$\rho(\boldsymbol{\theta}|\boldsymbol{x}) = \frac{\rho(\boldsymbol{x}|\boldsymbol{\theta})\pi(\boldsymbol{\theta})}{\pi(\boldsymbol{x})}, \tag{5.1}$$

given a likelihood model $\rho(\mathbf{x}|\boldsymbol{\theta})$ and priors $\pi(\boldsymbol{\theta})$. Usually, this equality is solved through the use of MCMC as the evidence, $\pi(\boldsymbol{x})$, hides a multidimensional integral which in most practical cases cannot be solved analytically. In the following sections we will design multiple likelihood models, and in order to test the accuracy of these models we require sufficiently realistic mock data vectors. As such, this first section will be devoted to designing these mock data, which will then be used throughout the rest of the chapter.

5.1.1 Targeted samples

Targeted samples of objects are usually associated with astrophysical studies, where one is more interested in the physics of the object rather than the background cosmology. They have nonetheless been at the forefront of the search for new physics, from dark energy (e.g. Allen et al., 2004) to the nature of dark matter (e.g. Eckert et al., 2022b), as these data are usually of very high quality allowing the precise determination of the physical properties of objects. Recently, in the specific case of galaxy clusters (Umetsu et al., 2020; Eckert et al., 2022a, e.g.), targeted studies have been able to not only extract the masses of clusters but also obtain information about the mass profile, albeit in the form of concentration measurements.

In order to forecast possible applications of sparsity to this type of data-set we generate a mock catalogue loosely based around the Cluster HEritage project with XMM-Newton Mass Assembly and Thermodynamics at the Endpoint of structure formation (CHEX-MATE) (CHEX-MATE Collaboration et al., 2021). This XMM-Newton observation program targets a total of 118 X-ray emitting clusters selected from the *Planck-SZ* cluster catalogue (Planck Collaboration et al., 2014b) with masses, M_{500c}, spanning between $2 \cdot 10^{14}\ h^{-1}\mathrm{M}_\odot$ and $1.3 \cdot 10^{15}\ h^{-1}\mathrm{M}_\odot$ and redshifts, z, spanning between 0 and 0.6. The observation program is split into two tiers,

- Tier 1: a representative sample of nearby clusters with $z < 0.2$,
- Tier 2: a sample of the most massive systems known with redshift $z < 0.6$.

Each tier comprising 61 systems with 4 systems being common to both data-sets. As a crude approximation we assume that the entire sample is representative of the general population of galaxy clusters with $z \leq 0.63$ and assume a mass cut $M_{200\mathrm{c}} > 10^{14}\ h^{-1}\mathrm{M}_\odot$. While this does not match the CHEX-MATE sample, this particular selection is simpler to implement, both to generate the sample and in the likelihoods presented below. As such the mock catalogue comprises 118 randomly selected clusters from the Uchuu simulation with each object being assigned a redshift z, three masses $M_{200\mathrm{c}}$, $M_{500\mathrm{c}}$ and $M_{2500\mathrm{c}}$, as well as the NFW scale radius r_s fitted by ROCKSTAR to the halo profile. Note that we ensure that there is no duplication of objects in this sample by ensure that no object is sampled twice at different redshifts.

5.1.2 Wide surveys

In opposition to targeted samples, wide surveys aim to collect vast amounts of relatively lower quality data. While the quality of these data usually does not allow for specific target by target studies, these data are however sufficient to measure sample

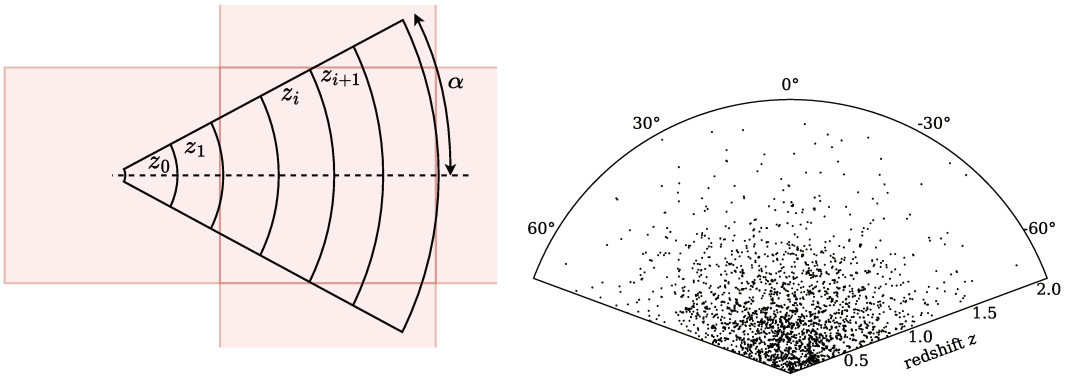

Figure 5.1: In the left panel, we show a two dimensional diagram illustrating the construction of mock light-cones. At each construction step we select all haloes in the snapshot at z_i that have a comoving distance from the centre $d_{\rm C}(z_i) < d < d_{\rm C}(z_{i+1})$. Here, the red squares illustrate how the simulation box is replicated as we construct the light-cone. In the right panel, we show all the clusters within a $60h^{-1}$Mpc slice of a light-cone generated from the Uchuu halo catalogues.

properties such as clustering or number counts which can in turn be used to constrain cosmology, with recent examples including the Dark Energy Survey (Abbott et al., 2020, 2022), Hyper Supreme Cam survey, (Sugiyama et al., 2023), or Planck Number counts (Planck Collaboration et al., 2014b). These types of surveys are expected to revolutionise cosmology in the coming decades with the arrival of extremely large amounts of high quality data from Euclid (Euclid Collaboration et al., 2022), the Dark Energy Spectroscopic Instrument (DESI Collaboration et al., 2016), eROSITA (Merloni et al., 2012), the Rubin Observatory's Legacy Survey of Space and Time (Ivezić et al., 2019) or CMB-S4 (Abazajian et al., 2016).

Here we are going to be specifically interested in cluster catalogues from wide surveys such as Euclid. As such, from the Uchuu halo catalogues, we generate a second mock data-set consisting of 1000 *Euclid* sized light-cones with each light-cone representing a field of view of 15000 deg^2 generated out to $z \simeq 2$ (Euclid Collaboration et al., 2020). We construct the light-cones as follows:

- We first uniformly select a random comoving position $[x_i,\, y_i,\, z_i]^\top$ inside the simulation and wrap the positions all haloes to place this position at the centre of the simulation box.
- We then select three angles θ, ϕ, and ψ that define which direction we chose to project the light-cone. These angles are chosen such that,

$$\begin{cases} \theta = \cos^{-1}(2U - 1), \\ \phi = 2\pi V, \\ \psi = 2\pi W, \end{cases} \tag{5.2}$$

  where $U,\ V$, and W are uniform random variates $[U,\ V,\ W]^\top \sim \mathcal{U}(0, \mathbf{I})$.
- We rotate the frame reference as to line up the x axis with the randomly selected vector, $[\cos\phi \sin\theta,\ \sin\phi \sin\theta,\ \cos\theta]^\top$, before rotating the frame around this axis by the angle ψ. This particular choice allows to uniformly sample all possible

viewing angles on the sphere as well as all possible orientations of the field of view.

- In this new reference frame the chosen line of sight is aligned with the x axis meaning that, after switching to spherical coordinates, we can simply select a square of angular side length 2α, where α is chosen as to solve,

$$4\alpha \sin(\alpha) = 4\pi f_{\rm sky}, \tag{5.3}$$

for the desired sky fraction $f_{\rm sky}$, which in the case of *Euclid* $f_{\rm sky} \simeq 0.364$.

- We convert the comoving distance, d_i, between each object and the origin to the corresponding redshift, z_i, to which we add the contribution from the radial peculiar velocities of the haloes. We use the redshifts of the simulation's output snapshots as bin edges within which we select all haloes with masses $M_{\rm 200c} > 10^{13} h^{-1} {\rm M}_\odot$. Note that, when selecting haloes we only select haloes from the snapshot at the lower redshift and do not add any fading between the snapshots which can generate discreteness effects when binning the light-cone data.

- As we advance to higher redshifts we eventually encounter the edge of the simulation box, at which point we add replications of the simulated volume. We detect the required replications by randomly sampling 300 points on both surfaces corresponding to the lower and upper comoving distances used for the selection, simply selecting all boxes within which at least one of these points falls. Note that, as these are simple mocks, we do not introduce an additional rotation to the replicated boxes.

The resulting geometry of the selected light-cone can be seen in Fig. 5.1 where we represent the edges of the redshift bins as solid lines and the replicated simulation boxes as red squares. For each selected cluster we recover the comoving positions, comoving velocities and three masses $M_{\rm 200c}$, $M_{\rm 500c}$ and $M_{\rm 2500c}$. In addition, we recover the redshift of each cluster calculated from the comoving distance while also incorporating the doppler shift corresponding to the line of sight velocity.

5.2 Concentration based inference

Now that we have data-sets on which we can calibrate and test models, in the following sections, we present a series of increasingly complex likelihoods, which allow us to constrain cosmology using the internal structure of dark matter haloes.

Before getting to sparsity, we naturally have to ask the question: *can we assume the NFW profile and use the standard description of the $c - M$ relation to constrain cosmology?* Although we have seen in Chapter 3 that assuming concentrations follow a log-normal distribution around the $c - M$ relation results in a distribution that is too narrow when translated to sparsity, we have also seen that this description is still in general agreement with the distribution of sparsities.

As such, we assume each cluster in our CHEX-MATE mock sample to be an independent realisation of the $c - M$ relation and describe the data as being log-normally distributed with a width of $\sigma = 0.2$ dex around the median which we choose to correspond to a $c - M$ relation that we denote $c_{\rm th} = c(M_{\rm 200c}, z, \mathbf{\Theta})$, resulting in a location parameter $\mu = \ln(c_{\rm th} - \sigma^2/2)$. Assuming each halo is independent from the rest, we

define the likelihood,

$$\ln \mathcal{L} = -\frac{1}{2}\sum_{i=0}^{N} \ln(c_i) + \frac{(\ln(c_i) - \mu)^2}{\sigma^2}, \tag{5.4}$$

where the sum is over all the cluster in the sample. This model is then evaluated over 10^5 MCMC iterations to sample to $\Omega_\mathrm{m} - \sigma_8$ plane with a uniform prior.

In Fig. 5.2 we show the resulting posterior distributions for the $c-M$ relation models of Diemer & Joyce (2019), Ishiyama et al. (2021), and López-Cano et al. (2022). We note that all three models primarily provide constraints on the amplitude of matter fluctuations parameter $S_8 = \sigma_8\sqrt{\Omega_\mathrm{m}/0.3}$. Indeed, we will see that this is in fact a recurrent feature of using the internal structure of haloes to constrain cosmology.

These models provide strong constraints on the S_8 parameter,

- Diemer & Joyce (2019): $S_8 = 0.914^{+0.038}_{-0.032}$,
- Ishiyama et al. (2021): $S_8 = 0.873^{+0.045}_{-0.036}$,
- López-Cano et al. (2022): $S_8 = 0.717^{+0.048}_{-0.025}$,

however, we note that they are all biased by at least $1-\sigma$ with respect to the fiducial value of the simulation, $S_8 = 0.8279$. This is particularly problematic considering that the model of Ishiyama et al. (2021) is calibrated on the same simulation as the data that is used for the constraint, and indicates that the standard log-normal description is inadequate for this application. However, it is difficult to pin-point where this description fails because, as we have seen in Chapter 3, it has many weaknesses ranging from the fundamental assumptions on the shape of the profile and shape of the probability distribution function to the more basic assumption of a constant scatter.

We can nonetheless attribute the discrepancies between the different models to differences in the $c-M$ relations. For instance, as can be seen in Fig. 2.9 that Diemer & Joyce (2019) and Ishiyama et al. (2021), which both calibrate their models on N-body simulations leading to an inflexion of the $c-M$ relation at high masses, while López-Cano et al. (2022) calibrates the relation of Ludlow et al. (2016) based on the mass accretion history of haloes; this relation resulting in a higher median concentration which is monotonously decreasing.

5.3 Mean sparsity based inference

As mentioned on multiple occasions, the use of sparsity allows us to avoid many of the problem encountered above. Nonetheless sparsity does come with the drawback of not being as studied as concentration, and as such not many predictions or models are available in the literature. In fact, prior to the work that will be presented below, one could only predict the mean sparsity of a sample (Balmès et al., 2014; Corasaniti et al., 2018, 2021). Thus, we first focus on models, such as that of Corasaniti et al. (2018), which make use of the mean sparsity of a given sample.

These approaches are designed to handle large samples of clusters with relatively poorly constrained individual sparsities. Indeed, in this case using the mean sparsity as our observable considerably reduces the scatter and error on the observable at the cost of losing some information. In this context, the data are binned into N_z redshift bins which are considered independent. In each of these bins, we then calculate the mean sparsity $\langle s_{\Delta_1,\Delta_2}\rangle(z_i)$, which produces the data vector we use in the likelihood.

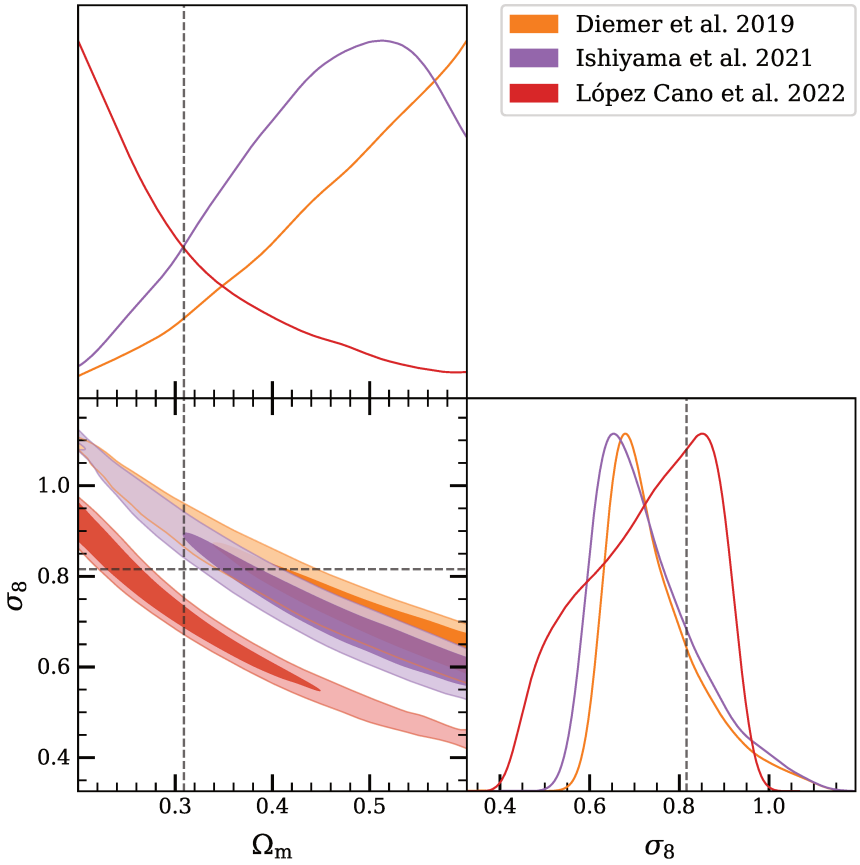

Figure 5.2: Posterior distributions resulting from the concentrations of 118 randomly selected haloes from the Uchuu simulation. In each case we assume that the concentrations follow the standard log-normal description of the $c - M$ relation centred around each model. We find that all three models yield tight constraints on S_8 which are significantly biased with respect to the fiducial cosmology, marked by black dashed lines.

The mean sparsity approach then relies on the ability to theoretically predict $\langle s_{\Delta_1,\Delta_2}\rangle$ from the mass function by solving the transcendental equation,

$$\int_{\ln M_\mathrm{i}}^{\ln M_\mathrm{f}} \frac{\mathrm{d}n}{\mathrm{d}M_{\Delta_2}} \mathrm{d}\ln M_{\Delta_2} = \langle s\rangle \int_{\ln\langle s\rangle M_\mathrm{i}}^{\ln\langle s\rangle M_\mathrm{f}} \frac{\mathrm{d}n}{\mathrm{d}M_{\Delta_1}} \mathrm{d}\ln M_{\Delta_1}, \tag{5.5}$$

which was first introduce by Balmès et al. (2014) and which we re-derived using the stochastic formalism of sparsity in Section 3.4.

This theoretical prediction, $\langle s^{\mathrm{th}}_{\Delta_1,\Delta_2}\rangle$, relies on two free parameters, M_i and M_f, the latter of which we can set to an arbitrarily large value with no influence on the prediction. On the other hand, the choice of M_i does influence the prediction. As such, the latter can either be selected as to reproduce the sparsity of a calibration sample, usually a simulation, or can be set to an arbitrary value and then correct the prediction to match the calibration sample. When using a HMF model, for instance here we use Despali et al. (2016), the second option is preferred (see Corasaniti et al., 2018, 2021) as to account for differences between the HMF model and the HMF of the simulation.

5.3.1 One-sparsity

Let us begin by considering the case where we are only able to measure a single sparsity, $s_{200,500}$. If we consider the data-set to be sufficiently large then according to the central limit theorem the distribution of the sample mean will be Gaussian. Thus, let us consider the likelihood of these data to be Gaussian,

$$\ln\mathcal{L} = -\frac{1}{2}\sum_{i=0}^{N_z} \frac{(\langle s_{\Delta_1,\Delta_2}\rangle(z_i) - \langle s^{\mathrm{th}}_{\Delta_1,\Delta_2}\rangle(z_i))^2}{\sigma^2}, \tag{5.6}$$

where the variance is estimated on the calibration sample.

We split the sample of 118 clusters into $N_z = 6$ redshifts bins and, similarly to Corasaniti et al. (2018), choose $\sigma = 0.2$. This choice results in each bin containing between 10 and 40 clusters. For each bin we solve Eq. (5.5) to obtain a theoretical prediction for the mean sparsity adding the correction term (Corasaniti et al., 2018, 2021),

$$\delta s_{200,500}(z) = 0.19372462z^3 - 0.28989702z^2 - 0.05460965z + 0.05186372. \tag{5.7}$$

This correction term is obtained by generating 1000 random samples of 118 clusters within the Uchuu simulation and matching the prediction to the measured value.

We sample the $\Omega_\mathrm{m} - \sigma_8$ plane with 10^5 MCMC steps using a uniform prior. We obtain a converged posterior shown as purple contours in Fig. 5.3. We see that in this particular case the posterior does not yield a strong constraint on either of the two sampled cosmological parameters. Nonetheless, we are able to recover a constrain on the amplitude of matter fluctuations parameter $S_8 = \sigma_8\sqrt{\Omega_\mathrm{m}/0.3} = 0.85^{+0.14}_{-0.25}$, which is consistent with the fiducial value, $S_8 = 0.8279$, used in the Uchuu simulation.

5.3.2 Multi-sparsity

It is possible to improve these constraints by adding additional information in the form of additional sparsities. As the sparsity can be interpreted as the local slope of the mass profile this additional data can be seen as better constraining the shape of the average

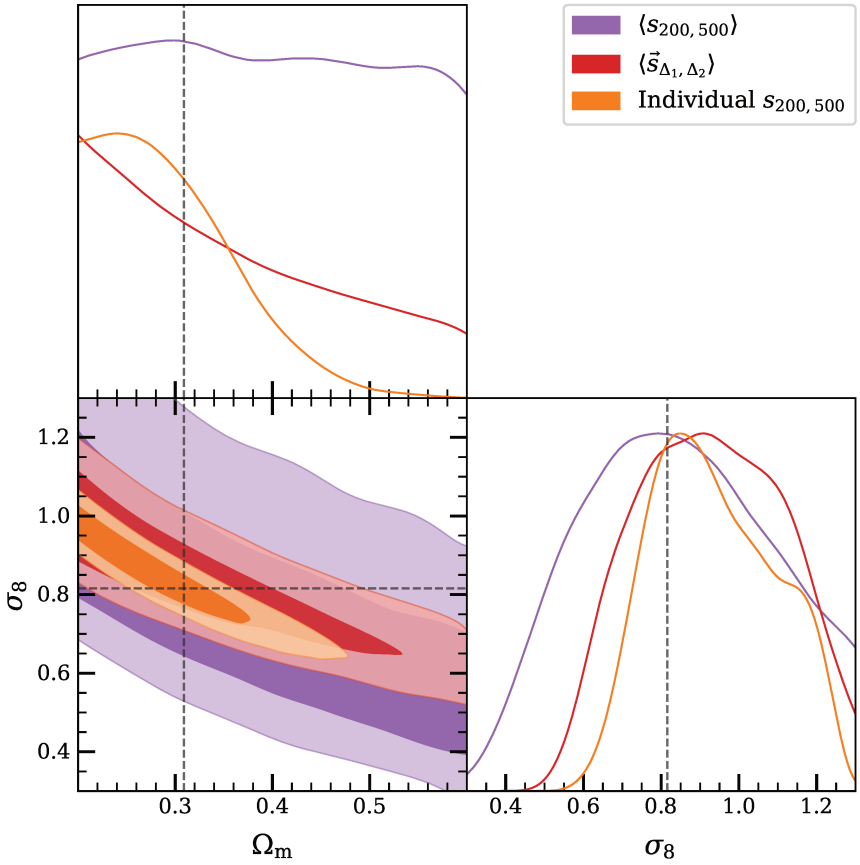

Figure 5.3: Posterior distributions resulting from the analysis of the sparsities of 118 randomly selected haloes from the Uchuu simulation. In purple, we apply the methodology of Corasaniti et al. (2018) calculating the mean sparsity in $N_z = 6$ redshift bins. In red, we use a joint likelihood for three mean sparsities evaluated of the same redshift bins (Corasaniti et al., 2022). In orange, we treat each cluster as an individual data point. The dashed lines mark the fiducial Uchuu cosmology. We see a gradual increase in the constraining power as we increase the complexity of the likelihood.

mass profile by allowing for a change in logarithmic slope. While we may be tempted to compare this change in slope to that in the NFW profile, this data is more versatile as the sparsity will not restrict the inner and outer logarithmic slopes.

As such we use the third mass measurement in our data-set, M_{2500c}, to define two additional sparsities, $s_{500,2500}$ and $s_{200,2500}$. Using the same binning as previously we measure the mean sparsity in each bin. The resulting data vector is simply the concatenation of all the sparsities in all bins.

We then use Eq. (5.5) to predict the two new averages. Note, we again have to add corrective terms to these predictions,

$$\delta s_{500,2500}(z) = 0.5452249z^3 - 0.88677583z^2 + 0.42642039z + 0.153177, \tag{5.8}$$

$$\delta s_{200,2500}(z) = 0.15492404z^3 - 1.09742678z^2 + 0.61161492z + 0.30996225, \tag{5.9}$$

which we calibrate in the same manner as Eq. (5.7). Again, because of the central limit theorem we can consider that the data follow a Gaussian distribution. Nonetheless, while two average sparsities evaluated at two distinct redshifts may be relatively independent from one another, $\langle s_{\Delta_1,\Delta_2}(z_i) s_{\Delta_1,\Delta_2}(z_j)\rangle \simeq 0$ for $i \neq j$, this is not *a priori* true of two different sparsities evaluated at the same redshift $\langle s_{\Delta_1,\Delta_2}(z_i) s_{\Delta_3,\Delta_4}(z_i)\rangle \neq 0$ as shown in Corasaniti et al. (2022). To include these correlations in the data we define $\mathbf{C}$, the covariance matrix between the mean sparsities, such that,

$$\mathsf{C}_{ij} = \frac{\langle s_{\Delta_1,\Delta_2}(z_i) s_{\Delta_3,\Delta_4}(z_j)\rangle - \langle s_{\Delta_1,\Delta_2}(z_i)\rangle\langle s_{\Delta_3,\Delta_4}(z_j)\rangle}{\sigma_{\Delta_1,\Delta_2}(z_i)\sigma_{\Delta_3,\Delta_4}(z_j)}, \tag{5.10}$$

where $\sigma_{\Delta_1,\Delta_2}(z_i)$, is the standard deviation of sparsities s_{Δ_1,Δ_2} in redshift bin i. We calibrate the covariance matrix by randomly selecting and binning 118 clusters in each of the 1000 mock light-cones from which we compute the unbiased sample covariance between the bins. Due to the noise in the resulting covariance matrix, the only correlations we are able to measure are indeed between different sparsities at the same redshift bin.

We describe the likelihood as a multivariate Gaussian distribution,

$$\ln \mathcal{L} = -\frac{1}{2}(\langle \vec{s}\rangle - \langle \vec{s}_{\rm th}\rangle)^\top \mathbf{C}^{-1}(\langle \vec{s}\rangle - \langle \vec{s}_{\rm th}\rangle), \tag{5.11}$$

where $\langle \vec{s}\rangle$ and $\langle \vec{s}_{\rm th}\rangle$ are respectively the sparsity data vector and theory vector.

We sample the posterior shown as red contours in Fig. 5.3 with 10^5 MCMC steps, again restricting ourselves to the $\Omega_{\rm m} - \sigma_8$ plane and using a flat prior. We see that the additional sparsities provide an significant increase in the constraining power with this method providing a tighter constraint on $S_8 = 0.83^{+0.08}_{-0.11}$. This is a similar increase to that presented by Corasaniti et al. (2022) although here we have a much smaller sample of clusters. In Corasaniti et al. (2022), the authors further note that increasing the number of sparsities further increases the constraining power of the method to the point where even the S_8 degeneracy can be broken and one can obtain separate constraints on $\Omega_{\rm m}$ and σ_8. In fact, we can already see this effect on our smaller sample with the red contour in Fig. 5.3 having a slightly different degeneracy than the purple contour.

In this study, the authors use a total of four masses and note that the constraints saturate for three sparsities, this is consistent with what we have seen in Section 3.2 where for a given number of masses, N, the profile can be at best reconstructed with $N-1$ sparsities. This would mean that in our case we may not gain a significant amount, in terms of constraining power, from the addition of $s_{200,2500}$.

5.4 Predicting the sparsity distribution

So far the likelihoods we have designed and presented all focus on using the mean sparsity to extract cosmological information from the data. One of the weaknesses of this approach is that using the mean as a summary statistic results in a considerable loss of information. Thus, it is of considerable interest to avoid this operation and go beyond this type of approach. In this section, we will therefore focus on predicting the sparsity distribution directly which we will then use as a likelihood model.

Let us focus on extracting the sparsity distribution from the HMF. We recall that in Section 3.4, we showed that the sparsity distribution function and HMF at two distinct over densities are linked through two transformation equations,

$$\frac{\mathrm{d}n}{\mathrm{d}M_{\Delta_2}}(M_{\Delta_2}) = \int_1^\infty s\,\rho_\mathrm{s}(s|sM_{\Delta_2})\frac{\mathrm{d}n}{\mathrm{d}M_{\Delta_1}}(sM_{\Delta_2})\,\mathrm{d}s, \tag{5.12}$$

$$\frac{\mathrm{d}n}{\mathrm{d}M_{\Delta_1}}(M_{\Delta_1}) = \int_1^\infty \frac{1}{s}\rho_\mathrm{s}(s|M_{\Delta_1}/s)\frac{\mathrm{d}n}{\mathrm{d}M_{\Delta_2}}(M_{\Delta_1}/s)\mathrm{d}s, \tag{5.13}$$

which we respectively named the inward and outward transformation equations. We have also shown throughout Chapter 3 that under simplifying assumptions these equations can be used not only to recover Eq. (5.5) but also to derive equations for the mass dependent means, $\langle s_{\Delta_1,\Delta_2}\rangle(M_{\Delta_1})$ and $\langle s_{\Delta_1,\Delta_2}\rangle(M_{\Delta_2})$, as well as providing predictions of the $c-M$ relation.

These predictions all relied on the assumption that the sparsity distribution is described by a Dirac distribution. While this particular choice of distribution significantly simplifies these equations, it reduces the description of the distribution to the modal ridge of $\rho_\mathrm{s}(s|M_\Delta)$, neglecting the scatter. However, to design a likelihood we also require this additional information on the scatter. As such, let us now consider a generic sparsity distribution that depends on two parameters s_0 and σ_s which define the location and scale of the distribution and are *a priori* functions of mass, cosmology and redshift.

The difficulty of this problem then resides in the small number of constraints we can place on these two functions, most notably their mass dependence. Indeed, while the cosmology and redshift dependence can be associated to the HMF model, in both Eq. (5.12) and Eq. (5.13) we integrate over masses implying that for each cosmology and redshift we only have two constraints on the mass dependence. Using classical optimisation methods, this limits the space of possible solutions we can investigate considerably. Empirically we find that this system only admits unique solutions for two specific class of distribution, which we name Dirac solutions and *constant Gaussian* solutions. The former corresponding to the approximations we have studied in detail in Chapter 3.

The second class of solution covers certain two parameter probability distribution functions which admit a singular solution to the system assuming s_0 and σ_s are constant. In particular we find that this is the case of but not limited to the normal and log normal distributions. Note that this particular choice of distribution theoretically allows for non-physical sparsities, $s_{\Delta_1,\Delta_2} < 1$. Moreover, if we enforce this constraint, for instance by looking at a log normal distribution of $s_{\Delta_1,\Delta_2}-1$, then we are unable to find solutions with non-vanishing scatter.

As such, for simplicity we assume that the sparsity distribution is Gaussian with mean s_0 and standard deviation σ_s. Under this assumption, we then solve the system of equations at fixed mass, redshift and cosmology, further assuming that both parameters are independent of mass which implies that we may also assume $\rho_\mathrm{s}(s|M_{\Delta_2}) \simeq$

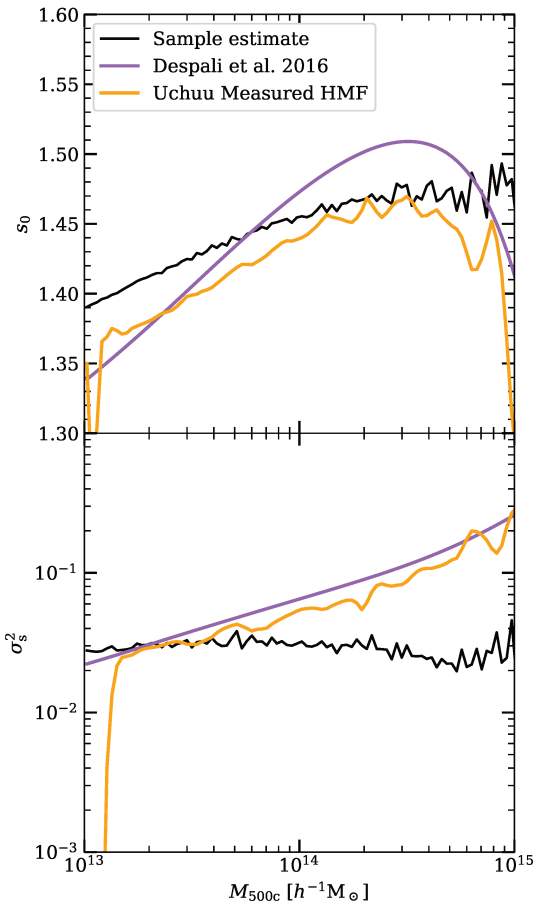

Figure 5.4: Parameters s_0 and σ_s^2 (top and bottom panels respectively), for a Gaussian conditional sparsity distribution, $\rho_s(s_{200,500}|M_{500c})$. These parameters are obtained for the distribution that jointly solves the inward, Eq. (5.12), and outward, Eq. (5.13), reconstructions assuming two HMF models: Despali et al. (2016) (purple) and using the HMF measured from the simulation data (orange). A comparison of the parameters to the sample mean and variance measured from the data (black lines) shows that s_0 is only accurate to a few percent at recovering the sample mean, this error is carried into the variance which deviates significantly from the simulation data.

$\rho_s(s|M_{\Delta_1}) \simeq \rho_s(s)$. As a result we find two solutions to the systems, one with scatter and one without scatter. In Fig. 5.4 we repeat this operation assuming the HMF model of Despali et al. (2016) and using the HMF measured from the simulation and varying the input mass. We find that the resulting mean and standard deviation change as a function of mass.

While this may appear as a violation of our assumptions, because the HMF is modulated by the sparsity distribution this means both the integrands of Eq. (5.12) and Eq. (5.13) and the sparsity distribution have a restricted width. This further implies that the assumptions we have made previously are compatible with the looser assumption that the parameters are only locally constant, i.e. they do not vary rapidly with mass. As can be seen in Fig. 5.4 and as we have discussed in Section 3.3, we have seen that this is indeed the case. Specifically, the mean sparsity only increases by less than 10 per cent over two order of magnitude in mass and that the variance is almost constant. We see that this approach provides a reasonable approximation to the measured

moments of the distribution, with the prediction of the mean being accurate to five per cent, although we note that the prediction of the variance is offset by almost an order of magnitude at high masses. We infer, from the fact that there is no significant difference between the model HMF and measured HMF, that this is a consequence of the chosen shape of the sparsity distribution.

Nonetheless we can use this prediction within a simple Gaussian likelihood model,

$$\ln \mathcal{L} = -\frac{1}{2}\sum_{i=1}^{N}\left\{\ln\left[2\pi\sigma_{\rm s}^2(M_i,z_i)\right] + \frac{[s_i - s_0(M_i,z_i)]^2}{\sigma_{\rm s}^2(M_i,z_i)}\right\}, \tag{5.14}$$

where we assume each cluster to be independent from the rest of the sample. Here we respectively note s_i, M_i, and z_i, the sparsity, mass, and redshift of the $i-$th cluster in the sample of $N = 118$ clusters. For each cluster we predict the local mean $s_0(M_i, z_i)$ an variance $\sigma_{\rm s}^2(M_i, z_i)$. Empirically, we find that using $M_i = M_{500c}$ results in a marginally better agreement of the prediction. Note that in opposition to the mean sparsity approaches here we do not add any correction terms.

Running the MCMC to convergence we obtain the orange contours shown in Fig. 5.3 with the same flat priors between $0.1 < \Omega_m < 0.6$ and $0.3 < \sigma_8 < 1.3$. We see that we recover an unbiased constraint, $S_8 = 0.799^{+0.052}_{-0.037}$ which is almost as tight as the constraints obtained using the $c - M$ relation. Note that here we have not added any additional data with respect to the purple contours produced by estimating the mean sparsity, which shows that taking the mean results in a considerable loss in cosmological information, if we have high quality data.

Although this approach provides a substantial increase in constraining power, this comes at the cost of having a likelihood model that is far more expensive to compute, requiring on average, optimising 100 two dimensional problems, to find $s_0(M_i, z_i)$, and $\sigma_{\rm s}(M_i, z_i)$, in contrast with using the sample mean, $\langle s_{\Delta_1,\Delta_2}\rangle$, which would only require on average optimising 10 one dimensional problems. This issue can be avoided by predicting the distribution through other means. For instance, in Appendix A we present an ongoing effort to predict the sparsity distribution from first principles, or by using emulation techniques which massively reduce the required computation time, while also being able to capture more complex distribution shapes, beyond normal distributions, thus allowing for more accurate likelihood models at a reduced cost.

5.5 Errors and biases

In the previous sections we have investigated how we can predict properties of the halo sparsity distribution. These can be used within various likelihood models, that we have applied to a simulated data-set with negligible uncertainties and selected adopting criteria designed to have minimal impact on the sparsity measurements. Here, we will relax this approximation and investigate how sparsity based constraints react to more realistic setups. As such, we will first investigate how selection effects, with a particular interest on dynamical selection criteria, may alter constraints using the mean sparsity. We will then study how observational uncertainties impact constraints using individual sparsity measurements. Finally, will briefly overview how systematic effects can be accounted for at the level of the likelihood.

5.5.1 Selection effects: the influence of mergers

In Chapter 4, we have seen that the distribution of sparsities is strongly influenced by major mergers, which shifts individual clusters to higher sparsities. We have seen that this has the overall effect of imparting a strong tail to the distribution. Here, we focus on how mergers may impact the cosmological inference based on mean sparsity values. In principle, as this method relies on the computation of the mean sparsity of a sample from two HMFs, the resulting mean reflects the population of haloes which was used to calibrate HMFs. This implies that selecting a particular population may bias the resulting mean sparsity and therefore the inferred cosmological parameters.

To do so we revisit the criteria we set out in Eq. (4.5) to separate merging haloes from quiescent haloes and take all haloes with $M_{200c} > 10^{13}h^{-1}\mathrm{M}_{\odot}$ from the MDPL2 simulation catalogues. We thus separate them according to the number of dynamical times, $T(a_{\mathrm{LMM}}|a(z))$, at which their last major merger occurred, i.e. within or prior to two dynamical times. In the left panels of Fig. 5.5, we show the impact of such a selection. It is clear that if we only select quiescent haloes we incur a 10 per cent bias on $\langle s_{200,500}\rangle$ at $z = 0$, which decreases to 4 per cent at $z = 1$, while in the same redshift range the bias is of the order of 20 per cent for $\langle s_{500,2500}\rangle$ and 30 per cent for $\langle s_{200,2500}\rangle$.

While the previous selection would result in a substantial change in the likelihood, the number of dynamical times since the last major merger is a quantity that is difficult to acquire. In most practical situations however, one might face the reverse problem of a certain number of outlier sparsities biasing the estimation of the sample mean, this is particularly the case for small cluster samples.

Therefore, the question we can ask ourselves is, *can we consider certain clusters as outliers and if so which ones can we remove without biasing the inference?* To answer this question we use the thresholds we defined in Section 4.3.1 and show in Fig. 4.6, which are based on p-values. This kind of selection can be seen as akin to shaving the tail of the distribution which may be over represented due to selection effects. In the right hand plots of Fig. 5.5 we show the impact of removing all haloes with $p \leq 0.005$ and $p \leq 0.01$. We can see that excluding these haloes from the computation of the mean only alters the result at the sub-per cent level for $\langle s_{200,500}\rangle$ and only of the order of a few percent $\langle s_{500,2500}\rangle$ and $\langle s_{200,2500}\rangle$ at higher redshift. This indicates that it is safe to remove a few outlier clusters from a cosmological analysis, especially since these significantly alter the sample mean when handling small samples.

5.5.2 Observational uncertainties

When considering observational measurement, we must always remember that these are accompanied by a certain degree of uncertainty. Naively we associate uncertainty to perpendicular errorbars, but more generally uncertainty will manifest as a correlated volume. This correlated volume is typically what is depicted in most figures showing a posterior distribution, Fig. 5.3 for instance, and can potentially have a highly complex structure.

Within the context of Bayesian analysis, dealing with such complex distributions can be done in a robust and systematic way. By explicitly including the uncertainty distribution into the likelihood, we can formally marginalise over the uncertainties to obtain the new likelihood model. For instance, in the case of a likelihood using a single cluster this can be written explicitly,

$$\ln \mathcal{L}_{\mathrm{corr}} = \int_0^\infty \int_1^\infty \ln \mathcal{L}(M, s|\mathbf{\Theta})\rho_{\mathrm{err}}(M, s)\mathrm{d}M\mathrm{d}s, \tag{5.15}$$

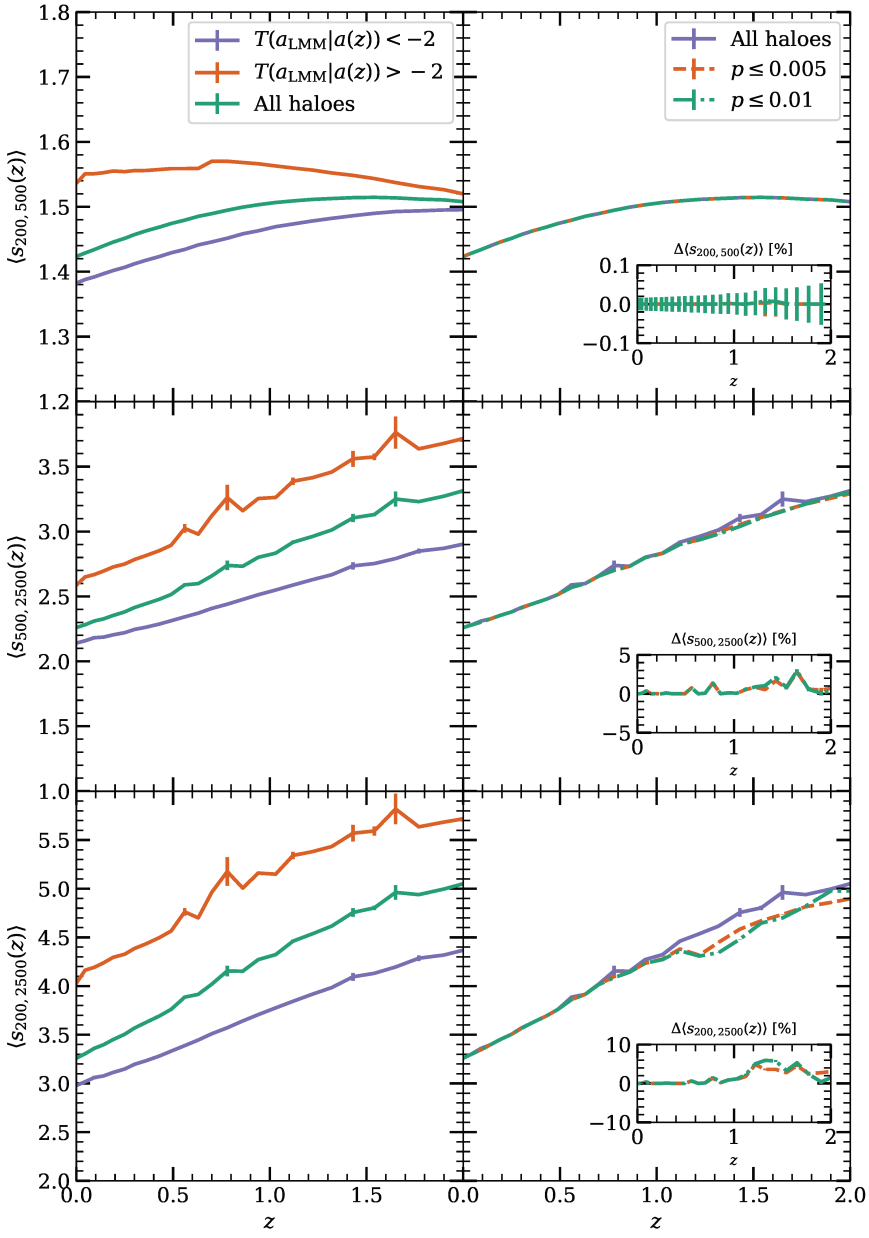

Figure 5.5: Redshift evolution of the average halo sparsity $\langle s_{200,500}\rangle$ (top panels), $\langle s_{500,2500}\rangle$ (middle panels) and $\langle s_{200,2500}\rangle$ (bottom panels). In the left panels we show the average sparsity estimated for the full halo samples (green curves), for haloes which are within two dynamical times from the last major merger event (blue curves) and for haloes which are at more than two dynamical times from it (orange curves). In the right panels we show the average sparsity estimate from the full halo samples (blue curves) and for selected samples from which we removed outliers whose sparsity lies above thresholds corresponding to p-values of $p \leq 0.01$ (green curves) and $p \leq 0.005$ (orange curves). In the inset plots we show the relative differences with respect to the mean sparsity estimated from the full catalogues.

where $\rho_{\rm err}$ is the joint error distribution on the mass and sparsity, note that we neglect the redshift error which is often much smaller. If we consider a larger sample of N clusters this operation theoretically requires us to solve a $2N$-dimensional integral. By assuming the errors on the measurements of each cluster to be independent from the measurements of other clusters, we can reduce this down to calculating a set of $N \times 2$-dimensional integrals.

As an example, let us consider that both mass measurements, $M_{\rm 200c}$ and $M_{\rm 500c}$ are independent, and that the error distribution on each mass can be described as a log-normal distribution with mean $M_{\Delta,i}$ and variance $\delta M^2_{\Delta,i}$, the error on the mass measurement. These quantities translate into,

$$\mu_{\Delta,i} = \ln\left[\frac{M_{\Delta,i}}{\sqrt{\delta M^2_{\Delta,i} + M^2_{\Delta,i}}}\right] \quad \text{and} \quad \sigma_{\Delta,i} = \ln\left[1 + \frac{\delta M^2_{\Delta,i}}{M^2_{\Delta,i}}\right] \tag{5.16}$$

the log-normal location and width parameters. Here the second index, i, is used to mark measurements relating to the i-th cluster in opposition to variables of functions which do not carry the index.

It is easy to imagine that even if we consider both mass measurements to be independent form one another, the error on the resulting sparsity will not be independent from the masses because the three variables are related through an algebraic operation. In a similar fashion to how we derived the HMF transformation equations in Section 3.4, we can derive the joint error distributions,

$$\begin{aligned}\rho_{\rm err}(s, M_{\Delta_2}) = &\frac{1}{\sqrt{2\pi\sigma_{\Delta_1,i}\sigma_{\Delta_2,i}sM_{\Delta_2}}} \\ &\exp\left\{-\frac{1}{2}\left[\left(\frac{\ln(sM_{\Delta_2}) - \mu_{\Delta_1,i}}{\sigma_{\Delta_1,i}}\right)^2 + \left(\frac{\ln(M_{\Delta_2}) - \mu_{\Delta_2,i}}{\sigma_{\Delta_2,i}}\right)^2\right]\right\}\end{aligned} \tag{5.17}$$

and

$$\begin{aligned}\rho_{\rm err}(s, M_{\Delta_1}) = &\frac{1}{\sqrt{2\pi\sigma_{\Delta_1,i}\sigma_{\Delta_2,i}M_{\Delta_1}/s}} \\ &\exp\left\{-\frac{1}{2}\left[\left(\frac{\ln(M_{\Delta_1}) - \mu_{\Delta_1,i}}{\sigma_{\Delta_1,i}}\right)^2 + \left(\frac{\ln(M_{\Delta_1}/s) - \mu_{\Delta_2,i}}{\sigma_{\Delta_2,i}}\right)^2\right]\right\}.\end{aligned} \tag{5.18}$$

As we previously found that using $\rho(s|M_{\rm 500c})$ yields the best agreement between theory and data, in the following we only consider the corrected likelihood,

$$\mathcal{L}_{\rm corr} = \prod_{i=1}^{N}\int_0^\infty\int_1^\infty \frac{1}{\sqrt{2\pi\sigma^2_{\rm s}(M, z_i)}}\exp\left[-\frac{1}{2}\frac{[s - s_0(M, z_i)]^2}{\sigma^2_{\rm s}(M, z_i)}\right]\rho_{\rm err}(s, M)\mathrm{d}s\mathrm{d}M. \tag{5.19}$$

Note that here both the uncorrected likelihood and the error distribution allow for sparsities lower than one. This causes an issue at low sparsities as both distributions are heavily weighted towards low sparsities. In practice, this means that the larger the errors on the masses becomes the more the posterior distribution is biased in favour of high S_8 values. As such we introduce a second corrective term,

$$\rho_{\rm p}(s) = 1 - \exp\left[-\frac{1}{2}\frac{(s-1)^2}{\sigma^2_{\Delta_1,\Delta_2,i}}\right], \tag{5.20}$$

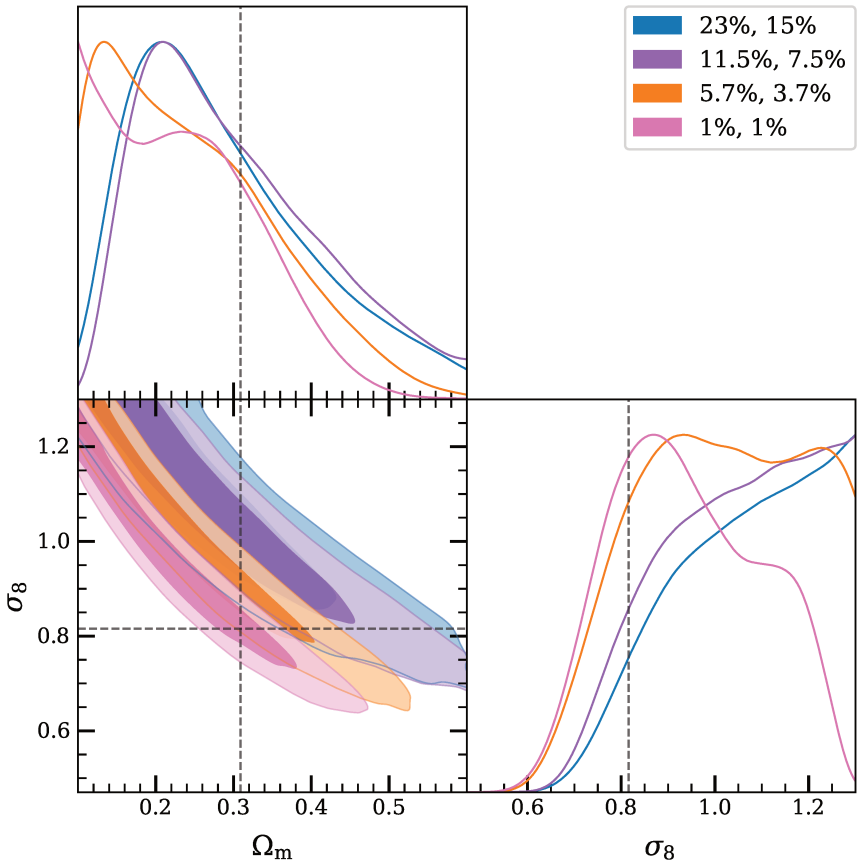

Figure 5.6: Posterior distributions resulting from the analysis of a sample of 118 randomly selected haloes from the Uchuu simulation modelling measurement errors. Each contour corresponds to a model for the relative errors on clusters masses ($\delta M_{200c,i}/M_{200c,i}$, $\delta M_{500c,i}/M_{500c,i}$): in blue (23%, 15%) the magnitude of errors estimated for the CHEX-MATE sample; in purple (11.5%, 7.5%); in orange (5.7%, 3.7%); and in pink (1%, 1%). For the smallest errors the posterior from Fig. 5.3 is recovered where errors were neglected. Also seen is that a naive modelling of errors induces a bias towards increasingly large values of S_8.

which acts as a prior to ensure that the probability distribution goes to zero for $s = 1$. Here,

$$\sigma^2_{\Delta_1,\Delta_2,i} = \left(\frac{M_{200c,i}}{M_{500c,i}}\right)^2 (\delta M^2_{200c,i}/M^2_{200c,i} + \delta M^2_{500c,i}/M^2_{500c,i}) \tag{5.21}$$

corresponds to the width of the error distribution if the errors are propagated classically. This particular choice is motivated in order to adaptively correct the likelihood when the errors on the mass measurements are large and leaving it relatively untouched when errors are sufficiently small. Note that this correction is only required due to the likelihood and error distributions allowing for nonphysical sparsity values. Hence, it should not be needed when using more realistic likelihood and error models, as provided for instance through the use of emulators.

In Fig. 5.6, we show the posterior distributions using this likelihood for four relative errors models on the masses. In blue we show the case of the forecast cluster mass errors estimated by Corasaniti et al. (2022) for the CHEX-MATE sample, $\delta M_{200c,i}/M_{200c,i} =$

0.23, $\delta M_{500c,i}/M_{500c,i} = 0.15$; in purple is shown the case where we halve these errors; for the orange contours we have reduced the original errors by a factor of 4; and in pink we use percent level errors. We can clearly see a biasing effect induced by the crude error modelling, with the constraints becoming more biased, the larger the errors become.

Further analysis of the large error regime is not possible as the likelihood is dominated by the correction term, nonetheless, the width of the posteriors, which are smaller than when we use the mean sparsity, hints to the fact that using this approach on current and upcoming data may already be more constraining than using the mean, given we are able to control the bias by using a more complex likelihood and error models. Focusing on the very low error posterior we see that we recover similar constraints as the ideal confirming that this approach is in agreement with the case where we have neglected errors.

Although here we have focused on incorporating measurement uncertainties, we note that observational systematics, such as weak lensing and hydrostatic mass biases, can be treated in the same fashion. Indeed, in Section 4.4 we studied the impact of simple systematics models (e.g. Becker & Kravtsov, 2011; Biffi et al., 2016) on the detection of mergers. These same models could be applied in the context at hand requiring us to alter the likelihood to incorporate their effect. Nonetheless, a crucial point is missing in these simple models such as the correlations between systematics on the different masses, as these strongly influences the implementation. As such, in order to best incorporate these effects in our likelihood, we require mock observations upon which these types of bias can be measured and characterised. These types of mocks can only be acquire through a thorough investigation of simulations and in particular if we are interested in using X-masses, large volume hydrodamical simulations like the FLAMINGO runs Schaye et al. (2023) or large representative samples of cluster zoom-simulations such as THE300 runs (Cui et al., 2018).

5.6 Towards observational applications

In the theoretical settings presented above, we see that sparsity has strong potential to become a novel probe of cosmology. This aspiration is however held back by observational limitations. Indeed, accessing three dimensional masses in observational settings can provide a considerable challenge which makes the use of sparsity very delicate in practice. In this sections we study how sparsity can be used in practical scenarios, first we will investigate if and how to treat the sparsities from stacked weak lensing observations of clusters and secondly we will study how to combine sparsity with other probes.

5.6.1 AMICO clusters sparsities

As in many fields in astronomy, stacking observations of similar objects is a common practice in weak lensing. Increasing the signal-to-noise ratio and allowing to measure *stacked* properties of clusters to a high degree of precision, these observations can essentially be seen as treating individual objects as independent realisations of a single object, which we will simply refer to as the stacked object. While the data for this stacked object have been significantly manipulated, one would still expect the final object to retain some of the properties of the underlying set of clusters that were used to create the singular stacked object. This therefore brings forward the question: *what are*

Table 5.1: Selection criteria of the 14 AMICO cluster stacks and inferred properties. The inferred parameters were produced by Lorenzo Ingoglia using the methodology of Bellagamba et al. (2019) and Ingoglia et al. (2022). Here the masses M_{200c} are in units of $10^{14}\ h^{-1}\mathrm{M}_{\odot}$.

z	λ^*	$z_{\ell,\mathrm{eff}}$	$z_{s,\mathrm{eff}}$	M_{200c}	c_{200c}	f_{off}	σ_{off}
$[0.1; 0.3]$	$[0; 15]$	0.192	0.700	$0.183^{+0.038}_{-0.031}$	$8.2^{+7.1}_{-4.6}$	$0.27^{+0.15}_{-0.17}$	$0.22^{+0.16}_{-0.12}$
$[0.1; 0.3]$	$[15; 25]$	0.216	0.725	$0.411^{+0.082}_{-0.066}$	$3.0^{+3.5}_{-1.3}$	$0.31^{+0.14}_{-0.19}$	$0.28^{+0.15}_{-0.16}$
$[0.1; 0.3]$	$[25; 35]$	0.226	0.741	$1.17^{+0.20}_{-0.17}$	$1.55^{+0.83}_{-0.40}$	$0.31^{+0.13}_{-0.17}$	$0.31^{+0.14}_{-0.18}$
$[0.1; 0.3]$	$[35; 45]$	0.232	0.740	$2.12^{+0.34}_{-0.30}$	$3.1^{+2.1}_{-1.1}$	$0.30^{+0.15}_{-0.19}$	$0.29^{+0.14}_{-0.17}$
$[0.1; 0.3]$	$[45; 150]$	0.228	0.746	$3.40^{+0.43}_{-0.40}$	$4.3^{+2.4}_{-1.3}$	$0.31^{+0.14}_{-0.19}$	$0.24^{+0.15}_{-0.13}$
$[0.3; 0.45]$	$[0; 20]$	0.373	0.860	$0.420^{+0.096}_{-0.069}$	$8.8^{+6.7}_{-4.4}$	$0.28^{+0.15}_{-0.17}$	$0.29^{+0.15}_{-0.18}$
$[0.3; 0.45]$	$[20; 30]$	0.388	0.863	$0.89^{+0.16}_{-0.13}$	$2.46^{+2.08}_{-0.95}$	$0.31^{+0.14}_{-0.19}$	$0.33^{+0.13}_{-0.20}$
$[0.3; 0.45]$	$[30; 45]$	0.389	0.862	$1.63^{+0.24}_{-0.21}$	$1.68^{+0.86}_{-0.46}$	$0.33^{+0.12}_{-0.19}$	$0.27^{+0.14}_{-0.14}$
$[0.3; 0.45]$	$[45; 60]$	0.392	0.865	$2.65^{+0.49}_{-0.45}$	$9.9^{+5.8}_{-4.2}$	$0.32^{+0.13}_{-0.18}$	$0.36^{+0.10}_{-0.19}$
$[0.3; 0.45]$	$[60; 150]$	0.381	0.859	$4.80^{+0.73}_{-0.65}$	$4.6^{+2.9}_{-1.4}$	$0.31^{+0.14}_{-0.19}$	$0.25^{+0.14}_{-0.14}$
$[0.45; 0.6]$	$[0; 25]$	0.497	0.886	$0.398^{+0.10}_{-0.084}$	$7.1^{+7.6}_{-4.3}$	$0.30^{+0.14}_{-0.18}$	$0.27^{+0.15}_{-0.14}$
$[0.45; 0.6]$	$[25; 35]$	0.517	0.887	$0.90^{+0.13}_{-0.12}$	$8.5^{+6.4}_{-3.8}$	$0.31^{+0.14}_{-0.18}$	$0.20^{+0.12}_{-0.09}$
$[0.45; 0.6]$	$[35; 45]$	0.513	0.887	$1.77^{+0.31}_{-0.29}$	$4.8^{+4.2}_{-1.9}$	$0.33^{+0.13}_{-0.20}$	$0.23^{+0.13}_{-0.11}$
$[0.45; 0.6]$	$[45; 150]$	0.516	0.887	$3.52^{+0.85}_{-0.75}$	$1.48^{+0.78}_{-0.35}$	$0.33^{+0.13}_{-0.18}$	$0.29^{+0.14}_{-0.15}$

the properties of stacked sparsities and can we use them to constrain cosmology?

To answer this question we turn our attention towards the latest stacked analysis performed using the Adaptive Matched Identifier of Clustered Objects (AMICO) sample of galaxy clusters from the Kilo Degree Survey (KiDS) Data Release 3 analysis (Maturi et al., 2019; Lesci et al., 2022). In this analysis the authors, create 14 stacks from the sample of 7988 cluster candidates detected in the survey area. Each stack corresponds to a cut in richness λ^*, a measure of the number of galaxies found within a cluster weight by their membership probability (see e.g Bellagamba et al., 2018, 2019), and redshift range, and is produced by combining all the positions, relative to the peak surface galaxy number density, and ellipticities of background galaxies. In addition, this procedure gives the stacks effective redshifts $z_{\ell,\mathrm{eff}}$ as well as giving effective redshifts to the combined background sources $z_{s,\mathrm{eff}}$. Finally, it is worth noting that, the galaxy density and the minimum of the gravitational potential aren't necessarily aligned, to account for this authors allow for a fraction of clusters, f_{off}, to be offset and be normally distributed around the centre with a variance σ_{off}.

To assess how the measurement procedure affects the sparsities we generate a series of profiles following the assumptions of the AMICO pipeline. First we sample the masses, redshifts, and number of clusters in each stack according to the KiDS footprint and using the Despali et al. (2016) HMF model and in addition we radomly assign a sparsity to each cluster assuming that it is drawn from the likelihood function of Section 5.4. For each of these clusters we assign a richness according to the AMICO richness-mass scaling relation (Bellagamba et al., 2019),

$$\log_{10}\left(\frac{M_{200\mathrm{c}}}{10^{14}h^{-1}\mathrm{M}_{\odot}}\right) = \alpha + \beta\log_{10}\left(\frac{\lambda^*}{30}\right) + \gamma\log_{10}\left(\frac{E(z)}{E(0.35)}\right), \tag{5.22}$$

where $\alpha = 0.004 \pm 0.038$, $\beta = 1.71 \pm 0.08$, and $\gamma = -1.33 \pm 0.64$. After inverting this relation and propagating the errors on the three parameters, we use the resulting richness error, $\Delta\log_{10}(\lambda^*/30)$, to add a stochastic component to the richness in the form

of Gaussian noise, note that this typically underestimates the level of stochasticity of the richness-mass scaling relation. Finally we randomly select a fraction $f_{\rm off}$ of clusters to be offset from the centre by a radius $R_{\rm off}$ sampled from

$$\rho_{\rm off}(R_{\rm off}) = \frac{R_{\rm off}}{\sigma_{\rm off}^2} \exp\left[-\frac{1}{2}\left(\frac{R_{\rm off}}{\sigma_{\rm off}}\right)^2\right], \tag{5.23}$$

and which we place at uniformly selected angles $\phi \sim \mathcal{U}(0; 2\pi)$. Note that for each stack we take the corresponding values of $f_{\rm off}$ and $\sigma_{\rm off}$ from Tab. 5.1.

From these randomly generated halo catalogues we produce synthetic profiles by projecting each halo as a truncated NFW profile (Baltz et al., 2009),

$$\rho(r) = \frac{\rho_0}{r/r_{\rm s}(1 + r/r_{\rm s})^2}\left(\frac{r_{\rm t}^2}{r^2 + r_{\rm t}^2}\right)^2, \tag{5.24}$$

where the scale radius, r_s, and characteristic density, ρ_0, are chosen to match the randomly sampled mass and sparsity, while the truncation radius is fixed at $r_t = 3r_{\rm 200c}$. This profile is numerically integrated along the line of sight to produce the mass surface density profile, $\Sigma_{\rm 1h}(\theta)$, known as the 1-halo term, where we have switched from physical coordinates to angular coordinates to easily handle objects at different redshifts by working on a fixed grid in angular coordinates. If a halo is selected to be displaced from the centre then we simply apply the shift to the coordinates.

In addition to the halo profile, the AMICO analysis pipeline includes a second term to account for the presence of secondary structures around the clusters, known as the two-halo term (Oguri & Takada, 2011; Sereno et al., 2017). This term,

$$\Sigma_{\rm 2h}(\theta; M_{\rm 200c}, z) = \int_0^{+\infty} \frac{\ell {\rm d}\ell}{2\pi} J_0(\ell\theta) \frac{\rho_{\rm m}(z) b_{\rm h}(M_{\rm 200c}; z)}{(1+z)^3 D_{\rm d}^2(z)} P_{\rm lin}(k_\ell; z), \tag{5.25}$$

where $k_\ell = \ell/(1+z)/D_{\rm d}(z)$, $D_{\rm d}(z)$ is the angular diameter distance to the cluster, and J_0 is the zeroth order Bessel function, exhibits a strong dependence on cosmology through the linear matter power spectrum $P_{\rm lin}$, which is modelled with the approximate form of Eisenstein & Hu (1999), and halo bias $b_{\rm h}$, which is modelled by the form of Tinker et al. (2010).

The surface mass profile,

$$\Delta\Sigma(R) = \bar{\Sigma}(< R) - \Sigma(R) = \Sigma_{\rm crit}\gamma_+, \tag{5.26}$$

being related to the tangential shear γ_+, which can be measured from the ellipticities of galaxies, is thus our primary observable. Here, $\bar{\Sigma}(< R)$ is the mean mass surface density within a radius R, and $\Sigma_{\rm crit} = \frac{c^2}{4\pi G}\frac{D_{\rm s}}{D_{\rm d} D_{\rm ds}}$ is the lensing critical surface density (Bartelmann & Schneider, 2001), with c is the speed of light, G is the gravitational constant, and $D_{\rm s}$, $D_{\rm d}$, and $D_{\rm ds}$ respectively the angular diameter distance from the observer to the source plane, deflector and between the deflector and the source planes. We generate 10^3 realisations of each stack shown in Tab. 5.1. For illustration in Fig. 5.7 we show one such stack sampled corresponding to the fourth row of Tab. 5.1.

In order to recover the masses and concentrations of the stacks a few more steps need to be implemented. First, we must implement the AMICO fitting function (Bellagamba et al., 2018; Ingoglia et al., 2022) to fit the azimuthally averaged profiles. Similarly to how we generate the profile, the fitting function is split into two terms. The 2-halo term

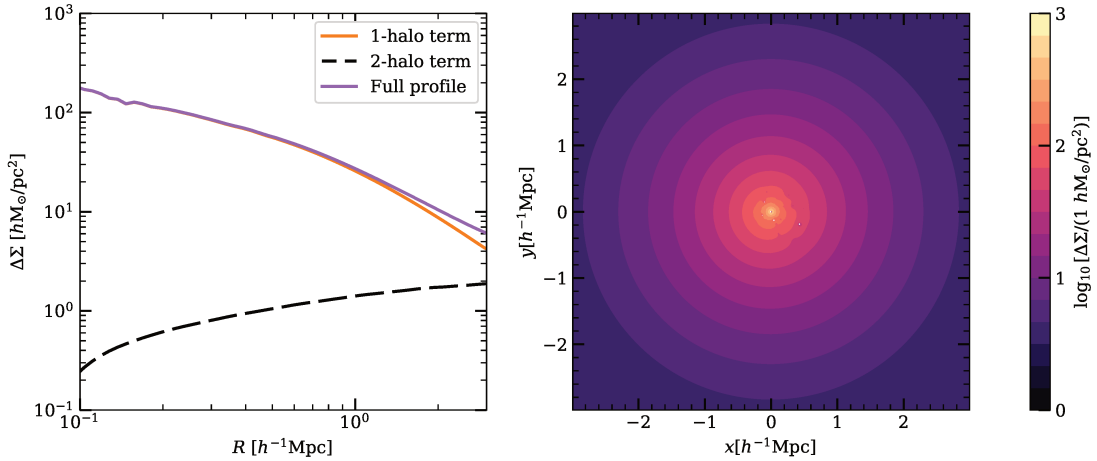

Figure 5.7: In the right panel we show the mass surface density generated following the assumptions of the AMICO pipeline and corresponding the fourth row of Tab. 5.1. In the left panel we show the resulting mass surface density profile in purple which we decompose into the corresponding 1-halo and 2-halo contributions.

remains unchanged and as such we simply use Eq. (5.25) assuming the stack is placed at a effective redshift $z_{\ell,\mathrm{eff}}$, while the 1-halo term is split into two parts,

$$\Sigma_{1\mathrm{h}}(R) = (1 - f_{\mathrm{off}})\Sigma_{\mathrm{cen}}(R) + f_{\mathrm{off}}\Sigma_{\mathrm{off}}(R), \tag{5.27}$$

a centred contribution, $\Sigma_{\mathrm{cen}}(R)$, and an offset contribution, $\Sigma_{\mathrm{off}}(R)$. The centred contribution is simply modelled as the integral along the line of sight of Eq. (5.24), while the off-axis contribution accounts for the probability of the displacement,

$$\Sigma_{\mathrm{off}}(R) = \frac{1}{2\pi}\int_0^\infty \rho_{\mathrm{off}}(R_{\mathrm{off}}) \int_0^{2\pi} \Sigma_{\mathrm{cen}}\left(\sqrt{R^2 + R_{\mathrm{off}}^2 + 2RR_{\mathrm{off}}\cos\theta}\right) \mathrm{d}\theta \mathrm{d}R_{\mathrm{off}}. \tag{5.28}$$

This model depends only on four parameters $M_{200\mathrm{c}}$, $c_{200\mathrm{c}}$, f_{off}, and σ_{off} when focusing on inner radii where the 2-halo term is subdominant, at outer radii this second term begins to dominate making the result sensitive to the halo bias model and effective redshift of the lens $z_{\ell,\mathrm{eff}}$. Note that this model also implicitly depends on the effective source redshift $z_{s,\mathrm{eff}}$, as it is required to transform from the shear profile to the surface mass profile.

Finally, once these measurements are performed we want to compare each stack's sparsity to the mean sparsity of the clusters in the stack in order to assess the bias induced by the stacking procedure. This quantity can theoretically be predicted as the richness weighted average,

$$\langle s_{200,500}\rangle_i = \int_{\lambda^*_{\mathrm{min}}}^{\lambda^*_{\mathrm{max}}} \int_1^\infty s\rho_{\mathrm{s}}(s|M_{200\mathrm{c}})P(M_{200\mathrm{c}}|\lambda^*)\mathrm{d}s\mathrm{d}\lambda^*, \tag{5.29}$$

where we marginalise over each richness bin $[\lambda^*_{\mathrm{min}};\lambda^*_{\mathrm{max}}]$, including the richness distribution $P(M_{200\mathrm{c}}|\lambda^*)$ coming from the scaling relation. We can then use the resulting bias within a cosmology inference pipeline resembling that of Section 5.3.1. Note that this will first have to be done using a simulated data set generated using the light-cones of Section. 5.1.2, in order to correct for possible unforeseen systematics in a semi-blind fashion before making a cosmological constrain using the AMICO data of Tab. 5.1 in a final step.

5.6.2 Combining sparsity with other probes

In Section 5.3.2, we investigated how we can combine multiple sparsities to obtain stronger cosmological constraints. This philosophy can also be extended to combine sparsity with other probes. Indeed much like 3-point correlation analyses (e.g. Abbott et al., 2022; Sugiyama et al., 2023) which combine the galaxy-galaxy, weak lensing shear-shear, and galaxy-shear 2 point correlations, we can imagine it is possible to combine sparsity with other cosmological probes such as cluster number counts and cluster gas fractions.

Here as a first step we will focus on combining cluster number counts and the average sparsity analysis of section 5.3.2. We place ourselves within the framework of a wide survey such as Euclid and assume both probes have Gaussian likelihoods (Corasaniti et al., 2022; Payerne et al., 2023). Combining both probes then simply becomes a matter of estimating the covariance matrix between both probes.

To estimate the covariance we use the 10^3 Euclid sized light-cones generated in Section 5.1.2. For each of these light-cones we measure the number counts of clusters as well as their sparsity, which we bin as a function of redshift. In Fig. 5.8 we assume that we are able to measure the sparsities of all the haloes in the light-cones and show the resulting correlation matrices. In the top panels we use the same binning for both the number counts and the sparsity. Here, in the bottom-right of the matrices we see the strong correlations between the individual sparsities that we made use of in Section 5.3.2. In addition, we can see a faint correlation between the number counts and the mean sparsities. To get some intuition as to the impact of we bin the sparsity data, in the lower panels of Fig. 5.8 we use different binning for the sparsity and number counts, here we simply half the number of sparsity bins. Following this change, we see the correlation significantly diminish and begin to be absorbed into the noise, indicating that such correlations indeed depend on the chosen binning strategy.

This scenario is however idealistic as in practice it is very difficult to measure the internal structure of galaxy clusters. As we have discussed above, in the near future we can only expect to have access to homogenous samples of a few hundred sparsities, as opposed to tens of thousands. Under this new assumption, in Fig. 5.9, we repeat the exercise but this time randomly sampling 200 haloes within each light-cone. In this case we see that the covariance completely vanishes into the noise, leaving the sparsity sector independent from the number counts. In the lower panels we again decrease the number of bins to see the impact this may have on the correlations. We see that the change to the binning strategy does not influence not influence the correlation significantly enough for it to become larger than the noise level.

The results presented above indicates that in practical applications sparisity measurements can be treated as independent from number counts allowing them to be easily combined into joint analyses. In future endeavours, we plan to investigate the correlation between sparsities and cluster gas mass fraction measurements (e.g. Ettori et al., 2009) as a second step towards a unified *cluster-only* cosmology.

5.7 Summary

At the end of this chapter we have reached the state-of-the-art in terms of probing cosmology with halo sparsity. In a theoretical setting, we over-viewed the method of Corasaniti et al. (2018, 2022) using the binned mean sparsity of a sample. We then developed a novel method of probing cosmology using each halo in the sample as an

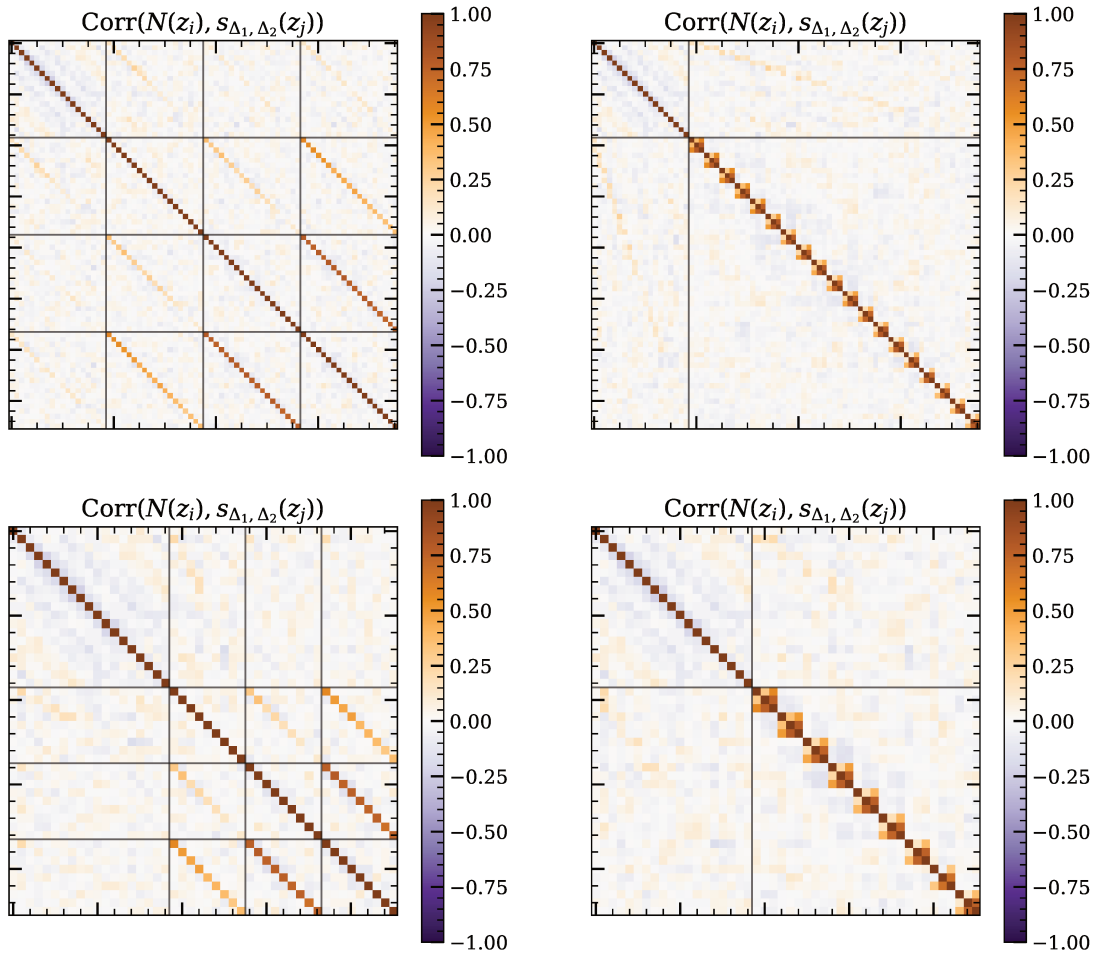

Figure 5.8: Correlation matrices between cluster number counts (top-left of the matrices) and mean sparsities (bottom-right of the matrices) assuming that we can measure the sparsities of all haloes in the light-cones. In the top panels we use the same binning in redshift for both the number counts and sparsities and in the bottom panels we only use half as many bins for sparsities. The left and right panels simply show permutations of the sparsity data vectors, on the left we group the data vectors according to sparsities, on the right we group the data vectors according to redshift bins.

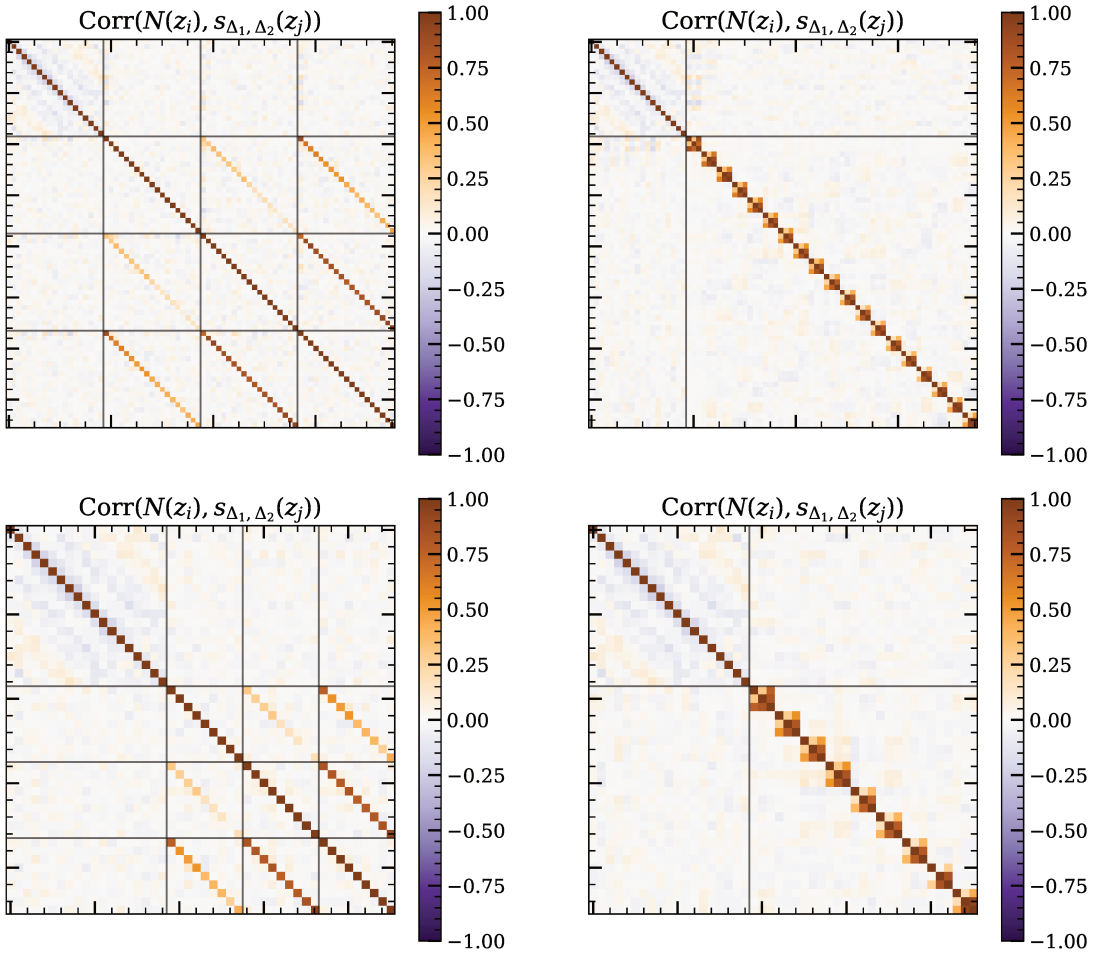

Figure 5.9: Correlation matrices between cluster number counts (top-left of the matrices) and mean sparsities (bottom-right of the matrices) assuming that we can only measure the sparsities of 200 haloes among those within the light-cones. In the top panels we use the same binning in redshift for both the number counts and sparsities and in the bottom panels we only use half as many bins for sparsities. The left and right panels simply show permutations of the sparsity data vectors, on the left we group the data vectors according to sparsities, on the right we group the data vectors according to redshift bins.

individual data point rather than simply binning their sparsities. We have seen that this novel approach significantly improves the constraints on the cosmological parameters without requiring any additional data. Nonetheless this improvement comes with the drawbacks of a higher computational cost and having a probe that is more sensitive to mass measurement uncertainties and systematics.

We have studied in detail the impact of mass measurement uncertainties. In particular, we have found that improper modelling of both the likelihood and mass measurement errors leads to a biased constraint on the cosmological parameters. As such, these findings call for further investigations into realistically modelling of the likelihood through the use of emulators as well as measurement errors and systematic biases by quantifying the covariances between mass definitions. Focusing on the second aspect, we have begun to investigate the possibility of using sparsity measurements from the AMICO pipeline, to do so we have generated a large sample of mock observations that need to be analysed in order to extract the sparsity bias.

Finally, throughout this chapter we have reviewed ongoing efforts to improve this type of analysis. In this perspective we have begun designing an excursion set model of halo sparsity as an alternate method of predicting the sparsity distribution, and have also started combining halo sparsity with other cosmological probes taking the specific example of cluster number counts. While plenty of work remains to be done on these topics, this anounces an exciting future for sparsity based constraints which have the potential, if we only use X-ray sparsities, to be completely independent from both sides of the S_8 tension, thus bringing a new voice into the debate.

6 | Lensing with non-halo structures

So far we have mainly been interested in the internal structure of dark matter haloes in the context of the ΛCDM model. While in standard CDM cosmologies most of the mass is contained within haloes, there is nonetheless always a fraction of this mass which is contained within structures that have not collapsed along three dimensions. These objects not being very abundant in CDM cosmologies, usually carrying only 5 per cent of the total mass, which makes them difficult to study or even identify. In contrast in Warm Dark Matter (WDM) models, particularly in scenarios which are already excluded by current constraints, these structures can represent up to 50 per cent of the total mass, allowing to study their properties and how they may impact observations more effectively.

In this chapter we briefly study some of the properties of dark matter filaments in these models to then see the possible effect they may have on observations of multiply lensed quasar which are used to constrain the warmth of dark matter. These observations measure anomalies in the fluxes of the replicated images of a single quasar which cannot be explained using a singular lens. Typically these anomalies are thought to be sourced solely by a population of haloes along the line of sight and sub-haloes within the lens galaxy's halo. Under this assumption the mass of a thermal relic dark matter particle has been constrained to $m_\chi > 5.2$ keV, and thus the question we ask ourselves here is, *do non-halo structures have a substantial impact on these constraints?*

To answer this specific question we employ novel simulations of 1 and 3 keV WDM cosmologies that are free of fragmentation allowing the study of non-halo structures with unprecedented accuracy. In the following we will briefly characterise the structures we find in these simulations and evaluate the impact they have on observations of quadruply lensed quasars. We find that these structures exhibit sharp changes in density and as a result can have a considerable effect on observations.

6.1 Constraining the nature of dark matter

One of the biggest questions that dominates both modern cosmology and particle physics is the nature of dark matter (DM). Indeed throughout this work we have seen that most of the matter within the Universe is composed of DM, that it is required to explain many cosmological observations (e.g. Markevitch et al., 2004; Tegmark et al., 2004; de Blok et al., 2008) and is an essential component allowing cosmological N-body simulations to predict the large scale structure of the Universe (for reviews see Frenk & White, 2012; Kuhlen et al., 2012; Angulo & Hahn, 2022). Despite this need for DM in cosmology, particle physics experiments such as the Large Hadron Collider or direct detection experiments such as LUX (Akerib et al., 2017), LUX-ZEPLIN (Aalbers et al., 2023), XENON1T (Aprile et al., 2018), and DarkSide-50 (Agnes et al., 2023) have not been able to detect any sign of traditional candidates. Sparking renewed interest in

more exotic models such as axions (see Sikivie, 2008; Marsh, 2016, for reviews) and primordial black holes (e.g. Carr & Kühnel, 2020).

At cosmological scales these various DM models have distinct phenomenologies which would allow observations to distinguish between them. For example sterile neutrino WDM, with masses $\gtrsim$ 3keV (e.g. Boyarsky et al., 2019) and ultralight axion-like particles with masses $\sim 10^{-20} eV$ which form a fuzzy dark matter (FDM) condensate (e.g. Niemeyer, 2020), are in general agreement with large-scale structure data. These models however predict very different structures at small scales, with sterile neutrinos predicting smooth distributions of dark matter below a mass scale defined by the mass of the DM particle, while FDM models predict the presence of quantum interference patterns at sub-galactic scales. Such differences, which leave traces in cosmological observations, allow to slowly constrain the parameter space of these models. One particular consequence of the damping of small scale seen in these models as suppression of the formation of low-mass haloes which result in a damping of mass function at small masses. This damping is used to define what is known as the half-mode mass, $M_{\rm hm}$, defined as the mass scale corresponding to the length scale at which the WDM transfer function drops to 0.5 (Schneider et al., 2012).

At the time of writing there are four main methods used to constrain the nature of DM through astrophysical observations:

1. by counting the number and studying the properties of Milky Way satellites, as these galaxies are expected to be sensitive to the amount of primordial small-scale structure, although they are also sensitive to baryonic process such as gas cooling and supernova explosions (e.g. Dekel & Silk, 1986; Ogiya & Mori, 2011; Pontzen & Governato, 2012; Zolotov et al., 2012; Arraki et al., 2014),

2. by measuring the small scale clustering of gas using Lyman$-\alpha$ forest data, which have historically put very strong constraints on both WDM and FDM down to scale degenerate with astrophysical processes (e.g. Narayanan et al., 2000; Viel et al., 2013; Iršič et al., 2017; Kobayashi et al., 2017),

3. by examining perturbations in stellar streams which constrains the DM model by constraining the population of invisible sub-haloes around the Milky-Way and local group galaxies (e.g. Yoon et al., 2011; Banik et al., 2018, 2021; Hermans et al., 2021),

4. by measuring perturbations to strong gravitational lenses, to constrain both the population of haloes along the line of sight and sub-haloes within the lens galaxy (e.g. Inoue et al., 2015; Vegetti et al., 2018; Gilman et al., 2019, 2020; Hsueh et al., 2020).

In addition, recent efforts have been made to combine these various probes, providing the most stringent constraints (Enzi et al., 2021; Nadler et al., 2021).

Here we will focus on a specific case of constraints obtained through the observation of the flux ratios of quadruply lensed quasars, which are simply the replicated images of the single quasar around a lens galaxy. As the light in each image follows different paths it is susceptible to encounter different structures along the line of sight. These differential encounters produce anomalies in the flux that is received from the individual images with respect to the case where there are no perturbations to the path of the light rays, excluding the main lens. These anomalies can be studied directly by using ratios of the fluxes of different images hence removing the dependence on the intrinsic flux of

the background source. The resulting signal has been found to be highly sensitive to DM structures even at low halo masses. This sensitivity allows to constrain the HMF along the line of sight and therefore provide constraints on WDM models with recent analyses constraining the mass of thermal relic dark matter to above $m_\chi > 5.2$ keV in order to explain the level of perturbation seen in observations. (Gilman et al., 2019, 2020; Hsueh et al., 2020)

In these studies the perturbations are modelled through a population of DM haloes which the abundance, as measured by the HMF, and internal structure, as measured by the $c - M$ relation, both depend on the type of DM that is being studied. These studies however neglect structures outside of haloes which in WDM and FDM models can represent a significant fraction of the total mass of DM. As mentioned in Chap. 2, As haloes form through the triaxial collapse of the density field, there also exists a population of partially collapsed structures, namely pancakes and filaments, which have only collapsed along one and two dimensions respectively (Zel'dovich, 1970; Shandarin & Zeldovich, 1989). These structures exist in all DM models including CDM but are usually smaller and fragmented into smaller substructures in colder DM models (Bond et al., 1996). While these structures have much lower densities than haloes, WDM simulations have shown that they typically present high-contrast caustic structures, creating sharp high-contrast edges in the density field (Buchert, 1989; Shandarin & Zeldovich, 1989; Angulo et al., 2013). With the increasing precision of observations it is important to understand what systematic effects may alter our conclusions. It is thus, within such a context that we investigate the impact these structures may have on observations of quadruply lensed quasars.

While this was investigated in pioneering work using simplified analytical models (Inoue, 2015), here we are able to address this question in a fully cosmological context thanks to the advent of new fragmentation free simulations (Hahn & Angulo, 2016; Stücker et al., 2020) that allow us to study these structures with unprecedented precision. In section 6.2 we first discuss the fragmentation free cosmological simulations that we use to study the small scale properties of the WDM density field. In section 6.3 we then present the gravitational lensing simulations specifically developed to reproduce flux ratio observations. In section 6.4 we investigate the type of structure that are formed within the WDM simulations and in section 6.5 we use these structures to produce and analyse synthetic flux ratio anomalies. Finally we summarise this study in section 6.6. The work presented in this chapter culminated in the publication of Richardson et al. (2022)

6.2 Simulating structure formation in WDM cosmologies

We begin by describing the type of simulation used here to solve the dynamics of the WDM density field. Note that we will mainly focus on how these simulations differ from the standard N-body CDM simulations presented in Chap. 2 in particular in terms of initial conditions and force calculations. For specifics we refer to the works of Stücker et al. (2020, 2022) where both the methods and properties of this set of simulations are discussed at length.

6.2.1 Initial conditions and simulation set-up

The main difference between WDM models and their CDM counterpart is that a non-negligible velocity dispersion is imparted to the particles after they are created in the

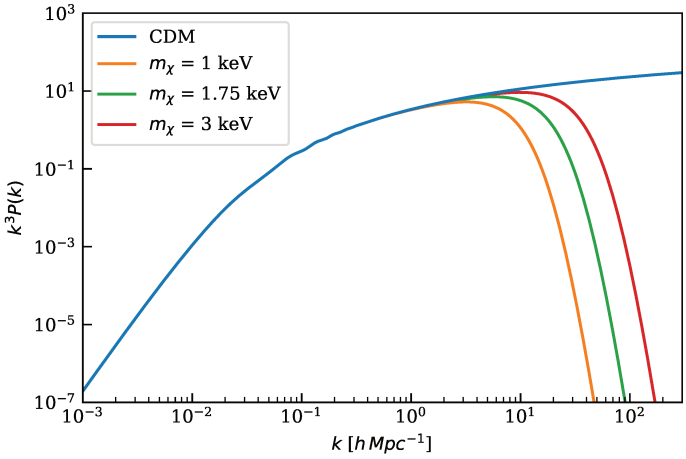

Figure 6.1: Power spectra of matter fluctuations used to generate the initial conditions of three WDM simulations corresponding to three thermal relic masses.

very early universe. While this velocity can be thermal or non-thermal origin depending on the specifics of the model, in all cases it allows the particles to free-stream over large distances and out of small scale perturbations in the early Universe, effectively suppressing the growth of structure at very small scale. As the Universe expands the particle distribution cools adiabatically allowing gravitational collapse to take place similarly to CDM. As we expect the fluid to be cold before structures form we can therefore, to very good approximation, model WDM in the same way as CDM, and simply truncating the matter power spectrum at small scales.

Similarly to how we define the CDM power spectrum in Chap. 2, the WDM power spectrum can simply be defined through the use of a transfer function. In this case we use the parametrisation of Bode et al. (2001)[1],

$$P_{\rm WDM}(k) = \left(1 + (\alpha k)^2\right)^{-10} P_{\rm CDM}(k) \tag{6.1}$$

with

$$\alpha = \frac{0.05}{h\,{\rm Mpc}^{-1}} \left(\frac{\Omega_\chi}{0.4}\right)^{0.15} \left(\frac{h}{0.65}\right)^{1.3} \left(\frac{1{\rm keV}}{m_\chi}\right)^{1.15} \left(\frac{1.5}{g_\chi}\right)^{0.29} \tag{6.2}$$

where $g_\chi = 1.5$ is the number of degrees of freedom which contribute to the number density, m_χ is the mass of the DM particle in units of keV, and Ω_χ is the DM density parameter. Here we will study the specific case of two thermal relic DM models with particles masses of 1 keV and 3 keV along with a CDM model. From hereon we will refer to these two simulations as the '1 keV' and '3 keV' simulations respectively. Note that these simulations are part of a wider set which aim to triangulate the parameter space of possible cut off functions (see Stücker et al., 2022). As such the parameterisation of the transfer function differs slightly from more recent estimates for thermal relics (Schneider et al., 2012). If we explicitly match the resulting half-mode masses of these two parametrisations we find that these simulations in fact correspond to slightly warmer models with thermal relic masses of $m_\chi = 0.82$ keV and $m_\chi = 2.6$ keV. Each simulation consists of a periodic box with side length $L_{\rm box} = 20\ h^{-1}$Mpc. The initial conditions

[1] Viel et al. (2005) offer an alternative parametrisation

Table 6.1: Parameters used in the simulations and throughout this work. The last line indicates the fraction of mass which was found to be outside of haloes at $z = 0$.

Parameter	1 keV Sim.	3 keV Sim.
h	0.679	–
Ω_{m}	0.3051	–
Ω_{Λ}	0.6949	–
Ω_{K}	0	–
σ_8	0.8154	–
M_{hm}	$2.5 \cdot 10^{10} h^{-1}\mathrm{M}_{\odot}$	$5.7 \cdot 10^{8} h^{-1}\mathrm{M}_{\odot}$
L_{box}	$20 h^{-1}\mathrm{Mpc}$	–
N_{tracer}	512^3	–
m_{tracer}	$5.0 \cdot 10^{6} h^{-1}\mathrm{M}_{\odot}$	–
$f_{\mathrm{non-halo}}$	45.7%	34.8%

for the simulations are generated using MUSIC[2] using the cosmological parameters in Tab. 6.1 and are based on the same Gaussian random field ensuring that each volume provides the same large scale information.

6.2.2 Avoiding fragmentation

As we have mentioned previously, we assume that WDM cools rapidly. This means that, similarly to CDM, in the late-time universe a WDM fluid is governed by Vlasov-Poisson dynamics. While we have seen that for CDM the evolution of the density field can be solved using N-body techniques, and have in the past been very successful at doing so, this is not the case for WDM. This is because, due to the perturbation spectrum being truncated at small scales, the configuration space density distribution of WDM exhibits smooth structures on large scales. When evolving these structures using N-body particles, they artificially fragment into small clumps due to discreteness effects (Wang & White, 2007).

To overcome this artificial fragmentation problem new methods based on tessellations of the phase space distribution function have been developed (e.g. Abel et al., 2012; Shandarin et al., 2012; Hahn & Abel, 2013). Under the assumption that the phase space distribution is cold the latter only occupies a three dimensional hypersurface within the full six dimensional phase space. In these simulations, N-body particles no longer represent phase space elements but instead trace the distribution function by acting as the vertices of three dimensional simplicial elements, which are colloquially referred to as tetrahedra. The main advantage of this approach is that the volume of these tetrahedra determines the density of DM throughout space, meaning that one can then reproduce the density field and thus gravitational potential without coarse graining.

While these methods are very efficient at overcoming the artificial fragmentation problem they do however suffer from a loss of precision inside virialised structures, where strong phase space mixing takes place. This entails that one requires an ever increasingly large number of vertices in order to accurately track the distribution function inside haloes (Sousbie & Colombi, 2016). Recently adaptive refinement approaches have been developed (Hahn & Angulo, 2016; Sousbie & Colombi, 2016) but are still computationally prohibitive when it comes to simulating the interior of haloes where the number of required refinement levels increases exponentially as a simulation advances. In order

[2] https://www-n.oca.eu/ohahn/MUSIC

to circumvent this issue a hybrid tesellation-N-body solution was proposed by Stücker et al. (2020). This hybrid solution, separates the distribution function, specifically the sheet tracing particles, into regions corresponding to four dynamically defined classes, i.e. voids, pancakes, filaments, and haloes. These classes are differentiated using a criterion, inspired by Zel'dovich (1970) and Hahn et al. (2007), defining each type of structure through the number of axes that have gravitationally collapsed. In these simulations voids, pancakes, and filaments are regarded as having a relatively simple phase space distribution function and can therefore be accurately modelled using the tessellation. Haloes on the other hand are regarded as dynamically complex and therefore the tracer particles are converted into N-body particles and released into these regions. This criterion also allows us to trace and separate between the different structures, a feature we will use in the following.

Within this framework the simulations we use here employ 256^3 particles to act as the vertices of the tessellation from which we reconstruct the density field and compute force, where this approximation is valid. Additionally, these simulations contain 512^3 tracer particles which are released into regions where the interpolation fails (see Stücker et al., 2022, for details). The phase space interpolation also allows us to recover the density field with much higher sampling than the original output when post-processing the simulation (Abel et al., 2012; Hahn & Angulo, 2016). This allows to recover small scale features that are not visible from the distribution of tracer particles alone. This technique, which we will refer to as resampling the density field, can also be used to reduce discreteness noise in gravitation lensing simulations (Angulo et al., 2014). It is thanks these high resolution density fields that in the following we are able to simulate the effect they have on strong gravitational lenses.

6.3 Gravitational lensing simulations

In addition to the cosmological simulations that we have reviewed in the previous section we also need to simulate how the path of light rays is perturbed by the structures we find in this cosmological volume. For this explicit purpose we develop a gravitational lensing simulation code which we present below. We will first briefly review the equations that are solved by this code before discussing how these are implemented.

6.3.1 Theory of gravitational lensing

Due to the small size of the cosmological simulations, we restrict the geometry of the problem to the case where light rays coming from a source are only deflected once by a single effective lens (see e.g. Schneider et al., 1992; Bartelmann & Schneider, 2001; Dodelson, 2003, for more general reviews). As can be seen in Fig. 6.2, in this context light rays originate from a source at an angular diameter distance D_s and are deflected by a single lens placed at a angular diameter distance D_d from the observer, these two planes are separated by an angular diameter distance D_ds. When projecting this onto the plane of the sky this can effectively be seen as displacing the angular position $\boldsymbol{\beta}$ of the source, by a deflection angle $\boldsymbol{\alpha}$, making it appear at a new position $\boldsymbol{\theta}$. These angular positions are related through the lens equation,

$$\boldsymbol{\beta} = \boldsymbol{\theta} - \boldsymbol{\alpha}, \tag{6.3}$$

which essentially, knowing the position of the source and the deflection angle allows us to predict where images of this source will form. Note that one of the prominent

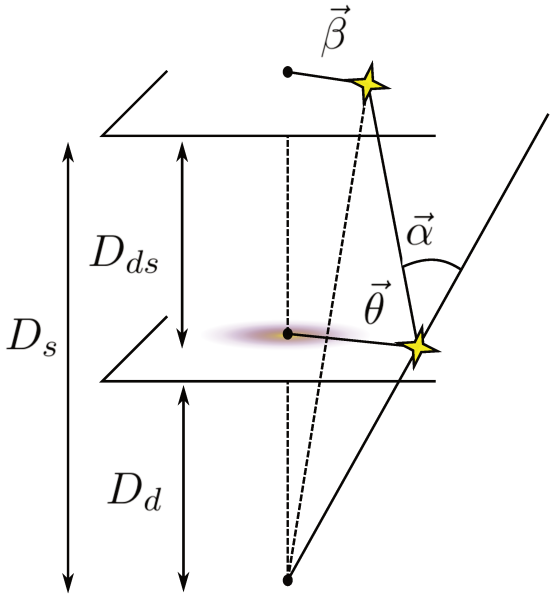

Figure 6.2: Sketch of the simplified gravitational lens geometry assumed throughout this chapter, where the trajectory of a light ray produced by a source place at angular position $\boldsymbol{\beta}$ shown as a solid line is perturbed by an angle $\boldsymbol{\alpha}$ produced by a single deflector, producing an image at an angular position $\boldsymbol{\theta}$.

features of this equation is that it allows for a single position in the source plane to map to several positions in the image plane. In this approximation the surface brightness of sources is conserved, as such the observed surface brightness

$$I_{\rm o}(\boldsymbol{\theta}) = I_{\rm s}(\boldsymbol{\beta}) \tag{6.4}$$

can directly be expressed as a function of the intrinsic surface brightness, $I_{\rm s}(\boldsymbol{\beta})$, of the source.

In this approximation the deflection $\boldsymbol{\alpha}$ is defined as,

$$\boldsymbol{\alpha} = \nabla\psi, \tag{6.5}$$

the gradient of the lensing potential ψ,

$$\nabla^2\psi = 2\kappa, \tag{6.6}$$

sourced by the normalised surface density field

$$\kappa = \frac{\Sigma(\theta) - \bar{\Sigma}}{\Sigma_{\rm cr}}, \tag{6.7}$$

also referred to as convergence, where $\Sigma(\boldsymbol{\theta})$ is the projected surface density, $\Sigma_{\rm cr} = \frac{c^2}{4\pi G}\frac{D_{\rm s}}{D_{\rm d}D_{\rm ds}}$ is the critical surface density, c is the speed of light, G is the gravitational constant, and $\bar{\Sigma} = \int_0^{z_{\rm bg}} \rho_{\rm m} dz$ is the mean surface density.

Finally, we will make use of two additional quantities, the distortion matrix $\mathbf{A}$, which is defined as the Jacobian of the mapping between the source and image planes:

$$\mathbf{A} = \left|\frac{\partial\boldsymbol{\beta}}{\partial\boldsymbol{\theta}}\right| \quad \text{i.e.} \quad \mathsf{A}_{ij} = |\partial_j\beta_i| = |\delta_{ij} - \partial_i\partial_j\psi| \tag{6.8}$$

where δ_{ij} is the Kronecker delta symbol. and the inverse of its determinant,

$$\mu = \frac{1}{\det\left[\mathbf{A}\right]} \tag{6.9}$$

known as magnification. We see that for regions where $\det\left[\mathbf{A}\right] = 0$ the magnification becomes infinite, this typically occurs along curves in the image plane known as critical curves and delimit the regions in which multiple images are formed. If traced back to the source plane these curves are called caustics and mark the regions which will be multiply imaged.

6.3.2 Numerical implementation

Now that we have an overview of the equations we need to solve we now present the numerical algorithms we have implemented to do so. We start by defining a grid in the image plane representing a set of light rays which we propagate back towards the source. It is on this same grid that we define the convergence field κ from which we deduce the lensing potential

$$\psi = g * 2\kappa \tag{6.10}$$

where $g = (2\pi)^{-1}\ln(\theta)$ is the Green's function of the 2 dimensional Laplacian, with $\theta = \|\boldsymbol{\theta}\|$. This filtering approach is however non trivial to implement as the Green's function exhibits a singularity at $\boldsymbol{\theta} = \mathbf{0}$. To avoid this issue we employ the regularised integration kernel of Hejlesen et al. (2013)

$$g_m = -\frac{1}{2\pi}\left[\ln(\theta) - Q_m\left(\frac{\theta}{\epsilon}\right)\exp\left(-\frac{\theta^2}{2\epsilon^2}\right) + \frac{1}{2}E_1\left(\frac{\theta^2}{2\epsilon^2}\right)\right], \tag{6.11}$$

where ϵ is a smoothing parameter set to 1.5 times the grid spacing, Q_m is a polynomial setting the order $m \in \mathbb{N}$ of the kernel and E_1 is the exponential integral distribution. This particular function has a finite value at $\theta = 0$

$$g_m(0) = \frac{1}{2\pi}\left[\frac{\gamma}{2} - \ln\left(\sqrt{2}\epsilon\right) + Q_m(0)\right], \tag{6.12}$$

where $\gamma = 0.5772156649$ is the Euler's constant.

Similarly, the deflection angles, distortion matrix components and magnifications can be obtained using analytical derivatives of this same kernel, thanks to the differentiation property of convolutions. Such that the deflection angle

$$\alpha_i = \partial_i g_m * 2\kappa, \tag{6.13}$$

is computed with the first derivative,

$$\begin{aligned}\partial_i g_m = -\frac{1}{2\pi}\Bigg\{&\frac{\theta_i}{\theta^2}\left[1 - \exp\left(-\frac{\theta^2}{2\epsilon^2}\right)\right] \\ &+\frac{\theta_i}{\epsilon^2}\exp\left(-\frac{\theta^2}{2\epsilon^2}\right)\left[Q_m\left(\frac{\theta}{\epsilon}\right) - \frac{\epsilon}{\theta}Q'_m\left(\frac{\theta}{\epsilon}\right)\right]\Bigg\},\end{aligned} \tag{6.14}$$

which is vanishing at $\theta = 0$, and the distortion matrix is computed using the second derivatives,

$$\mathsf{A}_{ij} = \delta_{ij} - \partial_i\partial_j g_m * 2\kappa. \tag{6.15}$$

For which we require two expressions for the different possible combinations of derivatives. Leading to,

$$\begin{aligned}\partial_i^2 g_m = &-\frac{1}{2\pi}\left\{\frac{(-1)^i(\theta_2^2-\theta_1^2)}{\theta^4}\left[1-\exp\left(-\frac{\theta^2}{2\epsilon^2}\right)\right]\right.\\ &+\frac{1}{\epsilon^2}\exp\left(-\frac{\theta^2}{2\epsilon^2}\right)\left(\left(1-\frac{\theta_i}{\epsilon^2}\right)\left[Q_m\left(\frac{\theta}{\epsilon}\right)-\frac{\epsilon}{\theta}Q'_m\left(\frac{\theta}{\epsilon}\right)\right]\right.\\ &\left.\left.\frac{\theta_i^2}{\theta^2}\left[\left(\frac{\theta^2+\epsilon^2}{\theta\epsilon}\right)Q'_m\left(\frac{\theta}{\epsilon}\right)-\frac{\epsilon}{\theta}Q''_m\left(\frac{\theta}{\epsilon}\right)-1\right]\right)\right\},\end{aligned} \tag{6.16}$$

for the diagonal terms, which at $\theta = 0$ yields $\partial_i^2 g_m|_{\theta=0} = \frac{1}{2\pi\epsilon^2}\left(\frac{1}{2}+Q_m(0)-Q''_m(0)\right)$, and

$$\begin{aligned}\partial_i\partial_j g_m = &-\frac{1}{2\pi}\left\{\frac{\theta_i\theta_j}{\theta^4}\left[-\frac{\theta^2}{\epsilon^2}\exp\left(-\frac{\theta^2}{2\epsilon^2}\right)+2\left(1-\exp\left(-\frac{\theta^2}{2\epsilon^2}\right)\right)\right]\right.\\ &-\frac{\theta_i\theta_j}{\epsilon^2}\exp\left(-\frac{\theta^2}{2\epsilon^2}\right)\left(-\frac{1}{\epsilon^2}\left[Q_m\left(\frac{\theta}{\epsilon}\right)-\frac{\epsilon}{\theta}Q'_m\left(\frac{\theta}{\epsilon}\right)\right]\right.\\ &\left.\left.+\frac{1}{\theta^2}\left[\frac{\theta^2+\epsilon^2}{\theta\epsilon}Q'_m\left(\frac{\theta}{\epsilon}\right)-Q''_m\left(\frac{\theta}{\epsilon}\right)\right]\right)\right\},\end{aligned} \tag{6.17}$$

for the cross terms, which yields $\partial_i\partial_j g_m|_{\theta=0} = 0$.

These convolutions can be efficiently solved using FFTs making this method theoretically more efficient than standard methods based on finite differences. This approach does however come with the drawback of limiting us to a uniform grid of points. This is problematic as we want to accurately model effects taking place at very small scales while taking into account contributions coming from large scale features in the density field. To remedy this we incorporate a 'force splitting' approach where we split all quantities into a long range and a short range contribution, for example $\psi = \psi_\ell + \psi_\mathrm{s}$ in this case of the lensing potential, where,

$$\psi_\ell = (2\kappa * g_m) * h_\ell \qquad , \qquad \psi_\mathrm{s} = (2\kappa * g_m) * h_\mathrm{s}, \tag{6.18}$$

and

$$\hat{h}_\ell := \exp\left\{-8\pi^2 k^2 \ell^2\right\} \qquad , \qquad \hat{h}_\mathrm{s} := 1 - \hat{h}_\ell, \tag{6.19}$$

where ℓ is the splitting length-scale and the hat denotes the Fourier transform. As such we compute the large scale contribution on a coarse mesh with periodic boundaries and the small scale contribution on a much finer mesh with non-periodic boundary conditions. Once we have both contributions the large scale contribution is then linearly interpolated onto the high resolution mesh to obtain the complete solution.

We test the numerical convergence of this scheme using a circular Gaussian lens

$$\kappa = \frac{K_\mathrm{m}}{2\pi\sigma^2}\exp\left(-\frac{\theta^2}{2\sigma^2}\right), \tag{6.20}$$

where K_m is the physical mass of the profile in units of the critical surface density and σ is the width of the profile. With this particular lens we can derive an analytical solution to which we can compare the outputs of our numerical simulations.

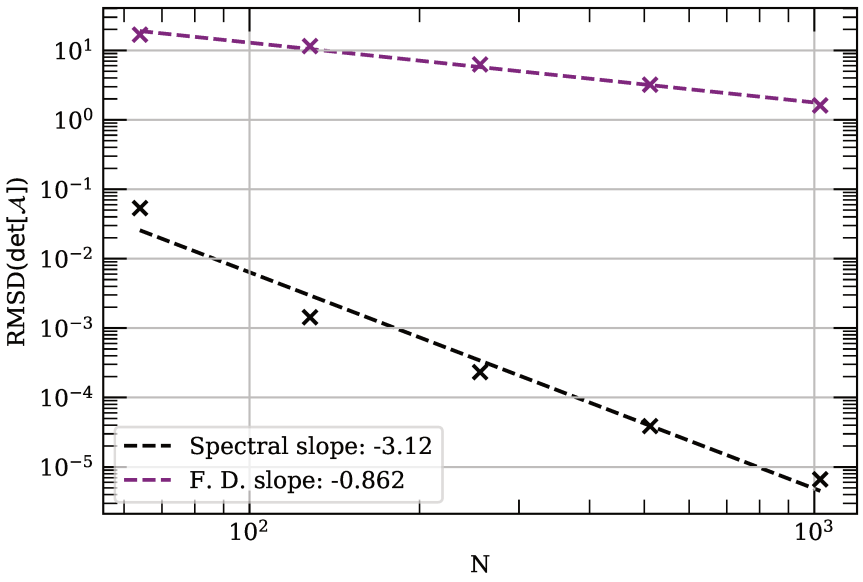

Figure 6.3: RMSD of the determinant of distortion matrix with respect to the analytical solution for increasing resolution. The purple curve corresponds to the FD scheme and the black curve corresponds to the spectral method. We observe that the spectral method is overall more accurate and converges at a faster rate than the FD scheme.

Solving Eq. (6.6) we obtain the analytical lensing potential

$$\psi = \frac{K_{\rm m}}{4\pi}\left[\ln\left(\frac{\theta^4}{4\sigma^4}\right) - 2E_i\left(\frac{\theta^2}{2\sigma^2}\right)\right] + C, \tag{6.21}$$

where E_i is the exponential integral and C is a constant gauge term. We express the deflection angles and magnification by taking derivatives of this potential. While the radial symmetry of this problem means the solution is fully described by the norm α of the deflection angle

$$\alpha = \frac{K_{\rm m}}{\pi\theta}\left[1 - \exp\left(-\frac{\theta^2}{2\sigma^2}\right)\right], \tag{6.22}$$

this is not the case for the three independent components of the distortion tensor $\mathbf{A}$,

$$\begin{cases} \mathsf{A}_{11} = 1 - \frac{K_{\rm m}}{\pi}\left[\frac{\theta_2^2-\theta_1^2}{r^4}\left(1-\exp\left(-\frac{\theta^2}{2\sigma^2}\right)\right) + \frac{\theta_1^2}{\theta^2\sigma^2}\exp\left(-\frac{\theta^2}{2\sigma^2}\right)\right] \\ \mathsf{A}_{22} = 1 - \frac{K_{\rm m}}{\pi}\left[\frac{\theta_1^2-\theta_2^2}{\theta^4}\left(1-\exp\left(-\frac{\theta^2}{2\sigma^2}\right)\right) + \frac{\theta_2^2}{\theta^2\sigma^2}\exp\left(-\frac{\theta^2}{2\sigma^2}\right)\right] \\ \mathsf{A}_{12} = \frac{K_{\rm m}}{\pi}\frac{\theta_1\theta_2}{\theta^4}\left[2\left(1-\exp\left(-\frac{\theta^2}{2\sigma^2}\right)\right) - \frac{\theta^2}{\sigma^2}\exp\left(-\frac{\theta^2}{2\sigma^2}\right)\right] \end{cases} \tag{6.23}$$

With this solution we now compute the Root Mean Square Deviation (RMSD) between the numerical solution and the analytical solution, imposing in the numerical case that the total mass of the profile is conserved, while increasing the resolution. In Fig. 6.3 we show the resulting measurements for five resolutions, along with a power law fit giving an indication of the convergence rate. In addition, as a point of comparison, we implement a classical finite difference scheme. We observe that the scheme presented above achieves a higher degree of convergence than the finite difference scheme providing both smaller errors and an overall faster rate of convergence.

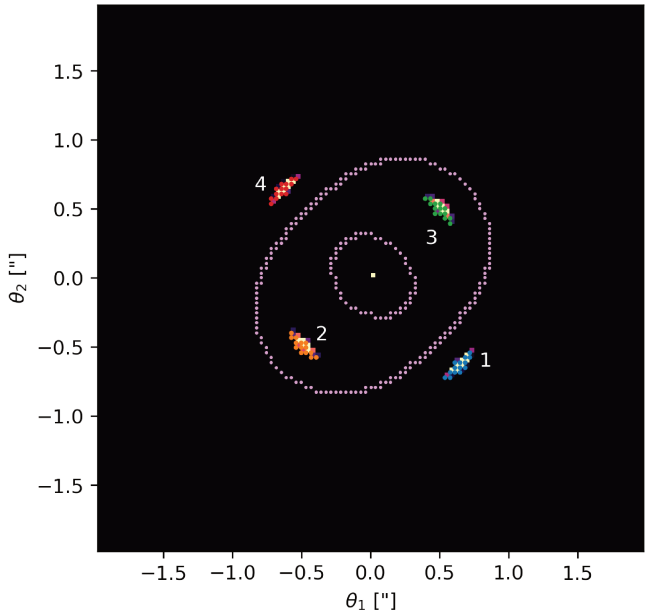

Figure 6.4: Distorted image produced by the reference lens model described in § 6.3.3, showing the position of critical curves and detected multiple images. Note that the colours of the individual images are only for display purposes. The pink curves represent the two critical curves of this particular lens.

6.3.3 Flux ratio measurements

With the simulation setup presented above we are now able to generate synthetic observations of quadruply lensed quasars, we will first describe the lens and source models before discussing how we extract measurements from the resulting simulated image.

Lens & source models

We model the main deflector as a single lens which we generate using a projected elliptical NFW profile (Golse & Kneib, 2002) with mass $M_{200c} = 4 \cdot 10^{13} \mathrm{M}_{\odot}$ and concentration $c_{200c} = 8$. The profile has an eccentricity $\epsilon = 0.05$, and has its main axes rotated by an angle $\lambda = \pi/4$ with respect to the coordinate frame. As to mimic the configuration of the quadruply lensed system PG1115+080 (Weymann et al., 1980; Chiba et al., 2005) we place this lens at a redshift $z_{\mathrm{l}} = 0.29$ and assume a point like source at redshift $z_{\mathrm{s}} = 1.71$ exactly aligned with the lens. In this configuration we produce four evenly space images at a radius of $\theta_{\mathrm{E}} \sim 1$ arcsec along with fifth central image as can be seen in Fig. 6.4, in the lens plane this corresponds to the physical displacement of $\theta_{\mathrm{E}} D_{\mathrm{d}} \sim 3\, h^{-1} kpc$. We note that in this figure the source is replaced by a disk of constant surface brightness of radius 0.01 arcsec for visual purposes. In the following we will use this particular model as point of comparison when adding perturbations and as such in the following we refer to this configuration as the reference lens model.

The statistical properties we will study in the following are highly sensitive to the configuration of the images. This is particularly the case of the observable we are modelling here of which the absolute value can change substantially depending on the geometry of the problem. The main consequence of this is that certain configurations are more sensitive to perturbations than others. We note however that the general

trends and conclusions presented here are valid for many configurations and for the sake of conciseness we will not discuss the particular impact of other configurations.

Image extraction and measurements

As can be seen in Fig. 6.4 the configuration mentioned above gives rise to five images in total, four magnified and hence easily visible images located near the outer critical curve and a fifth strongly demagnified image which is impossible to see in observations as it is often too dim to be observed and hidden by the luminous component of the deflector, typically a galaxy, as such in the following we will discard this fifth image and focus on the four outer replications.

To measure the magnification of each image we infer the position $\boldsymbol{\theta}$ at which the path of a light ray connecting the observer to the point source intersects the plane of the main deflector. This is achieved by finding the positions which solve the lens equation,

$$\boldsymbol{\theta} - \boldsymbol{\alpha}(\boldsymbol{\theta}) - \boldsymbol{\beta} = \mathbf{0} \tag{6.24}$$

using a two dimensional root finding algorithm. This equation admits five solutions, the five images discussed above, as such in order to ensure the convergence of the root finding procedure we introduce an intermediate step to provide initial guesses close to each image of interest. We do this by first launching a grid of light rays towards the source and selecting those which fall close to the source, typically a few m.a.s. We then group these rays into four images based on proximity to one another and use the mean position of each group as a starting point for the gradient decent. This procedure, which we implement in PYTHON using the SCIPY library (Weaver, 1985; Kelley, 1995; Virtanen et al., 2020), ensures that we are indeed measuring the contributions of all four images.

We then measure the flux of each image,

$$F_k = \mu_k F_{\rm int} \tag{6.25}$$

by evaluating the local value of the magnification μ_k produced by the lens at the inferred position of each image, indexed here with the letter k. In observational settings the intrinsic flux, $F_{\rm int}$ of the source is unknown and as such it is not possible to recover the magnifications of individual images. This limitation is however avoided by studying flux ratios which remove the dependency on the intrinsic flux while retaining that on the magnification. Formally one can define a total of six pairs of images, however the resulting ratios will not be independent as we are able to define three of these measurements using the three others. As such it is common practice to define only three flux ratios choosing the ratio of three of the images with respect to the brightest,

$$f_k = F_k/F_4 = \mu_k/\mu_4 \tag{6.26}$$

which in our case corresponds to image 4 in Fig. 6.4.

Note that this is only valid because we are considering a point source. In practice, such an assumption can artificially increase the sensitivity to small scale contributions, caused by stars or black holes for instance and known as micro-lensing events. We test this assumption by implementing an extended source and retrieving the fluxes by integrating over the brightness distribution of each replicated image. Repeating this operation not only with the reference lens but also in the perturbed cases presented below we find that this assumption does not significantly impact our qualitative conclusions. As such we consider the density field to be sufficiently smooth for this approximation to be valid in this case, and revert to using a point source as the use of an extended source significantly increases the computation time needed to measure a set of flux ratios.

6.3.4 Scale filtering

In observational settings the lens model is not known *a priori* meaning that is has to be fitted simultaneously to the data before extracting the flux ratio signal. For example Gilman et al. (2020) achieve this by fixing the positions of the four replicated images and using these data to fit the lens parameters, using priors on these parameters based on the dynamics of the baryonic components of the lenses, they then measure flux ratio anomalies with respect to the flux ratios produced by the resulting lens model. Note that this procedure has to be done every time the line of sight is perturbed as the perturbations may displace the images and therefore requires the lens model to compensate for this displacement. Here implementing such a procedure induces a large scatter in the resulting flux ratios as we cannot place the appropriate priors on the parameters. This scatter being of the same order as the signal we are looking to simulated this results in unreliable measurements.

Thus to avoid the need of refitting the lens parameters for each type of perturbation we instead opt to filter out the large scale modes of the projected density field as it is these modes which contribute the most to displacing the images while small scale modes contribute to altering the flux ratios. To this effect we repurpose the force splitting kernels of Eq. (6.19) as to define a large scale, $\kappa_{\rm l}$, and a small scale, $\kappa_{\rm s}$, density field. Here we choose a splitting length, $\ell = 0.85$ arcsec, approximately the size of the deflector's Einstein radius. While the exact value of the splitting has little impact on the final result we will however discuss it further when we investigate the statistical properties of the flux ratio anomalies.

6.4 Properties of the WDM density field

As a case study, in this section we will compare how the magnifications of the individual images are perturbed by the presence of either a dark matter halo close to the half-mode mass or a filament coming from the WDM simulation. As such we will first examine the properties of these two types of objects before using them as perturbations to our reference lens model.

6.4.1 Haloes

As mentioned previously haloes are the primary target of many studies of WDM structure formation (e.g. Bode et al., 2001; Schneider et al., 2012; Angulo et al., 2013). Similarly to there CDM counterparts these haloes have been found to be reasonably well fitted by the NFW profile (Lovell et al., 2014; Bose et al., 2016). Although in contrast with CDM, the HMF in WDM models is highly suppressed at the low mass end due to the small scale cut off in the matter power spectrum. The characteristic mass-scale of this suppression is known as the half mode mass,

$$M_{\rm hm} = \frac{4\pi}{3}\rho_{\rm m}\left(\frac{\lambda_{\rm hm}}{2}\right)^3 \tag{6.27}$$

with

$$\lambda_{\rm hm} = 2\pi\lambda_{\rm s}^{\rm eff}(2^{1/5}-1)^{-1/2} \simeq 16.29\lambda_{\rm s}^{\rm eff} \tag{6.28}$$

defining the length scale for which the transfer function drops by a factor 2 and $\lambda_{\rm s}^{\rm eff} \simeq \alpha$, defined in Eq. (6.2), is the effective free streaming length. In Tab. 6.1 we report this mass scale for the two WDM models studied here. The suppression of small scale

perturbations also suppresses the number of subhaloes leading to WDM haloes having smaller substructure fractions than their CDM counterparts.

Studies have also found that free-streaming not only suppresses the abundance of small haloes but also alters their density structure (Bose et al., 2016; Ludlow et al., 2016). Quantifying the shape of the profile using NFW concentrations Bose et al. (2016) find that the $c - M$ relation is also suppressed below the half mode mass,

$$\frac{c_{\rm WDM}(M,z)}{c_{\rm CDM}(M,z)} = (1+z)^{\beta(z)} \left(1 + 60\frac{M_{\rm hm}}{M}\right)^{-0.17}, \tag{6.29}$$

where $\beta(z) = 0.026z - 0.04$.

6.4.2 The density structure of a filament

While WDM haloes have been widely studied in the literature, this has not been the case of other structures such as WDM filaments and pancakes. While these structures can represent a considerable proportion of the total mass of the cosmic web, from 5 to 50 per cent depending on the model (Angulo & White, 2010; Buehlmann & Hahn, 2019), they are difficult to simulate accurately as N-body methods typically struggle with smooth matter distributions, typically fragmenting into smaller clumps due to numerical noise. As the simulations used here avoid this issue we are able to study these structures in unprecedented detail.

Here we focus on the second most massive class of structure, filaments. We detect and extract these filaments using DisPerSE[3](Sousbie, 2011) which, using Morse theory, identifies filaments as ridges of in the three dimensional density field. Here we chose to study a filament in the 1 keV simulation that remains roughly straight over its entire length of $3.8h^{-1}$Mpc. We show this object in Fig. 6.5 where we depict it both from a sideways view along with multiple projections aimed along the primary axis of the structure, gradually increasing the projection depth. We produce these density fields by resampling the distribution function by a factor 64^3 leading to an effective particle mass resolution of the order of $m \simeq 20h^{-1}{\rm M}_\odot$. Such a level of refinement is possible as the the phase-space distribution function of the filament is sufficiently simple in this region to be accurately reconstructed from the tracer particles.

In the top panel of Fig. 6.5 we see that the filament is made up of a complex network of caustic structures which are formed during shell crossing and appear as sharp steps in the density field. Looking along the main axis of the filament reveals a rich structure. We see, for instance, that the filament is embedded within a pancake which spans from the top left to the lower right of each projection. We also find that the internal structure of the filament is very different to that of haloes, with the densest regions not corresponding to a single peak but rather to the superposition of caustics and presents sharp edges beyond which the density drops significantly. In this same figure we are also able to see how filaments connect to the haloes due to the presence of three haloes on the right of Fig. 6.5. Indeed in these regions the number of caustics increases drastically which is the leading reason why haloes cannot be resampled.

In order to gauge the influence that this type of structure may have on our synthetic flux-ratio observations in Fig. 6.6 we estimate the distribution of column densities, in units of $\rho_{\rm m}h^{-1}{\rm Mpc}$[4], in each projection. We observe that the highest column densities reached by the filament are of the order of $100\rho_{\rm m}h^{-1}$Mpc. By overlaying the distribution

[3] http://www2.iap.fr/users/sousbie/web/html/indexd41d.html

[4] Here this corresponds to $\rho_{\rm m}h^{-1}{\rm Mpc} = 8.33 \cdot 10^{10}h^2{\rm M}_\odot{\rm Mpc}^{-2}$ at redshift $z = 0$.

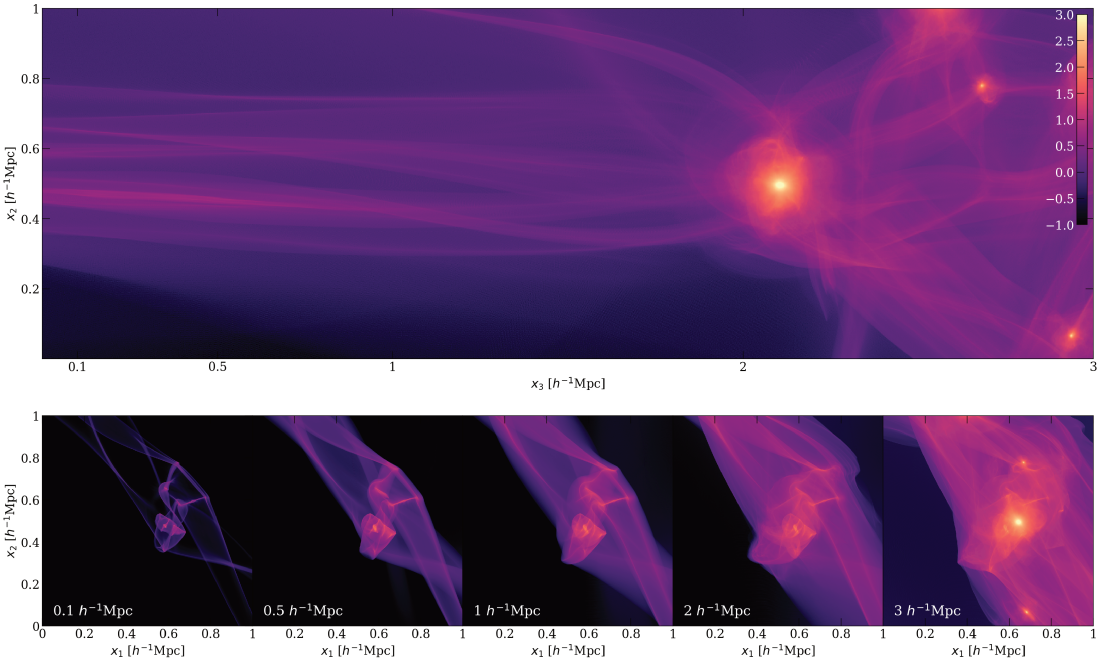

Figure 6.5: *Top panel:* Column density of a filament from the 1 keV simulation in logarithmic units of $\rho_{\mathrm{m}} h^{-1}$Mpc, seen side on. *Bottom panels:* Same filament but projected along its axis for increasing projection depths. All panels are normalised to the same colour scale and the column density increases monotonically as the projection depth increases. We can observe the diagonal structure in all projections, this structure is the pancake within which the filament is embedded. In the right most panel the haloes at the end of the filament are visible, it is these haloes that generate the high density tail of the corresponding black curve of Fig. 6.6.

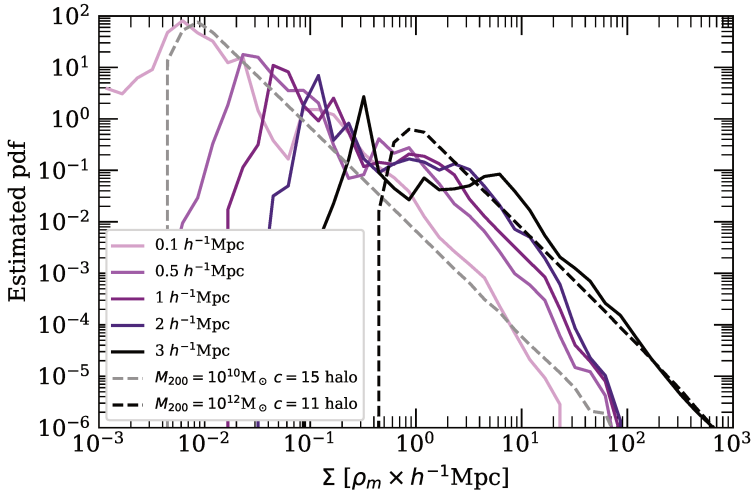

Figure 6.6: Column density distribution functions, $\phi(\Sigma)$, with Σ in units of $\rho_{\rm m} h^{-1}$Mpc for increasing projection depths.The high-density tail (likely caused by caustics) stops adding up coherently around $10^2 \rho_{\rm m} h^{-1}$Mpc . The black curve is produced by the presence of high-mass haloes at the end of the filament as can be seen in Fig. 6.5. The two dashed lines indicate the column density distributions of typical (CDM) NFW haloes with masses of 10^{10}M$_\odot$ and 10^{12}M$_\odot$. We see that the filament achieves peak column densities comparable with a 10^{10}M$_\odot$ halo, while at the same time having much more total mass associated with intermediate density levels as well.

corresponding to a single low mass, $M_{200c} = 10^{10} h^{-1}M_\odot$, halo modelled by an NFW profile with concentration $c_{200c} = 15$, we see that the filament is able to produce similar column density to these haloes. For comparison we also overlay the distribution of a more massive halo, $M_{200c} = 10^{12} h^{-1}M_\odot$, $c_{200c} = 11$, which matches the deepest projection of the filament. This last projection containing haloes it is reasonable to assume that the higher column densities reached here are sourced by the haloes. From this we can already conclude that we do not expect filaments to produce there own strong lensing effect but they may act as significant perturbers to the signal.

We note however that here we have aligned the filament with the projection axis in order to maximise the column densities. What Fig. 6.6 shows is that the high density features do not add coherently past $\sim 0.5 h^{-1}$Mpc where we see the high density tail of the distribution saturate. Instead the contribution of these structures becomes overshadowed by regions with which do add up coherently such as the wall which sees its column density gradually increase as we increase the projection depth. The end result is that the resulting density simply resembles a set of overlapping sharp caustics, which increase in number as we increase the projection depth. Finally the most important feature is that these caustics do produce extremely sharp density gradients where the column density can increase by several orders of magnitude over a very short length scale.

6.4.3 A strong lens perturbed by a filament

We now want to quantitatively estimate the effect that such a filament would have on flux ratio observations. To do so we simulate the reference lens model presented in section 6.3.3, using a grid of side length $L = 0.1 h^{-1}$Mpc ~ 23 arcsec and $N = 1024$

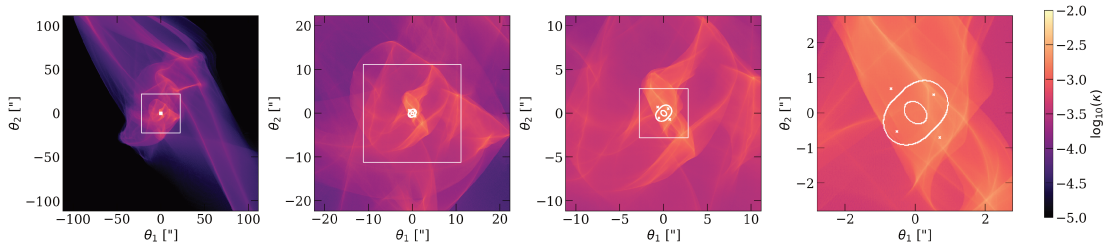

Figure 6.7: The filament used to perturb the lens in the first experiment. From left to right we show smaller and smaller scales. In each panel the white square represents the size of the panel to the right. In addition, we show the critical curves of the lens used in the first experiment along with the positions of the four replicated quasar images. Filaments can present significant density perturbations on scales smaller than the Einstein radius due to caustics.

points per dimension for the fine grid, $L = 1h^{-1}\text{Mpc} \sim 230$ arcsec and $N = 4096$ points per dimension for the coarse grid and the splitting length $\ell = 0.92$ arcsec.

We first perturb this lens by adding the column density of the filament projected over $2h^{-1}$Mpc assuming it is at the same redshift as the deflector. We centre the lens on the densest region of the projection, we then offset this regions with respect to the lens by displacing the filament by a distance d along a path which makes the densest part of the projected filament travel through the strongly lensed region. Note that the sign of d simply marks whether the densest part of the filament is approaching, $d < 0$, or moving away from $d > 0$, the strong lensing region. In Fig. 6.7 we show the projected filament along with the critical curves produced by the lens and the positions of the four quasar images. Here we can clearly see the difference in scale between these two structures, where the multiple images form at a physical distance between 3 and $4h^{-1}kpc$. We can see by successively enlarging the projection that even at such small scales the density field still shows sharp caustic features at scales typically smaller than the Einstein radius.

For comparison we repeat this procedure replacing the filament by a small mass halo. We model this perturber as a spherical NFW profile (Golse & Kneib, 2002) with mass $M_{200c} = 10^9 h^{-1}\text{M}_\odot$ and concentration $c_{\text{WDM}} = 5.82$ corresponding to the combined prediction of Ludlow et al. (2016) and Bose et al. (2016).

In Fig. 6.8 we track the change in the flux ratios, f, relative to the case where there is no perturbation affecting the lens, f_0. Note that, as described in section 6.3.4 we filter out the large scale modes in both density fields. This results in the images not being displaced by more than 5 m.a.s. ensuring that we are indeed comparing similar perturbations. When looking at the flux ratio anomalies sourced by the halo, we observe that the flux ratios are only significantly altered when the halo passes close to individual images producing sharp peaks. In the case of the filament, due to the complex geometry, the we see that the flux ratios present anomalies no matter the distance from the lens. We conclude that both structures are able to cause anomalies of similar magnitude. As such at the end of this case study we are confident that non-halo structure are indeed able to source considerable flux ratio anomalies.

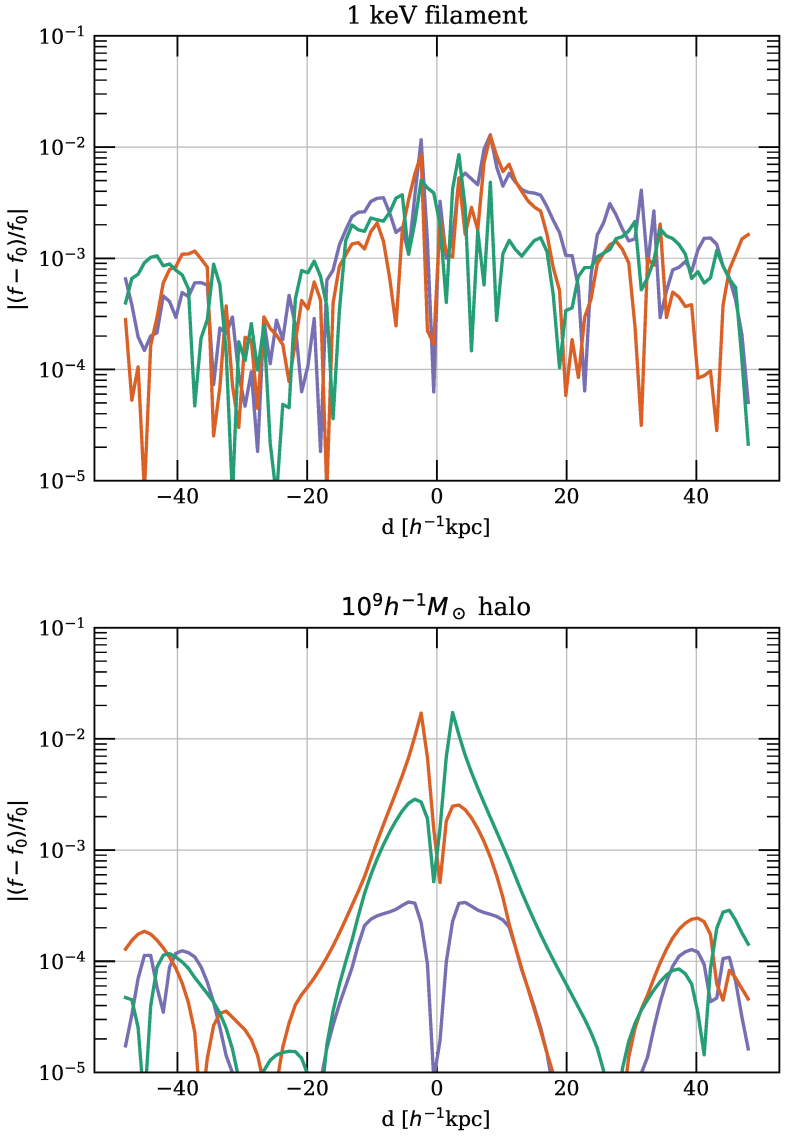

Figure 6.8: Relative change in flux ratio measurements in the presence of a perturbation, f with respect to the unperturbed flux ratios f_0. The abscissas represent the offset of the perturbation with respect to the centre of lens plane in physical scale as measured in the lens plane. In this coordinate system, the multiple images of the quasar form at $4h^{-1}$kpc. Each line represents a different quasar image and are coloured according to the labelling of the images in Fig. 6.4, the flux ratios are measure with respect to image 4 (red image). Top Panel: The lens is perturbed with a filament aligned with the line of sight for 2 h^{-1}Mpc. bottom panel: The lens is perturbed by a small 1 keV halo of mass $M_{200} = 10^9 \mathrm{M}_\odot$ and $c_{200} = 5.82$. In both cases the perturbation follows the same path through the lens. One can observe that the filament is able to produce a considerable effect, similar to that produced by the halo.

6.5 Flux ratio anomalies

The case study presented in the previous section has allowed us to conclude that non-halo structures do indeed have a measurable impact on flux ratio observations. Now we will adopt a more statistical approach, by sampling the density field at random here we quantify how typical perturbations will affect these measurements.

To do so we perturb our reference lens model with column density maps extracted from the WDM simulations along random lines of sight. Due to the small simulation box size ($L_{\rm box} = 20h^{-1}$Mpc), we limit the depth of these projections to $80h^{-1}$Mpc, projecting the replicated volume along an off axis line of sight to avoid spurious alignments of replicated structures. Note that this projection depth is considerably shorter than the typical distance of background sources used for this type of analysis, $\sim 1h^{-1}$Gpc, meaning here we will not be able to quantify the absolute effect of non-halo structures on this type of observation. As such, we will only quantify their relative contribution to this signal with respect to the haloes which also inhabit the same lines of sight. By repeating this work for shorter, $40h^{-1}$Mpc and longer $160h^{-1}$Mpc projections depths, we find that the relative contribution is not significantly altered by the choice of the line of sight. As a simplifying assumption we consider all the matter to be contained within the lens plane, we expect this assumption to have little impact as due to the filtering procedure removing large scale contributions the paths of individual light rays are not significantly changed.

As we have presented in section 6.3.2 we separate lensing quantities into large and small scale components to achieve high accuracies at a lower computational cost. Here the large scale lensing fields are estimated using an $8 \times 8h^{-2}$Mpc^2 projection over $N = 8182$ grid points per dimension resulting in a large scale resolution of $0.98h^{-1}$kpc per grid cell. We estimate these low resolution quantities only once. In addition to this we randomly select 1000 regions within the larger projection to become the perturbations that will be applied to the lens. The 'cut-outs' have a much smaller side length $L_{\rm c} \simeq 160h^{-1}$kpc which is estimated over fewer grid points $N_{\rm c} = 1024$. This however grants a much higher resolution of $0.15h^{-1}$kpc per grid element allowing to fully resolve the Einstein radius $\theta_{\rm E}D_{\rm d} \sim 3h^{-1}$kpc. with a splitting length $\ell = 1.84$ arcsec, which is equivalent to a $5.60h^{-1}$kpc in the lens plane. This particular choice of variables results in the fine grid being computed out to $50\theta_{\rm E}$ and the coarse grids being calculated out to $2900\theta_{\rm E}$.

We split the density field into two components:

- haloes, which are modelled as spherical NFW profiles using the parameters of the haloes inside the simulation in order to reduce numerical noise. We fade the profiles beyond the viral radius using a cubic spline step function as to create a smooth enough boundary while avoid numerical artefacts. We only select haloes with masses $M_{\rm 200c} < 10^{10}h^{-1}{\rm M}_\odot$ as more massive haloes are expected to host a visible component and would therefore be taken into account when fitting the lens.

- non-haloes, which we select as the set of all non released tracer particles (Stücker et al., 2020) and resample them down to a mass resolution of $M \sim 20h^{-1}{\rm M}_\odot$. This allows us to generate high resolution images of these structures without resorting to analytical profiles and without suffering from discreteness effects due to an insufficient number of particles.

We show the resulting density fields in Fig. 6.9 where we also illustrate the size of

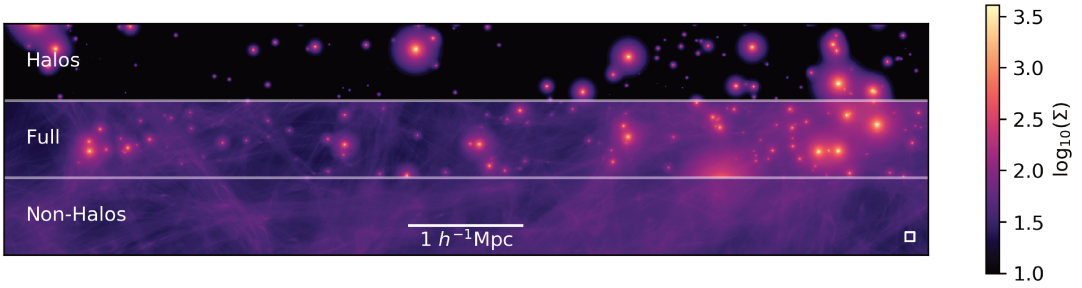

Figure 6.9: Exerts from the three large projections of the simulation volume. Top, we project only haloes as spherical NFW profiles. Bottom, we project only non-halo structures. Centre, we project both haloes and non-haloes simultaneously. This image has a width of $8h^{-1}$Mpc and a height of $2h^{-1}$Mpc. The small white square in the bottom right shows the size of the individual lines of sight to scale.

the high resolution regions using a small white square in the bottom right. In addition to the projections mentioned above we show the sum of both types of structure that we will also be using to perturb our lensing simulations. Note however that in this figure we have kept haloes with masses $M_{200c} > 10^{10}h^{-1}\mathrm{M}_\odot$ for visual effect.

As Eq. 6.6 is linear, the potential and deflection caused by the lensing effect of the perturbation simply needs to be added to the reference lens model. Note that we however need to compensate for the overall gradient induced by the perturbation. Once this correction is applied we recover the positions of the multiple images within a few m.a.s.

For each cut-out we measure the three flux ratios f_i and quantify the total anomaly,

$$S = \sqrt{\sum_{i=1}^{3}(f_i - f_{\mathrm{ref}(i)})^2}, \tag{6.30}$$

as the root mean square deviation of the flux ratios with respect to their counterparts produced by the reference model $f_{\mathrm{ref}(i)}$ (see e.g. Gilman et al., 2019), where the larger S is the more perturbed the flux ratios are. We again note that here we cannot compare absolute measures of S as we are working with very short lines of sight which result in perturbations being on average 10 times smaller than expected. As such, we will only compare how the distributions of this variable change relative to one another.

In Fig. 6.10 we show the cumulative distributions for S from our 1000 lines of sight. These distributions can be interpreted as the probability of observing a flux ratio anomaly higher than a given level. The colours of the lines correspond to the different types of structures and the style corresponds to the DM model, dashed lines for 1 keV versus solid lines for 3 keV. The top panel shows the effect the full field (large and small scale) has on the flux ratios, while in the lower panel we only show the effect of small scale perturbations. This entails that the top panel includes contributions that could possibly be absorbed into the lens model while the bottom panel only includes contribution that do not significantly alter the positions of the individual images and therefore cannot be absorbed. By comparing both panels we see that while this procedure has an impact on the absolute level of the distributions it does not impact their relative behaviours.

First let us compare the curves produced using only haloes as these are the structures that are typically used in cosmological analyses. Comparing the orange lines in the lower panel we do indeed observe a considerable difference between the 1 keV and 3

keV models, with haloes in the 3 keV simulation producing a much stronger signal than their 1 keV counterparts. This is to be expected as it is this difference which is typically used to constrain the warmth of the DM particle.

Turning our attention to non-halo structures we see that they are the dominant contributor in the 1 keV cosmology, both in the filtered and un-filtered distributions. This tells us that the flux ratio anomalies generated by non-halo structures cannot be neglected in very warm cosmologies and that their contribution cannot be absorbed into the lens model through the addition of an external shear component or a uniform mass sheet. If we consider the same structures in the colder 3 keV cosmology we see that the overall impact of non-halo structures is slightly reduced. This is to be contrasted with the contribution of haloes which has greatly increased leaving non-halo structures as only a sub-dominant contribution to the total signal. While haloes are now the main contributor, if we compare the distributions of anomalies sourced by the full density field 'Sum' we see that neglecting non-halo structures would result in underestimating the flux ratio anomalies by between 5 and 10 per cent. The decrease seen in the non-halo contribution, by $20 \sim 30$ per cent is consistent with the decrease in the mass fraction that these structures occupy. Indeed as can be seen in Tab. 6.1 the mass fraction of non-halo structures decreases from $f_{\rm non-halo} = 46$ per cent in the 1 keV simulation to $f_{\rm nonhalo} = 35$ per cent in its 3 keV counterpart. Simple excursion set models have shown that the mass outside of haloes changes very slowly with the cut-off scale, meaning that even very cold DM models such as a 100 GeV neutralino still have between 5 and 20 per cent of the total DM mass which resides outside of haloes at $z = 0$ (Angulo & White, 2010), with this fraction increasing as one looks at higher redshifts. Therefore we expect that in DM models colder than the 3 keV model studied non-halo structures will have a smaller impact than seen here but not significantly.

So far we have focused on separating small scales and large scales, assuming that small scale contributions cannot be absorbed by the lens model as they do not significantly displace the positions of the multiple replications of the quasar. To investigate this assumption further we decompose the density field using a multitude of scale filters,

$$\hat{h}_{k_{\rm s}} := \exp\left\{-\frac{(k-k_{\rm s})^2}{2\sigma_k^2}\right\}, \tag{6.31}$$

to isolate the scale $k_{\rm s}$. we separate each mode using a linear step, $\Delta k_{\rm s} \simeq 0.142$ arcsec^{-1} and use a filter width of $\sigma_k \simeq 0.043$ arcsec^{-1}, resulting in each filter being separated by $\Delta k_{\rm s} \simeq 3.28\sigma_k$. This procedure, inspired by Inoue & Takahashi (2012), allows us to study the scale dependence of our results.

On the left hand side of Fig. 6.11 we show the root mean square deviation of image locations with respect to their un-perturbed positions as a function of the scale of the perturbation. We see that in general haloes are more efficient at displacing images than non haloes and that most of the displacement is indeed sourced by large scale modes. We also see that perturbations with scales similar or smaller than the Einstein radius, corresponding to $k_{\rm E} = 1/\theta_{\rm E} \simeq 1.1$ arcsec^{-1}, are unable to efficiently strongly displace the images.

On the right hand side of Fig. 6.11 we show how the mean flux ratio anomaly changes as a function scale. Here we see a similar behaviour as in Fig. 6.10 where in the 1 keV model, non-halo structures contribute significantly to the total anomalies at all scales, while in the 3 keV model they become sub-dominant to haloes even though in absolute terms their contribution has not significantly decreased. Nonetheless they still contribute between 5 and 10 per cent of the total signal. Overall if we look at the relative

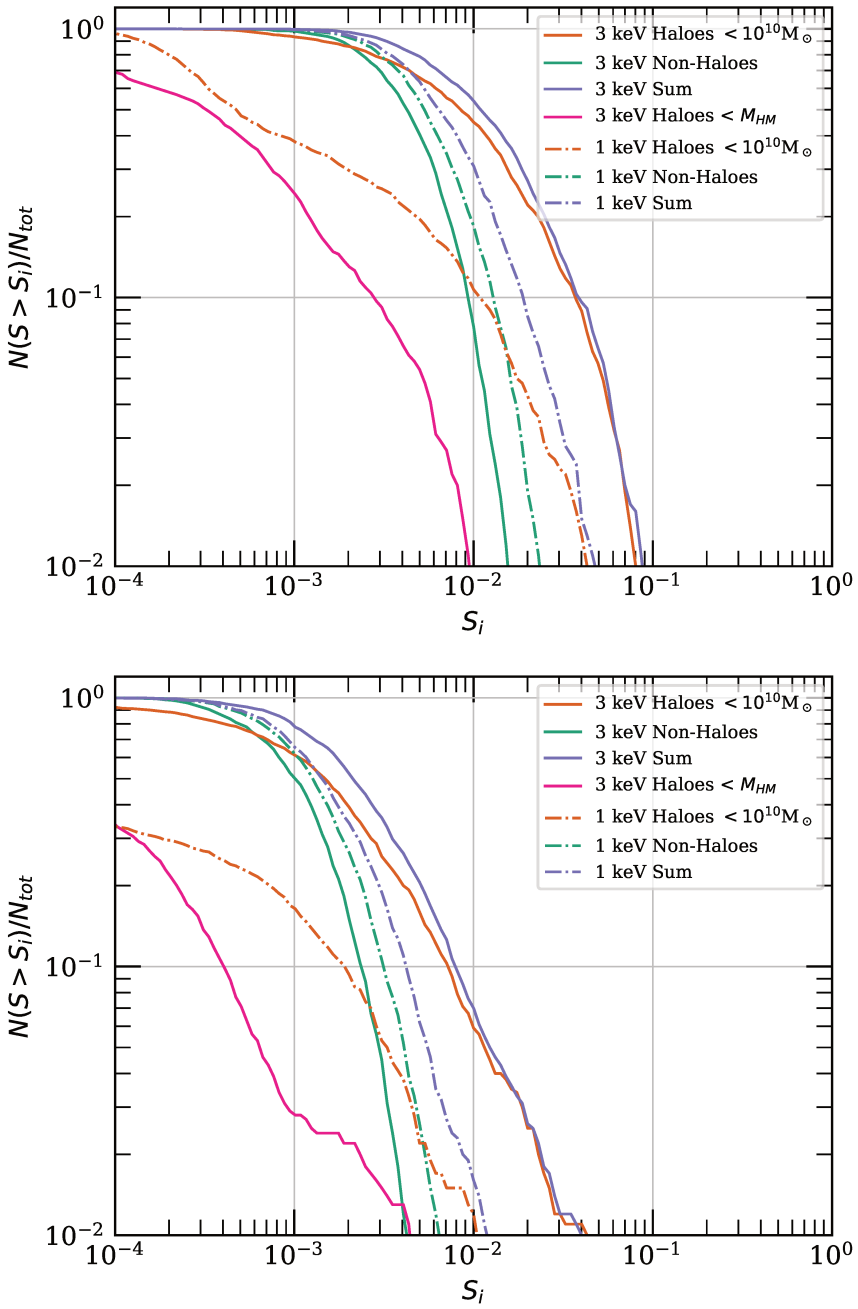

Figure 6.10: Cumulative histograms showing the fraction of summary statistics S larger than S_i. The different colours show the statistics when modeling only haloes with masses $M_{200} < 10^{10}\mathrm{M}_\odot$ (orange), only non-halo material (green), both types simultaneously, *Sum*, (blue), and the contribution of haloes below the half-mode mass, M_{hm}, (magenta). In the *top panel* Using the full, i.e. large and small scale, contributions to the statistic and in the *bottom panel* using only the small scale contribution. In very warm 1keV cosmologies the non-haloes constitute about half of the total flux-ratio signal. In colder cases, like 3keV, the relative contribution is much lower (around $5 - 10\%$). These estimates also hold when only considering the short-range part of the signal – which cannot be absorbed by the fitting procedure in observational setups.

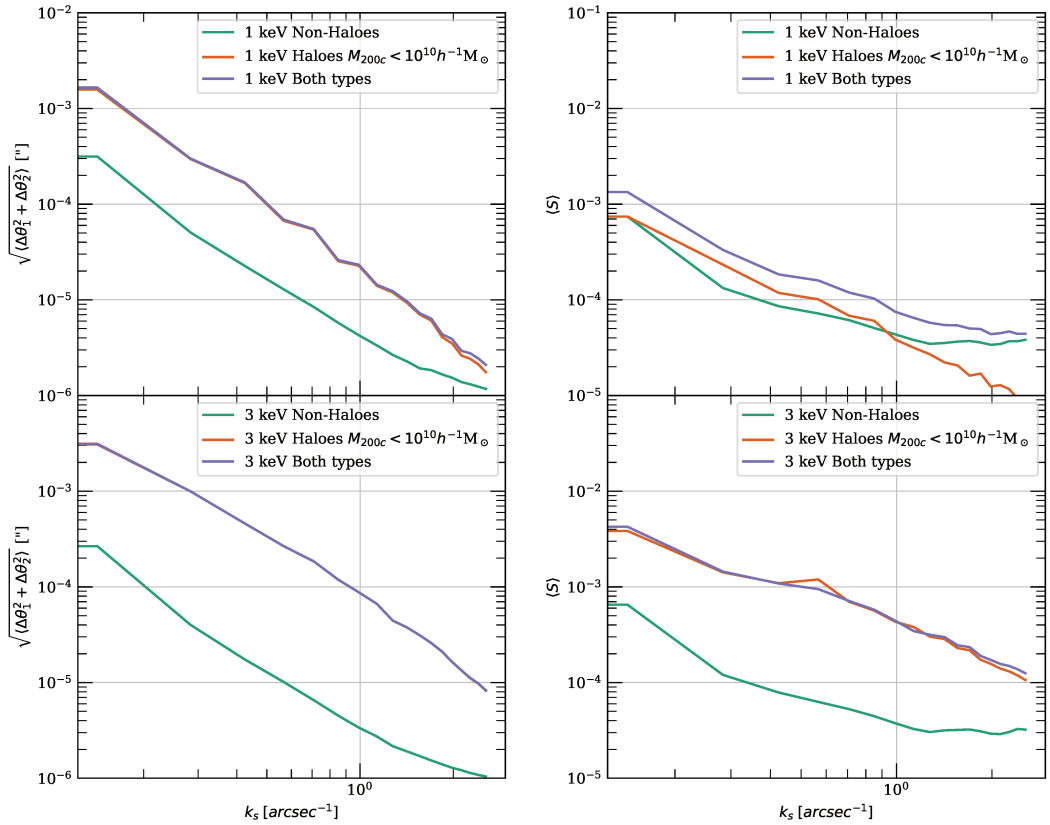

Figure 6.11: *Left panels:* Scale dependent estimate of the RMS displacement of the images with respect to their unperturbed positions. Top: in a 1keV cosmology, bottom: in a 3keV cosmology *Right panels:* Scale dependent estimate of the observed mean flux ratio anomaly. Top: in a 1keV cosmology, bottom: in a 3keV cosmology. We see that haloes are far more efficient at displacing the images than Non-halo structures. In the 1keV scenario Non-halo structures are a major component of the signal at all scales, while in the 3 keV case they only represent ∼10 percent of the observed signal. The relative contributions of the different components are relatively scale-independent.

contributions we see that these do not vary significantly with scale, with the exception of scale much smaller than the Einstein radius, comforting us in our assumption that specific choice of filtering scale does not impact our results.

At the end of this section, we find that non-halo structures are not only able to cause considerable flux ratio anomalies but that they contribute significantly to these anomalies in WDM cosmologies. In very warm models this component can even dominate over the contribution sourced by haloes, however this only occurs in models that are already excluded by observations. While the absolute impact of non-halo structures only decrease slowly as one looks at colder models, their relative contribution with respect to haloes decreases rapidly due to significant increase of the contribution of haloes, resulting in a sub-dominant contribution of the order of 5 to 10 percent. We conclude from this study that non-halo structures can be neglected for sufficiently cold cosmologies $m_\chi > 3$ keV as long as the methodology used is robust to biases of up to 10 per cent. We note however that a more in depth investigation should be conducted if a high accuracy and precision cosmological analysis is performed.

6.6 Summary

In this chapter we set out to answer the question: *Are non-halo structures, such as filaments and pancakes, able to produce significant perturbation to strong gravitational lenses?* focusing specifically on observations of quadruply lensed quasar, as these observations have been used in the literature to constrain the abundance of structures along the line of sight, providing insight on the nature of DM (Gilman et al., 2019, 2020; Hsueh et al., 2020). These studies have however only focused on the abundance of haloes along the line of sight and neglected other structures. Here we have seen that these structures are not only abundant, representing a significant fraction of the total DM mass inside our simulations, but also present many small scale features known as caustics creating sharp gradients and steps in the density field.

In a preliminary case study we find that aligning a filament, devoid of haloes, with the line of sight is sufficient to generate perturbations to a strong gravitation lens of the same order of magnitude as a small mass halo. This shows that, at least in an ideal case, these structures are indeed able to induce significant effects on flux ratio observations.

We perform a more general analysis by randomly selecting a large number of lines of sight from two state of the art WDM simulations. We project the matter density field along these lines of sight, separating the contribution of haloes from that of other structures. Solving the lens equation for a standard configuration while using these projections as perturbation fields, we find that non-halo structures have a significant contribution to the measured lensing signal. While the relative contribution of non-halo structures decreases significantly as we increase the WDM particle mass, we observe that this is primarily due to the increased abundance of haloes in these models and only secondly to the decreased fraction of mass within non-structures. In our 3 keV simulation we find that these structures contribute significantly more than a population of haloes with masses below the half mode mass, contributing between 5 and 10 per cent of the total signal. As such we argue that the structures could have a potential impact on constraints on the WDM particle mass as these are usually neglected in these analyses.

This was however only possible through a number of simplifying hypotheses which prevent us from making absolute statements on the magnitude of the effect. Indeed here we have modelled the entire system as a single lens; our perturbations only extend

for $80h^{-1}$Mpc; we did not account for baryonic features; and we only investigated two WDM models which are already ruled out by current constraints. Nonetheless we argue that our qualitative arguments are sufficiently robust. As such we argue in favour of rigorous modelling of these structures within flux ratio analysis pipelines, as neglecting these structures may result in measurements of the DM particle mass being biased towards larger values.

7 | Conclusions

Throughout this work we see that sparsity, a humble mass ratio, has a wide range of applications. From the astrophysics of massive dark matter haloes all the way to constraining cosmology, sparsity shows that it has great potential, but that there is still many hurdles to overcome.

From the astrophysical perspective, we see that sparsity is highly versatile, being able to describe a wide range of physical profile in a non-parametric fashion. This versatility allows us to derive a generic mathematical formalism which relates the halo mass function to the internal structure of dark matter haloes. We show that, by relating sparsity to the parameters at a given mass profile, this generic formalism can then be specialised to get expressions in terms of the desired parameters. Nevertheless, the assumption of a profile shape introduces a certain degree of error, varying from a few percent to beyond 10 percent. Moreover, we show that these relations can be inverted allowing us to predict properties of the sparsity distribution from models of the halo mass function.

Looking at individual objects, we see that the sparsity of a halo is tightly linked to its internal physics and in particular its dynamical state. Specifically, we find that sparsity reacts in a systematic way to major mergers, exhibiting a strong pulse like feature. We exploit this systematic reaction to design a statistical testing procedure to rapidly identify recent mergers within galaxy cluster catalogues. We have shown that this statistical test can be further expanded into an estimator of the time since the last merger.

While we have focused on major mergers, it could be interesting in the future to study the impact of other astrophysical processes on halo sparsity. In particular with relation to baryonic and beyond ΛCDM physics, where still many questions remain:

- *What is the influence of baryonic structures such as galaxies and massive gas clouds?*
- *Do strong baryonic feedback events, such as active galactic nucleus flares, leave traces in the sparsity?*
- *Do alterations to gravity or dark energy influence sparsity?*
- *What is the influence of alternate dark matter scenarios?*

Some exploratory work is being conducted to address these questions. Regarding dark energy, Balmès et al. (2014) and Corasaniti et al. (2020) have shown that sparsity is sensitive to modifications of gravity and dark energy model models. These explorations have fuelled ongoing efforts to create a wCDM sparsity emulator (Sáez Casares et al. in prep.) and possibly constrain these models. Regarding baryons, current efforts focus on estimating the impact of baryonic physics on sparsity, primarily through the quantification of baryon sparsity biases from the The300 galaxy cluster zoom simulations

(Corasaniti et al. in prep.). Nonetheless, with the arrival of larger samples of full hydro galaxy clusters it will be possible to perform similar studies to those presented in this work including baryonic physics.

From a cosmological perspective, we show that the sparsity distribution has a cosmological dependence, and in particular it is most influenced by the amplitude of matter fluctuations parameter, S_8. Having reviewed current methods based on the measurement of the mean sparsity of a sample, we design a novel approach which removes the need for the mean and instead treats each object in the sample as a separate data point. We find that this novel approach significantly improves the constraining power of sparsity with respect to approaches based on the mean, without requiring additional data. Nevertheless, this method is numerically much more costly and comes with a completely new set of systematic effects which still need to be controlled.

These systematics come in many forms, and in particular many of which where only briefly mentioned. As such, several question remain:

- *Can we use sparsity with biased mass measurement, such as weak lensing masses or hydrostatic masses?*
- *How does assuming a profile shape influence the inferred cosmological parameters?*
- *How do we incorporate the influence of selection effects?*

Only begining to investigate these questions, we adopt a modelling approach to try and quantify the resulting biases. In particular we create mock stacked weak lensing observations of KiDS galaxy clusters. After following the AMICO pipeline, which will also be applied to *Euclid*, we will soon be able to measure how the pipeline biases the sparsity, and as a result soon be able to put this approach into practice and obtain a novel cosmological constraint using sparsity.

Finally, we show that sparsity has the potential to synergise with other cosmological probes, such as cluster number counts and gas mass fractions. This however requires that we measure the covariance between these different probes. We show that, in the case of cluster number counts, there is only a non-negligible correlation between the two probes if we use the same sample of clusters for the number counts and the sparsities. In the case where the sparsity sample is much smaller, similarly to currently available observations, then the two probes become independent from one another. In the near future we hope to expand this study to also include gas mass fractions and potentially provide the first constraints using this joint approach.

A | Modelling the evolution of haloes

In Section 5.4 we explored the possibility of constraining cosmology through the use of sparsity while treating clusters as individual data points. We show that this is possible by extracting the distribution of sparsities from a model of the HMF, such as Despali et al. (2016). This approach is however numerically costly increasing the evaluation time of the likelihood by a factor of 10. In this appendix, we present work in progress investigating an alternate approach by predicting the sparsity distribution from first principles, namely through the use of excursion set theory.

In Section 2.6.2, we have seen how excursion set theory can be used to predict the HMF. While this may have been the initial success that popularised this approach (Bond et al., 1991) excursion set theory can also be applied to construct merger trees (see Jiang & van den Bosch, 2014, for a review), which link a halo at given epoch to all its progenitors at earlier epochs. These merger trees have in turn been used to predict the $c - M$ relation by applying semi-analytical models (e.g. Jiang et al., 2021; Johnson et al., 2021) calibrated on simulations.

Sampling a merger tree using excursion set is much faster computationally than running a cosmological simulation. However, an even faster approach would be to predict the internal structure of haloes from the merger tree's condensed form known as the mass accretion history (MAH), where we only follow the most massive branch of the tree. In Chapter 4 we have seen, in agreement with Wang et al. (2020a), that it is merger events which primarily drive the evolution of the sparsity, imprinting a characteristic impulse into the sparsity history, see e.g. Fig. 4.2 and Fig. 4.3.

The definition of sparsity, $s_{\Delta_1,\Delta_2} = M_{\Delta_1}/M_{\Delta_2}$, can simply be seen as a relation between three random variables. If we now write the differential with respect to redshift,

$$\begin{aligned}\frac{\mathrm{d}s_{\Delta_1,\Delta_2}}{\mathrm{d}z} &= \frac{1}{M_{\Delta_2}}\frac{\partial M_{\Delta_1}}{\partial z} - \frac{M_{\Delta_1}}{M_{\Delta_2}^2}\frac{\partial M_{\Delta_2}}{\partial z},\\ &= \left(\frac{1}{M_{\Delta_2}} - \frac{M_{\Delta_1}}{M_{\Delta_2}^2}\frac{\partial M_{\Delta_2}}{\partial M_{\Delta_1}}\right)\frac{\partial M_{\Delta_1}}{\partial z},\\ &= \left(1 - s_{\Delta_1,\Delta_2}\frac{\partial M_{\Delta_2}}{\partial M_{\Delta_1}}\right)\frac{s_{\Delta_1,\Delta_2}}{M_{\Delta_1}}\frac{\partial M_{\Delta_1}}{\partial z},\end{aligned} \tag{A.1}$$

we are able to formally relate the change in sparsity to the change in halo mass.

Note that here we are handling a first order stochastic differential equation and hence it is convenient to represent the evolution of the variables as random walks. As such, derivatives can be discretised,

$$\Delta s_{\Delta_1,\Delta_2} = \left(1 - s_{\Delta_1,\Delta_2}\eta_{\Delta_1,\Delta_2}\right)\frac{s_{\Delta_1,\Delta_2}}{M_{\Delta_1}}\Delta M_{\Delta_1}, \tag{A.2}$$

as to recover the sparsity step $\Delta s_{\Delta_1,\Delta_2}$ which is induced by a given mass step ΔM_{Δ_1}. In addition, we introduce, $\eta_{\Delta_1,\Delta_2} = \partial M_{\Delta_2}/\partial M_{\Delta_1}$, a stochastic variable which we dub the

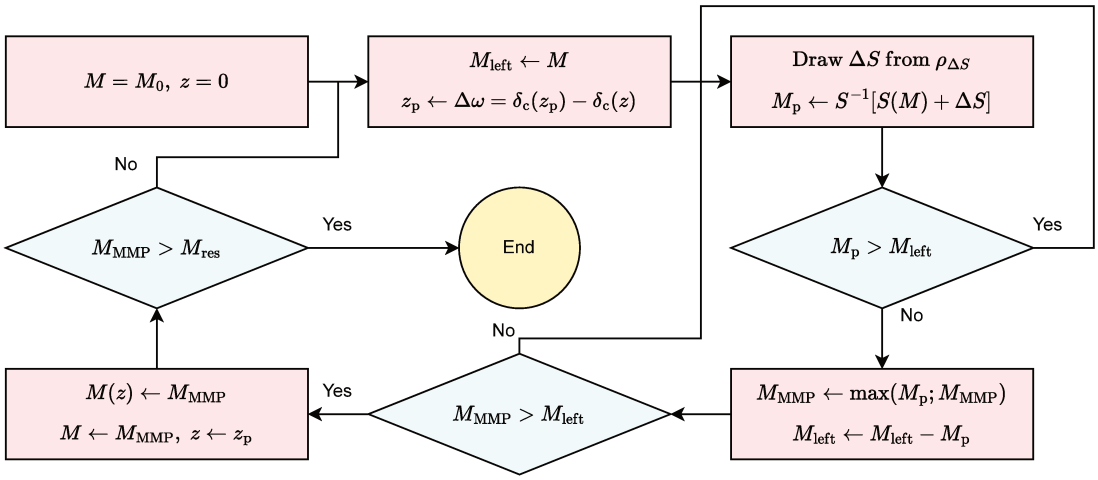

Figure A.1: Flowchart of the van den Bosch (2002) MAH generation algorithm

mass transfer efficiency. This equation has two main caveats. Firstly, it assumes that when mass is accreted by the halo it virialises instantaneously, which as we have seen in Chapter 4 is not the case. Secondly, it requires prior knowledge of how the inner mass varies when mass is accreted as parameterised by, η_{Δ_1,Δ_2}. This term can be calibrated on simulations. Moreover, it can also be used to add *memory* of previous steps in the random walk, meaning that with sufficient complexity it can solve both of these caveats.

To begin applying this equation, we generate MAHs as to obtain the ΔM_{Δ_1} term. To do so we use the excursion set based algorithm of van den Bosch (2002), illustrated as a flow chart in Fig. (A.1). This algorithm builds the MAH backwards, meaning that starting from a halo with mass $M = M_0$ at the current epoch, $z = 0$ the MAH is iteratively constructed by generating progenitors at some anterior redshift, z_p, which is defined with respect to the excursion set barrier $\omega(z) = \delta_{\rm c}(z)$.

The van den Bosch (2002) algorithm is as follows:

1. Choose a present-day halo mass M_0 and set $M = M_0$ and $z = 0$.

2. Set $M_{\rm left} = M$ and compute the progenitor redshift $z_{\rm p}$ from $\Delta\omega = \delta_{\rm c}(z_p) - \delta_{\rm c}(z)$, where $\Delta\omega$ is set by the user and kept constant.

3. We draw a progenitor of mas $M_{\rm p}$ such that $S(M_{\rm p}) = S(M) + \Delta S$ where ΔS is drawn from the probability distribution,

$$\rho(\Delta S, \Delta\omega)\mathrm{d}\Delta S = \frac{1}{\sqrt{2\pi}}\frac{\Delta\omega}{\Delta S^{3/2}}\exp\left[-\frac{\Delta\omega^2}{2\Delta S}\right]\mathrm{d}\Delta S, \tag{A.3}$$

   recalling $S(M) = \sigma^2(M)$.

4. If $M_{\rm p} > M_{\rm left}$ the progenitor is considered too massive, and we return to step 3

5. Else, we set the mass of the Most Massive Progenitor (MMP) to $M_{\rm MMP} = \max(M_{\rm p}; M_{\rm MMP})$, and the left over mass is the set to $M_{\rm left} = M_{\rm left} - M_{\rm p}$

6. We continue sampling progenitors until $M_{\rm MMP} > M_{\rm left}$ which indicates that we have found the MMP.

7. Finally, we check if the mass of the MMP is still larger than a given mass resolution $M_{\rm res}$. If so we proceed to the next redshift-step by setting $M(z_{\rm p}) = M_{\rm MMP}$, $M = M_{\rm MMP}$, $z = z_{\rm p}$, and returning to the second step, if not we recover and output the MAH from $M(z)$.

This algorithm thus requires only four user inputs, M_0, z_0, $\Delta\omega$, and $M_{\rm res}$, to fully model the MAH. We note, that Eq.(A.3) assumes spherical collapse, and that, as with most excursion set results, the masses M cannot be directly related to the SO used to measure sparsity. In van den Bosch (2002), the author addresses the first issue directly by introducing an ellipsoidal collapse barrier model,

$$\delta_{ce}(z, M) = \delta_c(z) \left\{ 1 + 0.47 \left[\frac{\sigma^2(M)}{\delta_c^2(z)} \right]^{0.615} \right\}, \tag{A.4}$$

and simply replacing this into the definition of $\omega(z)$ and using the PDF of Eq. (A.3).

This can be considered as an over-simplification, as by doing so one does not recover the halo mass function from N-body simulations (Sheth & Tormen, 2002). Taking this further, Sheth & Tormen (2002) find a correspondence between the definition of their conditional mass function fit parameters and the parameters of the ellipsoidal collapse barrier. Defining a generalised barrier model

$$\delta_{ce}(z, M) = \sqrt{a}\delta_c(z) \left\{ 1 + \beta \left[\frac{S(M)}{a\delta_c^2(z)} \right]^{\alpha} \right\} \tag{A.5}$$

with a, α, β three parameters that are defined by fitting the conditional halo mass function to

$$\nu f(\nu) = \sqrt{\frac{a\nu}{2\pi}} e^{-a\nu\left[1+\beta(a\nu)^{-\alpha}\right]^2/2} \times \left\{ 1 + \frac{\beta}{(a\nu)^{\alpha}} \left[1 - \alpha + \frac{\alpha(\alpha-1)}{2} + \cdots \right] \right\}, \tag{A.6}$$

where $\nu = (\delta_c(z)/\sigma(M))^2$, which was introduced simultaneously with the more commonly used form of Eq. (2.109) (Sheth & Tormen, 2002). In our case we recalibrate these parameters on the RayGalGroupSims halo catalogues (Rasera et al., 2022) This relationship between the barrier and the conditional mass function allows to put physical definitions to the mass that is being studied (i.e. M_{200}, $M_{500}, \ldots$) simply by fitting the parameter for the desired mass definition. In addition, Sheth & Tormen (2002) show that the PDF of excursions S_{i+1} from which we previously defined the mass of progenitor haloes is also modified,

$$\rho(S_{i+1}|S_i)\mathrm{d}S_{i+1} = \frac{|T(S_{i+1}|S_i)|}{\sqrt{2\pi}(S_{i+1} - S_i)^{3/2}} \exp\left\{ \frac{(\omega(z_{i+1}, S_{i+1}) - \omega(z_i, S_i))^2}{2(S_{i+1} - S_i)} \right\} \mathrm{d}S_{i+1}, \tag{A.7}$$

with

$$T(S_{i+1}|S_i) = \sum_{n=0}^{5} \frac{(S_{i+1} - S_i)^n}{n!} \frac{\partial^n(\omega(z_{i+1}, S_{i+1}) - \omega(z_i, S_i))}{\partial S_{i+1}^n}, \tag{A.8}$$

thus introducing correlations between the individual steps of the random walks.

We plot this distribution along with its spherical collapse counterpart in the left panel of Fig. A.2 placing ourselves at $z = 3$ for $S_i = 11$ which would correspond to $M_{200c} \simeq 10^6 h^{-1}\mathrm{M}_{\odot}$. We see that the modification to the sampling distribution introduces a large tail followed by a rapid cut-off at high ΔS which prohibits sampling large values of ΔS. In practice, what this means is that the elliptical collapse distribution disfavours

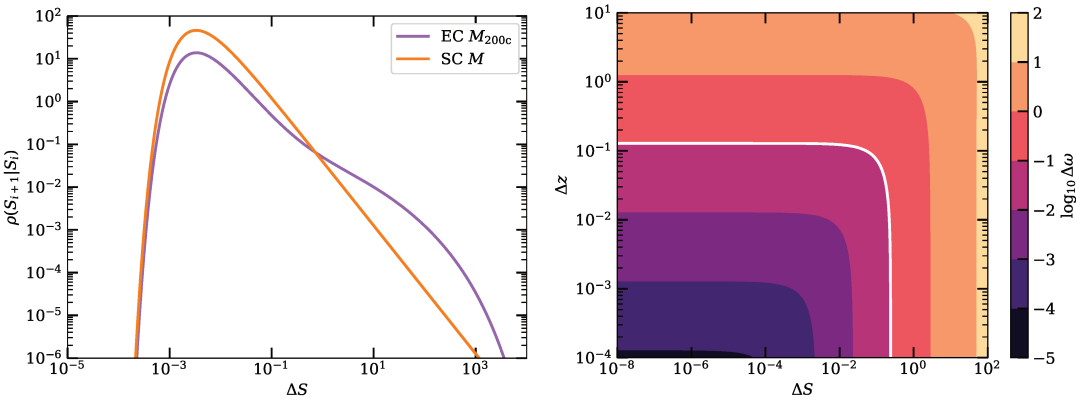

Figure A.2: In the left panel, we plot the distributions used to sample ΔS in the van den Bosch (2002) algorithm, in orange using the original spherical collapse (SC) model and in purple using the ellipsoidal collapse (EC) model of Sheth & Tormen (2002), placing ourselves at $z = 3$ for $S_i = 11$, which would correspond to $M_{200c} \simeq 10^6 h^{-1}\mathrm{M}_\odot$. We see that the modification to the sampling distribution introduces a large tail followed by a rapid cut-off at high ΔS which disfavours sampling large values of ΔS. In the right panel we show the value of the change in the barrier $\Delta\omega$ in the EC case. We see that the alteration in the barrier also introduces a maximal ΔS beyond which we cannot solve $\omega(z_p) = \omega(z) - \Delta\omega$ to retrieve the progenitor redshift. The white line corresponds to $\Delta\omega = 0.1$.

very sudden large increases in mass. The alteration in the barrier poses the additional difficulty, indeed for a fixed $\Delta\omega$, we no longer obtain a fixed z_p as the barrier now also depend on the change in of S as can be seen in the right panel of Fig. A.2. In practice we continue to fix $\Delta\omega$ and sample $\Delta S = S_{i+1} - S_i$, before inverting the barrier to obtain the progenitor redshift. Note that fixing the value of $\Delta\omega$ also introduces a maximal ΔS beyond which the is no solution for the progenitor redshift. This can be seen in the right panel of Fig. A.2 where if we choose $\Delta\omega = 0.1$, corresponding to the white line, then we are only able to sample up to $\Delta S \simeq 0.2$ beyond which we cannot solve $\omega(z_p) = \omega(z) - \Delta\omega$ to retrieve the progenitor redshift.

In Fig. A.3 we plot 25 MAH for haloes with $M_0 = 5 \cdot 10^{13} h^{-1}\mathrm{M}_\odot$ and with $\Delta\omega = 0.1$, using both the original spherical collapse based algorithm of van den Bosch (2002) on the left and with the modified ellipsoidal collapse sampling distribution of Sheth & Tormen (2002) on the right. We can see that the modification to the sampling distribution which disfavours major mergers results in MAH which appear more spread out due to longer periods of slow accretion between major merger events. We see that this on average slows down halo formation with the average MAH being shifted towards higher redshifts.

Now being capable of sampling ΔM_{Δ_1}, we still need a description of the behaviour of η_{Δ_1,Δ_2}. As mentioned previously, this variable encodes most of the internal physics of the halo. Let us first examine the behaviour of this variable inside simulations in a similar fashion to how we studied the impact of mergers on sparsity in Chapter 4. As such we use the merger trees from the MDPL2 simulation to plot the evolution of η_{Δ_1,Δ_2} and study the reaction to mergers.

In Fig. A.4 we show the median η_{Δ_1,Δ_2} for a sample of 10^4 haloes randomly selected in MDPL2 as a purple solid line around which we also plot the 68 percent confidence interval. We find that the median mass transfer efficiency remains roughly constant

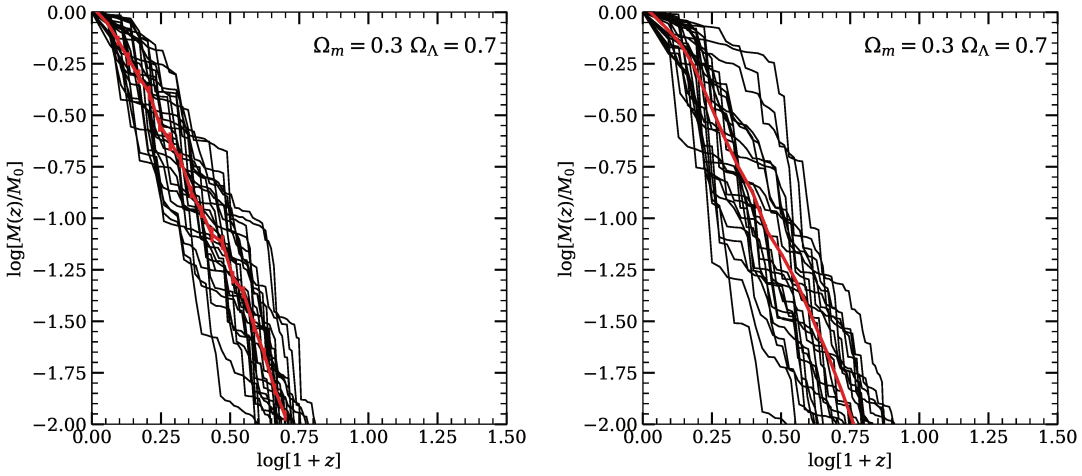

Figure A.3: Modelled MAH of 25 haloes with $M_0 = 5 \cdot 10^{13} h^{-1} \mathrm{M}_\odot$ and with $\Delta\omega = 0.1$. In the left panel using the original algorithm of van den Bosch (2002) and in the right panel using the modified sampling distribution of Sheth & Tormen (2002). the red lines correspond to the average MAH binned as a function of redshift.

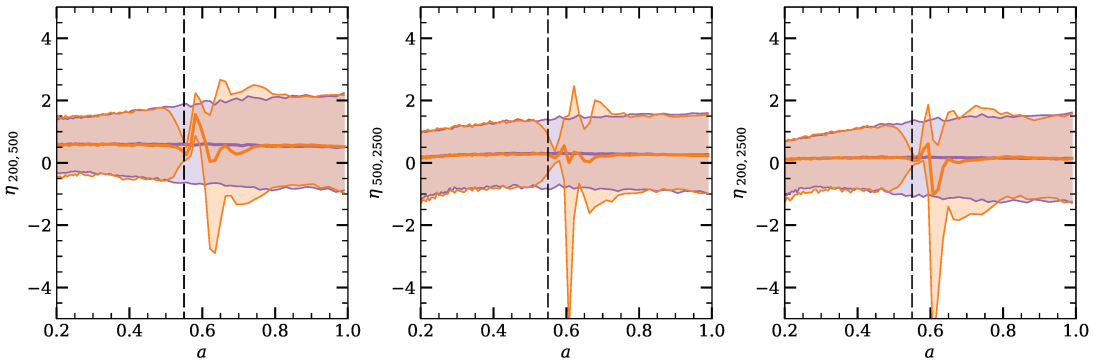

Figure A.4: Evolution of the median mass transfer efficiencies, η_{Δ_1,Δ_2}, shown as bold solid lines. In purple the variable is averaged over 10^4 haloes and is dominated by smoothly accreting haloes, while in orange we select a sub-sample of these haloes which have a major merger at $a = 0.55$ which is marked by a dashed vertical line, the shaded area represents the 68 percent confidence interval around the median. We see that the median η_{Δ_1,Δ_2} is roughly constant with respect to the scale factor while the scatter increases, for example the scatter around $\eta_{200,500}$ increases by 50 percent between $a = 0.2$ and $a = 1$. We note that, similarly to sparsity, η_{Δ_1,Δ_2} has a systematic reaction to major merger events.

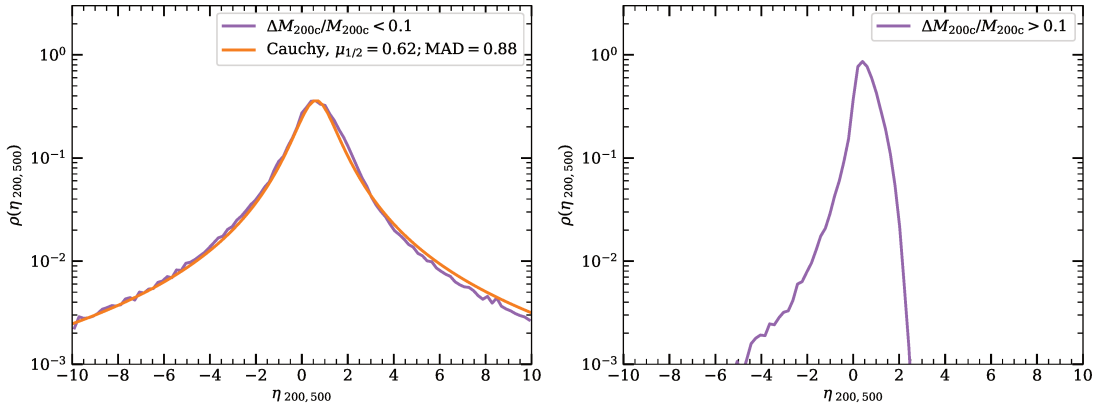

Figure A.5: In the left panel we show the distribution of mass transfer efficiencies, η_{Δ_1,Δ_2}, of smooth accreting haloes ($\Delta M_{200c}/M_{200c} < 0.1$) marginalised over their histories. In purple we show measurements from the MDPL2 merger trees and in orange we show a Cauchy distribution with the same median, $\mu_{1/2}$ and median absolute deviation, MAD. In the right panel we show the corresponding distribution in the high accretion regime ($\Delta M_{200c}/M_{200c} > 0.1$). In this second case the distribution is strongly skew and has a non standard shape.

as a function time but the scatter around the latter increases, for example the scatter around $\eta_{200,500}$ increases by about 50 percent between $a = 0.2$ and $a = 1$. Repeating this exercise but this time selecting a sub-sample of haloes which experience a major merger at $a = 0.55$, shown as the orange line and shaded area in Fig. A.4, we find that the mass transfer efficiency, similarly to sparsity, reacts in a systematic way to mergers, with a clearly defined pulse feature. Similarly to sparsity this feature dissipates rapidly after two dynamical times after which we recover the quiescent distribution.

We can therefore split the distribution into two components, a quiescent and a merging component. In Fig. A.5 we marginalise over the history to obtain the distributions of η_{Δ_1,Δ_2}. In the left panel, we find that when accretion is low, $\Delta M_\Delta/M_\Delta < 0.1$, the distribution of mass transfer efficiencies closely resembles a Cauchy distribution with the same median $\mu_{1/2}$ and median absolute deviation, MAD. This distribution often being associated with equilibrium processes in spectroscopy, warrants investigation as to why it is also produced here. The merging component remains to be modelled effectively, indeed in the right panel of Fig. A.5 we see that the distribution of η_{Δ_1,Δ_2} in this regimes is strongly skewed with a non standard shape. Nonetheless we note that if we are able to model η_{Δ_1,Δ_2} efficiently then we will be able to obtain the distribution of sparsities excursion set theory by simply sampling this distribution and solving Eq. (A.2).

Bibliography

Aalbers J., et al., 2023, Phys. Rev. Lett., 131, 041002
Abazajian K. N., et al., 2016, arXiv e-prints, p. arXiv:1610.02743
Abbott T. M. C., et al., 2020, Phys. Rev. D, 102, 023509
Abbott B. P., et al., 2021, ApJ, 909, 218
Abbott T. M. C., et al., 2022, Phys. Rev. D, 105, 023520
Abdalla E., et al., 2022, Journal of High Energy Astrophysics, 34, 49
Abel T., Hahn O., Kaehler R., 2012, MNRAS, 427, 61
Abul Hayat M., Stein G., Harrington P., Lukić Z., Mustafa M., 2020, arXiv e-prints, p. arXiv:2012.13083
Adam R., et al., 2018, A&A, 609, A115
Agnes P., et al., 2023, Phys. Rev. Lett., 130, 101001
Akeret J., Seehars S., Amara A., Refregier A., Csillaghy A., 2013, Astronomy and Computing, 2, 27
Akerib D. S., et al., 2017, Phys. Rev. Lett., 118, 251302
Allen S. W., Schmidt R. W., Ebeling H., Fabian A. C., van Speybroeck L., 2004, MNRAS, 353, 457
Angulo R. E., Hahn O., 2022, Living Reviews in Computational Astrophysics, 8, 1
Angulo R. E., White S. D. M., 2010, MNRAS, 401, 1796
Angulo R. E., Springel V., White S. D. M., Jenkins A., Baugh C. M., Frenk C. S., 2012, MNRAS, 426, 2046
Angulo R. E., Hahn O., Abel T., 2013, MNRAS, 434, 3337
Angulo R. E., Chen R., Hilbert S., Abel T., 2014, MNRAS, 444, 2925
Annunziatella M., et al., 2017, ApJ, 851, 81
Aprile E., et al., 2018, Phys. Rev. Lett., 121, 111302
Arraki K. S., Klypin A., More S., Trujillo-Gomez S., 2014, MNRAS, 438, 1466
Bahar Y. E., et al., 2022, A&A, 661, A7
Balmès I., Rasera Y., Corasaniti P. S., Alimi J. M., 2014, MNRAS, 437, 2328
Baltz E. A., Marshall P., Oguri M., 2009, J. Cosmology Astropart. Phys., 2009, 015
Banik N., Bertone G., Bovy J., Bozorgnia N., 2018, J. Cosmology Astropart. Phys., 2018, 061
Banik N., Bovy J., Bertone G., Erkal D., de Boer T. J. L., 2021, J. Cosmology Astropart. Phys., 2021, 043
Bardeen J. M., Bond J. R., Kaiser N., Szalay A. S., 1986, ApJ, 304, 15
Bartelmann M., Schneider P., 2001, Phys. Rep., 340, 291
Becker M. R., Kravtsov A. V., 2011, ApJ, 740, 25
Behroozi P. S., Wechsler R. H., Wu H.-Y., 2013a, ApJ, 762, 109
Behroozi P. S., Wechsler R. H., Wu H.-Y., Busha M. T., Klypin A. A., Primack J. R.,

2013b, ApJ, 763, 18
Bellagamba F., Roncarelli M., Maturi M., Moscardini L., 2018, MNRAS, 473, 5221
Bellagamba F., et al., 2019, MNRAS, 484, 1598
Bhattacharya S., Heitmann K., White M., Lukić Z., Wagner C., Habib S., 2011, ApJ, 732, 122
Biffi V., et al., 2016, ApJ, 827, 112
Bleem L. E., et al., 2015, ApJS, 216, 27
Bocquet S., Saro A., Dolag K., Mohr J. J., 2016, MNRAS, 456, 2361
Bode P., Ostriker J. P., Turok N., 2001, ApJ, 556, 93
Böhringer H., et al., 2004, A&A, 425, 367
Bonafede A., Giovannini G., Feretti L., Govoni F., Murgia M., 2009, A&A, 494, 429
Bond J. R., Cole S., Efstathiou G., Kaiser N., 1991, ApJ, 379, 440
Bond J. R., Kofman L., Pogosyan D., 1996, Nature, 380, 603
Boschin W., Barrena R., Girardi M., 2010, A&A, 521, A78
Bose S., Hellwing W. A., Frenk C. S., Jenkins A., Lovell M. R., Helly J. C., Li B., 2016, MNRAS, 455, 318
Boyarsky A., Drewes M., Lasserre T., Mertens S., Ruchayskiy O., 2019, Progress in Particle and Nuclear Physics, 104, 1
Breiman L., 2001, Machine Learning, 45, 5
Bryan G. L., Norman M. L., 1998, ApJ, 495, 80
Buchert T., 1989, A&A, 223, 9
Buehlmann M., Hahn O., 2019, MNRAS, 487, 228
Bullock J. S., Kolatt T. S., Sigad Y., Somerville R. S., Kravtsov A. V., Klypin A. A., Primack J. R., Dekel A., 2001, MNRAS, 321, 559
Burr I. W., 1942, The Annals of Mathematical Statistics, 13, 215
CHEX-MATE Collaboration et al., 2021, A&A, 650, A104
Cañameras R., et al., 2020, A&A, 644, A163
Carlberg R. G., Couchman H. M. P., 1989, ApJ, 340, 47
Carr B., Kühnel F., 2020, Annual Review of Nuclear and Particle Science, 70, null
Castro T., Borgani S., Dolag K., Marra V., Quartin M., Saro A., Sefusatti E., 2021, MNRAS, 500, 2316
Chen H., Avestruz C., Kravtsov A. V., Lau E. T., Nagai D., 2019, MNRAS, 490, 2380
Cheng T.-Y., Huertas-Company M., Conselice C. J., Aragón-Salamanca A., Robertson B. E., Ramachandra N., 2021, MNRAS, 503, 4446
Chiba M., Minezaki T., Kashikawa N., Kataza H., Inoue K. T., 2005, ApJ, 627, 53
Child H. L., Habib S., Heitmann K., Frontiere N., Finkel H., Pope A., Morozov V., 2018, ApJ, 859, 55
Ćiprijanović A., et al., 2021, MNRAS, 506, 677
Clowe D., Gonzalez A., Markevitch M., 2004, ApJ, 604, 596
Collett T. E., et al., 2017, ApJ, 843, 148
Corasaniti P. S., Achitouv I., 2011, Phys. Rev. D, 84, 023009
Corasaniti P. S., Rasera Y., 2019, MNRAS, 487, 4382
Corasaniti P. S., Ettori S., Rasera Y., Sereno M., Amodeo S., Breton M. A., Ghirardini V., Eckert D., 2018, ApJ, 862, 40
Corasaniti P. S., Giocoli C., Baldi M., 2020, Phys. Rev. D, 102, 043501
Corasaniti P.-S., Sereno M., Ettori S., 2021, ApJ, 911, 82

Corasaniti P. S., Le Brun A. M. C., Richardson T. R. G., Rasera Y., Ettori S., Arnaud M., Pratt G. W., 2022, MNRAS, 516, 437

Courtin J., Rasera Y., Alimi J. M., Corasaniti P. S., Boucher V., Füzfa A., 2011, MNRAS, 410, 1911

Cristianini N., Shawe-Taylor J., 2000, An Introduction to Support Vector Machines and Other Kernel-based Learning Methods. Cambridge University Press, doi:10.1017/CBO9780511801389

Crocce M., Pueblas S., Scoccimarro R., 2006, MNRAS, 373, 369

Crocce M., Fosalba P., Castander F. J., Gaztañaga E., 2010, MNRAS, 403, 1353

Cui W., et al., 2018, MNRAS, 480, 2898

Cypriano E. S., Sodré Laerte J., Kneib J.-P., Campusano L. E., 2004, ApJ, 613, 95

DESI Collaboration et al., 2016, arXiv e-prints, p. arXiv:1611.00036

Dahle H., Kaiser N., Irgens R. J., Lilje P. B., Maddox S. J., 2002, ApJS, 139, 313

De Luca F., De Petris M., Yepes G., Cui W., Knebe A., Rasia E., 2021, MNRAS, 504, 5383

Dekel A., Silk J., 1986, ApJ, 303, 39

Dekel A., Ishai G., Dutton A. A., Maccio A. V., 2017, MNRAS, 468, 1005

Despali G., Giocoli C., Angulo R. E., Tormen G., Sheth R. K., Baso G., Moscardini L., 2016, MNRAS, 456, 2486

Di Valentino E., et al., 2021, Classical and Quantum Gravity, 38, 153001

Diemer B., 2018, ApJS, 239, 35

Diemer B., 2020, ApJ, 903, 87

Diemer B., Joyce M., 2019, ApJ, 871, 168

Diemer B., Kravtsov A. V., 2015, ApJ, 799, 108

Dodelson S., 2003, Modern cosmology. "Academic Press"

Dolag K., Bartelmann M., Perrotta F., Baccigalupi C., Moscardini L., Meneghetti M., Tormen G., 2004, A&A, 416, 853

Dunkley J., Bucher M., Ferreira P. G., Moodley K., Skordis C., 2005, MNRAS, 356, 925

Ebeling H., Edge A. C., Mantz A., Barrett E., Henry J. P., Ma C. J., van Speybroeck L., 2010, MNRAS, 407, 83

Eckert D., et al., 2019, A&A, 621, A40

Eckert D., Ettori S., Pointecouteau E., van der Burg R. F. J., Loubser S. I., 2022a, A&A, 662, A123

Eckert D., Ettori S., Robertson A., Massey R., Pointecouteau E., Harvey D., McCarthy I. G., 2022b, A&A, 666, A41

Einasto J., 1965, Trudy Astrofizicheskogo Instituta Alma-Ata, 5, 87

Eisenstein D. J., Hu W., 1998, ApJ, 496, 605

Eisenstein D. J., Hu W., 1999, ApJ, 511, 5

Enzi W., et al., 2021, MNRAS, 506, 5848

Ettori S., Eckert D., 2022, A&A, 657, L1

Ettori S., Morandi A., Tozzi P., Balestra I., Borgani S., Rosati P., Lovisari L., Terenziani F., 2009, A&A, 501, 61

Ettori S., et al., 2019, A&A, 621, A39

Euclid Collaboration et al., 2019, A&A, 627, A23

Euclid Collaboration et al., 2020, A&A, 642, A191

Euclid Collaboration et al., 2022, A&A, 662, A112

Fawcett T., 2006, Pattern Recognition Letters, 27, 861
Foreman-Mackey D., Hogg D. W., Lang D., Goodman J., 2013, PASP, 125, 306
Freedman W. L., et al., 2020, ApJ, 891, 57
Frenk C. S., White S. D. M., 2012, Annalen der Physik, 524, 507
García R., Salazar E., Rozo E., Adhikari S., Aung H., Diemer B., Nagai D., Wolfe B., 2023, MNRAS, 521, 2464
Gavas S., Bagla J., Khandai N., Kulkarni G., 2023, MNRAS, 521, 5960
Gentile F., et al., 2021, arXiv e-prints, p. arXiv:2105.05602
Ghirardini V., et al., 2019, A&A, 621, A41
Ghirardini V., et al., 2021, ApJ, 910, 14
Gianfagna G., et al., 2021, MNRAS, 502, 5115
Gilman D., Birrer S., Treu T., Nierenberg A., Benson A., 2019, MNRAS, 487, 5721
Gilman D., Birrer S., Nierenberg A., Treu T., Du X., Benson A., 2020, MNRAS, 491, 6077
Giovannini G., Tordi M., Feretti L., 1999, New A, 4, 141
Golovich N., et al., 2019, ApJ, 882, 69
Golse G., Kneib J. P., 2002, A&A, 390, 821
Goodman J., Weare J., 2010, Communications in Applied Mathematics and Computational Science, 5, 65
Gunn J. E., Gott J. Richard I., 1972, ApJ, 176, 1
Gupta S., Hellwing W. A., Bilicki M., García-Farieta J. E., 2022, Phys. Rev. D, 105, 043538
Hahn O., Abel T., 2011, MNRAS, 415, 2101
Hahn O., Abel T., 2013, MUSIC: MUlti-Scale Initial Conditions (ascl:1311.011)
Hahn O., Angulo R. E., 2016, MNRAS, 455, 1115
Hahn O., Porciani C., Carollo C. M., Dekel A., 2007, MNRAS, 375, 489
Harris C. R., et al., 2020, Nature, 585, 357
He Z., et al., 2020, MNRAS, 497, 556
Hejlesen M. M., Rasmussen J. T., Chatelain P., Walther J. H., 2013, Journal of Computational Physics, 252, 458
Hermans J., Banik N., Weniger C., Bertone G., Louppe G., 2021, MNRAS, 507, 1999
Hinshaw G., et al., 2013, ApJS, 208, 19
Hocking A., Geach J. E., Sun Y., Davey N., 2018, MNRAS, 473, 1108
Hsueh J. W., Enzi W., Vegetti S., Auger M. W., Fassnacht C. D., Despali G., Koopmans L. V. E., McKean J. P., 2020, MNRAS, 492, 3047
Hu W., Kravtsov A. V., 2003, ApJ, 584, 702
Huang X., et al., 2020, ApJ, 894, 78
Huang X., et al., 2021, ApJ, 909, 27
Hunter J. D., 2007, Computing in Science & Engineering, 9, 90
Ingoglia L., et al., 2022, MNRAS, 511, 1484
Inoue K. T., 2015, MNRAS, 447, 1452
Inoue K. T., Takahashi R., 2012, MNRAS, 426, 2978
Inoue K. T., Takahashi R., Takahashi T., Ishiyama T., 2015, MNRAS, 448, 2704
Iršič V., et al., 2017, Phys. Rev. D, 96, 023522
Ishiyama T., Fukushige T., Makino J., 2009, PASJ, 61, 1319
Ishiyama T., et al., 2021, MNRAS, 506, 4210

Ivezić Ž., et al., 2019, ApJ, 873, 111
Jacobs C., Glazebrook K., Collett T., More A., McCarthy C., 2017, MNRAS, 471, 167
Jacobs C., et al., 2019, MNRAS, 484, 5330
Jenkins A., Frenk C. S., White S. D. M., Colberg J. M., Cole S., Evrard A. E., Couchman H. M. P., Yoshida N., 2001, MNRAS, 321, 372
Jiang F., van den Bosch F. C., 2014, MNRAS, 440, 193
Jiang F., van den Bosch F. C., 2016, MNRAS, 458, 2848
Jiang F., Dekel A., Freundlich J., van den Bosch F. C., Green S. B., Hopkins P. F., Benson A., Du X., 2021, MNRAS, 502, 621
Johnson T., Benson A. J., Grin D., 2021, ApJ, 908, 33
Kass R. E., Raftery A. E., 1995, Journal of the American Statistical Association, 90, 773
Kay S., 1998, Fundamentals of Statistical Signal Processing: Detection theory. Prentice-Hall PTR
Kelley C. T., 1995, Iterative Methods for Linear and Nonlinear Equations. Society for Industrial and Applied Mathematics, 172 p.
King L. J., Mead J. M. G., 2011, MNRAS, 416, 2539
Klein M., Israel H., Nagarajan A., Bertoldi F., Pacaud F., Lee A. T., Sommer M., Basu K., 2019, MNRAS, 488, 1704
Klypin A., Yepes G., Gottlöber S., Prada F., Heß S., 2016, MNRAS, 457, 4340
Kobayashi T., Murgia R., De Simone A., Iršič V., Viel M., 2017, Phys. Rev. D, 96, 123514
Koppula S., et al., 2021, arXiv e-prints, p. arXiv:2102.05182
Kuhlen M., Vogelsberger M., Angulo R., 2012, Physics of the Dark Universe, 1, 50
Lanusse F., Ma Q., Li N., Collett T. E., Li C.-L., Ravanbakhsh S., Mandelbaum R., Póczos B., 2018, MNRAS, 473, 3895
Laureijs R., et al., 2011, arXiv e-prints, p. arXiv:1110.3193
Lecun Y., Bengio Y., Hinton G., 2015, Nature, 521, 436
Lee C. T., Primack J. R., Behroozi P., Rodríguez-Puebla A., Hellinger D., Dekel A., 2017, MNRAS, 466, 3834
Lesci G. F., et al., 2022, A&A, 665, A100
Lesgourgues J., 2011, arXiv e-prints, p. arXiv:1104.2932
Lewis A., Bridle S., 2002, Phys. Rev. D, 66, 103511
Lewis A., Challinor A., Lasenby A., 2000, ApJ, 538, 473
Li Y., Mo H. J., van den Bosch F. C., Lin W. P., 2007, MNRAS, 379, 689
Liao S., 2018, MNRAS, 481, 3750
López-Cano D., Angulo R. E., Ludlow A. D., Zennaro M., Contreras S., Chaves-Montero J., Aricò G., 2022, MNRAS, 517, 2000
Lovell M. R., Frenk C. S., Eke V. R., Jenkins A., Gao L., Theuns T., 2014, MNRAS, 439, 300
Lovisari L., et al., 2017, ApJ, 846, 51
Ludlow A. D., Navarro J. F., Li M., Angulo R. E., Boylan-Kolchin M., Bett P. E., 2012, MNRAS, 427, 1322
Ludlow A. D., Bose S., Angulo R. E., Wang L., Hellwing W. A., Navarro J. F., Cole S., Frenk C. S., 2016, MNRAS, 460, 1214
Macciò A. V., Dutton A. A., van den Bosch F. C., Moore B., Potter D., Stadel J., 2007, MNRAS, 378, 55

Maggiore M., Riotto A., 2010a, ApJ, 711, 907
Maggiore M., Riotto A., 2010b, ApJ, 717, 515
Markevitch M., Vikhlinin A., 2007, Phys. Rep., 443, 1
Markevitch M., Gonzalez A. H., Clowe D., Vikhlinin A., Forman W., Jones C., Murray S., Tucker W., 2004, ApJ, 606, 819
Marsh D. J. E., 2016, Phys. Rep., 643, 1
Martin G., Kaviraj S., Hocking A., Read S. C., Geach J. E., 2020, MNRAS, 491, 1408
Maturi M., Bellagamba F., Radovich M., Roncarelli M., Sereno M., Moscardini L., Bardelli S., Puddu E., 2019, MNRAS, 485, 498
Mead J. M. G., King L. J., Sijacki D., Leonard A., Puchwein E., McCarthy I. G., 2010, MNRAS, 406, 434
Menanteau F., et al., 2013, ApJ, 765, 67
Merloni A., et al., 2012, arXiv e-prints, p. arXiv:1209.3114
Miyazaki S., et al., 2002, PASJ, 54, 833
Mo H., van den Bosch F. C., White S., 2010, Galaxy Formation and Evolution. Cambridge University Press
Molnar S., 2016, Frontiers in Astronomy and Space Sciences, 2, 7
Mulroy S. L., et al., 2019, MNRAS, 484, 60
Nadler E. O., Birrer S., Gilman D., Wechsler R. H., Du X., Benson A., Nierenberg A. M., Treu T., 2021, ApJ, 917, 7
Narayanan V. K., Spergel D. N., Davé R., Ma C.-P., 2000, ApJ, 543, L103
Navarro J. F., Frenk C. S., White S. D. M., 1997, ApJ, 490, 493
Neto A. F., et al., 2007, MNRAS, 381, 1450
Newman A. B., Treu T., Ellis R. S., Sand D. J., Nipoti C., Richard J., Jullo E., 2013, ApJ, 765, 24
Niemeyer J. C., 2020, Progress in Particle and Nuclear Physics, 113, 103787
Ogiya G., Mori M., 2011, ApJ, 736, L2
Oguri M., Takada M., 2011, Phys. Rev. D, 83, 023008
Okabe N., Smith G. P., 2016, MNRAS, 461, 3794
Okabe N., Takada M., Umetsu K., Futamase T., Smith G. P., 2010, PASJ, 62, 811
Ondaro-Mallea L., Angulo R. E., Zennaro M., Contreras S., Aricò G., 2022, MNRAS, 509, 6077
Payerne C., Murray C., Combet C., Doux C., Fumagalli A., Penna-Lima M., 2023, MNRAS, 520, 6223
Pedregosa F., et al., 2011, Journal of Machine Learning Research, 12, 2825
Pierre M., et al., 2016, A&A, 592, A1
Planck Collaboration et al., 2014a, A&A, 571, A16
Planck Collaboration et al., 2014b, A&A, 571, A29
Planck Collaboration et al., 2016, A&A, 594, A13
Planck Collaboration et al., 2020, A&A, 641, A6
Planelles S., Quilis V., 2009, MNRAS, 399, 410
Pontzen A., Governato F., 2012, MNRAS, 421, 3464
Postman M., et al., 2012, ApJS, 199, 25
Prada F., Klypin A. A., Cuesta A. J., Betancort-Rijo J. E., Primack J., 2012, MNRAS, 423, 3018
Pratt G. W., Arnaud M., Biviano A., Eckert D., Ettori S., Nagai D., Okabe N., Reiprich T. H., 2019, Space Sci. Rev., 215, 25

Press W. H., Davis M., 1982, ApJ, 259, 449
Press W. H., Schechter P., 1974, ApJ, 187, 425
Prunet S., Pichon C., Aubert D., Pogosyan D., Teyssier R., Gottloeber S., 2008, ApJS, 178, 179
Ragagnin A., Saro A., Singh P., Dolag K., 2021, MNRAS, 500, 5056
Rasera Y., et al., 2022, A&A, 661, A90
Rasia E., Mazzotta P., Evrard A., Markevitch M., Dolag K., Meneghetti M., 2011, ApJ, 729, 45
Reed D. S., Bower R., Frenk C. S., Jenkins A., Theuns T., 2007, MNRAS, 374, 2
Reichardt C. L., et al., 2013, ApJ, 763, 127
Rey M. P., Pontzen A., Saintonge A., 2019, MNRAS, 485, 1906
Richardson T. R. G., Corasaniti P. S., 2022, MNRAS, 513, 4951
Richardson T. R. G., Corasaniti P.-S., 2023, A&A, 674, A173
Richardson T. R. G., Stücker J., Angulo R. E., Hahn O., 2022, MNRAS, 511, 6019
Riess A. G., et al., 2022, ApJ, 934, L7
Romualdez L. J., et al., 2016, arXiv e-prints, p. arXiv:1608.02502
Roy F., Bouillot V. R., Rasera Y., 2014, A&A, 564, A13
Rykoff E. S., et al., 2016, ApJS, 224, 1
Sáez-Casares I., Rasera Y., Li B., 2023, arXiv e-prints, p. arXiv:2303.08899
Sartoris B., et al., 2020, A&A, 637, A34
Schaye J., et al., 2023, arXiv e-prints, p. arXiv:2306.04024
Schneider P., Ehlers J., Falco E. E., 1992, Gravitational Lenses. "Springer Science & Business Media", doi:10.1007/978-3-662-03758-4
Schneider A., Smith R. E., Macciò A. V., Moore B., 2012, MNRAS, 424, 684
Schöneberg N., Abellán G. F., Sánchez A. P., Witte S. J., Poulin V., Lesgourgues J., 2022, Phys. Rep., 984, 1
Seljak U., Zaldarriaga M., 1996, ApJ, 469, 437
Seppi R., et al., 2021, A&A, 652, A155
Sereno M., 2015, MNRAS, 450, 3665
Sereno M., Covone G., Izzo L., Ettori S., Coupon J., Lieu M., 2017, MNRAS, 472, 1946
Shajib A. J., et al., 2023, A&A, 673, A9
Shandarin S. F., Zeldovich Y. B., 1989, Reviews of Modern Physics, 61, 185
Shandarin S., Habib S., Heitmann K., 2012, Phys. Rev. D, 85, 083005
Sheth R. K., Tormen G., 1999, MNRAS, 308, 119
Sheth R. K., Tormen G., 2002, MNRAS, 329, 61
Sikivie P., 2008, Axions: Theory, Cosmology, and Experimental Searches. Springer Berlin Heidelberg, Berlin, Heidelberg, pp 19–50, doi:10.1007/978-3-540-73518-2_2, https://doi.org/10.1007/978-3-540-73518-2_2
Sousbie T., 2011, MNRAS, 414, 350
Sousbie T., Colombi S., 2016, Journal of Computational Physics, 321, 644
Spindler A., Geach J. E., Smith M. J., 2021, MNRAS, 502, 985
Springel V., 2005, MNRAS, 364, 1105
Springel V., White S. D. M., Tormen G., Kauffmann G., 2001, MNRAS, 328, 726
Springel V., Pakmor R., Zier O., Reinecke M., 2021, MNRAS, 506, 2871
Staniszewski Z., et al., 2009, ApJ, 701, 32
Stein G., Blaum J., Harrington P., Medan T., Lukic Z., 2021, arXiv e-prints, p.

arXiv:2110.00023
Stuardi C., Bonafede A., Lovisari L., Domínguez-Fernández P., Vazza F., Brüggen M., van Weeren R. J., de Gasperin F., 2021, MNRAS, 502, 2518
Stücker J., Hahn O., Angulo R. E., White S. D. M., 2020, MNRAS, 495, 4943
Stücker J., Angulo R. E., Hahn O., White S. D. M., 2022, MNRAS, 509, 1703
Sugiyama N., 1995, ApJS, 100, 281
Sugiyama S., et al., 2023, arXiv e-prints, p. arXiv:2304.00705
Sunyaev R. A., Zeldovich Y. B., 1970, Ap&SS, 7, 3
Tegmark M., et al., 2004, Phys. Rev. D, 69, 103501
Teyssier R., 2002, A&A, 385, 337
Tinker J., Kravtsov A. V., Klypin A., Abazajian K., Warren M., Yepes G., Gottlöber S., Holz D. E., 2008, ApJ, 688, 709
Tinker J. L., Robertson B. E., Kravtsov A. V., Klypin A., Warren M. S., Yepes G., Gottlöber S., 2010, ApJ, 724, 878
Torrado J., Lewis A., 2019, Cobaya: Bayesian analysis in cosmology, Astrophysics Source Code Library, record ascl:1910.019 (ascl:1910.019)
Treu T., Suyu S. H., Marshall P. J., 2022, A&A Rev., 30, 8
Trotta R., 2007, MNRAS, 378, 72
Umetsu K., Broadhurst T., Zitrin A., Medezinski E., Coe D., Postman M., 2011, ApJ, 738, 41
Umetsu K., Zitrin A., Gruen D., Merten J., Donahue M., Postman M., 2016, ApJ, 821, 116
Umetsu K., et al., 2020, ApJ, 890, 148
Vallés-Pérez D., Planelles S., Monllor-Berbegal Ó., Quilis V., 2023, MNRAS, 519, 6111
Vegetti S., Despali G., Lovell M. R., Enzi W., 2018, MNRAS, 481, 3661
Viel M., Lesgourgues J., Haehnelt M. G., Matarrese S., Riotto A., 2005, Phys. Rev. D, 71, 063534
Viel M., Becker G. D., Bolton J. S., Haehnelt M. G., 2013, Phys. Rev. D, 88, 043502
Vikhlinin A., Markevitch M., Murray S. S., Jones C., Forman W., Van Speybroeck L., 2005, ApJ, 628, 655
Virtanen P., et al., 2020, Nature Methods, 17, 261
Wang J., White S. D. M., 2007, MNRAS, 380, 93
Wang J., et al., 2011, MNRAS, 413, 1373
Wang K., Mao Y.-Y., Zentner A. R., Lange J. U., van den Bosch F. C., Wechsler R. H., 2020a, MNRAS, 498, 4450
Wang J., Bose S., Frenk C. S., Gao L., Jenkins A., Springel V., White S. D. M., 2020b, Nature, 585, 39
Warren M. S., Abazajian K., Holz D. E., Teodoro L., 2006, ApJ, 646, 881
Watson W. A., Iliev I. T., D'Aloisio A., Knebe A., Shapiro P. R., Yepes G., 2013, MNRAS, 433, 1230
Weaver J. R., 1985, The American Mathematical Monthly, 92, 711
Weinberg S., 2008, Cosmology. Oxford University Press
Weymann R. J., Latham D., Angel J. R. P., Green R. F., Liebert J. W., Turnshek D. A., Turnshek D. E., Tyson J. A., 1980, Nature, 285, 641
Yoon J. H., Johnston K. V., Hogg D. W., 2011, ApJ, 731, 58
Zel'dovich Y. B., 1970, A&A, 5, 84
Zhao H., 1996, MNRAS, 278, 488

Zhao D. H., Mo H. J., Jing Y. P., Börner G., 2003, MNRAS, 339, 12
Zhao D. H., Jing Y. P., Mo H. J., Börner G., 2009, ApJ, 707, 354
Zolotov A., et al., 2012, ApJ, 761, 71
Zuhone J. A., Roediger E., 2016, Journal of Plasma Physics, 82, 535820301
de Blok W. J. G., Walter F., Brinks E., Trachternach C., Oh S. H., Kennicutt R. C. J., 2008, AJ, 136, 2648
van den Bosch F. C., 2002, MNRAS, 331, 98

RÉSUMÉ

À une époque de tensions en cosmologie, les amas de galaxies offrent une opportunité unique et renaissante pour apporter de nouvelles réponses aux débats. Étant les structures gravitationnellement liées les plus massives de l'Univers, les amas de galaxies se situent à la frontière entre la cosmologie et l'astrophysique, et sont à présent bien établis en tant que sonde cosmologique grâce à leurs abondances et leur *'clustering'*.
Dans cette thèse, nous examinons l'utilisation potentiel de la structure interne des amas de galaxies en tant que nouvelle sonde à la fois, du modèle cosmologique et des processus astrophysiques qui ont lieu à l'intérieur de ces objets. Précisément nous caractérisons la structure interne par le biais d'un proxy non paramétrique de la forme du profile de masse que nous nommons *'halo sparsity'*, définis comme étant simplement le rapport de deux masses.
Nous montrons que l'utilisations de la sparsity permet de jauger l'impact de collisions et fusions d'amas ainsi que de concevoir une approche statistique permettant de rapidement détecter ces évènements dans les catalogues de grands relevés, en fournissant aussi une estimation préliminaire de l'époque à laquelle ces évènements ont eu lieu. De plus, nous quantifions la dépendance cosmologique de la sparsity nous permettant d'améliorer mais aussi de créer une nouvelle méthode pour contraindre les paramètres cosmologiques du modèle ΛCDM.
Enfin, nous franchissons les premières étapes permettant d'amener cette sonde au-delà du domaine des nouveautés théorique en étudiant comment elle est affectée par diverses contraintes observationnelles. En particulier, nous examinons l'impact des traceurs de masse biaisés, des hypothèses faites par les pipelines observationnels, des incertitudes sur les mesures de masses ainsi que la possibilité de combiné la sprasity avec d'autres sondes cosmologiques.

MOTS CLÉS

Cosmologie, Amas de Galaxies, Halos, Matière Noire, Simulations N-Corps

ABSTRACT

At a time of tensions in cosmology, galaxy clusters provide a unique and renewed avenue to possibly settle debates. As the largest gravitationally bound structures in the Universe, galaxy clusters find themselves at the interface between cosmology and astrophysics, and are now well established probes of the cosmological model through their abundances and clustering.
In this work, we investigate the potential of using the internal structure of galaxy clusters as a novel probe of both the underlying cosmology and the astrophysical processes which take place within these objects. Specifically, we characterise the internal structure through the shape of the mass profile which we quantify using a non-parametric proxy which we call halo sparsity, simply defined as the ratio of two masses.
We show how the use of sparsity can gauge the impact of individual merger events and design a statistical approach to quickly detect recent events in large survey catalogues while also providing a preliminary estimate of the time at which these mergers took place. Furthermore, we quantify the cosmology dependence of halo sparsity allowing us to improve and design a novel approach to constrain the ΛCDM cosmological parameters.
Finally, we begin to take this probe beyond the realm of theoretical oddities by investigating how it is affected by observational constraints. In particular, we study the impact of biased mass tracers, observational pipeline assumptions, mass measurement uncertainties as well as the possibility of combining halo sparsity with other cosmological probes.

KEYWORDS

Cosmology, Galaxy clusters, Haloes, Dark Matter, N-Body Simulations